Synthesis of Metal and Metal Oxide Nanoparticles for Electrocatalytic Hydrogen and Oxygen Evolution Reaction

THESIS

Submitted in partial fulfilment

of the requirement for the degree of

DOCTOR OF PHILOSOPHY

By

Roshan Nazir

Under the supervision of

Dr. Surojit Pande

BIRLA INSTITUTE OF TECHNOLOGY AND SCIENCE PILANI

PILANI CAMPUS (RAJASTHAN) INDIA

April, 2018

Birla Institute of Technology & Science
Pilani – 333 031 (Rajasthan) INDIA

Dr. Surojit Pande
Assistant Professor
Department of Chemistry

Phone: +91-1596-515709(O)
+91-9468646542(M)
Fax: +91-1596-244183
Email: surojitpande@gmail.com / spande@pilani.bits-pilani.ac.in

CERTIFICATE

This is to certify that the thesis entitled **Synthesis of Metal and Metal Oxide Nanoparticles for Electrocatalytic Hydrogen and Oxygen Evolution Reaction** submitted by **Roshan Nazir,** ID. No. **2013PHXF0015P** for award of Ph.D. Degree of the Institute, embodies original work done by him under my supervision.

Signature of Supervisor

_____

Name: **Dr. Surojit Pande**

Date: /   / 2018

Designation: Assistant Professor

innovate   achieve   lead

Birla Institute of Technology & Science, Pilani
Pilani Campus, Vidya Vihar
Pilani 333031, Rajasthan, India

Tel: +91 1596 245073 Ext: 279
Fax: +91 1596 244183
Web: www.pilani.bits-pilani.ac.in

Acknowledgement

Words are inadequate to express gratitude towards my family. My Parents Syed Nazir Ahmad Andrabi, Syeda Yasmeen and my brothers Mudasir, Irfan and Majid are the source of inspiration and courage in every ups and down of my life. I feel proud to say that they are finest people on the face of earth. I once again would like to show my heartfelt thanks to my parents as

I feel they are the true architect behind this glory. Every achievement of this thesis is the result of their prayers, encouragement and love. All my relatives deserve sincere thanks for the trust and confidence they put on me.

Last but not least I would like to thank the power in whose hands is my life, supreme power of universe, almighty Allah for his unparallel grace that leads me towards the ultimate goal through the lows and highs of my life and my PhD journey, I am highly thankful, for your love and care.

BITS Pilani

March 2018   Roshan Nazir

Index

Contents   **Page no.**

<u>Chapter I</u>: Introduction and scope of the work

Chapter III: Synthesis and characterization of bimetallic alloy nanoparticles (Ag/Pt, Ag/Pd, and Ag/Au) via galvanic exchange for hydrogen evolution reaction

Chapter IV: **Decoration of gold nanoparticles on copper sulfide surface**
via **photoreduction route for enhanced electrochemical**
hydrogen evolution and photocatalysis

Chapter VII: Conclusion and future scope

Appendices:

Abstract

Metal and metal oxide nanoparticles are known to have potential applications in multi-disciplinary fields. This thesis deals with design and synthesis of metal nanoparticles on semiconducting graphitic-carbon nitride (g-C$_3$N$_4$) and copper sulfide supports for photocatalysis and hydrogen evolution reactions. This thesis also contains a comprehensive study of shape dependent property of metal oxides for hydrogen evolution and oxygen evolution reaction. First chapter of this thesis describes the introduction and importance of nanoscience in our day-to-day life. New innovations in the field of electrocatalysis and future scope of hydrogen and oxygen evolution have been well elucidated at the end of this chapter. Second chapter illustrates the synthesis of Pt and Pd nanoparticles on g-C$_3$N$_4$ surface to prepare C$_3$N$_4$/Pd and C$_3$N$_4$/Pt nanoparticles. Pt nanoparticle decorated on C$_3$N$_4$ shows higher activity in hydrogen evolution than C$_3$N$_4$/Pd, whereas, C$_3$N$_4$/Pd exhibits better performance in nitro compound reaction. Third chapter elucidates the synthesis of AgPd, AgPt, and AgAu bimetallic alloy nanoparticles on g-C$_3$N$_4$ surface for hydrogen evolution. Bimetallic nanoparticles have been synthesized from C$_3$N$_4$/Ag *via* galvanic exchange, where Ag acted as sacrificial atom. Electrocatalytic study revealed that C$_3$N$_4$/AgPt is an efficient electrocatalyst than C$_3$N$_4$/AgPd and C$_3$N$_4$/AgAu nanoparticles. Fourth chapter delineates the synthesis of an efficient hydrogen evolution catalyst, CuS/Au heterostructure using a green synthetic approach. The as-synthesized catalyst has also been proved to be an active photocatalyst for methylene blue dye degradation under the illumination of visible light. Fifth chapter reported the synthesis of one-dimensional RuO$_2$ nanorod for hydrogen and oxygen evolution reaction, an efficient and stable bifunctional electrocatalyst. RuO$_2$ nanorod has been synthesized via calcination at 500 $^\circ$C and the mechanism of formation has also discussed in detail. Chapter sixth depicts a new and novel method for the synthesis of IrO$_2$ nanosheet, which has been used for electrocatalytic oxygen evolution reaction. The higher activity of IrO$_2$ nanosheet authenticates the fact that two dimension morphology has high surface area and more number of active sites that can make rapid electron flow during oxygen evolution reaction. Finally, overall conclusion and future scope of this work has been discussed in chapter seven.

Key words: Nanoparticles, Galvanic exchange, Calcination, Hydrogen evolution, Photocatalysis, and Oxygen evolution reaction.

List of Abbreviations

BE	Binding energy
CV	Cyclic voltammetry
CB	Conduction band
CE	Counter electrode
EDS	Energy dispersive spectroscopy
ECSA	Electrocatalytically active surface area
eV	Electron volt
FTIR	Fourier-transform infrared spectroscopy
GCE	Glassy carbon electrode
HER	Hydrogen evolution reaction
h	hour
ml	Millilitre
μM	Micromolar
mM	Millimolar
min	Minute
MB	Methylene blue
M	Molar
nm	Nanometer
NS	Nanosheet
NR	Nanorod
NP	Nanoparticle
NIR	Near-infrared radiation
NA	Nitroaniline

4-NP	4-nitrophenol
NBA	Nitrobenzoic acid
OER	Oxygen evolution reaction
QSE	Quantum size effect
RE	Reference electrode
Rs	Solution resistance
STEM	Scanning transmission electron microscopy
SPB	Surface plasmon band
SERS	Surface enhanced Raman scattering
SEM	Scanning electron microscopy
SAED	Selected area electron diffraction
Sec	Second
TEM	Transmission electron microscopy
UV	Ultra violet
VB	Valence band
XRD	X-ray diffraction
XPS	X-ray photoelectron spectroscopy

List of Symbols

α	Absorption coefficient
θ	Angle
E_g	Band gap
E_p	Discrete photo energy
°C	Degree celcious
e	Electron
E_f	Fermi level
F	Faraday
ν	Frequency
ε	Molar absorptivity
η	Overpotential
σ	Orbital identification
π	Pi
h	Planck's constant
Å	Size of atom
K	Temperature
R	Universal gas constant
V	Volt
λ	Wavelength

List of Reagents

K_2PdCl_4	Alfa Aesar
$CuSO_4.5H_2O$	Sisco Research Laboratory
K_2PtCl_4	Alfa Aesar
$HAuCl_4.3H_2O$	Sigma Aldrich
$RuCl_3.xH_2O$	Sigma Aldrich
$IrCl_3.3H_2O$	Sigma Aldrich
$AgNO_3$	Sigma Aldrich
5 % Pt/C	Sigma Aldrich
Urea	SD Fine Chemicals
Carbon powder	Sigma Aldrich
Alumina powder	Buhler
Multiwall carbon nanotubes	Alfa Aesar
Sodium borohydride	Sisco Research Laboratory
Perfluorinated nafion	Sigma Aldrich
Thioacetamide	SD Fine Chemicals
Thiourea	SD Fine Chemicals
Glucose	SD Fine Chemicals
Potassium bromide	Molychem
Barium sulphate	Sisco Research Laboratory
Methylene blue	Alfa Aesar
4-Nitrophenol	Sisco Research Laboratory
4-Aminophenol	Sisco Research Laboratory
Ethanol	Merck

Methanol	Merck
Isopropyl alcohol	Sigma Aldrich
NaOH	SD Fine Chemicals
KOH	SD Fine Chemicals
Commercial IrO_2	Sigma Aldrich
Commercial RuO_2	Sigma Aldrich
4-Nitrobenzoic acid	SD Fine Chemicals
2-Nitrobenzoic acid	Molychem
Hydrochloric acid	Sigma Aldrich
Nitric acid	SD Fine Chemicals
Sulfuric acid	Sigma Aldrich
Perchloric acid	Sigma Aldrich

List of Instruments

1. Magnetic stirrer: REMI, India.

2. Weighing balance: Denver Instrument India.

3. UV-visible Spectrophotometer: Jasco V-650 Spectrophotometer (UV-1800) was used. A Quartz cuvette of 1.0 cm path length was used during the measurements.

4. Powder X-ray diffraction (PXRD): Rigaku Mini Flex II diffractometer with Cu-Kα radiation at 25 °C. PXRD was recorded using $2\theta = 10\text{-}80°$ with 2° per min scan rate.

5. Fourier-transform infrared spectroscopy (FTIR): Powder samples (pellets in KBr, without moisture) was carried out using a Perkin Elmer 2000 infrared spectrometer in the range of 500-2000 cm^{-1}.

6. Field-emission scanning electron microscopy (FESEM): Nova Nano Sem 450 operating from 0.5 kV to 30 kV. EDS measurements were performed using Bruker XFlash 6130, attached with FESEM instrument.

7. Transmission electron microscopy (TEM): Bruker microscope operating at 200 kV was used for TEM analysis. 400-mesh carbon-coated copper grid was used for sample preparation and freshly prepared materials were drop casted on the grid and dried overnight. For size calculation ~ 75-100 particles were selected randomly.

8. X-ray photoelectron spectroscopy (XPS): Commercial Omicron spectrometer equipped with an Mg-Kα x-ray source (1256.6eV) was used for XPS analysis. Emission current of the X-ray source was fixed at 15 mA for an anode voltage of 15 kV for all measurements. Pass energy of 20 eV, with a step size of 0.1 eV was used for high resolution XPS spectra. Throughout the measurements, the UHV chamber base pressure was maintained $< 10^{-9}$ mbar. 10.0 μL of the aqueous dispersed solution of nanomaterials was deposited onto a small piece of conducting carbon tape and dried under a dry nitrogen line. C 1s binding energy peak at 284.5 eV was used as a reference to avoid any charging effect.

9. Raman analysis was carried out using Airix (ATR 500) Raman spectrophotometer.

10. Inductive coupled plasma mass analysis (ICP Mass): Varian 720-ES was used for IPC-mass analysis.

11. Electrochemical analysis: Potentiostat (CHI 604E, CH Instruments, USA) using a three-electrode cell system was employed for electrochemical measurements. In three electrode system, working, counter, and reference electrodes were used as glassy carbon electrode (GCE, 3 mm diameter), Pt wire/graphite rod, and Ag/AgCl, respectively.

List of Schemes

List of Figures

List of Tables

Chapter 1

Introduction and scope of the work

1. Introduction:

Nanoscience and nanotechnology is used directly or indirectly in every dimension of life, thus has been fascinating and revolutionizing the modern world. Nanotechnology is actually the science of manipulating the material at the nanosize regime to develop significantly interesting properties, which are different to that of bulk material. The nanodimension objects display different properties to that of bulk material. Nanoparticles have raised considerable interest as they display characteristic physical, chemical, biological, and optoelectronic properties. These attractive properties of nanoparticles have given birth to many potential applications in biology, chemistry, physics, material science, and various interdisciplinary fields. The interesting properties in nanoscale materials arise from the two important phenomenon, one is high surface-to-volume ratio and the other is quantum size effect. Metal nanoparticles in nanosize regime have great tendency to unite as they posses' high surface energies and thus aggregates readily. Therefore, synthesis of metal nanoparticles in nanosize regime has been a critical challenge in scientific community. Scientists have seen tremendous progress in design and synthesis of metal nanoparticles using new and innovative techniques in last couple of decades. Metal nanoparticles are decorated on semiconducting support like graphitic carbon nitride (g-C_3N_4) to form a metal-semiconductor nanocomposition (C_3N_4/M). The nanocombination so formed imparts extra stability and efficiency in catalytic and electrocatalytic reactions. Metal and metal oxide nanoparticles in recent years have shown great promise in oxygen and hydrogen evolution reactions. The size and shape dependent catalytic property of metal oxide nanoparticles have been extensively studied. The influence on electrocatalytic efficiency using morphology based approach of metal oxide nanoparticles have shown a great success in water splitting reactions. Production of hydrogen gas by electrocatalytic water splitting may serve as fuel of future while production of oxygen gas is important in chemical energy storage.

1.1. Nanoscience and Nanotechnology: A Brief Overview

Nanoscience and nanotechnology is the development of science and engineering by elucidation, manipulation, and application of the nanosized matter. The last decade has witnessed an exponential growth in this exciting field of nano. This fascinating world of nanoscience and technology actually emerged from a lecture of American theoretical physicist R. P. Feynman. In December 29, 1959, a meeting was organized by American Physical Society at California institute of technology where Feynman delivered a beautiful lecture entitled "there is huge space at the bottom". [1, 2] The great scientist further said that, "the rules of physics are not against manipulation of matter atom by atom". In this lecture he made a clear statement that the construction of nanosystems would be interdisciplinary and create new opportunities that could possibly change the future technology.

Nano is actually a Greek word means dwarf. Materials in nanometer length scale are not visible in naked eye, so to understand this unusual world it is compulsory to know the unit of measurement involved. The distance travelled by light in 1/2997292458 second is the basic unit of length called meter. Nanometer (1 nm) is equal to 1 billionth of meter. In common sense we can say 1 nm is equal to one millionth of a human hair or the width of three atoms. The nanodimension objects can be visible under powerful microscope. Nanometers are used to measure the things which are extremely small. The thickness of human hair is 10^6 nm (1 mm), blood cells have length of 1000 nm (1μm), viruses are of 100 nm in dimension and fullerene has length of 1 nm. [3] Though nanoscience and nanotechnology came into existence in the latter half of 20th century, but nature already posses signs and paradigms of nanotechnology.

There are many naturally available examples of nanoscience and nanotechnology. First, the abalone (a mollusk) develops a strong shell around his body with stiff fracture toughness. This stiff toughness increased the curiosity for material scientists to know the secret behind this toughness of shell. The shell is formed from nanostructured bricks of $CaCO_3$ and these nanostructured bricks are actually responsible for stiff toughness of the shell. [4] It was further revealed that these bricks were connected by a glue of carbohydrate and protein mixture. Second, flagella (a kind of bacteria), which rotates at a rate of 10,000 rpm. Studies have proved that the bacteria consist of biological molecular machine whose motor is driven into function by proton flow caused by potential difference across the membranes. The astonishing fact is that the motor has a diameter of 45 nm and clearance of 1 nm. [5, 6] Third, silk is also one of the basic example

of naturally occurring nanotechnology. Silk is very tough because the molecules are cross linked together and form meshwork structure which gives outstanding mechanical properties. Various bio-systems like bio-membranes, ion channels, colloidal solution of body (blood) are in nanometer length scale. Physiologically active substances like vitamins, DNA, RNA, fructose, glucose, ATP, fibrinogen and others are also in nanodomain. These bio-molecules work on the principle of maximum efficiency with least consumption of energy. Similarly, there are plenty of examples around us in nanodomain where nature is the manufacturer.

Nanotechnology is used to create new materials and devices which have better efficiency than the conventional materials and devices. These materials show vast applications in nanomedicines, nanoelectronics, biomaterials for conservation and production of energy. New scientific foundation of nanotechnology has evolved in last decade particularly in the area of physics which includes nanomechanics, nanophotonics and nonoionics.

1.2. Historical Background

Despite the fast growth in nanotechnology, nanoscale materials have been existing around the globe for millions of years. Gold has been considered as revolutionary material in developing nanotechnology as most of the current and past research revolved around it. In ancient time gold has been predominantly investigated. It was first extracted in the 5th millennium B.C. near Varna (Bulgaria). During the construction of famous statue of Touthakamon 10 tons per year of gold was supplied in Egypt around 1200-1300 B.C. It was presumed that "soluble" gold first appeared around 4th or 5th century B.C. in Egypt and China. [7] In ancient time materials were used for both ornamental and therapeutic purposes. Colloidal gold was considered for coloring the ceramics and ruby glass formation, in fact this practice is still common. One of the long memorable example of this is the Lycurgus Cup (Figure 1.1), presumably, it was the invention in 4th to 5th century B.C. The beauty of this cup is that it appears red in transmitted light and green in reflected light. Soluble gold had

Figure 1.1: The Lycurgus cup made from glass appears red in transmitted light and green in reflected light. The glass contains 70 nm particles as seen in the transmission electron micrograph. From the site http://www.thebritish museum.ac.uk

attained considerable attraction until mid century because it was used in treatment of heart

3

disease and diagnosis of Syphilis. It was also a potential drug for dysentery, epilepsy and tumors. Faraday did a comprehensive study on gold and in 1857 and synthesized deep red solution of colloidal gold. This fabulous discovery was based on the reduction of an aqueous solution of chloroaurate $(AuCl_4)^-$ using red phosphorus in CS_2 (a two-phase system) as a reducing agent. His investigation revealed that the bluish-purple color changes to green on application of pressure. [8] Later on the term "colloid" was coined by Graham, in 1861. [9] In 1908, G. Mie was the first person who tried to solve the mysterious red color of gold nanoparticles in solution. [10] It took 50 years to elucidate Mie's idea about the optical properties of nanoparticles having sizes less than the resolution limit of light microscopes. Later on his idea became a hot topic for research, which proved to be a great success in developing new field of cluster science.

1. 3. Important Aspect of Nanoparticles
Two important aspects of nanoparticles are quantum size effect and surface plasmon resonance

1. 3. 1. Quantum Size Effects and Quantum Dots
The properties of solid can be notably varied to that of bulk by decreasing the dimensions. [11, 12] This reduction of size has pretty much influence on the physiochemical, electrical, optical, and magnetic properties of solids. [13] This phenomenon of bringing drastic change in the properties by manifestation in the size of particles to quantum level is known as quantum confinement. Semiconductor quantum dots are a category of materials, where, concept of quantum confinement is significantly elucidated in detail. These quantum dots are sometimes also referred as 'semiconductor nanocrystals'.
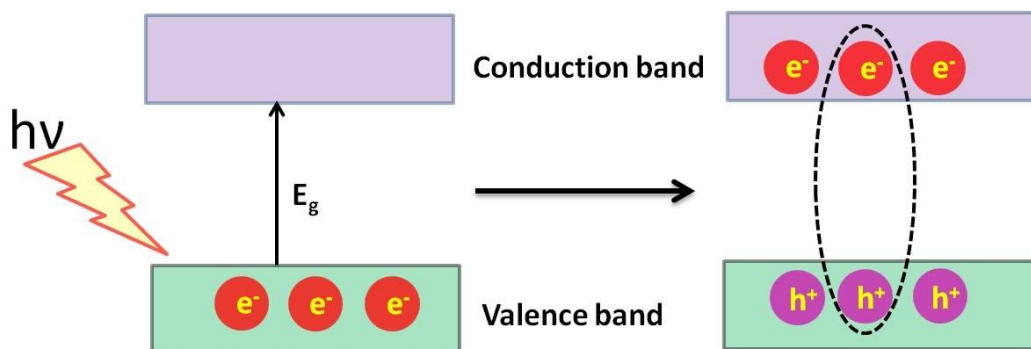
Figure 1.2: Exciton, e^--h^+ pair bounded by attractive electrostatic interaction

Quantum dot is in fact referring only to semiconductor while 'nanocrystals' can be any inorganic moiety having crystalline nature. In a macroscopic semiconductor crystal at absolute temperature (0 K) the valance band (VB) is filled and the conduction band (CB) is completely empty. These VB and CB are separated from each other by a specific band gap, E_g. However, with the increase in temperature there is a transition of electron from valence band to conduction band due to thermal vibrations, resulting in the formation of hole in the valence band. There is a definite interaction between the electron in the conduction band and the hole in the valence band when they approach each other at a finite distance. This bounded electron-hole pair is called an 'exciton', whose delocalization is found throughout the crystal. The Bohr radius (a) of the exciton can be given as: $a = h^2 \varepsilon /4\pi^2 e^2 (1/m_e + 1/m_h)$, where, ε is the dielectric constant of the material, 'e' is the charge of the electron and m_e and m_h are the effective masses of the electron and hole, respectively. When the size of the semiconductor crystal becomes comparable or smaller to that of Bohr radius, quantum confinement come into existence. Quantum confinement effects are observed when the size is sufficiently small, so that the energy level spacing of a nanocrystal exceeds kT (where k is Boltzmann's constant and T is temperature). Energy differences > kT restrict the electron and holes mobility in the crystal. In case of CdSe it is ~56 Å. The energy possessed by electron in the conduction band energy level is given by, $E_e = h^2n^2/8m_eL^2$, similarly, for hole in valence band, $E_h = h^2n^2/8m_hL^2$, where, L represents size of the nanocrystals. [14] Since the mass of electron is very much smaller than hole, the energy levels of electron are separated more widely than the hole levels. The energy levels have noticeable effect on the diameter of the semiconductor particles. [15-24] As energy is inversely dependent on the diameter, the energy levels of lowest conduction band level and highest valence band level change significantly with the diameter of particle and effective mass of electron and hole. For particles having small diameter, there will be change in the effective masses of the electron and hole resulting in separation of energy levels. This also results in quantization of the energy levels. Formation of exciton is shown schematically in Figure 1.2. The most important nanostructures required to design nanoelectronic devices are quantum wells, quantum wires and quantum dots, or these are the basic building blocks of nanoelctronic devices. Quantum dots (also known as quantum boxes) are defined by the tiny unit of matter or zero dimensional (0D) structures in which electrons have zero degrees of freedom. Otherwise, we can also mention that electrons are quantum mechanically confined to all directions. Quantum wires are one-

dimensional (1D) structure where electrons are confined in two directions and free to move in only one direction. In case of quantum wire the density of states (DOS) show the Lorenzian line shape. Quantum wells are actually two-dimensional (2D) structures, where, the electrons are confined in one dimension and free to move in two dimensions, which results in creation of 'quantum wells' or quantum films' the electrons feel a potential well as they are trapped in the film. A step like behavior is shown by the DOS. In case of bulk material, the electronic structure is not restricted by the dimension of material and are free to move in any dimension. The DOS exhibits smooth variation in bulk. The DOS were thoroughly studied by G. E. Volovik using high-temperature superconductor, $Bi_2Sr_2CaCu_2O_8$. [25] The variation in energy levels and DOS as one moves from bulk to quantum dot is shown in Figure 1.3.
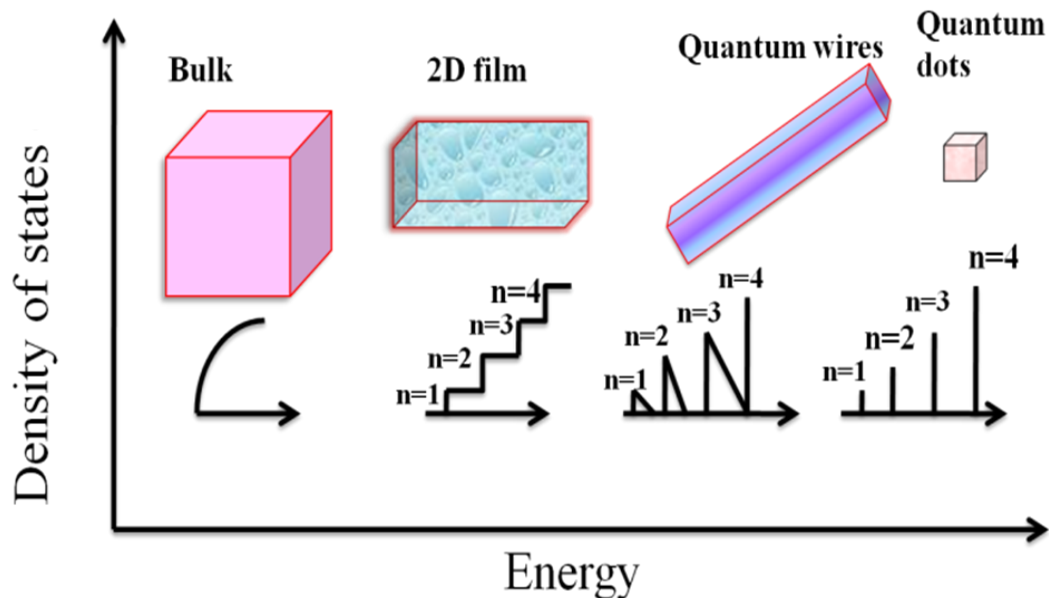
Figure 1.3: Quantization of the electronic density of states as a result of variation in the dimensionality of materials

1. 3. 2. The Surface Plasmon Resonance

Plasma is actually derived from Greek word "Plas" means molded or shape and mon is derived from Latin word "mons" means a mountain or a body. Before discussing the surface plasmon resonance it is important to get the elementary idea of plasmons. In introductory physics, metals has regular array of atoms. Each atom donates one or two electrons and these electrons are shared amongst all the atoms. In other words these positively charged nuclei are

surrounded by the sea of electrons (also known as gas of electrons). Nuclei remain stationary and electrons are free to move around them, that is why metals are conducting in nature. However, in case of bulk metal there are many electrons and the energy states are so close to each other that it seem to be continuous. The electrons in the highest occupied energy state at absolute zero is called the Fermi energy level. The Fermi level is typically a few electron volt ($E_{f=}$ 7 eV for Cu with density of states 1×10^{28} m^{-3} eV^{-1}). At absolute zero ($1/2mu^2 = E_f$) speed of Cu will be 1215446 m/s. [26] When electrons are displaced from their original position the remaining positive charge exerts an attractive force on the electrons trying to pull them back to original position. The net difference of charge exhibits restoring force, which result in creation of dipole oscillation of electrons. This type of oscillation is generated when electromagnetic light wave strikes the surface of metal nanoparticles whose diameter is less than the wavelength of light, the electric field associated with the wave interacts with conduction electrons. This electric field induces the polarization of the (free) conduction electrons with respect to the much heavier ionic core of a spherical nanoparticles. This oscillation of electron gas inside a given nanosphere is called plasmon. Plasmon is actually a quasi particle (explain the basic interaction of collection of electrons) that results in collective oscillation of free electron gas. [27, 28] Plasmons occur on the surface of metal and are quantized. The frequency of the surface plasmon depends upon dielectric constant of the material, it is also dependent on shape of the nanoparticles. This collective oscillation of free electron cloud is also sometimes called "dipole particle plasmon resonance" to avoid the term plasmon that is commonly used in bulk metal surfaces. The surface plasmon resonance (SPR) is the coherent excitation of all the "free" electrons within the conduction band, leading to an in-phase oscillation. The nature of the SPR was explained by G. Mie in 1908. [10] According to Mie's theory, the SPR of noble nanoparticles is due to polarized oscillation of the electron cloud, induced by the electric vector of electromagnetic wave. In case of bulk metals, electromagnetic wave is not allowed to penetrate the metal hence no excitation of electrons. However, the surface electrons can be excited by the electric vectors of electromagnetic wave, causing the displacement of the electron gas with respect to the equilibrium positions around the positively charged nuclei. The light with the maximum angle of incidence (i.e. with the electric wave vector of electromagnetic wave almost parallel to the surface) couples most efficiently with the free electron gas, such as in the attenuated total reflection configuration. In fact these type of oscillation are called propagating plasmon

polaritons (PSPP). This oscillating pattern causes a rippling wave pattern in the spatial distribution of electrons. However, the response of the electron wave is out of phase with the light wave. The energy used to form this electron wave is actually the dissipation of energy from the light wave. The oscillating electrons in the plasmon then re-emit the energy that they absorbed as a reflected light. That is why metal surfaces are shinny and reflective. In case of metal nanoparticles, the story is somehow different. The wavelength of light that hits the nanoparticles is often larger than the size of the particle and when the electron cloud is excited by this light wave, it creates distortion in its electron cloud and results in the formation of surface plasmon. Now, if the frequency of light resonate with the surface plasmon it gets absorbed, elsewhere reflected. In contrast to PSPP, plasmons in nanoparticles with much smaller size than photon wavelength are non-propagating excitations called localized surface plasmons (LSP) [29].
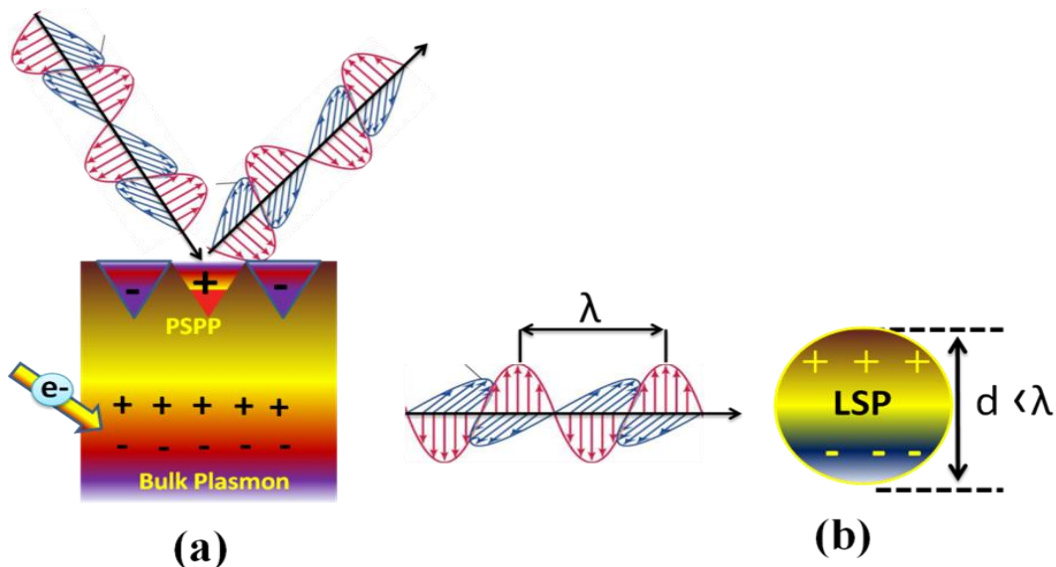
Figure 1.4: Graphical illustration of plasmons in (a) bulk gold and (b) gold NPs

Metal nanoparticles can be of different colors depending on their size. This is because confinement of surface plasmon to a small surface rather than bulk material. A schematic presentation to create surface plasmon oscillation is show in Figure 1.4. All the wavelengths are not available in a small particle, as they would be in bulk. There are only few elements (Au, Ag, Cu, Pd, and Pt) with appreciable plasmonic [30-32] property. Nanoparticles have extremely high proportions of surface area than bulk material. For example, if we compare the proportion of surface in a nanoparticles to a bulk gold we will find that it has the two million times more in

surface area compared to its volume than bulk. More surface area means more potential for surface plasmon resonance. Nanoparticles can experience surface plasmon resonance in the visible region of the spectrum. Therefore, a certain portion of visible wavelengths will be absorbed, while another portion will be reflected. It is actually the reflected light that imparts the material a certain color. In case of gold nanoparticles, small particles absorb light in the blue-green region of the spectrum (~400-500 nm) while red light (~700 nm) is reflected, yielding a

deep red color. As particle size increases, the wavelength of surface plasmon resonance related absorption shifts to longer wavelengths. [33] So, red light is now absorbed and blue light is reflected, yielding particles with a pale blue or purple color as shown in Figure 1.5. As particle size continues to increase toward the bulk limit, surface plasmon resonance wavelength move into the IR region of the spectrum and most visible wavelengths are

Figure 1.5: size dependent color of gold nanoparticle

reflected. This gives the nanoparticles clear or translucent color. These properties of metal nanoparticles have been used to create biosensors. Individual small gold nanoparticles appear red, however, when particles aggregate the plasmon resonance can shift to higher wavelength.

1.4. Synthesis of Metal Nanoparticles

Metal nanoparticles can be synthesized using physical and chemical approaches. [34] In physical approach, commonly known as top down, metal nanoparticles are prepared by decomposition of bulk matter with mechanical force, vaporization, laser abrasion etc. techniques. These techniques provide higher energy to bulk metal and that energy is sufficient to break the metallic bonds. In chemical approach, commonly known as bottom up, metal ions are subjected to reduction to form metal atoms. These atoms then start aggregating to form nanocluster. Both physical and chemical approaches have their own advantages, but chemical approach is preferred over physical from the viewpoints of morphology variation, reproducibility, homogeneity, and mass production. Schematic representation of top down and bottom up approaches are shown in Figure 1.6.

(a) Top down :

Physical method
(laser beam)

Bulk metal   Subdivision   Nanoparticles

(b) Bottom up :

Reducing agent

Metal ions   Atoms   Aggregated atoms   Nanoparticles
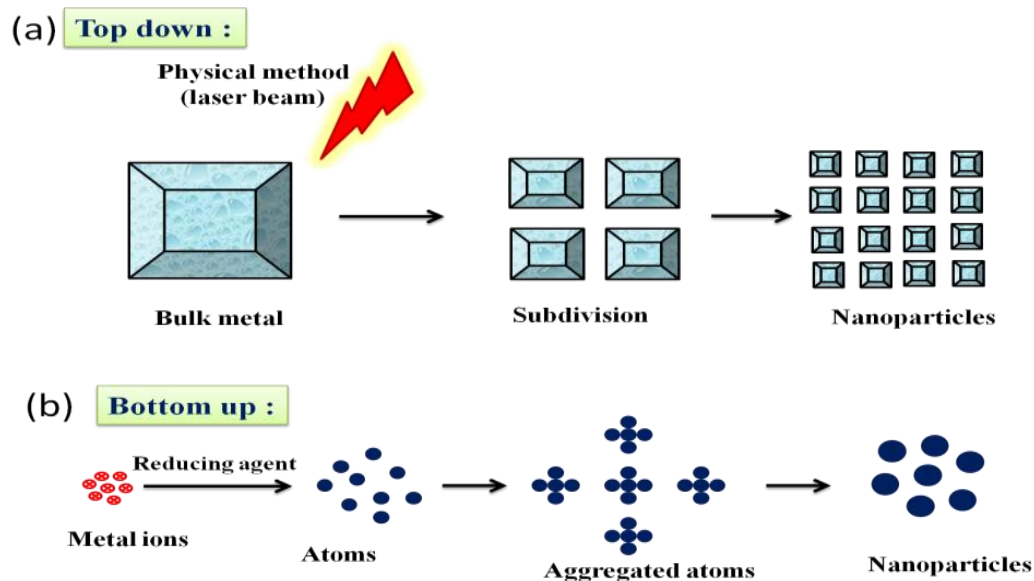
Figure 1.6: Diagrammatic representation of the (a) top-down and (b) bottom-up approach

1. 5. Bimetallic Nanoparticles

Bimetallic nanoparticles consist of two kinds of metals and are of great interest as compared to monometallic nanoparticles. [35, 36] Bimetallic nanoparticles are important than monometallic both in scientific and technological point of views. The crystal structure of bimetallic alloy may either resemble to the bulk alloy or even differs from it. They can also posses the crystal structure in which distribution of each metal element is different to that of bulk, this includes random alloy, alloy with an intermetallic compound, cluster-in-cluster, and core-shell structure. Over the years of time nanoalloys have been studied with pretty much interest. This is because of the fact that these studies have revealed some special characteristic properties. Their size and compositions are magical in nature, i.e., at certain compositions the alloy nanoclusters possess a special stability. Their reactivity especially the catalytic property, is determined by their surface structures, compositions, and segregation properties. [37, 38] The most interesting phenomena about nanoalloys is that they display characteristic features which are totally different from their individual metal clusters of same size. This is called synergism and because of this synergistic effect these nanoalloys display interesting properties. They also exhibit distinct properties to the alloys of the same elements in bulk region, this is due to small size of nanoscale alloys, e.g., pairs of iron and silver are immiscible in the bulk but readily mix in finite clusters. [39] In fact, it

has been proved that while moving from pure metal clusters to those of bimetallic nanoalloys there is change in the crystal pattern due to mixing of two different types of atoms, this leads to increase in possibilities of formation of new isomers. [40] These isomers are actually generated due to change in regular geometry, permutation, and perturbation of atoms.

1. 5. 1. Mixing Patterns

Four types of mixing patterns (Figure 1.7) have been explored for nanoalloys

Core-shell segregated nanoalloys (Figure 1.7 a), where shell is formed from one type of atom (B) and core consist of another type of atom (A), there is possibility of some mixing in between the shells. This is one of the most common mixing patterns and exists in variety of systems. These clusters are denoted as A_{core}- B_{shell}.

Sub cluster segregated nanoalloys consist of B and A sub clusters, they may share a mixed interface (Figure 1.7 b, left) or may be connected with only small number of A-B bonds (Figure 1.7 b, right). This mixing pattern is actually possible, but there is no specified example of this pattern so far.

Mixed A-B nanoalloys (Figure 1.7 c) contains two types of metal
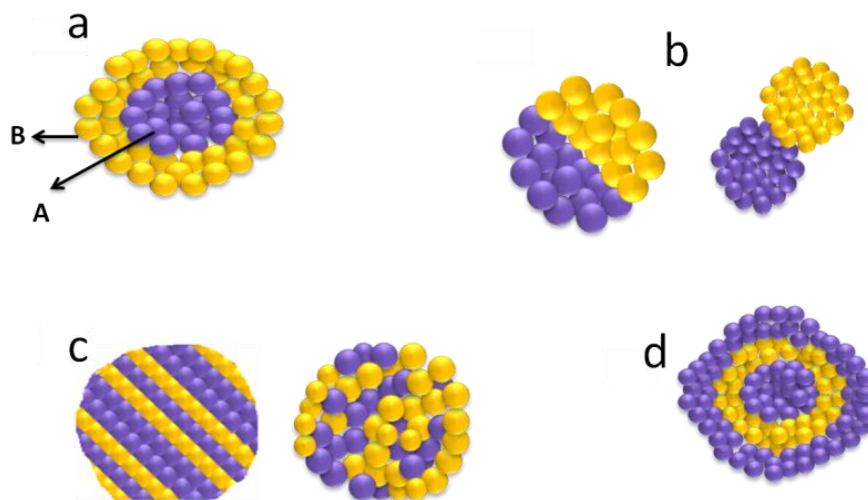
Figure 1.7: Diagrammatic representation of some possible mixing patterns: (a) core-shell, (b) sub-cluster segregated, (c) mixed, and (d) layer-by-layer

atoms may be either ordered (Figure 1.7 c, left) or random (Figure 1.7 c, right). In literature, random mixed nanoalloys are commonly addressed as "alloy" nanoparticles. This type of pattern is very common.

Multi shell nanoalloys (Figure 1.7 d) consist of layered pattern or onion-like alternating A-B-A- shells. Some metastable structures are known in simulations of Cu-Ag, Ni-Ag and Pd-Ag clusters [41]; there has been also evidences which favored some stable arrangements A-B-A type (in case of Co-Rh) and A-B-A-B type (in case of Pd-Pt). [42, 43] In the recent past, three-shell of Pd-Au nanoparticles have been experimentally proved. [44] In these nanoparticles there is an intermixed core of both the metal nanoparticles, an outer shell of Pd rich atoms and in between core and outer shell exists a gold rich shell.

1. 5. 2. Nanocomposites

Composites are actually combinations of two materials in which one of the material is called the reinforcing phase, is in the form of fibers, sheets, or particles, and is embedded in the other material called the matrix phase (Figure 1.8). Matrix is a continuous phase and its purpose is to transfer stress on other phases and protect from environment. Typically, reinforcing materials are strong with low densities while the matrix is usually a ductile or tough material. Nanocomposite is actually a multiphase solid material in which the dimensions of at least one phase is within 100 nanometers (nm) or less than 100 nm. Composites are formed by incorporating multiple phase components in a material in such a way that the properties of the resultant material are unique. The general idea behind the addition of the nanoscale second phase is to create a synergy between the various constituents, such that novel properties capable of meeting or exceeding design expectations can be achieved. The properties of nanocomposites rely on a range of variables, particularly the matrix material, which can exhibit nanoscale dimensions, loading, degree of dispersion, size, shape, and orientation of the nanoscale second phase and interactions between the matrix and the second phase. The most interesting for the nanocomposites is that the matrix are embedded with nanotubes, nanographite, nanosilica, nanoclay etc. morphologies. These nanodimension particles are having multifunctional capabilities. That is why nanocomposites have replaced traditional microcomposites. Nanoparticles can be deposited on the surface of solid (such as, graphitic carbon nitride, graphene or any inorganic metal oxides) resulting in the formation of nanocomposites. Transition metal nanoparticles can be either

adsorbed on inorganic support (graphitic carbon nitride, graphene, charcoal, silica, alumina or oxides such as TiO_2 or MgO) or chemically bonded to polymeric support. Toshima and co-workers formed Pd colloids on chelating resin by reducing $PdCl_2$ precursor salt.[45-47] Nakao and co-workers also embedded Rd, Pd, Pt, Ag, and Au colloids stabilized by a wide range of surfactants in ion-exchange resin. [48] There are numerous literature reports of heterogeneous catalysts in which metal nanoparticles are synthesized on polymeric supports directly. However, recently Kralik and Biffis *et al.,* reported organic functional polymer supported dispersed metal catalysts for hydrogenation of alkenes. [49]
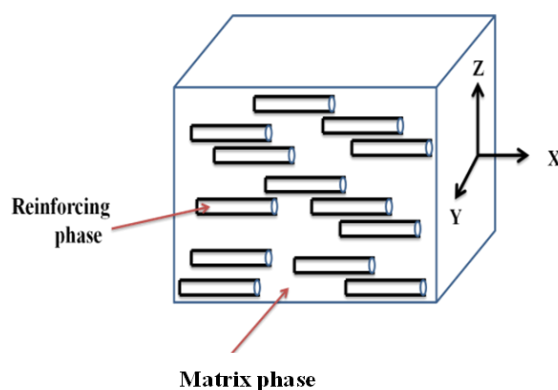
Figure 1.8: Nanocomposite showing the reinforcing phase and matrix phase

1. 6. Stabilization of Nanoparticles

The importance of colloidal particles is smaller size domain. Unfortunately, these metallic nanoparticles are subjected to agglomeration that leads to the formation of bulk. This aggregation results in loss of characteristic properties associated with the colloidal state. As it has been already proved that at short distances (interparticle distances) the van der Walls force come into existence, which varies inversely to the sixth power of distance. [50] So, it has been confirmed that these colloidal metal particles undergo aggregation in absence of repulsive forces. Hence, it becomes necessary to induce repulsive forces that can overcome attractive van der Walls forces in order to bring stability in the colloidal solution. Use of stabilizing agents to induce necessary repulsive forces becomes important to provide stable nanoparticles in solution. Derjaguin-Landau-Verwey-Overbeek theory has described the general stabilization mechanisms. [50]

Nanocluster stabilization is usually discussed in terms of (i) electrostatic stabilization (ii) steric stabilization (iii) electrosteric stabilization, and (iv) stabilization by a ligand or solvent.

1. 6. 1. Electrostatic Stabilization

The electrostatic stabilization arises due to separation of charges. Ionic compounds such as halides, carboxylates, or polyoxoanions, when dissolved in (generally aqueous) solution created electrostatic stabilization in the system. The adsorption of these compounds on the metal surface and their related counter ions generates an electrical-double layer around the particles (Figure 1.9 a). To induce the electrostatic repulsion it is obvious that the electric potential associated with the double layer should exceeds the attractive forces, then only electrostatic repulsion will prevent particle aggregation.

1. 6. 2. Steric Stabilization

Steric stabilization is a technique of using macromolecules such as polymers or oligomers to stablize metal colloids. [51] The adsorption of larger size molecules develop a protective layer around the nanoparticles. In this method, the approach of two metallic colloids is actually restricted. The motion of colloidal particles are ceased by these macromolecules. The restriction imposed to move the colloids in interparticle space results in decrease in entropy and thus increase in free energy (Figure 1.9 b). Steric stabilization takes place in organic or aqueous phase, which is different to electrostatic stabilization that occurs in aqueous media only. Nevertheless, the length and/or the nature of the adsorbed macromolecules influenced the thickness of the protective layer and thus modify the stability of the colloidal metal particles.
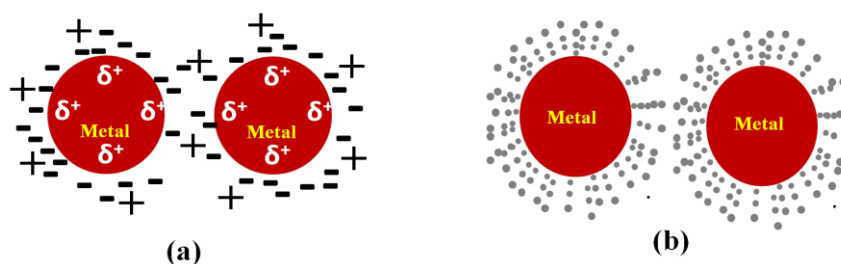
Figure 1.9: Diagrammatic representation of (a) Electrostatic stabilization and (b) Steric stabilization of metal nanoparticles

1. 6. 3. Electrosteric Stabilization

The combined effect of both steric and electrostatic stabilization provides efficient stabilization of nanoparticles in solution. [52, 53] Ionic surfactants are the best candidates for this type of stabilization. Water loving polar head group present in ionic surfactants generates an electrical double layer while hydrophobic tail is responsible for steric repulsion and cease the mobility of nanoparticles. Polyoxoanions such as $(P_2W_{15}NbO_{62}{}^{9-})^+$ in association with tetrabutyl ammonium ion (Bu_4N^{+4}) also provide an efficient electrostatic stability.

1. 6. 4. Stabilization by a Ligand or Solvent

Ligands are also used to stabilize the metal nanoparticles. Ligands make coordination with transition metal surfaces and stabilize the nanoclusters. Most common ligands that have been used in stabilization of transition metal nanoparticles are phosphines, thiols, amines, carbon monoxide etc. Schmid and co-workers used phosphines as ligand to stabilize Au, Pd, Pt, and Ni colloids. [54-57] Ligands like octanethiol, phenanthroline and its derivates have successfully stabilized Pt and Pd colloids. [54] Recently literature reports have revealed that nanoparticles can be stabilized by solvent only. [58, 59] Nanoparticles of Ti and Ru are stabilized by tetrahydrofuran and thioether without addition of any steric or electrostatic stabilizers. [58, 59]

1. 7. Characterization of Nanoparticles

In order to prove authenticity of mono-, bimetallic, and oxide nanoparticles a number of techniques, including electron microscope, X-ray diffraction, X-ray photoelectron spectroscopy and other spectroscopy are being used for the characterization of nanoparticles. Some of the important techniques are briefly discussed in the following section.

1. 7. 1. Ultraviolet-visible Spectroscopy

The optical properties of nanoparticles are studied by UV-vis spectroscopy. The surface of nanoparticles is very much sensitive to light. The absorption of light depends on the chemical composition, geometry or permutation of bimetallic nanoparticles, particularly that of noble metals. [60] Reduction of metal ions, and the formation of metal clusters can be studied by UV-vis spectroscopy.

1. 7. 2. Infrared Spectroscopy

The vibration of small molecules that are attached or absorbed on metallic nanoparticle surface is widely studied by IR spectroscopy. [60] IR study is also used as a probe to study the interaction of metal nanoparticles with the semiconducting support. For example, when AgPd, AgPt, and AgAu are synthesized on the semiconducting graphitic-carbon nitride surface (g-C_3N_4) there is a shift of C=N and C-N stretching vibrations.

1. 7. 3. Diffraction

X-ray and electron diffraction are one of the best technique to authenticate the synthesized nanoparticles. It is applicable not only on an array of nanoparticles but also on a single nanoparticles. Various parameters like crystallinity, lattice spacing, particle size, and qualitative chemical composition of nanoparticles can be determined by XRD technique. [61] XRD is also very helpful in determining the extent of mixing or separation (if the two metals have different lattice spacing) of the two metals and thus predicting the formation of alloy, core-shell or any other physical mixture.

1. 7. 4. Electron Microscopy

Electron microscopy is very useful to study surface, morphology, size, and shape of the nanoparticles. In spite of light in electron microscopy it is electron beam that is focused to very small dimensions. [62] In transmission electron microscopy (TEM), sample preparation is quite tricky and the nanoparticles have to be dispersed in the small chambers of thin carbon-coated copper microgrid. The importance of carbon-coated copper microgrid is that it is transparent to electrons. The electrons are allowed to strike the sample and the transmitted electrons are used to create an image. TEM is very much informative in determining the difference between the metal atoms (particularly of heavy atoms) and their coating of organic molecule or polymers. With high resolution transmission electron microscope (HRTEM) resolution in the vicinity of 1Å can be possible there by determines the space between crystal planes.

Scanning transmission electron microscopy (STEM) is actually one of the mode of operation of TEM in which electron beam is scanned across the sample. STEM is the hybrid instrument which have both the features of SEM and TEM. Scanning electron microscopy (SEM) resembles STEM but the image is formed due to secondary electrons emitted by the

sample surface following the excitation of primary electron beam. Even though the SEM is having low resolution than TEM, SEM is more beneficial for bulk samples in determining morphology of the samples.

1.**7. 5. X-ray Photoelectron Spectroscopy**

X-ray photoelectron spectroscopy (XPS) works on the concept of photoelectric effect, in which the electrons are emitted from the surface, provided the energy of striking photons (greater than threshold energy) that exceeds the binding energy of the electron. The photons of Mg KR (1253.6 eV) or Al KR (1486.6 eV) are generally used. [62] These powerful photons (X-ray radiation) can emit both valence and core electrons. As it is known that each element has different arrangement of core electrons as they are attached to nuclei with different binding energies, so when these powerful radiations are bombarded to emit electrons, each element behaves differently. For each element a different pattern of characteristic peak and peak areas are described. These peaks can be used for qualitative and quantitative analysis of elements present in a given sample. The shape of a peak and the binding energy can provide exclusive information about the oxidation state of metal, chemical bonding and presence of impurities. The XPS technique is very much sensitive and surface specific because of the short range of ejected electrons.

1. 7. 6. Energy Disperse Spectroscopy

Energy dispersive spectroscopy (EDS) is an analytical technique that is used to determine the chemical composition of individual nanoparticles. This analytical technique is often associated with SEM and TEM. In this technique a typical 10-20 keV electron beam is allowed to strike the surface of a conducting sample resulting in the emission of X-rays, the energies of X-rays so generated depends solely on the sample under observation. It is interesting that the X-rays are emitted in the region whose depth is 2.0 µM. X-rays from the specimen are generated when high energetic beam of charged particle electrons and protons are focused on the sample to be studied. At rest, an atom within the sample have unexcited ground state and electrons are residing in the discrete energy levels or electron shells bounded to nucleus. When electron beam emits the electrons in the inner shells, this ejection results in creation of electron hole. An electron from the higher energy shell or outer shell then fills the vacancy of the emitted electron. This transfer

of electron from higher energy shell to lower energy shell is released in the form of X-ray. The number of rays and energy possessed by these X-rays is measured by an energy-dispersive spectrometer. The energies of the X-rays are actually the characteristic energy difference between the two shells and the atomic structure of the emitting element, which makes EDS a very important analytical technique to determine the elemental composition of the specimen to be measured.

1. 7. 7. Other Characterization Techniques

Apart from the above discussed techniques there are several other techniques, such as atomic force microscopy, neutron diffraction, magnetochemistry, secondary ion mass spectroscopy, electron energy loss spectroscopy, cyclic voltammetry, scanning tunneling microscopy, thermogravimmetry and differential scanning calorimetric, Raman spectroscopy, scanning electrochemical microscopy etc. that have been applied to characterize nanoparticles. [63-65]

1. 8. Application of Nanomaterials

Nanodimension particles have exhibit potential applications in display devices, microelectronics (light-emitting diodes and photovoltaic cells), nanofabrication, nanopatterning, self-assembly, drug delivery etc. [3, 6, 14] Other characteristic application of nanoparticles include ultra-fine wiring, efficient solar cell, doping for metal, ceramic, epoxy-material, fiber and coating for surfaces of glass, lens, film, electrode etc. Beside these wonderful applications, nanoparticles are also very much useful in various catalytic processes such as photocatalysis (dye degradation), hydrogenation of nitrocompounds and electrocatalysis (water splitting). Very recently, the applications of metallic nanoparticles have shown a great promise in magnetic resonance imaging (MRI) and cancer therapy. [66, 67]

1.8.1. Electrocatalysis

The concept of using electric current to control various chemical reactions achieved much attention, since the time when humankind invented first power resources. Splitting of water to produce hydrogen and oxygen gas started much earlier, but now it has started at large scale in industrial process and seems to play a crucial role in future energy crisis. In fact hydrogen gas is quite often called the 'fuel of future'.

Electrocatalysis is actually an attempt to elucidate and predict observable phenomena like overall activity of the reactions that occur on the surface of electrode by the interactions of electrode/electrolyte interface. Development of an efficient electrocatalyst is very important to minimize the energy losses during the electrocatalytic splitting of water to produce hydrogen and oxygen gas. Figure 1.10 shows a diagrammatic representation of evolution of hydrogen (figure a) and oxygen (figure b) gas on the surface of glassy carbon electrode (GCE) after deposition of catalyst on its surface.

$$4H^+ + 4e^- \rightarrow 2H_2$$
$$2H_2O \rightarrow O_2 + 4H^+ + 4e^-$$
$$\text{Net reaction: } 2H_2O \rightarrow 2H_2 + O_2$$
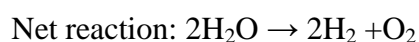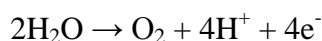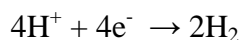
1.8.1.1. Hydrogen Evolution and Hydrogen Oxidation Reactions

The reactions which are central to hydrogen energy are two types. These are hydrogen evolution $(2H^+ + 2e^- \rightarrow H_2)$ and hydrogen oxidation $(H_2 \rightarrow 2H^+ + 2e^-)$ reactions. The research of oxidizing and evolving hydrogen was started in 1960 but it gained importance in 1970 and 1990 when the shortage of oil was realized. [68] The most success in this regard was achieved when precious metals like Pt were used. Metal nanoparticles on the surface of carbon also showed great success in hydrogen evolution reaction (HER) and hydrogen oxidation reaction (HOR). [69] Despite the fact that metallic nanoparticles decorated carbon enhances the electrocatalytic activity because of synergistic effect, but itself exhibit HER only at high overpotentials with no HOR activity. However, literature has revealed that single wall carbon nanotubes and few graphitic carbons when activated to electrochemical potentials exhibits both HER and HOR activity at zero overpotentials. [69] In water splitting, HER is actually a cathodic reaction, while, its converse HOR that occurs in fuel cell is basically anodic reaction.

HER kinetics has a long history and have been explained in detail. [68] In the world of HER electrochemistry, recent merge of computational quantum chemistry and nanotechnology have shown great progress in explaining fundamentals and basics of HER with much emphasize on its utility and storage. [70-72] Metallic Pt is considered as 'state of the art catalyst' and exhibits small Tafel slope values and extremely high exchange current density (j_0). [73-77] However, because of high cost and less availability of Pt, a sustainable, cost effective, and stable catalyst needs to be developed. So, there have been efforts to synthesize the HER active catalysts

from the transition metals that are abundant in nature. Recently, large no of such catalysts from the metals (Fe, Co, Ni, Mo) and their compounds have been developed. All these catalysts have been proving as excellent candidates in HER electrochemistry in both acidic or alkaline conditions. [69] Furthermore, there are reports where carbon and its modified morphological
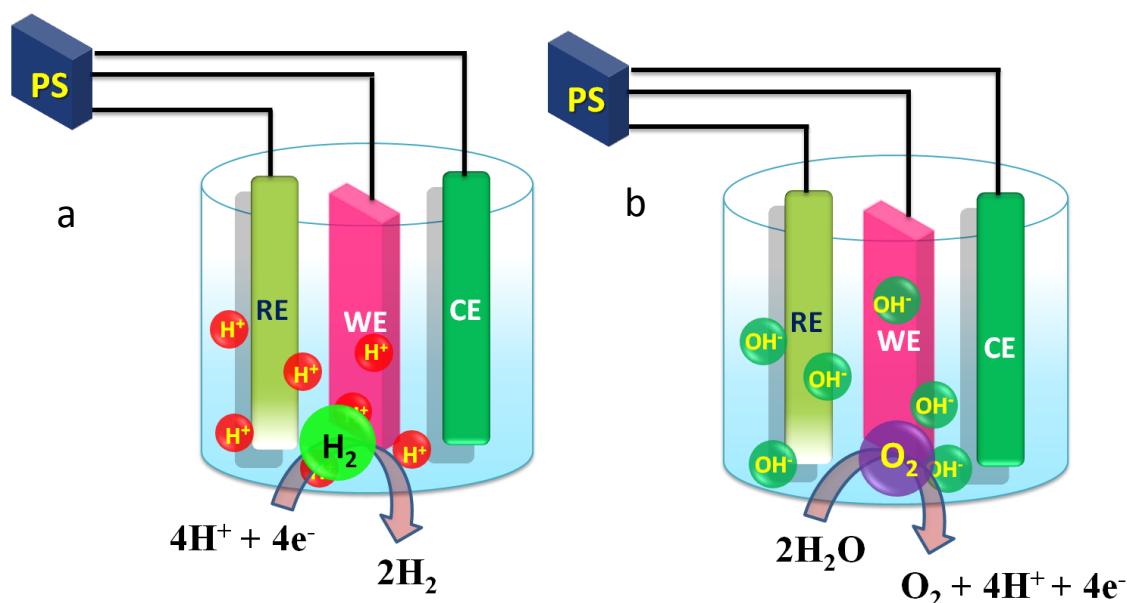
Figure 1.10: Schematic representation for the evolution of (a) hydrogen gas and (b) oxygen gas

based nanostructures (with exciting electronic properties) have been successfully accepted as new alternatives of Pt catalyst. [73-74]

1.8.1.2. Mechanism of HER

HER ($2H^+ + 2e^- \rightarrow H_2$) is a process involving a series of electrochemical steps which takes place on the electrode surface and results in the evolution of hydrogen. There are two mechanisms in acidic and basic conditions accepted universally. [69] The steps are:

(1) Electrochemical hydrogen adsorption (Volmer reaction) [Eq. (a), (b)]

$H^+ + M + e^- \leftrightarrow M\text{-}H^*$ (acidic solution)   (a)

$H_2O + M + e^- \leftrightarrow M\text{-}H^* + OH^-$ (alkaline solution)   (b)

This step is followed by

(2) Electrochemical desorption (Heyrovsky reaction) [Eq. (c), (d)]

20

M-H* + H$^+$ ↔ H$_2$ (acidic solution) (c)

M-H* + H$_2$O ↔ M + OH$^-$ + H$_2$ (alkaline solution) (d)
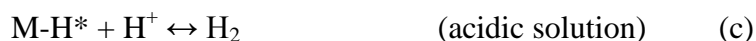
Or,

(3) Chemical desorption or combination reaction (Tafel reaction) [Eq. (e)]

2 M-H* ↔ 2M + H$_2$ (both acidic & alkaline) (e)
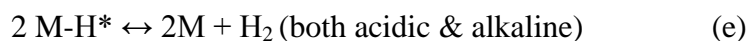
In the above reactions, H* indicates an adsorbed hydrogen atom that has been adsorbed chemically on the surface of electrode (M) at the active site. These reaction pathways are highly dependent on electronic and chemical properties of the electrode surface. [78] Tilak *et. al.,* explained that rate controlling steps (1, 2 and 3) is predicted by deducing Tafel slope values from HER polarization curves. [73] The mechanism and rate determining step is studied by the Tafel slope. Tafel slope is an inherent and interesting property because it gives information about the potential difference required to increase or decrease the current density by 10-fold. Tafel slope is also useful to determine the effectiveness of a catalyst. In order to calculate the Tafel slope the linear portion of the Tafel plots is to be fitted in the Tafel equation (η = b log (j) + a, where η = overpotential, b = Tafel slope, and j = current density). [79, 80] Theoretical facts about Tafel slope have been derived from Butler-Volmer equation and it is proved for three limited cases. First, if the discharge reaction proceeds very quickly and H$_2$ is evolved by the rate determining combination reaction (Tafel step). The slope value is 29 mV dec^{-1} at 25 °C (2.3RT/2F*)*. Second, if the discharge reaction proceeds very quickly and H$_2$ is evolved by the rate determining desorption reaction (Heyrovsky step). The slope value for this step is 40 mV dec^{-1} at 25 °C (4.6RT/3F). Third, if the discharge reaction proceeds very slowly and then the rate determining step will be Volmer step irrespective of the fact whether H$_2$ is evolved by the combination reaction or the desorption reaction. The Tafel slope is 116 mV dec^{-1} at 25 °C (4.6RT/F). The detailed mechanism is shown in Figure 1.11. It is evident that reaction (1) represents chemical adsorption, whereas, reaction (2) and (3) exhibits H atoms desorption from the electrode surface, which are competing with each other. Sabatier and co-workers came with an idea (Sabatier principle) that a better catalyst should not only form a strong bond with absorbed H* and facilitates the proton electron transfer process, but also it should be weak enough in facial bond breaking to assure quick release of H$_2$ gas. [81] It is difficult to establish a quantitative relationship between energies of H* intermediate and rate of electrochemical reaction owing to

absence of directly measured surface-intermediate bonding energy values. [82] However from the perspective of physical chemistry, both for H* adsorption and H_2 evolution on the catalyst surface can be determined from the change in free energy of H* adsorption ($\Delta GH*$) using HER free energy diagram. [83] According to Sabatier principle, under the condition $\Delta GH* = 0$ will have maximum overall reaction rate (expressed in terms of HER exchange current density, j_0).
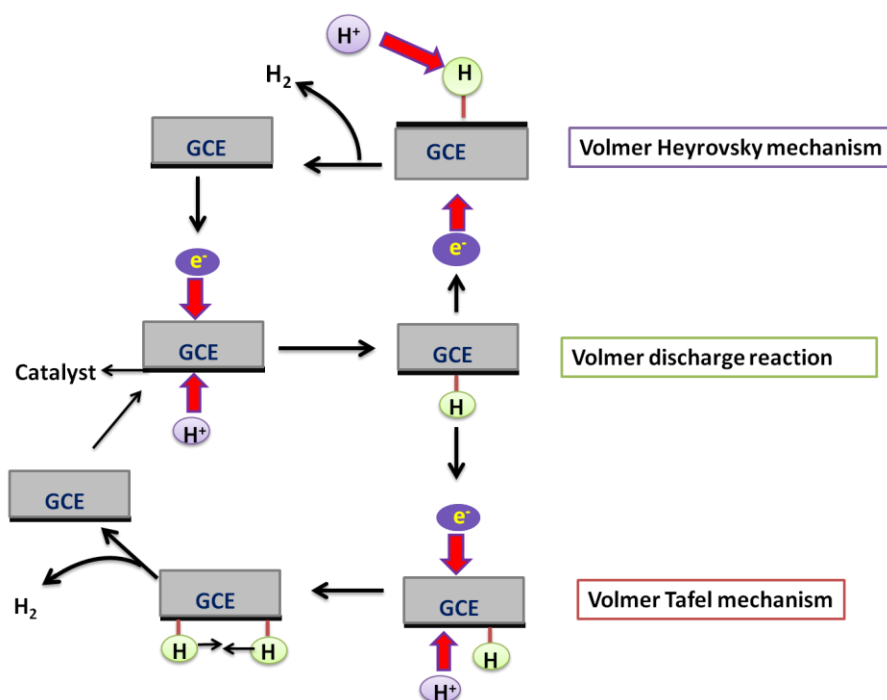
Figure 1.11: Mechanism of hydrogen evolution reaction on surface of glassy carbon electrode (GCE)

An important correlation between $\Delta GH*$ and j0 have been proposed in the form of "volcano curve" for a wide variety of electrode surfaces. [83, 84]

1.8.1.3. Oxygen Evolution and Oxygen Reduction Reactions

Oxygen evolution reaction (OER) and oxygen reduction reaction (ORR) have been studied with lot of interest because of its importance in various practical technologies and industries. [85] water splitting via oxygen evolution is playing a vital role in chemical energy storage. [86] OER and ORR is a basic phenomenon for many important and convenient energy conversion and storage technologies like electrolysis of water and rechargeable metal-air batteries. [87, 88] The oxygen electrochemistry in fuel cells, metal-air batteries, industrial processes, water electrolysis,

alkaline batteries and other miscellaneous applications is shown in Figure 1.12. In ORR, the electrons are combine with the molecular oxygen to form a product, whereas, molecular oxygen is generated when electrons are taken from reactants in case of OER. Oxygen catalysis is a phenomenon through which rate of OER and ORR is promoted on the surface of electrode polarized by an electric potential. To understand the concept of OER and ORR it is important to discuss the following redox reaction:
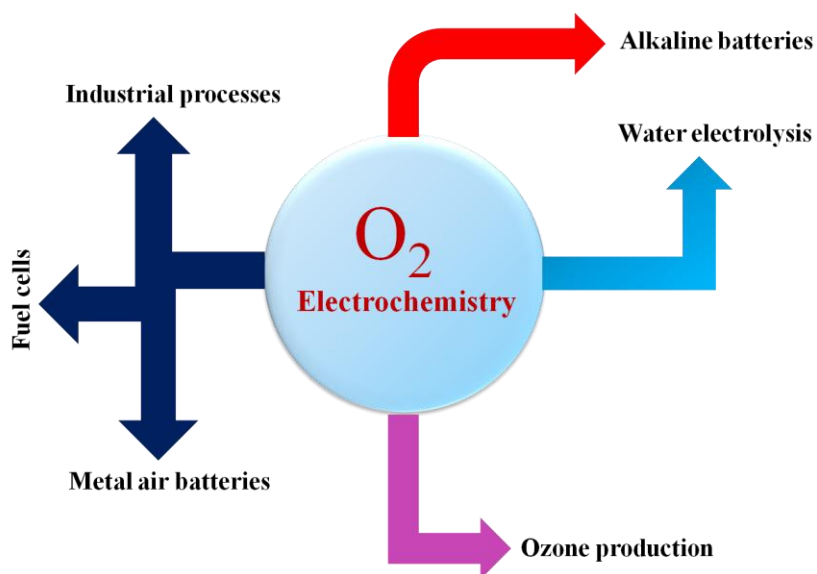
Figure 1.12: Representation of oxygen electrochemical technologies and processes where O_2 electrochemistry plays a vital role

$$2H^+ + O_2 + 2e^- \leftrightarrow 2H_2O, E^0 = 1.23 \text{ V vs. SHE}$$
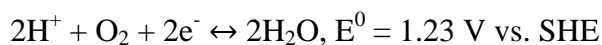
At a potential of 1.23 V vs. SHE, this reaction is in thermodynamic equilibrium on the electrode surface. Therefore, the rate of backward reaction is in equilibrium with the forward reaction. When there is a shift of electric potential from equilibrium in positive direction transfer of electrons from water molecule to the electrode surface takes place. There will be oxidation of water and formation of oxygen gas in this potential window. In case of ORR, the electric potential moves in negative direction and there is transfer of electrons from electrode to the solution and reduction of O_2 takes place, i.e., cathodic current support oxygen reduction. The additional

potential that is required to drive the electric current in these electrochemical reactions is termed as overpotential. [89] The overpotential mainly depends on the electrode material. Platinum is a benchmark electrocatalyst for ORR. It has been experimentally proved that Au electrode shows less overpotential than Pt in ORR. [90] ORR to water and OER from water have attained plenty of interest in O_2 electrochemistry. These reactions are actually the bottle necks that limit power density of hydrogen in fuel cells and efficiency of energy of water electrolysis. Therefore, to design a cost-effective and highly efficient electrocatalyst for energy storage applications is highly essential.

1.8.2. Catalysis

Metal nanoparticles (Au, Ag, Pd, and Pt) have been used significantly in the reduction of nitro compounds into amines. [91, 92] The reduction of nitro compounds is very important because nitrophenol are determined as water pollutants, a serious global concern. [91] Nitrophenol can be reduced into aminophenol using metal nanoparticles as a catalyst. During the synthesis of dyes and pigments as the main intermediates and precursors are polymers of aromatic amines that also correlate the importance of nitro compound reduction. Metal nanoparticles are also used in the reduction of $C = C$ and $C-C$ bond formation. [93, 94]

1.8.3. Photocatalysis

The disposals of dye waste products into streams and rivers is a big threat to human and marine life. For example, azodyes and textile dyes are nonbiodegradable and highly toxic, so need of time demands the degradation of these harmful disposals. In this regard metal and metal oxide nanoparticles have been pretty successful. Mostly metal oxide semiconductors like ZnO, TiO_2 etc. have played a significant role in photo degradation of dyes. In presence of light, electrons in the lower energy valance band are shifted into conduction band, which results in the formation of electron hole pair. [95, 96] Both the electrons in the conduction band as well as holes in valance band are responsible in dye degradation. Recombination of electron and hole is a serious concern in dye degradation, but, now-a-days metal nanoparticles are decorated on the oxide surface to minimize the recombination. These decorated metal nanoparticles act as an electron scavenger and prevents electron hole recombination. [95, 96]

1.9. Aim of the Thesis

The main aim of this thesis is to develop a new material for generation of hydrogen and oxygen gas *via* electrocatalysis. Over the years, hydrogen is a promising and efficient energy source due to its high energy density, efficiency, and low pollutant emission. Hydrogen have been generated from sources like water, coal, biomass etc., but electrochemically water splitting is widely investigated as a sustainable method to evolve H_2 via hydrogen evolution reaction. Generation of hydrogen from water splitting is environmental friendly and globally accepted pathway. Water splitting *via* oxygen evolution is also playing a vital role in chemical energy storage. Oxygen evolution reaction is a basic phenomenon for many important and convenient energy conversion and storage technologies like electrolysis of water and rechargeable metal-air batteries.

1.10. Conclusion

In brief, nanotechnology has done wonders in every field of science. With the advancement in techniques and new innovations in electron microscopes, the characterization of nanomaterials is not too difficult. Methods to develop nanomaterials are highly improved and efficiently executed. Nanomaterials have been used in therapeutic, biological, electrical, optical etc. purposes. In the field of catalysis, photocatalysis, and electrocatalysis metal nanoparticles are mostly studied. Splitting of water, reduction of CO_2, degradation of dyes, reduction of aromatic nitro compounds, reduction of olefins, C-C coupling reactions etc. are few important recent advances in nanochemistry.

1.11. References

[1] A. D. R. Jr., A. B. Baker, J. Johannes, T. Zipperian , K. Eijkel , B. Kirchhoff , H.S. Mani , C. N. R. Rao, S. Walsh, Technol. Forecast. Soc. Change, 74 (2007) 1634 -1642.

[2] R. P. Feynmann, Eng. Sci., 23 (1990) 296.

[3] M. A. Shah, T. Ahmad, Principles of Nanoscience and Nanotchnology, Narosa Publishing House, New Delhi, (2010) 5-7.

[4] F. Barthelat , J. E. Rim, H. D. Espinosa, Applied Scanning Probe Methods XIII, Springer Berlin, (2008)17-44.

[5] C. J. Jones, S. Aizawa, 32 (1991) 109-172.

[6] K. K. Chattopadhyay, A.N. Banerjee, Introduction to Nanoscience and Nanotechnology, PHI Learning Private Limited, Delhi, (2014) 2.

[7] M. C. Daniel, D. Astruc, Chem. Rev.,104 (2004) 293-346.

[8] M. Faraday, Philos., Trans. 147 (1857) 145-181.

[9] T. Graham, Philos. Trans. R. Soc., 151 (1861)183-190.

[10] G. Mie, Ann. Phys., 25 (1908) 377-445.

[11] J. A. A Parenboom, P. Wyder, F. Meier, Phy. REP., 78 (1981) 173-292.

[12] W. P. Halperin, Rev. Mod. Phys., 58 (1986) 533-606.

[13] A. P. Alivisatos, Science, 271 (1996) 933-937.

[14] T. Pradeep, Nano The Essentials, The McGraw Hill Companies, Delhi, (2007) 180.

[15] A. I. Ekimo, A. A .Onushchenko, JETP Lett., 34 (1981) 345-349.

[16] A. I. Ekimov, F. Hache, M. C Schanne-Klein, D. Ricard, C. Flytzanis, 1. A. Kudryavtsev, T. V. Yazeva, A.V. Rodina, Al. L. Efros, J. Opt. Soc. Am. B, 10 (1993) 100.

[17] D. J. Norris, M. G. Bawendi, Phys. Rev. B, 53 (1996) 16338.

[18] Al. L. Efros, M. Rosen, M. Kuno, M. Nirmal, D. J. Norris, M.G. Bawendi, Phys. Rev. B 54 (1996) 4843.

[19] J. B. Xia, Phys. Rev. B, 40 (1989) 8500.

[20] Al. L. Efros, Phys. Rev. B, 46 (1992) 7448.

[21] Al. L. Efros, M. Rosen, Annu. Rev. Mater.Sci., 30 (2000) 475.

[22] E. Martin, C. Delerue, G. Allan, Lannoo Phys. Rev. B, 50,(1994) 18258.

[23] K. Leung, S. Pokrant, K. B. Whaley, Phys. Rev. B, 57 (1998) 12291.

[24] A. I. Ekimov, A. L. Efros, A. A. Onushchenko, Solid State Commun., 56, (1985) 921-924.

[25] G. E. Volovik, JETP Lett., 58 (1993) 469-473.

[26] D. Halliday, R. Resnick, J. Walker, Fundaments of Physics Electricity and Magnetism, Wiley India (2001) 1045.

[27] V. Amendola, R. Pilot, M. Frasconi1, O. M. Maragò, M. A. Iati, J. Phys.: Condens. Matter, 29 (2017) 203002.

[28] M. Brack, Rev. Mod. Phys., 65 (1993) 677-732.

[29] P. Biagioni , J. Huang, B. Hecht, Rep. Prog. Phys., 75 (2012), 024402

[30] M. G. Blaber, M. D. Arnold, M. J. Ford J. Phys.:Condens. Matter, 22 (2010) 143201

[31] M. D. Arnold, Blaber M G, Opt. Express ,17 (2009) 3835-3847.

[32] M. B. Cortie , A.M. McDonagh Chem. Rev., 111 (2011) 3713-3748

[33] X. H. N. Xu, S. Huang, W. Brownlow, K. Salaita, R. B. Jeffers J. Phys. Chem. B, 108 (2004) 15543-15551

[34] S. Link, M. A. Int. Rev. Phys. Chem., 19 (2000) 409-453.

[35] N. Toshima, T. Yonezawa, New J. Chem., 22 (1998) 1179-1201.

[36] S. K. Ghosh, T. Pal, Chem. Rev. 107 (2007) 4797-4862.

[37] A. V. Ruban, H. L Skriver, J. K. Norskov, Phys. Rev. B, 59 (1999) 15990-16000.

[38] G. Bozzolo, J. Ferrante, R. D. Noebe, B. Good, F. S. Honecy, P. Abel, Comput. Mater. Sci., 15 (1999) 169-195.

[39] M. P. Andrews, S. C. O'Brien, J. Phys. Chem. 96 (1992) 8233-8241.

[40] R. Ferrando, J. Jellinek, L. J. Roy, Chem. Rev., 108, 2008, 845-910.

[41] F. Baletto, C. Mottet, R. Ferrando, Phys. Rev. Lett., 90 (2003) 135504-135508.

[42] M. C. Fromen, J. Morillo, M. J Casanove, Europhys. Lett., 73(2006) 885-891.

[43] D. J. Cheng, W. C. Wang, S. P. Huang, J. Phys. Chem. B, 110 (2006) 16193-16196.

[44] D. Ferrer, A. Torres-Castro, X. Gao, S. Sepulveda-Guzman, U. Ortiz-Mendez, M. Jose-Yacaman, Nano Lett., 7(2007) 1701-1705.

[45] H. Hirai, S. Komatsuzaki, N. Toshima, J. Macromol. Sci., Chem., A 23 (1986) 933-954.

[46] N. Toshima, M. Ohtaki, T. Teranishi, React. Polym., 15 (1991) 35-145.

[47] T. Teranishi, N.Toshima, J. Chem. Soc., Dalton Trans. (1994) 2967-2974.

[48] Y. Nakao, K. Kaeriyama, J. Colloid Interface Sci., 131 (1989) 131, 186-191.

[49] M. Kralik, A. Biffis, J. Mol. Catal. A: Chem., 177 (2001) 113-138.

[50] A. Roucoux, J. Schulz, H. Patin, Chem. Rev., 102 (2002) 3757-3778.

[51] R. J. Hunter, In Foundations of Colloid Science, Oxford University Press, New York, chapter 1 (1987) 316-326.

[52] M. A. Watzky, R. G. Finke, J. Am. Chem. Soc., 119 (1997), 10382-10400.

[53] M. A. Watzky, R. G. Finke, Chem. Mater., 9 (1997) 3083-3095.

[54] C. Amiens, D. De Caro, B. Chaudret, J. S. Bradley, R. Mazel, C. Roucau, J. Am. Chem. Soc., 115 (1993) 11638-11639.

[55] S. Chen, K. Kimura, J. Phys. Chem. B, 105 (2001) 5397-5403.

[56] G. Schmid, B. Morun, J. O. Malm, Angew. Chem., Int. Ed. Engl. 28 (1989) 778-780.

[57] A. Rodriguez, C.Amiens, B. Chaudret, M. J. Casanove, P. Lecante, J. S. Bradley, Chem. Mater., 8,(1996) 1978-1986.

[58] H. Bönnemann, B. Korall, Angew. Chem., Int. Ed. Engl., 31 (1992)1490-1492.

[59] O. Vidoni, K. Philippot, C. Amiens, B. Chaudret, O. Balmes, J. O. Malm, J. O. Bovin, F. Senocq, M. J Casanove, Angew. Chem., Int. Ed., 38 (1999) 3736-3738.

[60] J. S. Bradley, In Clusters and Colloids: From Theory to Applications, VCH: Weinheim, (1994) 459.

[61] A. J. Renouprez, K. Lebas, G. Bergeret, J. L. Rousset, P. Delichere, Stud. Surf. Sci. Catal., 101(1996) 1105-1114.

[62] United Kingdom Surface Analysis Forum, URL: http://www. uksaf.org/.

[63] L. O. Brown, J. E. Hutchison, J. Phys. Chem. B, 105 (2001) 8911-8916.

[64] Y. Chen, R. E. Palmer, E. J. Shelley, J. Preece, Surf. Sci., 502 (2002) 208-213

[65] D. G. Georganopoulou, M. V. Mirkin, R. W. Murray, Nano Lett., 4(2004)1763-1767.

[66] T. Shen, R. Weissleder, M. Papisov, A. J Bogdanov, T. J. Brady, Mag. Res. Med. 29 (1993) 599-604.

[67] L. R. Hirsch, R. J. Stafford, J. A. Bankson, S. R. Sershen, B. Rivera R. E. Price, J. D. Hazle, N. J. Halas, J. L. West, Proc. Natl. Acad. Sci. 100 (2003) 13549-13554.

[68] R. K. Das, Y. Wang, S. V. Vasilyeva, E. Donoghue, I. Pucher, G. Kamenov, H-Ping Cheng, Andrew G. Rinzler , ACS Nano, 8 (2014) 8447-8456.

[69] Y. Zheng, Y. Jiao, M. Jaroniec, S. Z. Qiao, Angew. Chem. Int. Ed., 52 (2015) 52-65.

[70] L. A. Kibler, ChemPhysChem, 7 (2006) 985-991.

[71] J. K. Nørskov, T. Bligaard, J. Rossmeisl, C. H. Christensen, Nat. Chem., 1(2009) 37- 46

[72] J. Greeley, N. M. Markovic, Energy Environ. Sci., 5 (2012) 9246 - 9256.

[73] B. E. Conway, B. V. Tilak, Electrochim. Acta, 47 (2002) 3571- 3594.

[74] M. G. Walter, E. L.Warren, J. R. McKone, S.W. Boettcher,Q. Mi, E. A. Santori, N. S. Lewis, Chem. Rev., 110 (2010) 110, 6446 - 6473;

[75] J. R. McKone, S. C. Marinescu, B. S. Brunschwig, J. R. Winkler, H. B. Gray, Chem. Sci., 5 (2014) 865 - 878.

[76] Y. Zheng, Y. Jiao, Y. Zhu, L. H. Li, Y. Han, Y. Chen, A. Du, M. Jaroniec, S. Z. Qiao, Nat. Commun., 5 (2014) 3783.

[77] Y. Zheng, Y. Jiao, L. H. Li, T. Xing, Y. Chen, M. Jaroniec, S. Z. Qiao, ACS Nano, 8 (2014) 5290 - 5296.

[78] H. Wolfschmidt, O. Paschos, U. Stimming, Fuel Cell Science (Eds.: A. Wieckowski, J. Norskov), Wiley, chapter 1 (2010)1 -70.

[79] T. Shinagawa, A. T. Garcia-Esparza, K. Takanabe, Scientific Reports, 5 (2015) 13801.

[80] A. Behranginia, M. Asadi, C. Liu, P. Yasaei, B. Kumar, P. Phillips, T. Foroozan, J. C.Waranius, K. Kim, J. Abiade, R. F. Klie, L. A. Curtiss, A. Salehi-Khojin, Chem. Mater., 28 (2016) 28, 549.

[81] P. Sabatier, La catalyse en chimie organique, 1920.

[82] N. M. Markovic, P. N. Ross, Jr., Surf. Sci. Rep., 45 (2002) 117 - 229.

[83] J. K. Norskov, T. Bligaard, A. Logadottir, J. R. Kitchin, J. G. Chen, S. Pandelov, U. Stimming, J. Electrochem. Soc., 152 (2005) J23-J26.

[84] R. Parsons in Catalysis in Electrochemistry (Eds.: E. Santos, W. Schmickler), Wiley, chapter 1 (2011) 1 - 15.

[85] D. K. Kinoshita, Electrochemical Oxygen Technology, first ed., Wiley-Interscience, (1992).

[86] J. Lee, B. Jeong , J. D. Ocon, Current Applied Physics 13 (2013) 309-321.

[87] F. Cheng, J. Chen, Chem. Soc. Rev., 41(2012) 2172-2192.

[88] K. JunLi, Q.Wang, X. Wang, D. Qian, J. Jiang, J. Li, Z. Chen, Journal of Alloys and Compounds, 725 (2017) 260-269

[89] A. J. Bard, L. R. Faulkner, Electrochemical Methods: Fundamentals and Applications, second ed., Wiley, (2000).

[90] D. K. Kinoshita, Electrochemical Oxygen Technology, first ed., Wiley-Interscience, (1992).

[91] R. Nazir, P. Fageria, M. Basu, S. Gangopadhyay, S. Pande, New J. Chem., 41 (2017) 9658-9667.

[92] P. Fageria, S. Uppala, R. Nazir, S. Gangopadhyay, C. Chang, M. Basu, S. Pande, Langmuir, 32 (2016) 10054-10064.

[93] R. M. Crooks, M. Zhao, L. Sun, V. Chechik L. K. Yeung, Acc. Chem. Res., 34 (2001) 181-190

[94] S. Sharma, R. Nazir, S. Pande, B. R. Sarkar, Chemistry Select, 2 (2017) 8745-8750.

[95] P. Fageria, S. Gangopadhyay, S. Pande, RSC Adv., 4 (2014) 24962-24972.

[96] M. Basu, R. Nazir, P. Fageria , S. Pande, Sci. Rep., 6, (2016) 34738.

Chapter 2

Graphite carbon nitride supported Pd and Pt nanoparticles for nitro compound reduction and hydrogen evolution reaction

Abstract

This chapter discusses the synthesis of Pd and Pt monometallic nanoparticles on carbon nitride (C_3N_4) surface for the reduction of nitrocompounds as well as for electrocatalysis. For the synthesis of C_3N_4/Pd and C_3N_4/Pt, metal ions were initially adsorbed on C_3N_4 surface and then subsequently reduced by $NaBH_4$. The as-synthesized heterostructures was authenticated by different characterization techniques, UV-vis, PXRD, XPS, TEM, FESEM, and EDS. Decorations of monometallic NPs on C_3N_4 not only improve the reduction efficiency of nitro-compounds but also enhanced the electrocatalytic activity in hydrogen evolution reaction. C_3N_4/Pt proved efficient electrocatalyst as it requires -0.339 V potential to attain current density of 10 mA/cm^2, whereas, C_3N_4/Pd requires -0.371 V to reach 10 mA/cm^2 current density vs. Ag/AgCl. Both C_3N_4/Pd and Pt heterostructures are better than bare C_3N_4, which needs -0.596 V to achieve 10 mA/cm^2 current density vs. Ag/AgCl. On the other hand, C_3N_4/Pd showed better performance in nitrocompound reduction as compared to C_3N_4/Pt and bare C_3N_4. The kinetic study reveals that the rate constant using C_3N_4/Pd catalyst is 6.7×10^{-1} min^{-1} for p-nitro aniline reduction, which is 101 times higher as compared to bare C_3N_4 and 4.7 times in comparison to C_3N_4/Pt. Formation of hydrogen gas and hydrogenation of p-nitro aniline is shown in scheme 2.1.
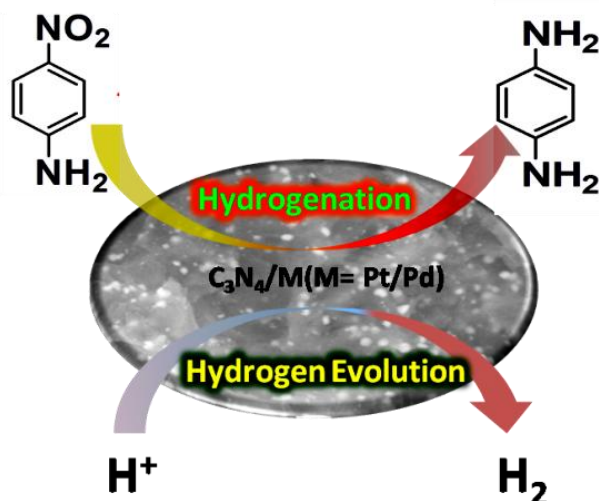
Scheme 2.1: Diagrammatic representation of nitrocompound reduction and evolution of hydrogen gas using C_3N_4/Pt, Pd as a catalyst

2.1. Introduction

Now-a-days increasing global population demands for clean, affordable and reliable energy source.[1] Currently, fossil fuels have been dominating the global energy demands but increasing concerns of global warming due to production of undesirable carbon-dioxide appeals for low pollutant emission and high efficient energy fuels.[2, 3] Over the years, hydrogen is a promising and efficient energy source due to its high energy density, efficiency, and low pollutant emission.[4] In recent times noble metal nanoparticles (NPs) have attained a tremendous attention for hydrogen evolution reaction, which is due to low resistance and excellent catalytic activity in acidic media. Amongst all effective HER electrocatalysts, Pt based nanocomposites were proved as an effective and efficient catalysts due to their low reduction overpotentials and fast kinetics. [5-7] However, limited sources and expensive availability of Pt based nanocomposites shifted the research for an alternative. Recently, Pd NPs were investigated as an active electrocatalysts and a good alternative for Pt NPs. [8,9] Mostly monometallic Pd NPs have been reported on supported material (e.g., carbon powder, Tungsten carbide (WC) etc.) [10-12] but the durability of supported catalyst is very low. [13] Therefore, it is very important to produce a new support based catalyst with high durability and superior electrocatalytic activity. One of the constructive strategy is incorporation of a heteroatom in the solid support, e.g., nitrogen, which can coordinate with metal NPs and overcomes the durability. [14,15]

Carbon nitride (C_3N_4) is a polymeric semiconductor and used as visible light photocatalyst. C_3N_4 has its unique layered structure and a characteristic electronic band structure consists of valence band and conduction band. [16] Porous matrix of C_3N_4 surface can easily functionalize with many organic/inorganic compounds with high reactivity. [17,18] Synthesis of Pd NPs on g-C_3N_4 surface for selective hydrogenation of phenol and its derivatives has been reported by Antonietti and co-workers. [19] Wang and co-workers reported Pd NPs loading on a hybrid solid support consist of C_3N_4 and graphene for oxidation of formic acid and methanol electro-oxidation. [20] The same group also reported oxidation of glycerol using Pd NP loaded hybrid C_3N_4 and graphene system. [21] Barman and co-workers described the synthesis of porous Pd NPs-C_3N_4 composite (Pd-CNx) for hydrogen evolution and hydrogen oxidation reactions in acidic media. [22] Porous Pd-CNx composite shows best catalytic activity towards HER than commercial Pt/C and Pd/C. They also mentioned Pd-CNx composite showed high

durability in strongly acidic media, much higher than that of commercial Pt/C. Recently, our group also reported the synthesis of mono- (Au and Pd) and bimetallic NPs using C_3N_4 quantum dot under the illumination of UV light for 4-nitrophenol reduction. [23] The advantages of C_3N_4 as a support for any catalytic and electrocatalytic reactions are manifold. [22,23] First, strong interaction between metal NPs with C_3N_4 provides large accessible active sites. Second, porous structure of C_3N_4 allows reactant to reach active site or edge easily and quick formation of product on metal surface. Third, synergistic effect between metal and C_3N_4 facilitates the rate of the catalytic reaction. Therefore, based on the literature report it is quite evident that C_3N_4 supported Pd NPs are durable and exhibit better electrocatalytic activity.

Being inspired from the above studies, we did a simple method for Pd and Pt monometallic NPs synthesis on C_3N_4 surface for hydrogen evolution and nitrocompound reduction. For the synthesis of C_3N_4/Pd and Pt NPs, precursor metal ions were initially adsorbed on C_3N_4 surface and then subsequently reduced by a reducing agent, $NaBH_4$. All the materials were characterized by UV-vis, powder X-ray diffraction, scanning electron microscopy, transmission electron microscopy, and X-ray photoelectron spectroscopy techniques. The as-synthesized materials were used as an electrocatalyst for HER and heterogeneous catalyst for reduction of nitro-compounds. For HER, best catalytic efficiency was achieved in case of C_3N_4/Pt. Pt NPs proved efficient catalyst in electrocatalysis as it requires potential of -0.339 V vs. Ag/AgCl. While C_3N_4/Pd showed best performance in nitro-compound reduction with a rate constant, k = 6.7 $\times 10^{-1}$ min^{-1} for 4-nitroaniline reduction, which is 101 times higher than bare C_3N_4. These results revealed that decoration of metal nanoparticles on C_3N_4 surface not only improved the reduction kinetics of nitro-compounds but also enhanced the electrocatalytic activity. The advantages for this work are manifold. First, syntheses of metal NPs on C_3N_4 surface, a stable support with better catalytic activity and high durability. Second, to develop a good electrocatalyst for HER in acid medium, which is comparable with commercial Pt/C.

2.2. Experimental Section

2.2.1. Synthesis of C_3N_4

Bulk C_3N_4 was synthesized via poly-condensation reaction from urea, which is reported elsewhere.[18, 24] In brief, thermal treatment was given in a silica crucible using a compound,

which is a rich source of carbon and nitrogen (e.g., urea). Firstly, 10 g urea was dried at ~ 80-90 $^{\circ}$C to remove adsorbed moisture. Secondly, dried urea was transferred in a covered silica crucible and placed in a muffle furnace for thermal treatment at 550 $^{\circ}$C for 2.5 h with a heating rate 10 $^{\circ}$C min^{-1}. Thirdly, at room temperature condition the light yellow color product was collected and washed with 0.1 M HNO$_3$ to remove extra impurities and dried at 80 $^{\circ}$C. 1.0 g C$_3$N$_4$ was exfoliated in 100 mL water using a sonicator for 5 h to obtain C$_3$N$_4$ nanosheet at a concentration of 10 mg mL^{-1}.

2.2.2. Synthesis of C$_3$N$_4$/Pd and Pt NPs

For the synthesis of C$_3$N$_4$/Pd, exfoliated C$_3$N$_4$ nanosheet (19 mL) was taken and 1 mL of 10^{-2} M aqueous solution of K$_2$PdCl$_4$ was added. Then the reaction mixture was stirred for 1 h and treated with NaBH$_4$ (1 mL of 1.0 M) to reduce Pd^{2+} ions and stirring was continued for another 2 h. After addition of NaBH$_4$, the brown color solution was changed into grey color due to the formation of palladium nanoparticles. Finally, the product was washed with distilled water and ethanol to remove impurities and dried in air.

To synthesize C$_3$N$_4$/Pt similar procedure for C$_3$N$_4$/Pd was followed except K$_2$PtCl$_4$ was used in place of K$_2$PdCl$_4$.

2.3. Catalysis in nitro-aromatic reduction

Nitro-aromatic reduction was carried out using NaBH$_4$ as a hydrogen donor and water as a solvent. For this reduction reaction aqueous solution of *p*-nitroaniline (4-NA) (2.0 mL of 10^{-3} M) and 2.0 mL of 10^{-1} M NaBH$_4$ was added in 16 mL water. Total volume of the solution was 20 mL. After that, in the reaction mixture 1.0 mg of catalyst was added. To monitor the reduction reaction, 3.0 mL solution was taken from the reaction vessel and UV-vis spectroscopy was measured. After UV-vis measurement 3.0 mL solution was poured again in the reaction container so that the total volume remain unchanged. All the as-synthesized catalysts (bare C$_3$N$_4$, Pd, and Pt) were used for the reduction reaction.

In case of other nitro compound reduction similar method was followed except *p*-nitrophenol and *o*-nitrobenzoic acid were used instead of 4-NA.

The percentage of conversion of the nitro-compound reduction can be calculated using:

$$\% \ Conversion = (A_0 - A_t)/A_0 \times 100$$

where, initial absorbance $= A_0$ and absorbance at time 't' $= A_t$.

2.4. Catalysis in hydrogen evolution reaction

Preparation of ink: 4.0 mg catalyst and 20 μL of 5 wt% nafion solution was dispersed in 200 μL of isopropanol by bath-sonication until a homogeneous suspension was formed. Then, 5.0 μL of the above catalyst suspension was drop-casted onto a GCE and dried in air. Electrochemical impedance measurements were performed using GC as working electrode and onset potentials of different catalysts were chosen as performing bias for the measurement with the sweeping frequency from 50 KHz to 10 Hz with a 10 mV AC dither. Pt and Ag/AgCl were used as counter and reference electrode, respectively.

2.5. Results and Discussion

Synthesis of Pd and Pt monometallic NPs on C_3N_4 surface is mentioned in experimental section. In brief, first, K_2PdCl_4 and K_2PtCl_4 were dispersed on the surface of C_3N_4 and then reduced using $NaBH_4$ as a reducing agent. All these materials were washed carefully and further used for characterization and application purposes. In the following sections complete characterization, mechanism of formation, and application will be discussed.

2.5.1. UV-vis spectrum of C_3N_4, C_3N_4/Pd and C_3N_4/Pt

Figure 2.1 shows UV-vis spectrum of bare C_3N_4 and monometallic (Pd and Pt) NPs. It can be
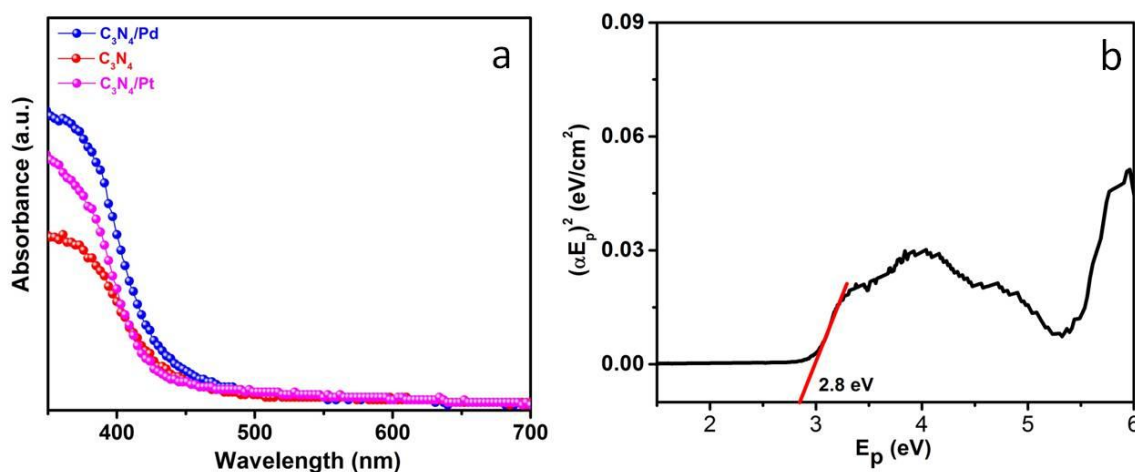
Figure 2.1: UV-vis DRS for (a) C_3N_4, C_3N_4/Pd and C_3N_4/Pt, where, all the powder samples were mixed with $BaSO_4$ as reference, (b) Band gap energy (E_g) of C_3N_4

seen from Figure 2.1a that C_3N_4 shows strong absorption in visible region with absorption edge at ~ 455 nm. Using classical Tauc approach, from the plot of $(\alpha E_p)^2$ vs. photon energy (E_p) the band gap energy (E_g) of C_3N_4 can be calculated (Figure 2.1b). The calculated E_g value for C_3N_4 is ~ 2.8 eV, which is well matched with previous reports. [16,18] Both C_3N_4/Pd and Pt shows comparable absorption in visible region and weak absorption in UV region with an absorption edge at ~ 455 nm.

2.5.2. FTIR analysis of Pd and Pt loaded C_3N_4 surface

The FTIR analysis result for C_3N_4, C_3N_4/Pd and C_3N_4/Pt is shown in Figure 2.2. In case of C_3N_4, C=N stretching vibration is observed at 1637 and 1571 cm^{-1}, while, C–N stretching vibration at 1411, 1322, and 1240 cm^{-1} are presented. Both the stretching vibration represent aromatic modes of C_3N_4 ring. The out-of-plane bending vibration for heptazine rings is experienced from the intense band at 809 cm^{-1}. Pd and Pt monometallic NPs decorated on C_3N_4 shows similar IR stretching frequencies for C=N and C-N stretching vibration without any significant shift. Young and co-workers also reported similar IR characteristic features of Pt loaded C_3N_4 and in case of pure C_3N_4. [25]
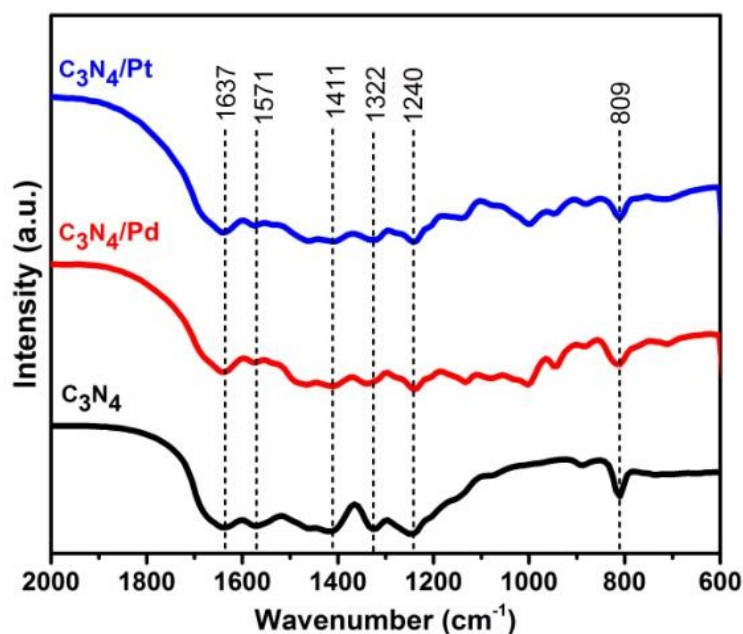
Figure 2.2: FTIR spectra of Pd and Pt loaded C_3N_4 surface

2.5.3. Powder X-ray diffraction patterns C_3N_4/Pd, C_3N_4/Pt and C_3N_4

The structural identity and phase purity of the as-synthesized metal NPs were studied by PXRD analysis shown in Figure 2.3. The PXRD spectrum of C_3N_4/Pd NPs shows two characteristics peak at 2θ = 39.9° and 46.2° for (111) and (200) planes, respectively (JCPDS-46-1043). The presence of (111) and (200) planes represent fcc structure of Pd along with a peak at 27.5°, which is due to presence of (002) plane of C_3N_4. It can be seen from Figure 2.3a that, the 2θ
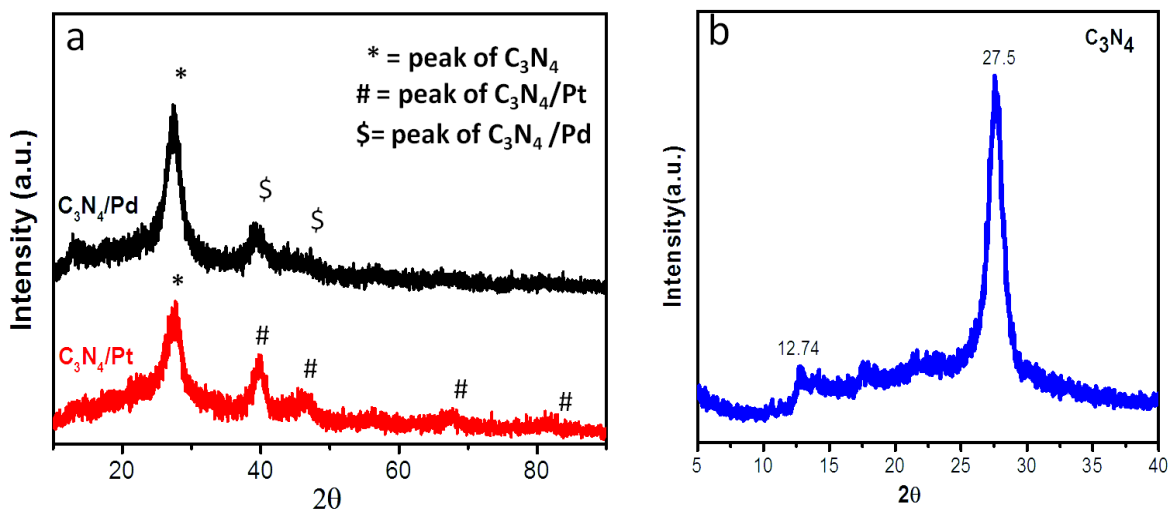
Figure 2.3: Powder X-ray diffraction patterns (a) C_3N_4/Pd and C_3N_4/Pt and (b) of C_3N_4

values are at 39.9°, 46.2°, 67.8°,and 81.8° for (111), (200), (220), and (311) planes, respectively, for C_3N_4/Pt NPs which represent fcc structure (JCPDS 04-0802) of Pt. In addition to those peaks, another peak at 2θ = 27.5° for (002) plane of C_3N_4 is also present. From Figure 2.3b that bare C_3N_4 contains a characteristic peak at 27.5°, which is associated with inter planar stacking of aromatic compounds. Absence of any extra peak in the PXRD analysis of monometallic (Pd and Pt) NPs confirms that the as-prepared compounds are pure and there is no remaining salt precursor.

2.5.4. XPS analysis Pt/C_3N_4 and Pd/C_3N_4 structure

XPS technique was employed to investigate the surface chemical properties of the metal NPs as well as their oxidation states. Successful formation of Pt and Pd nanoparticles has been observed on C_3N_4 surface as well as their oxidation states are also depicted in Figure 2.4. A clear existence

of Pt 4f (74.4 eV and 71.1 eV) and Pd 3d (340 eV and 335 eV) doublets for the Pt/C$_3$N$_4$ and Pd/C$_3$N$_4$ nanostructures, respectively, confirms the successful formation of metal nanoparticles
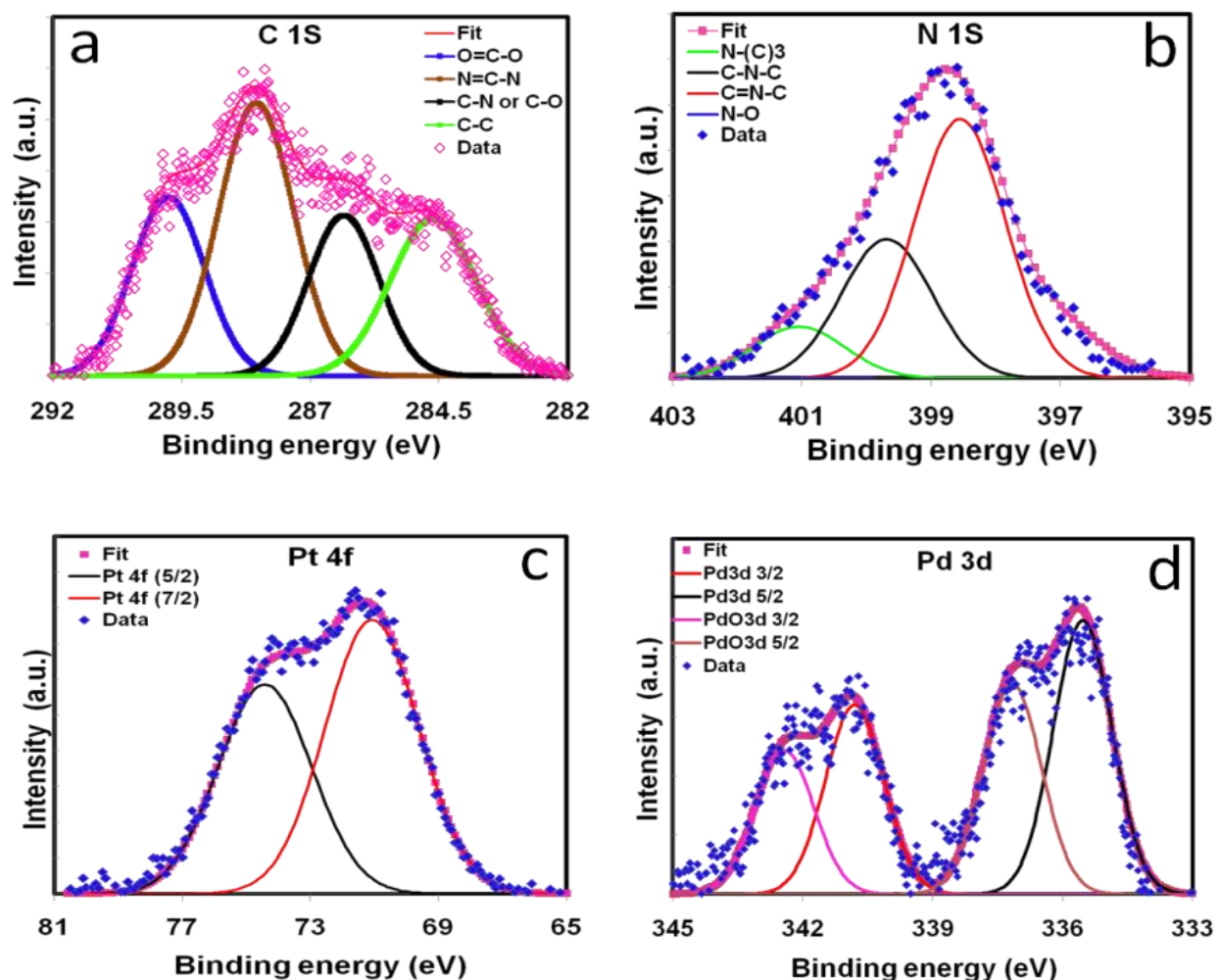
Figure 2.4: High resolution XPS spectra of (a) C1s (b) N1s spectra for C$_3$N$_4$, (c) Pt4f (d) Pd3d for Pt/C$_3$N$_4$ and Pd/C$_3$N$_4$ structure, respectively

on the C$_3$N$_4$ surface. High resolution scans of C 1s and N 1s core level spectra with their various deconvolution components are shown in Figure 2.4a and 2.4b, respectively, for a clean C$_3$N$_4$ surface. The deconvoluted C 1s binding energy spectrum can be fitted with four peaks centered at around 284.6 eV, 286.4 eV, 288.1 eV and 289.8 eV, which are attributed to C-C, C-N (or C-O), C=N and C=O, respectively (Figure 2.4a). Similarly, the N 1s BE spectrum of C$_3$N$_4$ is also deconvoluted into four peaks centering around 401 eV, 399.7 eV, 398.6 eV and 397 eV, representing N-O (or N-H), N-(C)3, C-N-C, and C=N-C bonding, respectively (Figure 2.4b).

These findings are in good agreement with earlier reported values of carbon nitrides. [23] Both the findings also indicate the formation of a high quality C_3N_4 layer which further acts as a substrate for the metal nanoparticles growth. Figure 2.4c shows the high resolution scans of Pt 4f binding energy peaks along with its deconvoluted spin orbit splitting components which is fitted with 4f $_{5/2}$ and 4f $_{7/2}$ doublet centered at 74.4 eV and 71 eV, respectively. The spin orbit splitting of 3.4 eV with an intensity ratio of about 0.76 have been observed. This finding is well matched with earlier reported values of Pt(0) oxidation state. [26] Similarly, the deconvolution of Pd 3d high-resolution spectrum is shown in Figure 2.4d. Deconvolution data mainly appears with two sets of Pd 3d doublets with an intensity ratio of about 2:3. One pair centered at 335.5 eV and 340.8 eV corresponds to the metallic Pd(0) state of Pd $3d_{5/2}$ and Pd $3d_{3/2}$, respectively. A spin orbit splitting of about 5.3 eV with an intensity ration of 0.69 has also been noticed which confirms the formation of metallic nanoparticles of Pd(0) oxidation state. [23] Whereas, the other Pd doublet positioned at 337.2 and 342.4 eV can be attributed to the Pd(I) oxidation state where we observed a spin orbit splitting of about 5.2 eV and an intensity ration of 0.68, suggesting that the Pd surface is partially oxidized.

Table 2.1: Binding energy positions and relative intensities of deconvoluted C1s and N1s spectra for C_3N_4 and Pt4f and Pd3d for Pt and Pd on C_3N_4, respectively

Samples	BE peaks	Sub-peaks	Area	Position
C_3N_4	C 1s	O=C-O	12279.79	289.761
		N=C-N	19435.63	288.052
		C-N or C-O	10759.05	286.352
		C-C	12880.8	284.616
	N 1s	N-O or N-H	3989.9	401.047
		N-(C)3	10757.6	399.69
		C-N-C	20052.3	398.555
		C=N-C	3855.78	397.021
Pt/C_3N_4	Pt 4f	Pt 4f 5/2	42976.07	74.425
		Pt 4f 7/2	56419.52	71.072
Pd/C_3N_4	Pd 3d	Pd $3d_{3/2}$	5424.266	340.801
		PdO $3d_{3/2}$	4112.645	342.417
		Pd $3d_{5/2}$	7846.58	335.536
		PdO $3d_{5/2}$	6035.727	337.165

A very similar kind of oxidation phenomena of Pd nanoparticles has also been noticed [23] for Au-Pd nanoparticles on C_3N_4 surface. However, for a better understanding, details of all the deconvoluted spectra are summarized in Table 2.1.

2.5.5. FESEM analysis of Pt/C_3N_4 and Pd/C_3N_4 structure

Figure 2.5a and 2.5b exhibits FESEM images of C_3N_4/Pd and C_3N_4/Pt NPs. FESEM image of
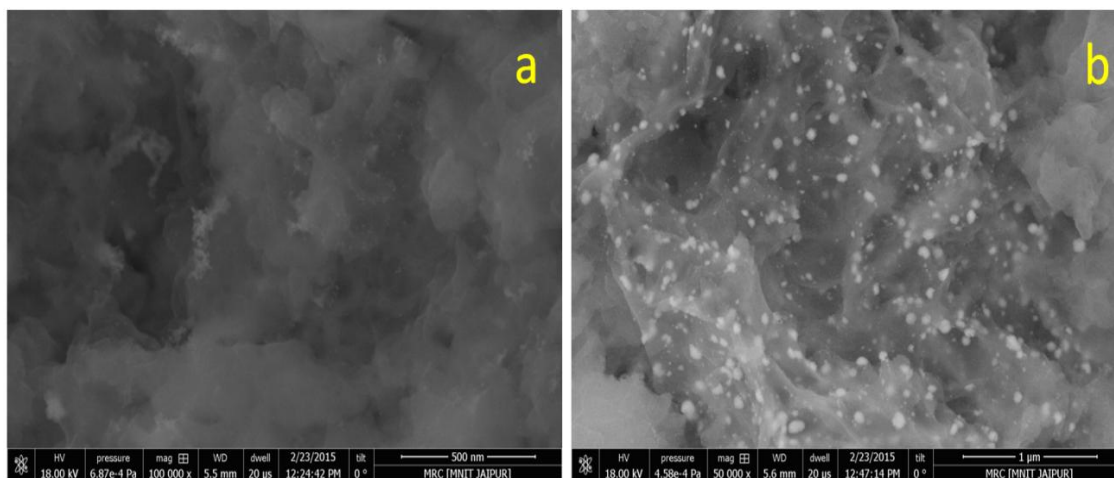
Figure 2.5: FESEM image of (a) C_3N_4/Pd and (b) C_3N_4/Pt NPs

bare C_3N_4 is shown in Figure 2.6, which exhibits highly dense C_3N_4 sheet like structures. Figure 2.5a shows FESEM image of C_3N_4/Pd, where, Pd NPs are very small in size and homogeneously
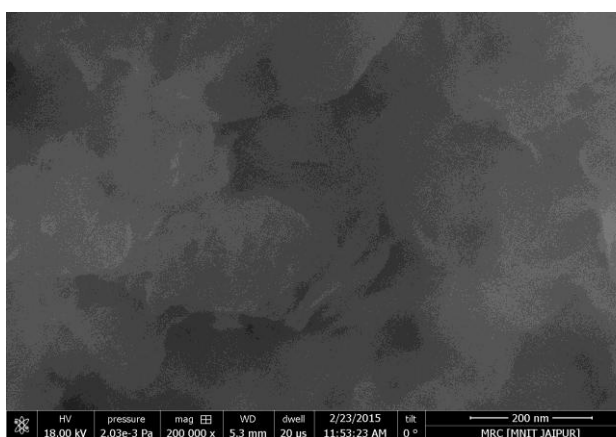
Figure 2.6: FESEM image of exfoliated C_3N_4 sheet after 5 h sonication

40

distributed on C_3N_4 surface. Figure 2.5b represents FESEM image of Pt NPs decorated on C_3N_4 surface. It can be seen from Figure 2.5b that Pt NPs are perfectly spherical and particle size-distributions are wide. Therefore, FESEM analysis confirms the distribution and spherical nature of Pd and Pt NPs on C_3N_4 surface
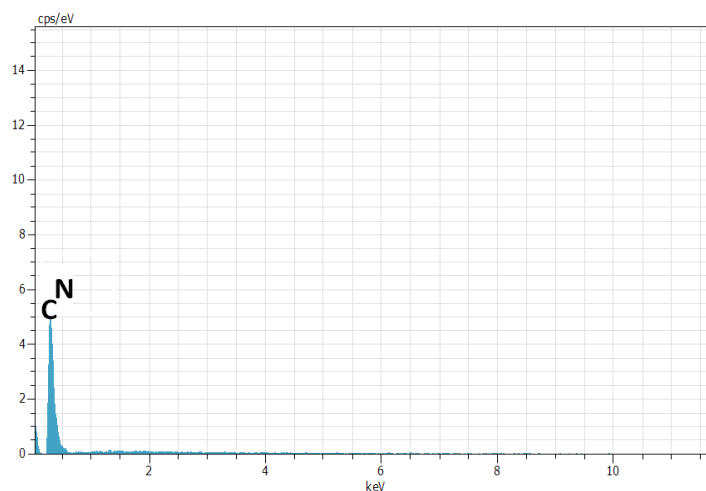
Figure 2.7: EDS analysis of C_3N_4

Elemental mapping analysis of C_3N_4 (Figure 2.7), confirms the presence of carbon and nitrogen. Line mapping analysis (Figure 2.8) substantiates the presence of Pd and Pt NPs on C_3N_4 surface.
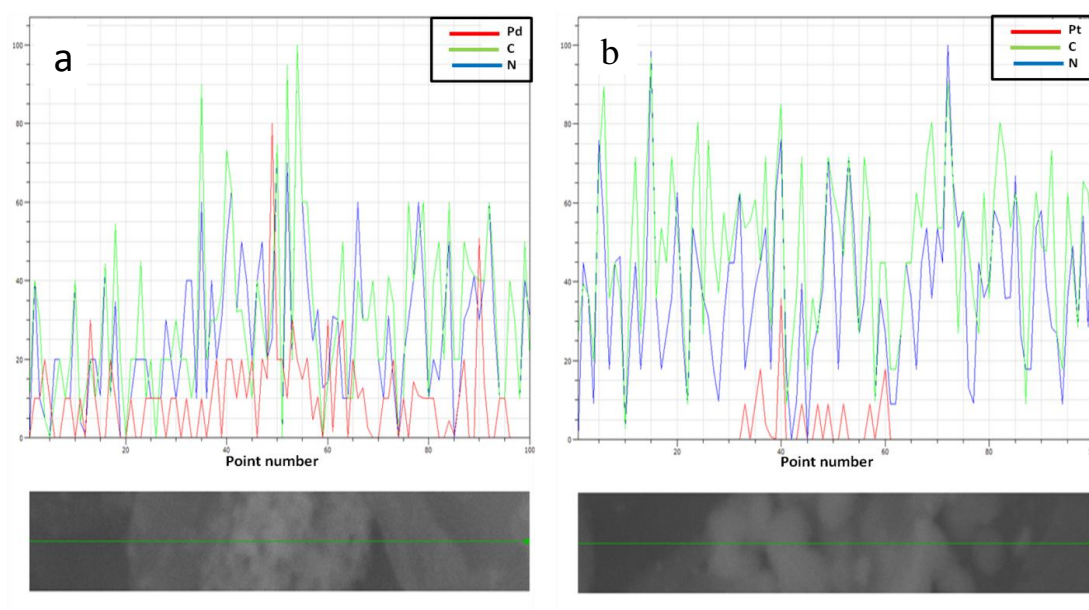
Figure 2.8: Line mapping of (a) C_3N_4/Pd (b) C_3N_4/Pt with FESEM image

41

2.5.6. TEM analysis of Pt/C$_3$N$_4$ and Pd/C$_3$N$_4$ structure

Figure 2.9 and Figure 2.10 represents TEM images of Pd and Pt nanoparticles on C$_3$N$_4$ surface. It can be seen from Figure 2.9a that Pd NPs are uniform and spherical in shape with an average particle size 8 ± 1 nm and homogeneously distributed on C$_3$N$_4$ surface. HRTEM image of Pd NP is shown in Figure 2.9b, where the interplaner spacing (d) value is 0.21 nm, which corresponds to (111) plane of Pd. Therefore, the growth of Pd cluster on C$_3$N$_4$ surface occurs through (111)
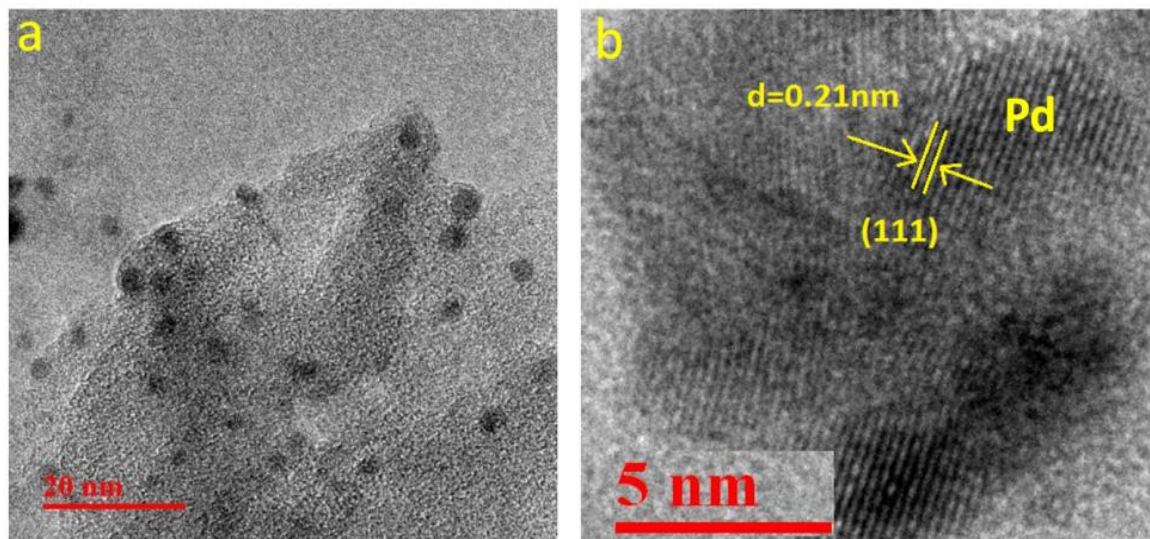
Figure 2.9: TEM (a) and HRTEM (b) image of C$_3$N$_4$/Pd NPs
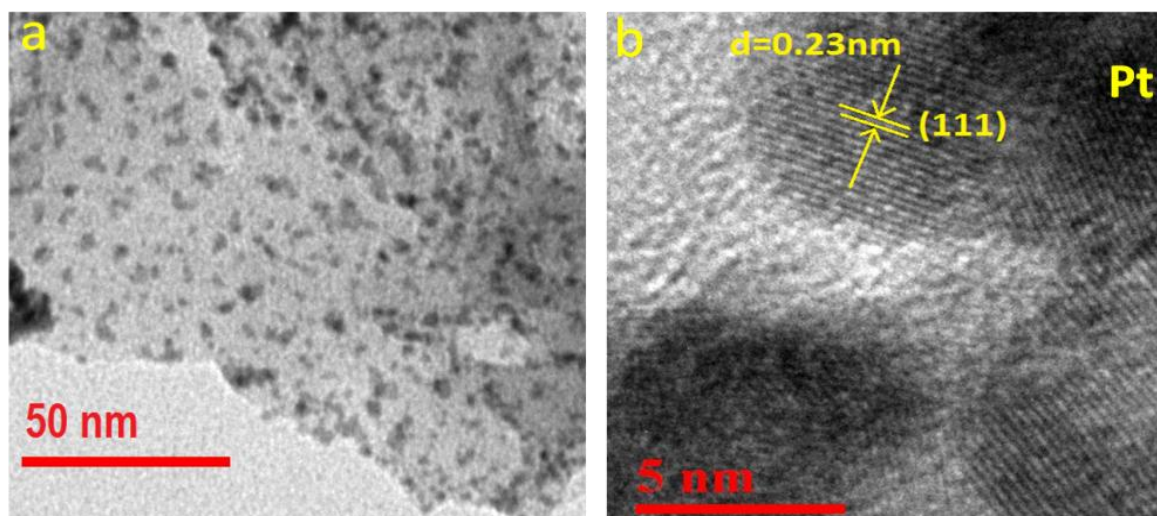
Figure 2.10: TEM (a) and HRTEM (b) image of C$_3$N$_4$/Pt NPs

plane. Shape of Pt NPs is spherical and is well distributed on C_3N_4 surface, shown in Figure 2.10a. Size of Pt NPs is 12 ± 1 nm and the interplanar spacing value is 0.23 nm (Figure 2.10b), which represents the growth of Pt nanocrystal through (111) plane. Therefore, TEM analysis of Pd and Pt NPs on C_3N_4 surface is well acquainted with their FESEM analysis. In this study C_3N_4 was used as a substrate, where, Pd and Pt NPs were decorated. Initially, C_3N_4 powder was sonicated for ~5 hour so that bulk C_3N_4 dispersed properly via exfoliation. In the exfoliated solution of C_3N_4, K_2PdCl_4 and K_2PtCl_4 were added and stirred for 1 hour. Upon stirring Pd^{2+} and Pt^{2+} ions were adsorbed on C_3N_4 surface via weak van der Waals interaction. Even, pi-conjugated electron cloud of C_3N_4 also helpful for the adsorption of Pd^{2+} and Pt^{2+} ions. After that a reduction reaction using $NaBH_4$ as a reducing agent was followed to synthesize monometallic Pd and Pt nanoparticles on C_3N_4 surface. Both the metal NPs were decorated uniformly on C_3N_4 surface, which confirm the uniform distribution of Pd^{2+} and Pt^{2+} ions on C_3N_4. Both Pd and Pt adsorb on porous C_3N_4 surface strongly, which is confirmed from XPS analysis. The overall synthesis of Pd^0 and Pt^0 on C_3N_4 surface is shown in Scheme 2.2.
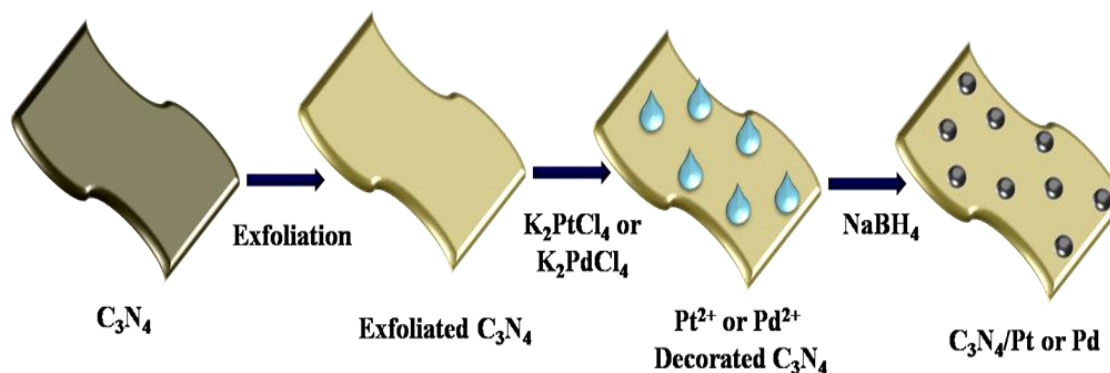
Scheme 2.2: The mechanism of decoration of Pd and Pt nanoparticles on the surface of C_3N_4

2.6. Applications in electrocatalysis and catalysis

2.6.1. Hydrogen evolution reaction using monometallic NPs:

2.6.1.1. Detailed study of LSV polarization curves of C_3N_4, C_3N_4/Pd, C_3N_4/Pt, and pristine Pt for hydrogen evolution reactions

The preliminary catalytic activity of C_3N_4, C_3N_4/Pd, and C_3N_4/Pt catalysts towards hydrogen evolution reaction was studied using linear sweep voltamograme (LSV) technique. 0.5 M aqueous H_2SO_4 solution and 50 mV/s scan rate were used to conduct all the electrochemical

measurements. Throughout the electrochemical study Ag/AgCl electrode was used as reference electrode and the potentials are reported with respect to Ag/AgCl. Cathodic polarization curves in Figure 2.11a shows that after decoration of metal nanoparticle on the surface of C_3N_4, there is remarkable increase in current density with successive anodic shift in the onset potential compared to bare C_3N_4. C_3N_4/Pt, C_3N_4/Pd, and bare C_3N_4 requires potential of -0.339 V, -0.371 V, and -0.596 V, respectively, vs. Ag/AgCl to reach current density of 10 mA/cm^2. Whereas, for pristine Pt (5% Pt on C) -0.307 V potential is required to reach 10 mA/cm^2. From the observed result it is clear that C_3N_4/Pt shows better activity compared to C_3N_4/Pd. The stability of catalysts (Pd and Pt) on electrode surface was checked up to 3000 cycles and shown in Figure 2.12. It can
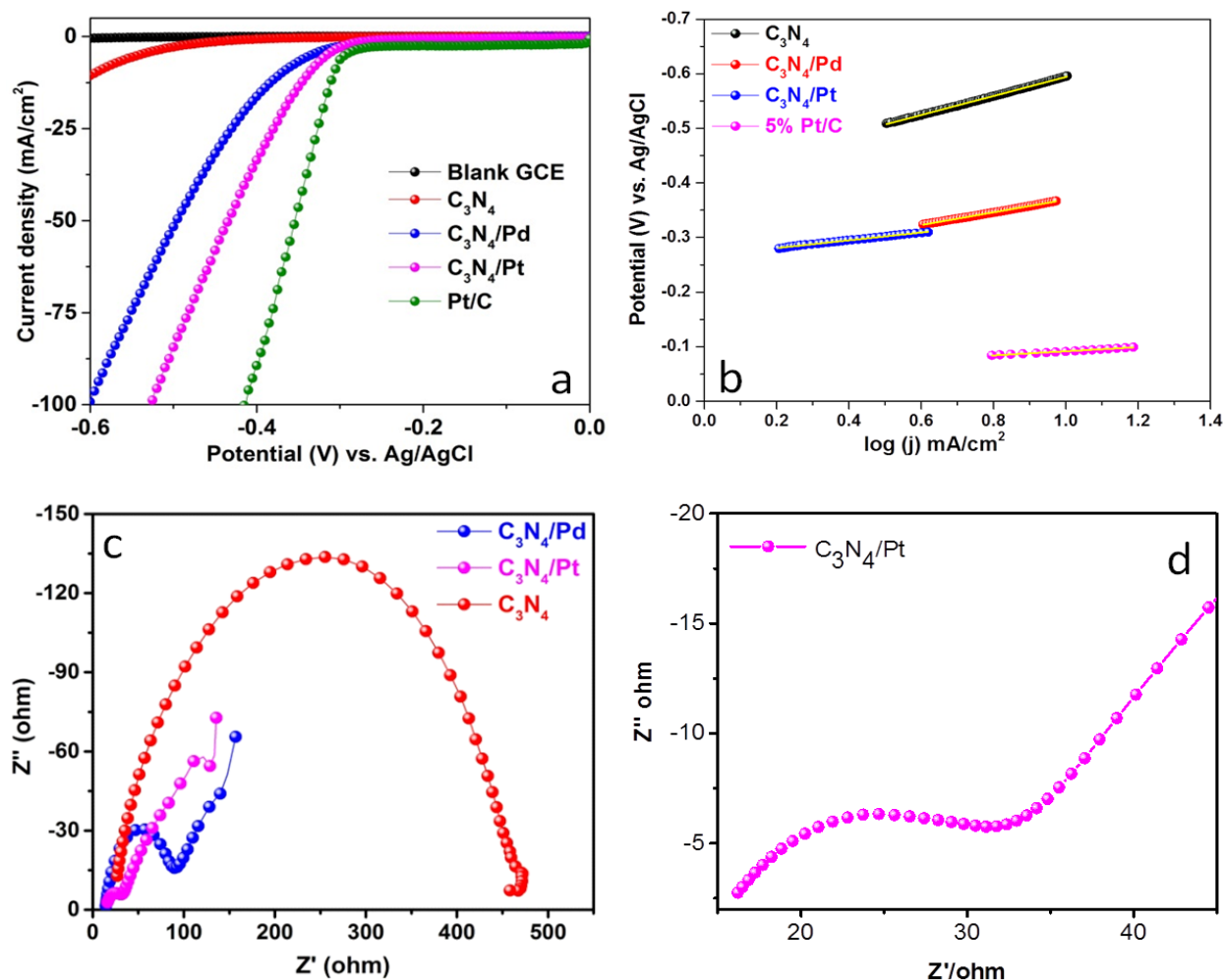
Figure 2.11: LSV polarization curves of (a) C$_3$N$_4$, C$_3$N$_4$/Pd, C$_3$N$_4$/Pt, and pristine Pt for hydrogen evolution reactions, (b) Tafel plot, (c) impedance measurement with Pd, Pt, and bare C$_3$N$_4$ and (d) Magnified version of impedance measurement with C$_3$N$_4$/Pt NPs

be seen from Figure 2.12 a and b that the catalyst are stable on electrode surface and there is no significant change before and after 3000 scan vs. Ag/AgCl. The probable shortcomings of HER catalysts are low surface area, poor electron transportation, and instability under different harsh operating conditions. The density and reactivity of active sites also governs the performance of the catalyst [27-29] Incorporation of metal nanoparticles on C_3N_4 overcomes these drawbacks to some extent. Metal NPs decorated on C_3N_4 surface not only increases the number of active sites but also improves the electron transportation through its porous surface. This superior activity of C_3N_4/Pd and C_3N_4/Pt as compared to bare C_3N_4 is attributed to the Gibbs free energy for hydrogen adsorption (ΔG_{H*}). [4] To be a better descriptor of the intrinsic activity of metal nanoparticles for HER, Gibbs free energy is proposed.
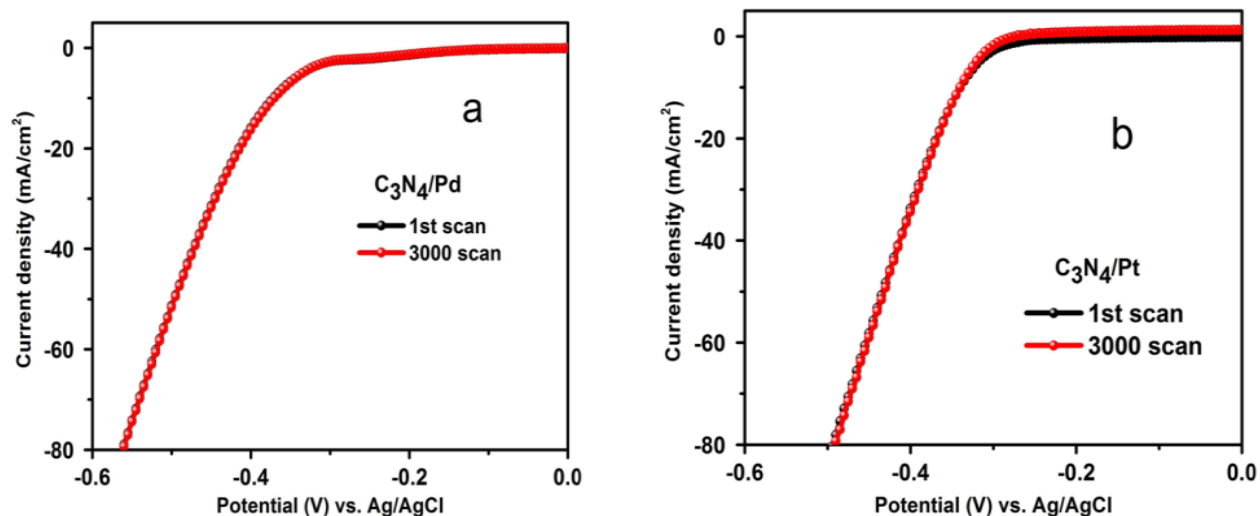
Figure 2.12: Comparative polarization curve of (a) C_3N_4/Pd and (b) C_3N_4/Pt initial run and after 3000 cycle

2.6.1.2. Mechanism of hydrogen evolution reaction:

HER reaction follows two mechanisms. First step is the discharge step and also called as Volmer step where there is the electron transfer to proton or H_3O^+ and lead to H_{ads}. Hydronium cation (H_3O^+) is the proton source in acidic electrolytes. $H_3O^+ + e^- \longrightarrow H_{ads} + H_2O$. Two different reaction pathways may follow in the second step. One way is Heyrovsky process also called desorption reaction ($H_{ads} + H_3O^+ + e^- \longrightarrow H_2 + H_2O$), i.e., transfer of second electron to the H_{ads} atom with simultaneously coupling of another proton to evolve hydrogen gas. The other possibility is already adsorbed two hydrogen atoms combine on catalyst surface to give H_2 gas. This third step is called as Tafel or recombination reaction ($H_{ads} + H_{ads} \longrightarrow H_2$). The mechanism

and rate-determining step are studied by the Tafel slope. Tafel slope is an inherent and intrinsic property of material, which is useful to determine the effectiveness of a catalyst. In order to calculate the Tafel slope the linear portion of the Tafel plots is to be fitted in the Tafel equation ($\eta = b \log (j) + a$, where η = overpotential, b = Tafel slope, and J = current density. [27, 28] In case of bare Pt, it has very high H_{ads} and it follows Volmer-Tafel mechanism and the Tafel step i.e., the recombination step is the rate-determining step. Measured Tafel slope for Pt is 30 mV/decade. If the rate-determining step is Heyrovsky step, Tafel slope value will be 40 mV/decade and if the Volmer step is the rate-determining step, then the Tafel slope will be 120 mV/decade.

Table 2.2: Comparative study of HER activity of reported references

Material	Loading amount (mg/cm^2)	Medium	Overpotential to generate 10 mA/cm^2 current density	Tafel slope (mV/decade)	Reference
Pd-C_3N_4	0.043	0.5 M H_2SO_4	-55 mV	35	22
PdCu@Pd nanocube	0.14	0.5 M H_2SO_4	-5 mV (onset)	35	34
Pd on rGO	-	0.5 M H_2SO_4	-3 mV (onset)	34	35
Pt dendrimer on C	-	0.5 M H_2SO_4	-16 mV (onset)	42	36
Pt on GO	-	0.5 M H_2SO_4	-26 mV (onset)	58	36
N-doped CNTs supported Pd	0.7	0.5 M H_2SO_4	- 300 mV (at 60 mA/cm^2)	-	37
Carbon supported Pt	5 $\mu g/cm^2$	0.1 M $HClO_4$	50 mV (at 2.4 mA/cm^2	Anodic = 260 ± 23 Cathodic = 133 ± 5	38
Carbon supported Pd	10 $\mu g/cm^2$	0.1 M $HClO_4$	70 mV (at 2.4 mA/cm^2	Anodic = 260 ± 23 Cathodic = 133 ± 5	38
Ultrafine Pt/Pd on MWCNTs	-	0.5M H_2SO_4	-0.21 V (onset)	38	39
Pd on C_3N_4	1.056	0.5M H_2SO_4	-0.339 V vs. Ag/AgCl	116	This work
Pt on C_3N_4	1.056	0.5M H_2SO_4	-0.371 V vs. Ag/AgCl	71	This work

In our present study, Tafel slope of 5% Pt on C, C_3N_4, C_3N_4/Pd, and C_3N_4/Pt, are 37, 174, 116 and 71 mV/decade, respectively (Figure 2.11b). Tafel slope values suggest that for C_3N_4/Pd, and C_3N_4/Pt, HER reaction follows Volmer-Heyrovsky mechanism. Heyrovsky step is the rate determining step for C_3N_4/Pt and for C_3N_4/Pd Volmer step is the rate determining. In case of Pt decorated C_3N_4, Tafel slope is lowest compared to others, which also indicates the superior activity of Pt. A comparative study of HER activity with reported references is given in Table 2.2. It can be seen from Table 2.2 that our reported C_3N_4/Pd and Pt catalyst shows comparable activity with reported literature.

2.6.1.3. Electrochemical impedance measurements

To account the comparative electrocatalytic activity of C_3N_4, C_3N_4/Pt, and C_3N_4/Pd electrochemical impedance measurements were carried out. Electrochemical impedance study gives information about the ease of charge transportation on different electrode surfaces. Impedance measurements for C_3N_4/Pt, C_3N_4/Pd, and C_3N_4 (Figure 2.11c) were measured at their respective onset potentials. Impedance curve for C_3N_4/Pd and C_3N_4/Pt is fitted with the equivalent circuit consisting resistance (R_s), Constant phase element (CPE) and Warburg constant (W_S) and the value of resistances are summarized in Table 2.3. Observed R_{CT} of C_3N_4/Pt, C_3N_4/Pd and C_3N_4 are 15 Ω, 75 Ω, and 431 Ω, respectively. Lower charge transfer resistance of C_3N_4/Pt (Figure 2.11d shows magnified version of impedance measurement with C_3N_4/Pt) reveals that C_3N_4/Pt composite electrodes offer the least resistance to the electron transportation followed by C_3N_4/Pd and C_3N_4. Pt nanoparticle decoration on the surface of C_3N_4 successfully enhances the electrochemical activity.

Table 2.3: R_{CT} values of bare C_3N_4, C_3N_4/Pd, and C_3N_4/Pt NPs

Materials used	R_{CT} value (Ω)
C_3N_4	431
C_3N_4/Pd	75
C_3N_4/Pt	15

2.7. Nitrocompound reduction using Pd and Pt NPs

2.7.1. Reduction of 4-NA, 4-NP and 2-NBA in the presence of C_3N_4/Pd and Pt NPs

To verify the activity of our as-synthesized catalysts (C_3N_4/Pd and Pt) we have chosen another reduction reaction. Reduction of nitrocompounds has raised considerable interest because nitrophenol compounds are determined water pollutants and thus a serious global concern. During the preparation of dyes, pigments, and polymers aromatic amines are important intermediates and precursors, which makes reduction of nitro-compounds equally significant.[30] Therefore, we have checked the catalytic activity of our as-synthesized catalyst (bare C_3N_4, Pd, and Pt NPs) for *p*-nitroaniline (4-NA), *p*-nitrophenol (4-NP), and *o*-nitrobenzoic acid (2-NBA) reduction reaction.

2.7.2. Kinetic study of 4-NA reduction

4-NA exhibits a distinct absorption spectrum at 381 nm, which is shown in Figure 2.13 When a freshly prepared $NaBH_4$ solution was added into 4-NA, there was slight decrease in the absorption peak. In absence of any catalyst the peak intensity of 4-NA at 381 nm remains unaffected with time, which verifies that the reduction reaction doesn't occur. After addition of catalyst (1.0 mg), the reduction of 4-NA was initiated, which can be visualized by gradual decrease in absorption intensity of 4-NA at 381 nm, accompanying the appearance of new peaks at ~307 nm and 240 nm. C_3N_4/Pd was used for reduction of 4-NA, which is shown in Figure 2.13a. The UV-visible absorption spectra showed the reactant peak at 381 nm disappeared and the product peak at 307 nm and 240 nm appeared with time. For C_3N_4/Pd catalyst the reaction is very fast and ~ 98% conversion of 4-NA to 4-phenelenediamine (4-PDA) occurs within 6 min. The conversion process is studied by UV-vis spectra at different time interval. The ratio of the concentrations of 4-NA and 4-PDA at different time interval gives A_t/A_0 values. The plot of A_t/A_0 vs. *t* (min) shows exponential decay (Figure 2.13b), which specify the pseudo first order kinetics. Finally, linear plot of $ln(A_t/A_0)$ vs. *t* (min) (Figure 2.13c) confirms the pseudo-first order kinetic reaction and the value of rate constant '*k*' was determined from the slope using the following equation. The rate constant value using C_3N_4/Pd catalyst is 6.7×10^{-1} min^{-1}.

$$ln(A_0/A_t) = kt$$

Similar catalytic conversion was also performed with C_3N_4/Pt and bare C_3N_4 catalyst. In both cases only 1.0 mg catalyst was used. C_3N_4/Pt catalyst needs 25 min for ~ 98% conversion of 4-NA to 4-PDA. The plot of A_t/A_0 vs. t (min) is exponential decay, which indicates pseudo-first order of the reaction. Furthermore, plot of $\ln(A_t/A_0)$ vs. t (min) shows linear nature and the rate
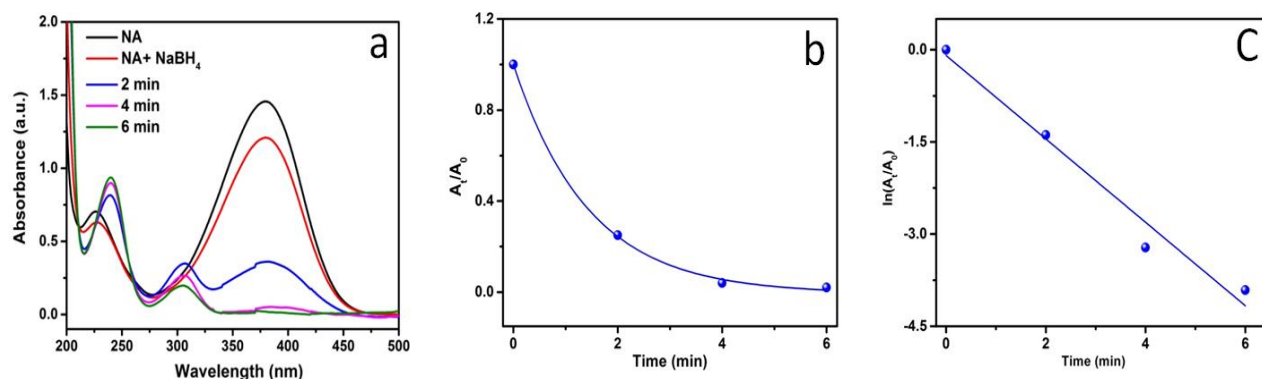
Figure 2.13: UV-vis spectra of (a) reduction of 4-NA in presence of C_3N_4/Pd NPs (b) A_t/A_0 vs. time (min) plot (c) ln (A_t/A_0) vs. time (min) plot. Conditions: [NA] = 10^{-4} M and amount of catalyst = 1.0 mg. In all cases water was used as reference solution

constant (*k*) value is 1.4×10^{-1} min^{-1} favors pseudo-first order kinetics. Using bare C_3N_4 the reduction reaction proceeds slowly and gives ~57% conversion in 90 min. The plot of *ln(A_t/A_0)* vs. *t* (min) shows linear nature and the rate constant (*k*) value is 6.6×10^{-3} min^{-1}. Therefore, the order of rate constant for 4-NA to 4-PDA conversion is $k_{C3N4/Pd} > k_{C3N4/Pt} > k_{C3N4}$.
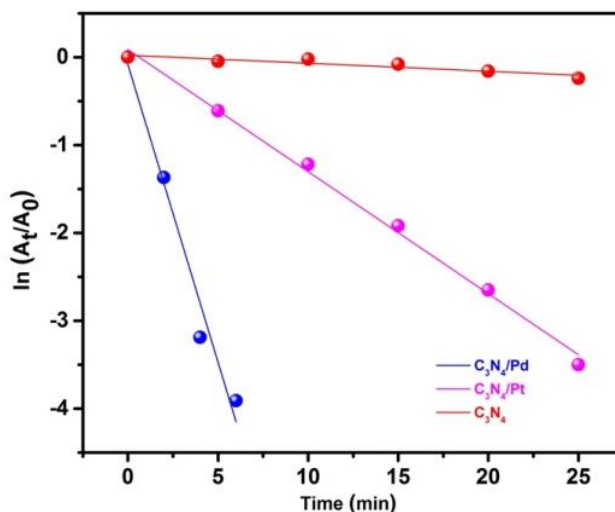
Figure 2.14: Comparative Study of reduction of 4-NA in presence of C_3N_4/Pd NPs

It can be seen from Figure 2.14 that the comparative study of the catalysts towards reduction of 4-NA to 4-PDA shows C_3N_4/Pd is a better catalyst than C_3N_4/Pt and bare C_3N_4. Rate constant (k) of C_3N_4/Pd is 4.7 times higher as compared to C_3N_4/Pt and 101 times better than bare C_3N_4. The better activity for C_3N_4/Pd is presumably due to proper adsorption of nitrocompounds on C_3N_4/Pd surface. To overcome the kinetic barrier, C_3N_4/Pd and C_3N_4/Pt can catalyze the reduction of nitro-compounds by acting as an electron relay system where, electrons are initially received from donor (BH_4^- group) and then passed to acceptor (nitro group). [31,32] In case of 4-NA to 4-PDA reduction, the reaction follows two steps. First, 4-NA and BH_4^- are chemically adsorbed on porous catalyst surface and electrons are transferred followed by 4-PDA formation. Second, the desorption of 4-PDA from the catalyst surface. Esumi and co-workers also reported higher activity of Pd NPs towards nitro-compound reduction.[33] Recently, our group reported the reduction of 4-NP using Au, Pd and AuPd NPs, where Pd shows 1.5×10^{-1} min^{-1} rate constant value, which is comparable with this study. [23]

As an advantage of heterogeneous catalyst, C_3N_4/Pd was used to check reusability for 4-NA reduction reaction. After 1st cycle of the reaction the catalyst was centrifuged and washed thoroughly with distilled water. The reduction of 4-NA to 4-PDA was repeated four times and the corresponding results shows 98%, 96%, 92%, and 88% conversion. Therefore, the catalyst is highly stable up to fourth cycle, which is shown in Figure 2.15.
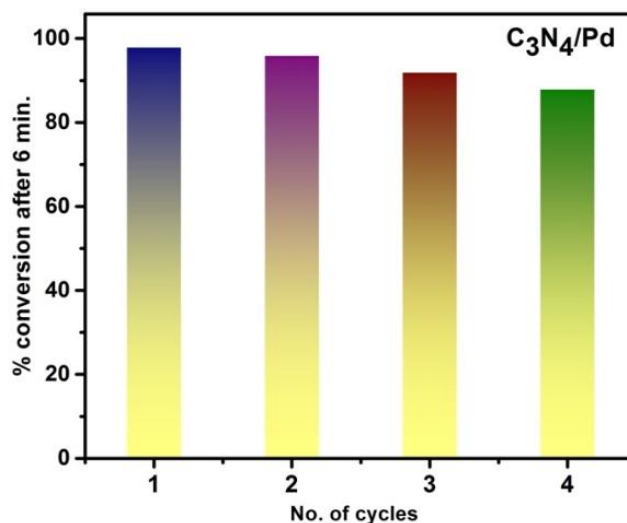
Figure 2.15: Comparative Study of reduction of 4-NA in presence of C_3N_4/Pd NPs

After fourth cycle of the catalytic reaction the morphology of C_3N_4/Pd NP was confirmed with the help of FESEM analysis (Figure 2.16), which shows similar morphology of Pd NP as discussed in FESEM analysis. To check the catalytic activity of the as-synthesized C_3N_4/Pd, C_3N_4/Pt, and bare C_3N_4 catalyst few other nitro-compounds (4-NP and 2-NBA) were used using similar experimental appeared in pure 4-NP (Figure 2.17). When a freshly prepared $NaBH_4$ (0.1 M) solution was added into 4-NP, the absorption peak was shifted to 400 nm, analogous to the
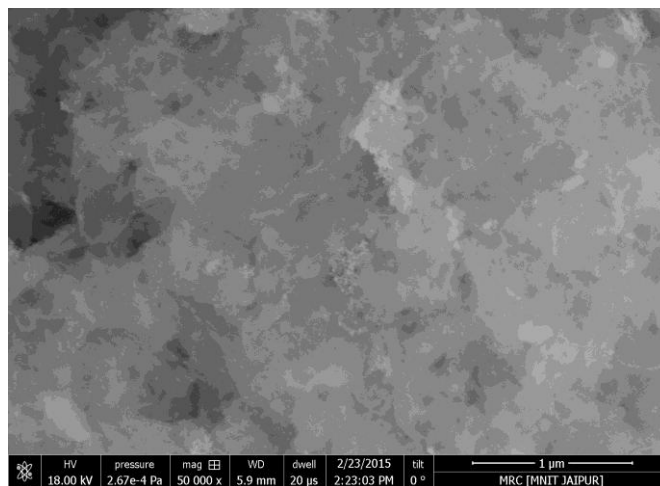
Figure 2.16: FESEM of reused C_3N_4/Pd after 4th cycle

4-nitrophenolate ions where, nitrophenolate ion behaves as an oxidant and BH_4^- as a reductant. After addition of a catalyst, the reduction of 4-NP was initiated, which can be visualized by monitoring the decrease in absorption intensity of 4-nitrophenolate ions at 400 nm, accompanying the appearance of a new peak of 4-aminophenol (4-AP) at 300 nm. In absence of
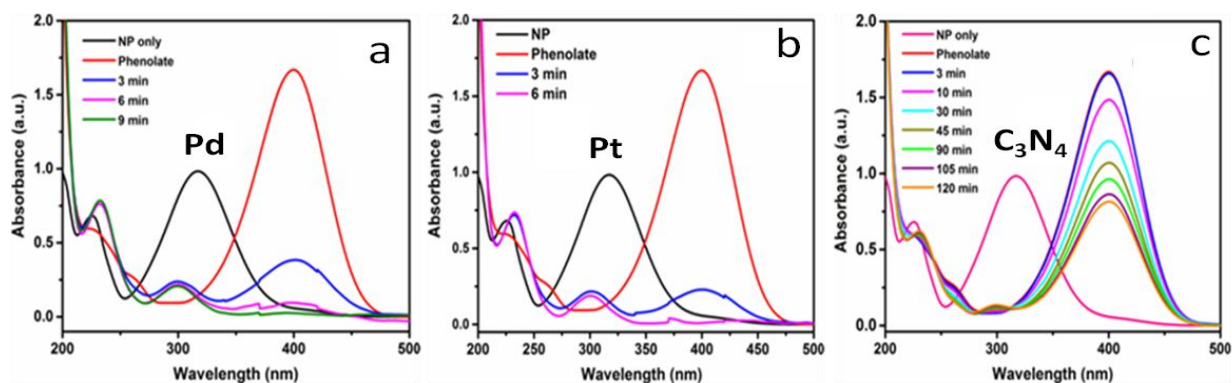
Figure 2.17: Reduction of 4-nitrophenol using (a) C_3N_4/Pd (b) C_3N_4/Pt (c) C_3N_4 catalyst

any catalyst the peak intensity of 4-nitrophenolate ion at 400 nm remains unaffected with time, which verifies the importance of catalyst for this reduction reaction. For C_3N_4/Pd catalyst, ~7 min was required for 99% conversion, whereas, for C_3N_4/Pt, 99% conversion occurs at ~6 min (Figure 2.17 a and b,). However, for bare C_3N_4 the reaction proceed very slowly and after 2 h only 55% converted into 4-AP (Figure 2.17 c). Therefore, the rate of the reaction is lowest with bare C_3N_4 and almost similar with Pd and Pt decorated C_3N_4 catalyst. It can be seen from Figure 2.18 that 2-NBA shows a significant absorption peak at 266 nm. In absence of any catalyst the peak intensity of 2-NBA at 266 nm remains unaffected. Upon addition of a catalyst, the reduction of 2-NBA was initiated, which can be visualized by appearing a new peak of anthranilic acid at 300 nm. For C_3N_4/Pd, very less time (~5 min) is required for complete conversion, whereas, for C_3N_4/Pt conversion into anthranilic acid is possible within 10 min. However, for bare C_3N_4 the reaction is very slow. Therefore, the rate of the reaction follows similar trend, C_3N_4/Pd is a better catalyst than C_3N_4/Pt and C_3N_4 only. The conversion of 2-NBA to anthranilic acid using C_3N_4/Pd, C_3N_4/Pt, and bare C_3N_4 catalysts is shown in Figure 2.18 a, b, and c.
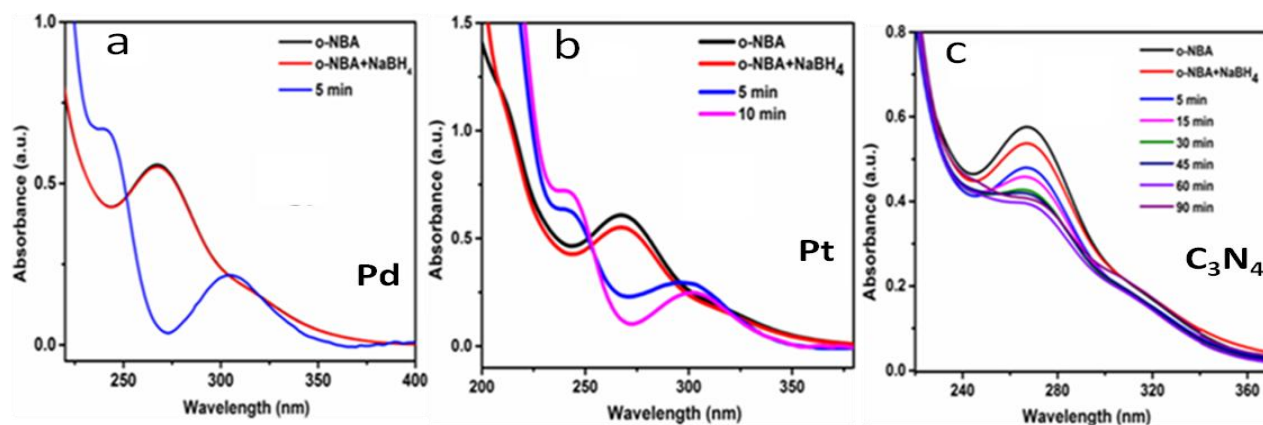
Figure 2.18: Reduction of ortho-nitrobenzoic acid using (a) C_3N_4/Pd (b) C_3N_4/Pt (c) C_3N_4
Conditions: [NBA] = 10^{-4} M and amount of catalyst = 1.0 mg

2.8. Conclusion:

Monometallic (Pd and Pt) nanoparticles can be successfully decorated on C_3N_4 surface using NaBH$_4$ as a reducing agent. Decoration of both Pd and Pt NPs on C_3N_4 surface improved both

the catalysis and electrocatalysis in reduction of nitro-compounds and hydrogen evolution reaction. Pt NPs decorated on C_3N_4 surface proved efficient electrocatalyst as it requires -0.339 V potential to reach current density of 10 mA/cm^2 vs. Ag/AgCl, which is comparatively better than Pd NPs. Using the value of Tafel slope it is suggested that for C_3N_4/Pd, and C_3N_4/Pt, HER reaction follows Volmer-Heyrovsky mechanism. Heyrovsky step is the rate determining step for C_3N_4/Pt and for C_3N_4/Pd Volmer step is the rate determining. On the other hand, Pd NPs decorated on C_3N_4 shows excellent catalytic activity in reduction of 4-NA with higher rate constant, $k = 6.7 \times 10^{-1}$ min^{-1} as compared to Pt and bare C_3N_4 and pseudo-first order kinetics. Various nitro-compounds have been used to verify the catalytic efficiency and C_3N_4/Pd shows better activity as compared to others. Therefore, this study leaves an avenue for the decoration of various mono- and bimetallic NPs on C_3N_4 surface.

2.9. References

[1] S. Chu, A. Majumdar, Nature, 488 (2012) 294.

[2] M. S. Dresselhaus, I. L. Thomas, Nature, 414 (2001) 332.

[3] J. A. Turner, Science, 285 (1999) 687-689.

[4] C. G. Morales-Guio, L.-A. Stern, X. Hu, Chem. Soc. Rev., 43 (2014) 6555-6569.

[5] Z. Peng, H. Yang, Nano Today, 4 (2009) 143-164.

[6] V. R. Stamenkovic, B. S. Mun, M. Arenz, K. J. J. Mayrhofer, C. A. Lucas, G. Wang, P. N. Ross, N. M. Markovic, Nat. Mater., 6 (2007) 241.

[7] N. Furuya, S. Motoo, Journal of J. Electroanal. Chem., 88 (1978) 151-160.

[8] F. Li, P. Bertoncello, I. Ciani, G. Mantovani, P. R. Unwin, Adv. Funct. Mater., 18 (2008) 1685-1693.

[9] F. Li, I. Ciani, P. Bertoncello, P. R. Unwin, J. Zhao, C. R. Bradbury, D. J. Fermin, Scanning J. Phys. Chem. C, 112 (2008) 9686-9694.

[10] S. R. Sivakkumar, J. Y. Nerkar, A. G. Pandolfo, Electrochim. Acta,55 (2010) 3330-3335.

[11] H.-Y. Park, I.-S. Park, B. Choi, K.-S. Lee, T.-Y. Jeon, Y.-E. Sung, S. J. Yoo, Phys. Chem. Chem. Phys., 15 (2013) 2125-2130.

[12] S. Han, D. H. Youn, M. H. Lee, J.S. Lee, ChemCatChem, 7 (2015) 1483-1489.

[13] K. H. Kangasniemi, D. Condit, T. Jarvi, J. Electrochem.Soc., 151 (2004) E125-E132.

[14] L. Perini, C. Durante, M. Favaro, V. Perazzolo, S. Agnoli, O. Schneider, G. Granozzi, A. Gennaro, ACS Appl. Mater. Interfaces, 7 (2015) 1170-1179.

[15] V. Di Noto, E. Negro, S. Polizzi, F. Agresti, G.A. Giffin, ChemSusChem, 5 (2012) 2451-2459.

[16] Y. Zhang, T. Mori, J. Ye, Sci. Adv. Mater., 4 (2012) 282-291.

[17] Z. Zhao, Y. Sun, F. Dong, Nanoscale, 7 (2015) 15-37.

[18] P. Fageria, R. Nazir, S. Gangopadhyay, H. C. Barshilia, S. Pande, RSC Adv., 5 (2015) 80397-80409.

[19] Y. Wang, J. Yao, H. Li, D. Su, M. Antonietti, J. Am. Chem. Soc., 133 (2011) 2362-2365.

[20] W. Zhang, H. Huang, F. Li, K. Deng, X. Wang, J. Mater. Chem. A, 2 (2014) 19084-19094.

[21] H. Wang, L. Thia, N. Li, X. Ge, Z. Liu, X. Wang, ACS Catal., 5 (2015) 3174-3180.

[22] T. Bhowmik, M. K. Kundu, S. Barman, ACS Catat., 6 (2016) 1929-1941.

[23] P. Fageria, S. Uppala, R. Nazir, S. Gangopadhyay, C.-H. Chang, M. Basu, S. Pande, Langmuir, 32 (2016) 10054-10064.

[24] Y. Zhang, J. Liu, G. Wu, W. Chen, Nanoscale, 4 (2012) 5300-5303.

[25] Q. Xu, C. Jiang, B. Cheng, J. Yu, Dalton Trans., 46 (2017) 10611-10619.

[26] S. Pande, M. G. Weir, B. A. Zaccheo, R. M. Crooks, New J. Chem., 35 (2011) 2054-2060.

[27] T. Shinagawa, A. T. Garcia-Esparza, K. Takanabe, Sci. Rep., 5 (2015) 13801.

[28] A. Behranginia, M. Asadi, C. Liu, P. Yasaei, B. Kumar, P. Phillips, T. Foroozan, J. C. Waranius, K. Kim, J. Abiade, R. F. Klie, L. A. Curtiss, A. Salehi-Khojin, Chem. Mater., 28 (2016) 549-555.

[29] S. Trasatti, Electrochim. Acta, 29 (1984) 1503-1512.

[30] P. S. Rathore, R. Patidar, T. Shripati, S. Thakore, Catal. Sci. Technol., 5 (2015) 286-295.

[31] Z. Jiang, J. Xie, D. Jiang, X. Wei, M. Chen, CrystEngComm, 15, (2013) 560-569.

[32] S. Panigrahi, S. Basu, S. Praharaj, S. Pande, S. Jana, A. Pal, S. K. Ghosh, T. Pal, J. Phy. Chem. C, 111, (2007) 4596-4605.

[33] K. Esumi, R. Isono, T. Yoshimura, Langmuir, 20 (2004) 237-243.

[34] J. Li, F. Li, S. X. Guo, J. Zhang, J. Ma, Appl. Mater. Interfaces, 9 (2017) 8151-8160.

[35] J. Li, P. Zhou, F. Li, J. Ma, Y. Liu, X. Zhang, H. Huo, J. Jin, J. Ma, J. Power Sources, 302, (2016) 343-351.

[36] B. Devadas, T. Imae, Electrochem. Commun., 72, (2016) 135-139.

[37] S. U. B. Ramakrishna, D. S. Reddy, S. S. Kumar, Int. J. Hydrogen Energy, 41 (2016) 20447-20454.

[38] J. Durst, C. Simon, F. Hasche, H. A. Gasteiger, J. Electrochem. Soc., 162 (2015) F190-F203.

[39] M. Xiao, X. Liang, W. Li, Y. Yang, Y. Miao, J. Electrochem. Soc., 162 (2015) H415-H418.

Chapter 3

Synthesis and characterization of bimetallic alloy nanoparticles (Ag/Pt, Ag/Pd, and Ag/Au) via galvanic exchange for hydrogen evolution reaction

Abstract

This chapter enlightens the synthesis of AgPt, AgPd and AgAu bimetallic nanoparticles (NPs) on carbon nitride (C_3N_4) surface via galvanic exchange technique for hydrogen evolution reaction (HER). Prior to the synthesis of C_3N_4/AgPt, AgPd, and AgAu, Ag NPs were synthesized on C_3N_4 surface. For the synthesis of Ag NPs, initially Ag^+ ions were adsorbed and then reduced by $NaBH_4$ resulting in decoration of Ag NPs. These Ag NPs were then subjected to galvanic exchange where sacrificial Ag was replaced by Pt^{2+}, Pd^{2+}, and Au^{3+} to fabricate AgPt, AgPd, and AgAu NPs. The galvanic exchange reaction occurs on a solid substrate, which favored slow exchange of Ag and resulting in the transformation of Ag into AgPt, AgPd and AgAu alloys. The synthesized heterostructures were characterized with the help of PXRD, XPS, TEM, FESEM, and EDS techniques. All the materials were applied for hydrogen evolution using 0.5 M H_2SO_4 solution. C_3N_4/AgPt shows efficient electrocatalytic activity as it requires only -150 mV potential to attain current density of 10 mA/cm^2. Bimetallic catalysts synthesized through galvanic exchange proved very efficient as compared to monometallic C_3N_4/Ag. Production of hydrogen using C_3N_4/AgPt alloy is shown in scheme 3.1.
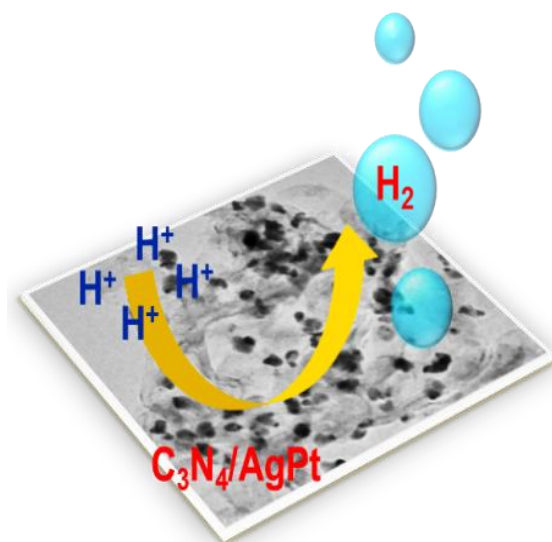
Scheme 3.1: Diagrammatic representation showing production of hydrogen gas using galvanically synthesized AgPt alloy on C_3N_4 as a catalyst

3.1. Introduction

Limitation in natural energy sources and day-by-day increase in the daily energy requirement have triggered the ways for a reliable and efficient energy source. Hydrogen have been proving an excellent and reliable energy source because it is environmentally benign, generates enormous amount of energy with admirable efficiency. [1, 2] Carbon dioxide, methane etc. greenhouse gases are produced from fossil fuels, which lead to global warming. Whereas, hydrogen is a clean and pollutant free green energy source often referred as "fuel of future". [3, 4] Generation of hydrogen from electrocatalysis of water is one of the best technique and has attained considerable attention in last few decades. [5-9]

The noble metal nanoparticles (NPs) show incredible activities in hydrogen evolution reactions (HER) when processed in electrocatalytic water splitting. This is because of the fact that their conductivity is not hampered in acidic media. Pt and Pt based compounds are the best candidates because they generate hydrogen with onset potential close to zero. [10, 11] As Pt is found very rear in earth's crust and thus processing HER through Pt is exorbitant, so it has remained a critical challenge to synthesize catalyst as effective as Pt. This limitation of Pt initiated the ways out to find the promising substitute. Pd NPs have been studied to overcome this limitation and reports have revealed Pd NPs show incredible electocatalytic activities and thus play a key role in HER reaction. [12, 13]

Bimetallic NPs are one of the important class of catalysts that have come into light over the years. Bimetallic NPs exhibits superior catalytic efficiencies as compared to monometallic NP, this is credited to strong synergistic effect between the two metals. [14-16] Plenty of research have been dedicated to synthesize bimetallic core-shell or alloy type NP. This is aimed to bring surface modifications and synergistic effect in bimetallic NPs for enhancing catalytic and electrocatalytic properties. [17] Bimetallic combination (alloy or core-shell) of Pd and other noble metals are very active for hydrogen evolution. [14, 18-20] Safavi and co-workers proved that carbon ionic liquid modified Ag/Pd alloy functionalized electrode has superior electrocatalytic activity towards HER than pure Pd. [21] Boukherroub and co-workers reported decoration of mono- (Pd, Au) and bimetallic (AuPd) NPs on reduced graphene oxide nanosheets for HER. They have reported better performance of Au-Pd bimetallic NPs supported on rGO as compared to their monometallic counterpart towards HER. [22] Synthesis and decoration of ultrafine (13 nm) Pt/Pd bimetallic NPs on multi-walled carbon nanotube surface for

electrochemically hydrogen evolution reaction has been shown by Miao and co-workers. [23] Lee and co-workers followed galvanic exchange method for shape-dependent (circular, hexagonal, and triangular) Ag-Pt nanoplate synthesis for hydrogen evolution and Ag-Pt$_{triangular}$ nanoplate showed maximum efficiency. [24] HER activity of Ag nanocubes substituted by various amounts of Pt via galvanic exchange and significance of bimetallic composition in the activity of alloy NPs have been reported by Bhargava and co-workers. [25]

Bimetallic nanoparticles have been synthesized on semiconducting support to aggrandize their catalytic efficiency. Semiconducting materials like graphene and carbon nitride have been successfully used as a solid support to synthesize metal and metal oxide NPs for catalysis and electrocatalysis. [22, 26, 27] Carbon nitride (C_3N_4) is a visible light active photocatalyst due to its characteristic electronic band structure and unique layered structure. [28, 29] The advantages of C_3N_4 as a support for an electrocatalytic reactions are multifold. The presence of heteroatom such as N-based ligand and repetitive *s*-triazine unit in the structure of C_3N_4 can coordinate and stabilize with NPs easily. Strong coordination and interaction between metal NPs and substrate may lead to facilitate electrical connection and electron transportation. Durante and co-workers reported the synthesis of Pd and Pt NPs on N-doped mesoporous carbon for electrocatalysis and showed that the presence of nitrogen functional groups can enhance NP and substrate interaction. [30] Di Noto and co-workers reported Pt-Ni and Pt-Fe core-shell carbon nitride nano-electrocatalyst and showed strong metal-ligand interaction. [31] Sun and co-workers exhibited the effect of nitrogen doping on carbon nanotubes (CNTs) and the improved electrocatalytic activity of loaded Pt/CNT catalyst. [32] The presence of N atom via C=N and C-N stretching vibrations and pyridinic N in C_3N_4 structure, which produce large no of active sites may improve the charge transfer during electrocatalysis. Kim and co-workers reported the synthesis of Co and carbon doped g-C_3N_4 nanosheet for enhanced electrocatalytic activity and ease of access to the N functionalities for better interaction between Co and C with improved charge transfer. [33] Furthermore, durability of the catalyst on electrode surface is high in presence of C_3N_4. Barman and co-workers decorated Pd NPs on porous carbon nitride surface for oxidation and evolution of hydrogen. [27] Recently, our group has also been reported synthesis mono- (Au and Pd) and bimetallic (AuPd) NPs using C_3N_4 quantum dot (QD) as a stabilizing agent for nitrophenol reduction. [34] Yuan and co-workers communicated the synthesis of AuPd bimetallic NPs on

graphitic carbon nitride surface using hydrazine as a reducing agent and exhibited higher electrocatalytic activity in oxygen reduction and hydrogen evolution reaction. [35]

Being interested from the above studies, here, we have synthesized various combinations of bimetallic nanoparticles (AgPd, AgPt, and AgAu) on semiconducting C_3N_4 surface using C_3N_4/Ag as a precursor via galvanic exchange technique. Initially, silver nanoparticles were synthesized on C_3N_4 surface using a reducing agent, $NaBH_4$. Considering the reduction potential of Ag^+ ion, which is less than Au^{3+}, Pd^{2+} and Pt^{2+} ions, that facilitates silver nanoparticles to undergo galvanic exchange with Au^{3+}, Pd^{2+} and Pt^{2+} ions resulting in the formation of C_3N_4/AgPd, AgPt, and AgAu nanocomposites. All the bimetallic NPs were used as electrocatalyst for HER. The best electrocatalytic efficiency was achieved in case of C_3N_4/AgPt as it needs potential of 150 mV vs. RHE to generate 10 mA/cm^2 current density. Electrochemical impedance analysis was also performed to study the electrode/electrolyte interface during HER. The significance of this work are multifold. First, synthesis of bimetallic NPs (AgPt, AgPd, and AgAu) via galvanic exchange on solid support, which may bring surface modifications for enhanced electrocatalytic activity. Second, use of conducting support to facilitate the electron transportation during electrocatalytic reaction. Third, comparison of different substrate for NP synthesis and electrocatalytic activity. Fourth, stability or durability of bimetallic NPs on C_3N_4 surface during electrocatalysis.

3.2. Experimental Section

3.2.1. Synthesis of carbon nitride

Literature reported method was followed for the synthesis of C_3N_4. [28, 29] In brief, C_3N_4 was synthesized using extra pure urea as a rich source of C and N. Initially, ~10.0 g urea was dried on water bath and placed inside muffle furnace in a covered crucible for thermal treatment at 550 $^{\circ}$C for 2.5 h. Finally, yellow color product was collected and washed with 0.1 M nitric acid to remove the extra impurities and dried at 80 $^{\circ}$C.

3.2.2. Synthesis of C_3N_4/Ag NPs

20.0 mg of as-synthesized C_3N_4 powder was taken in 19.0 ml water and sonicated for 0.5 h. After sonication, aqueous solution of $AgNO_3$ (200 μL of 1.0 M) was added. The whole reaction mixture was stirred for 1.0 h. 1.0 mL of 1.0 M $NaBH_4$ was added in the solution to reduce Ag^+ to

Ag^0 and stirring was continued for 1.0 h. Finally, brown color mixture of C_3N_4/Ag was washed with DI water followed by ethanol and dried in air.

3.2.3. Synthesis of $C_3N_4/AgPd$, $C_3N_4/AgPt$, and $C_3N_4/AgAu$ bimetallic NPs

Galvanic exchange method was followed for the synthesis of bimetallic nanoparticles from C_3N_4/Ag monometallic NPs. 5.0 mg of C_3N_4/Ag was measured and collected in a beaker followed by the addition of 2.0 mL of 10^{-2} M aqueous K_2PdCl_4 solution. No extra reducing or stabilizing agent were added in the reaction mixture. After addition of K_2PdCl_4, immediately, the color of the solution was changed from brown to grayish black. This color change reflected the formation of $C_3N_4/AgPd$ bimetallic NP via galvanic exchange. The reaction mixture was stirred continuously for 1.0 h. Finally, the product was washed properly with concentrated ammonia solution, DI water, followed by ethanol. During the galvanic exchange process to avoid AgCl deposition cleaning with NH_4OH was very essential. However, following this technique there was no AgCl precipitation on $C_3N_4/AgPd$ surface.

For the synthesis of $C_3N_4/AgPt$ and $C_3N_4/AgAu$ similar methodology was followed except K_2PtCl_4 and $HAuCl_4.3H_2O$ were used as precursors and same concentration instead of K_2PdCl_4. The color of $C_3N_4/AgPt$ and $C_3N_4/AgAu$ was grayish black and light blue, respectively. The overall synthetic procedure is shown in Scheme 3.2.
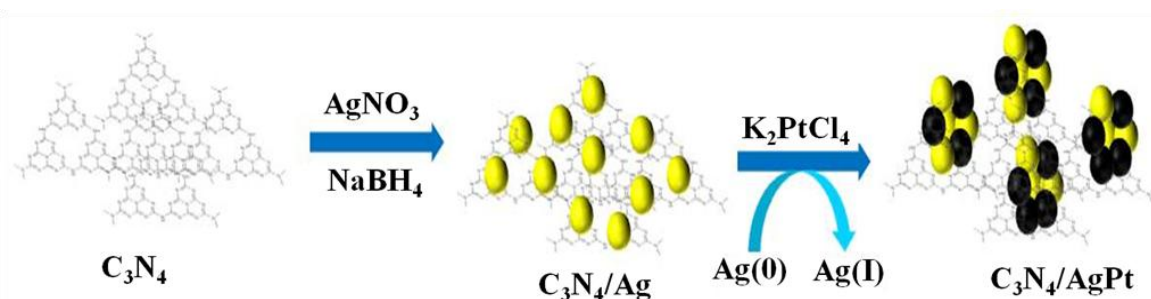
Scheme 3.2: Formation of galvanically synthesized AgPt alloy on C_3N_4 surface

3.3. Results and Discussion

Synthesis of bimetallic (AgPd, AgPt, and AgAu) NPs on C_3N_4 surface via galvanic exchange is mentioned in experimental section. Initially, C_3N_4/Ag monometallic NP was prepared using simple reduction technique and then Ag NP was galvanically exchanged with Pd^{2+}, Pt^{2+} and Au^{3+}

ions to get AgPd, AgPt, and AgAu on C_3N_4 surface, respectively. Finally, all the materials were washed carefully with NH_4OH, DI water, and ethanol to remove impurities and further used for characterization and application purposes. No residual AgCl is present on catalyst surface is an extra advantage of this work.

3.3.1. Powder X-ray diffraction analysis

The structural identity, purity and composition were studied with the help of powder X-ray diffraction analysis is represented in Figure 3.1. C_3N_4 has characteristic diffraction peak at 27.49^o which is associated with (002) plane. The PXRD patterns of C_3N_4/Ag (Figure 3.1a) showed $2\theta =$ 27.49^o, 38.10^o, 44.17^o, 64.40^o, 77.41^o, and 81.62^o peaks. The peak at 27.49^o is due to (002) plane of C_3N_4, while other peaks corresponds to (111), (200), (220), (311) and (222) crystal planes of Ag, which corroborates with fcc lattice structure (JCPDS 04-0783). After galvanic exchange, AgPd, AgPt, and AgAu bimetallic NPs were produced and the PXRD pattern is shown in Figure 3.1a For C_3N_4/AgPd, $2\theta = 38.3^o$, 44.62^o, 64.80^o and 77.94^o corresponds to (111), (200), (220) and (311) crystal planes of Ag and Pd which crystallizes in fcc structure (JCPD-65-2871). In case of C_3N_4/AgPt, four peaks at $2\theta = 38.27^o$, 44.54^o, 64.89^o and 77.94^o corresponds to (111), (200), (220), and (311) crystal planes of Ag and Pt indicating the formation of fcc crystal structure (JCPDS 04-0802). Similarly, PXRD patterns of C_3N_4/AgAu also exhibits four peaks at $2\theta = 37.78°$, $44.52°$, $64.80°$, and $77.94°$, which represents the presence of (111), (200), (220), and (311) planes of Ag and Au, respectively. It can be seen from Figure 3.1a that $2\theta = 27.40°$ is present in case of C_3N_4/AgPd, C_3N_4/AgPt, and C_3N_4/AgAu, which represents C_3N_4 surface was covered by as-synthesized bimetallic NPs. In the PXRD pattern of AgPd, AgPt, and AgAu a clear shift in 2θ values is observed as compared to C_3N_4/Ag, which is due to the decrease in the lattice parameters and represents alloy formation. Absence of any impurities or unreacted species can be claimed from PXRD pattern. Therefore, PXRD analysis confirm that AgCl is absent in the as-synthesized catalyst.

3.3.2. Fourier transform infrared analysis

The well-resolved and strong IR absorption bands for bare C_3N_4 and NPs decorated C_3N_4 is shown in Figure 3.2. In case of bare C_3N_4, the peaks at 1637, 1571 cm^{-1} is attributed to the C=N
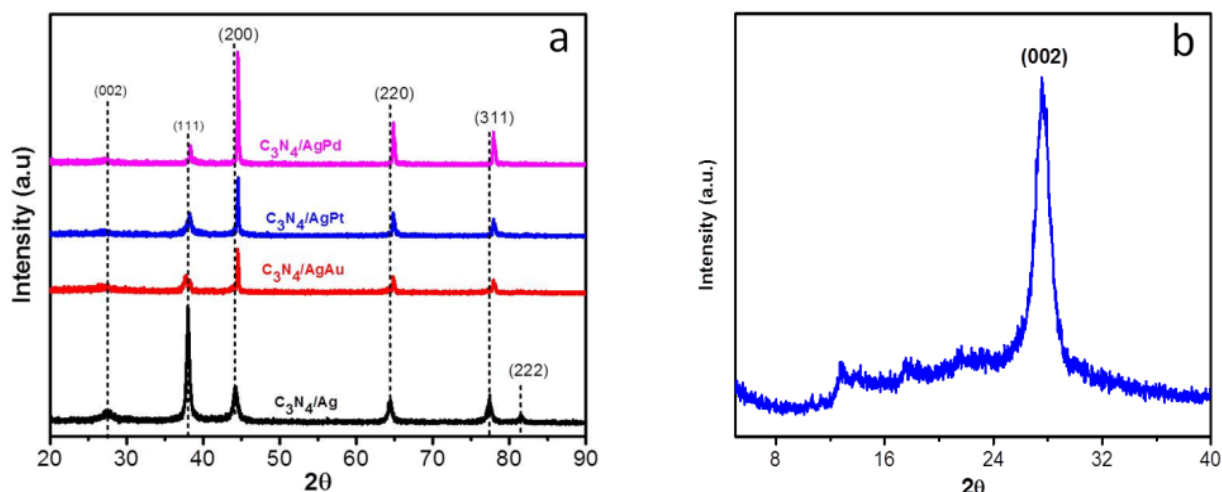
Figure 3.1: Powder X-ray diffraction patterns of (a) C_3N_4/Ag, C_3N_4/AgPd, C_3N_4/AgPt, and C_3N_4/AgAu and (b) C_3N_4 powder only

stretching vibration, while the peaks at 1411, 1322, and 1245 cm^{-1} represents aromatic C=N stretching vibration modes. The out-of-plane bending vibration of heptazine rings represents intense band at 809 cm^{-1}. A clear shift in the stretching frequency values are observed in the presence of metal NPs on C_3N_4 surface. C=N and C–N stretching vibration values are shifted
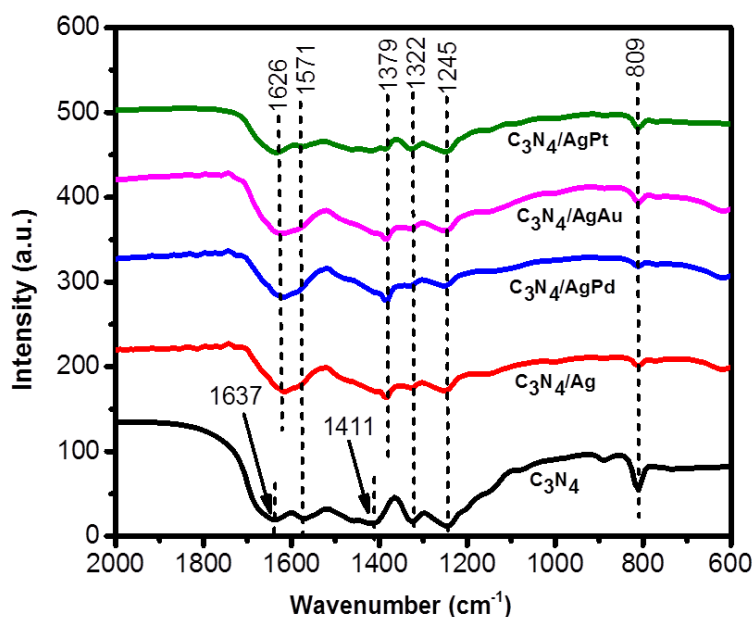
Figure 3.2. FTIR of C_3N_4, C_3N_4/Ag, C_3N_4/AgPd, C_3N_4/AgAu and C_3N_4/AgPt

from 1637 cm^{-1} to 1617.5 cm^{-1} and 1411 cm^{-1} to 1382 cm^{-1}, respectively. Shifting of stretching vibration values clearly indicates the presence of metals on C_3N_4 surface.

3.3.3. X-ray photoelectron spectroscopy analysis

Surface chemical property and oxidation state of the as-prepared metal NPs on C_3N_4 surface are confirmed by X-ray photoelectron spectroscopy. In case of C_3N_4/AgPd, successful formation of Ag and Pd NPs are observed and their oxidation state is shown in Figure 3.3. It can be seen from
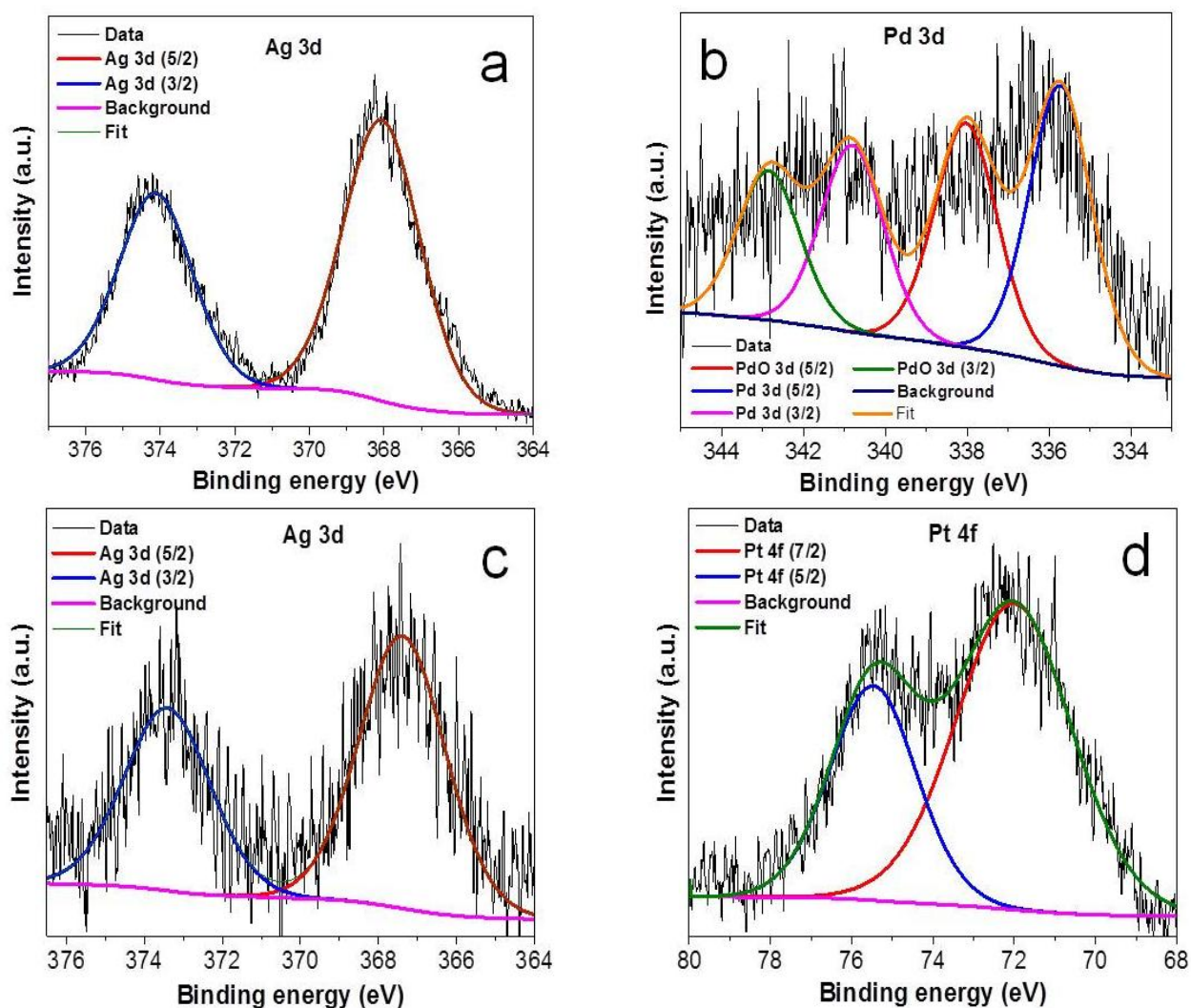
Figure 3.3: High-resolution deconvoluted XPS analysis of (a) Ag, (b) Pd, (c) Ag, and (d) Pt NPs on C$_3$N$_4$ surface

Figure 3.3a that the binding energies at 368.05 and 374.11 eV for $3d_{5/2}$ and $3d_{3/2}$ of Ag(0), respectively. Whereas, for Pd the binding energies are 340.80 and 335.71 eV for $3d_{3/2}$ and $3d_{5/2}$, respectively, shown in Figure 3.3b. It can be seen from the deconvoluted Pd 3d binding energy spectrum that a spin orbit splitting of ~ 5.1 eV, which confirms the formation of metallic Pd NPs. Whereas, the other two doublets positioned at 338.02 and 342.84 eV can be ascribed for Pd(I) oxidation state, which represents partial oxidation of Pd surface. During the synthesis of Pd NP using C_3N_4 quantum dots, similar oxidation of Pd NP has also been observed by our group. [34] Both the binding energies for Ag and Pd represents the formation of Ag(0) and Pd(0) NP, which is well matched with literature reported value. [36] Similarly, for C_3N_4/AgPt, deconvoluted binding energies for Ag(0) is observed at 367.4 and 373.4 eV for $3d_{5/2}$ and $3d_{3/2}$ and the binding energies are 72.0 and 75.4 eV for $4f_{7/2}$ and $4f_{5/2}$ respectively, which indicates the formation of Pt(0), shown in Figure 3.3c and d. The spin orbit splitting of 3.4 eV has been observed for Pt(0) oxidation state. However, for C_3N_4/AgAu, $4f_{5/2}$ and $4f_{7/2}$ of Au(0) are seen at 88 and 84 eV, respectively, shown in Figure 3.4. All the binding energy values for Ag, Pt, and Au are well acquainted with literature reported values. [34, 36] Survey spectrum of AgPt, AgPd, and AgAu (Figure 3.5 a, b, and c) shows peaks at 284.5, 398.61, and 532.91 eV, which is attributed to C1s, N1s, and O1s, respectively. Presence of C_3N_4 in case of all the bimetallic NPs is also confirmed from C1s, N1s, and O1s peaks.
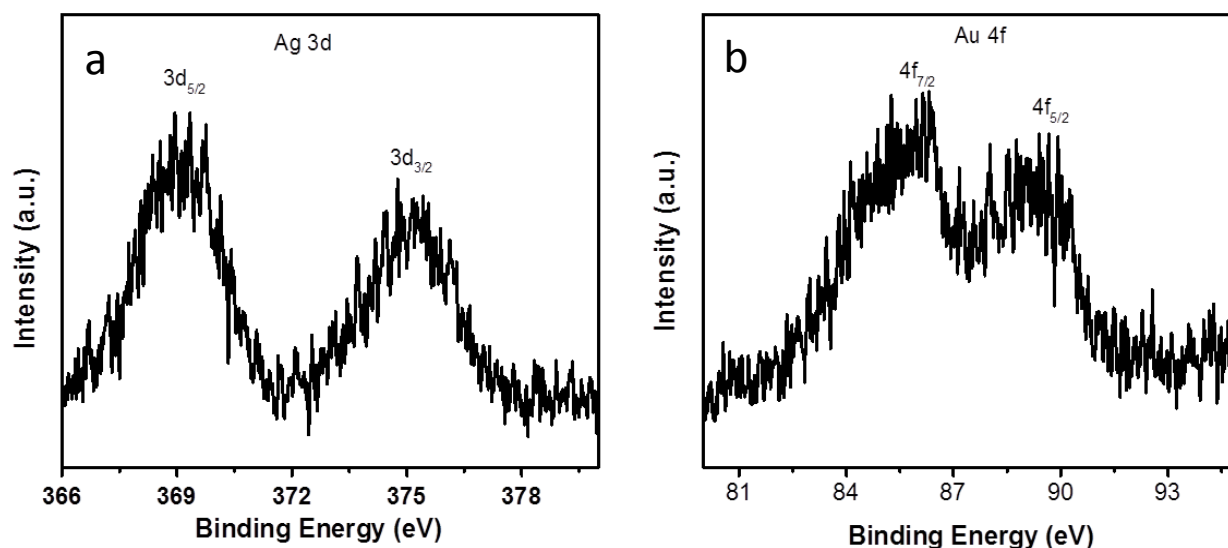
Figure 3.4: XPS of (a) Ag 3d and (b) Au 4f in C_3N_4/AgAu NP
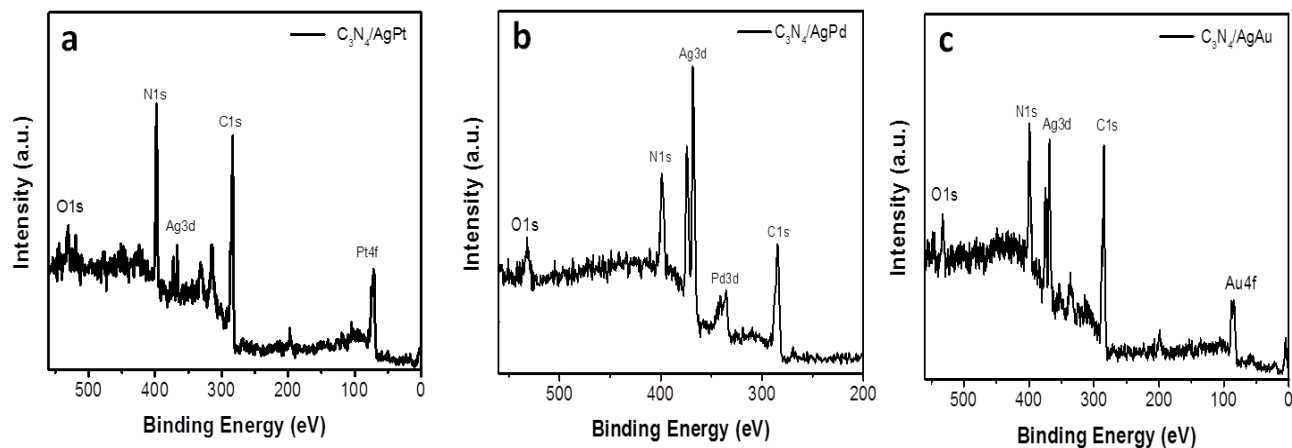
Figure 3.5: Survey spectrum of (a) C₃N₄/AgPt (b) C₃N₄/AgPd and (c) C₃N₄/AgAu NPs

3.3.4. Field emission scanning electron microscopy analysis

To determine the surface morphology of AgPd, AgPt, and AgAu on C_3N_4 surface FESEM analysis were performed. Figure 3.6a represents FESEM image of AgPd NPs, which shows uniform and narrow particle distribution with spherical shape. It can be seen from Figure 3.6b that spherical AgPt bimetallic nanoparticle distributed homogeneously and narrow particle size. Whereas, AgAu also follow the same distribution, which is shown in Figure 3.6c. Therefore, FESEM analysis confirms the consistent distribution and spherical nature of AgPd, AgPt, and AgAu bimetallic NPs on C_3N_4 surface.
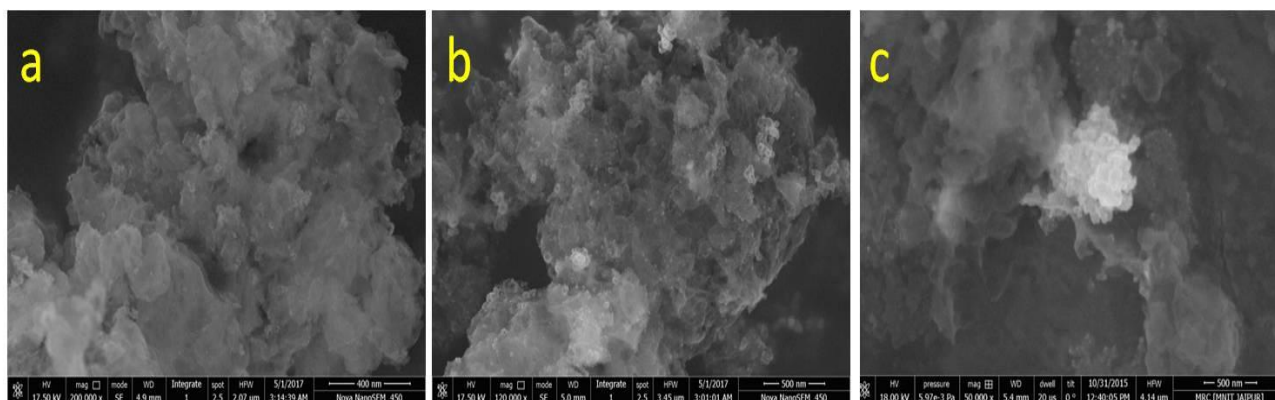
Figure 3.6: FESEM images of (a) C₃N₄/AgPd , (b) C₃N₄/AgPt and (c) C₃N₄/AgAu bimetallic NPs

3.3.5. Transmission electron microscopy analysis

To have a clear idea of the morphology of as-prepared bimetallic NP via galvanic exchange, TEM and HRTEM analysis was performed. TEM image of C_3N_4/Ag exhibits spherical shape and
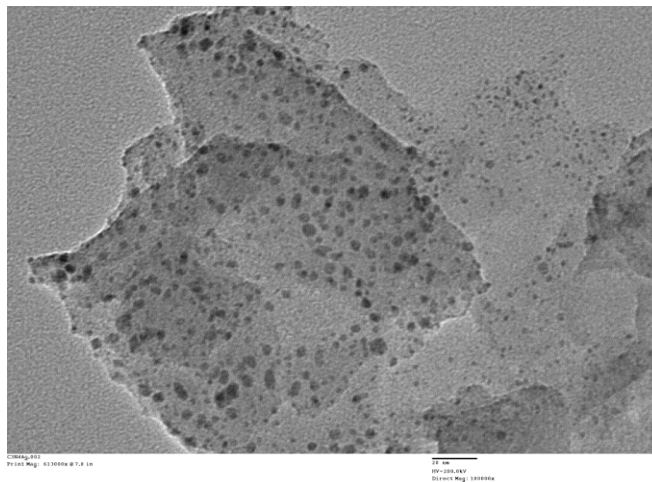
Figure 3.7: TEM image of C_3N_4/Ag

6 ± 2 nm particle size distribution, shown in Figure 3.7. All the Ag particles are distributed homogeneously on C_3N_4 surface. Figure 3.8 shows the TEM image of hollow spherical shaped AgPd nanoparticles on C_3N_4 surface with size distribution of 18 ± 3 nm. Inset of Figure 3.8a shows a high resolution TEM image, which confirms the formation of hollow structure. High resolution TEM image of C_3N_4/AgPd is shown in Figure 3.8b depicting lattice fringes of AgPd
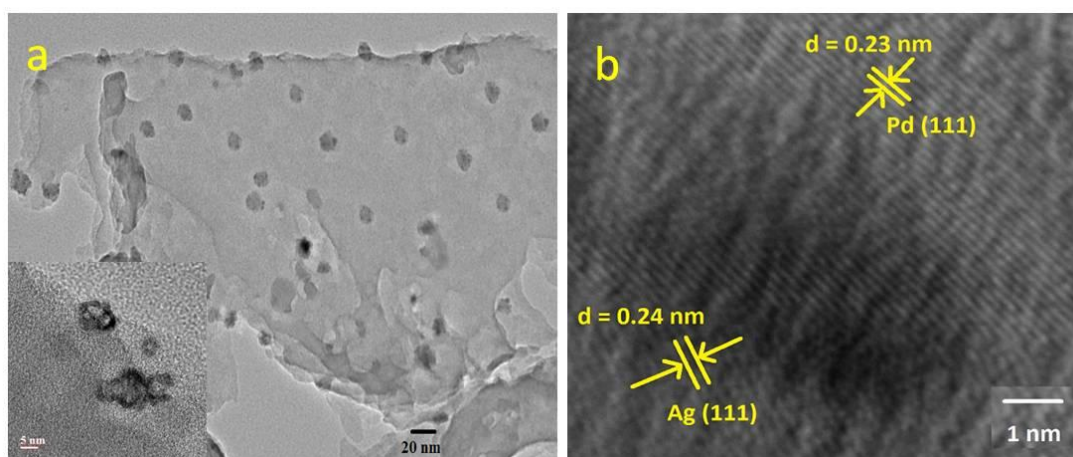
Figure 3.8: Representation of (a) TEM and (b) HRTEM image of C_3N_4/AgPd. HRTEM image shows the d-spacing calculation for Ag and Pd NPs

NPs. It can be seen from Figure 3.8b that the interplaner spacing 'd' = 0.21 nm corresponds to (111) plane of Ag and 'd'= 0.23 nm corroborates with (111) plane of Pd. Plain view TEM and HRTEM of C_3N_4/AgPt are shown in Figure 3.9a and b. AgPt particle shows hollow and spherical nature with size 9±4 nm. High resolution TEM image (inset of Figure 3.9a) of AgPt alloy
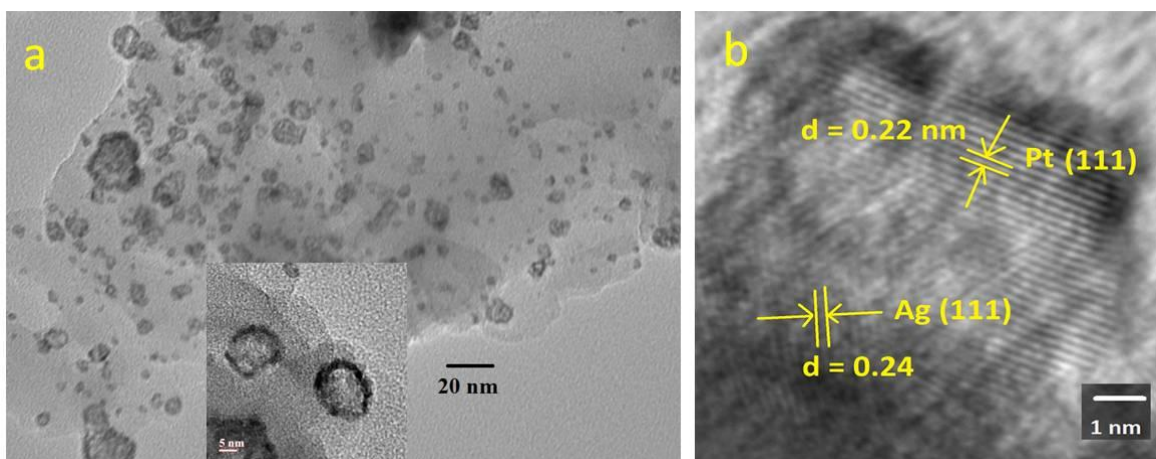
Figure 3.9: Representation of (a) TEM and (b) HRTEM image of C_3N_4/AgPt. HRTEM image exhibits the d-spacing calculation for Ag and Pt particles

particle further confirms hollow structure. HRTEM image of C_3N_4/AgPt is also having 'd' = 0.23 nm, which corresponds to (111) plane of Ag and 'd' = 0.22 nm for (111) plane of Pt. TEM images of AgPd and AgPt are well matched with FESEM analysis. In case of C_3N_4/AgAu, spherical particle is observed with 14 ± 4 nm size distribution. Hollow structure of AgAu is also observed in HRTEM analysis, shown in inset of Figure 3.10a. HRTEM confirms the 'd' spacing values for both Ag and Au, which appears at 0.23 nm and 0.22 nm for (111) plane, which is shown in Figure 3.10b. Similar hollow structures of mono- and bimetallic NPs have been reported by many scientist. [24, 25, 36-38] Lee and co-workers reported the synthesis of hollow Ag-Pt nanoplates via galvanic displacement. [24] Synthesis of hollow Pt nanocatalyst via galvanic exchange has been reported by Bhargava and co-workers. [25] Xia and co-workers also reported hollow structure of noble metal NP (Au, Pd, and Pt) via galvanic replacement method. [37-39]
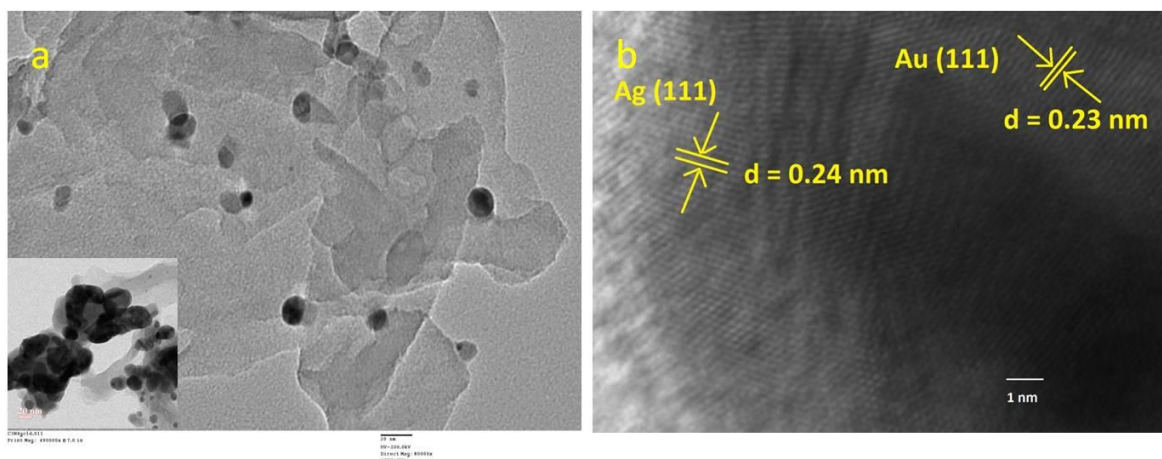
Figure 3.10: Representation of (a) TEM and (b) HRTEM image of C$_3$N$_4$/AgAu. HRTEM image exhibits the d-spacing calculation for Ag and Au particles

3.3.5.1. TEM-EDS mapping

TEM-EDS mapping (line and point) analysis of AgPd, AgPt, and AgAu heterostructure on C$_3$N$_4$ surface were performed to confirm the formation of alloy structure. Line mapping of hollow C$_3$N$_4$/AgPd NP shows the presence of both Ag and Pd line uniformly (Figure 3.11). Three points were chosen randomly in three different places in a hollow structure of AgPd and observed that
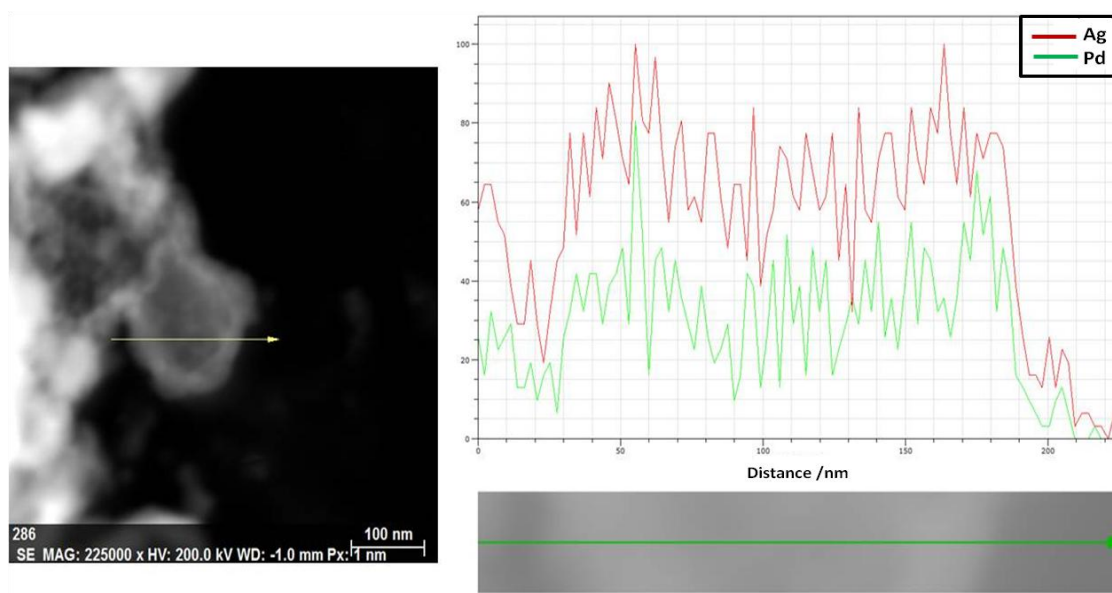
Figure 3.11: EDS Line mapping of C$_3$N$_4$/AgPd

the presence of Ag and Pd is uniform throughout the particle. Uniform distribution of Ag and Pd confirms the formation of alloy structure excluding core-shell or physical mixture. All the marked bright field STEM images and their corresponding EDS spectrum for C_3N_4/AgPd is C_3N_4/AgPt also shows uniform distribution of Ag and Pt NPs, as shown in Figure 3.13 and 3.14. Furthermore, for C_3N_4/AgAu, similar phenomena was observed (Figure 3.15 and 3.16). Therefore, alloy structure formation of AgPd, AgPt, and AgAu on C_3N_4 surface was finalized from TEM-EDS analysis.
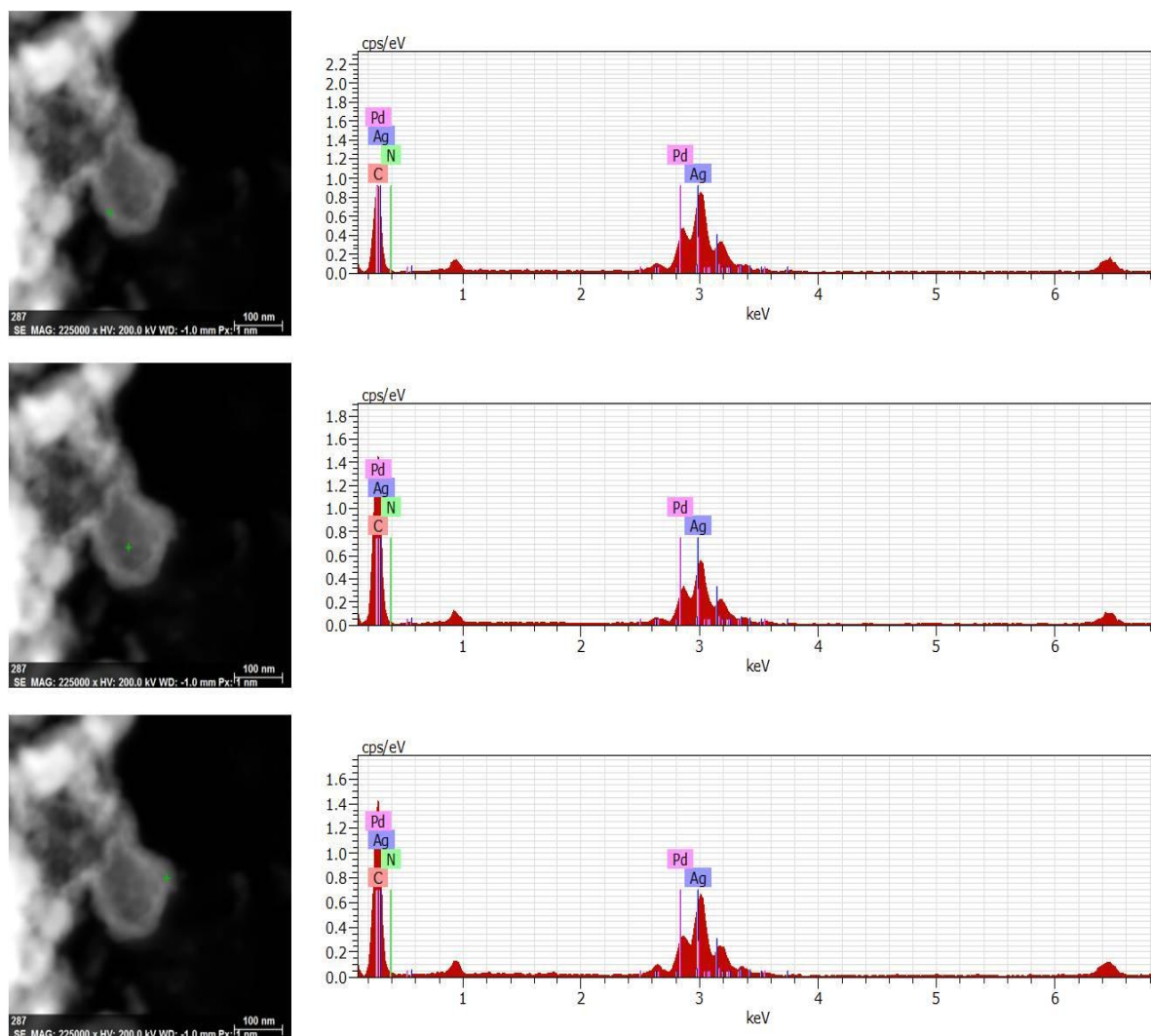
Figure 3.12: EDS Point mapping of C_3N_4/AgPd
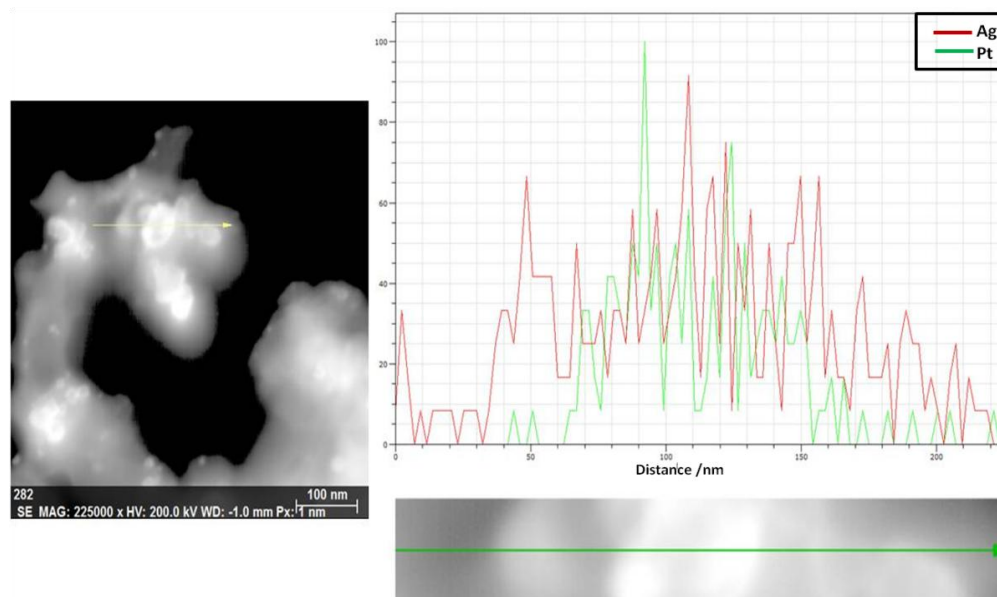
Figure 3.13: EDS Line mapping of C₃N₄/AgPt
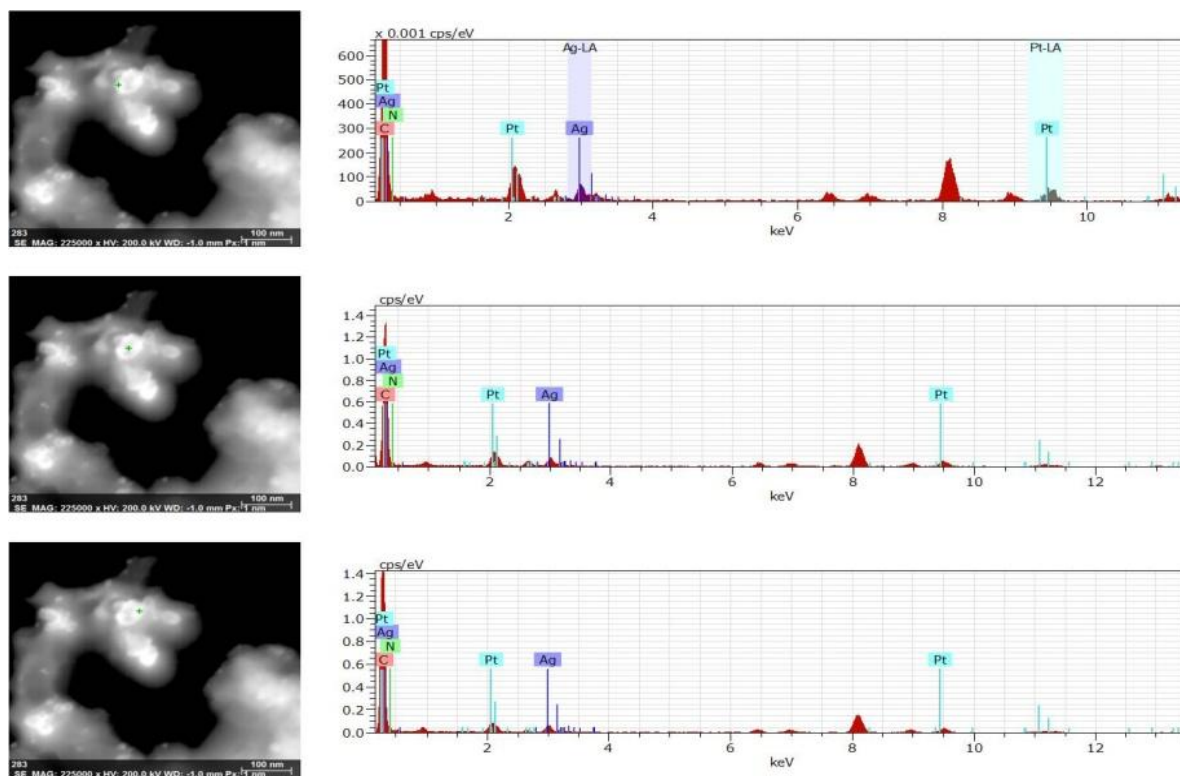
Figure 3.14: EDS point mapping of C₃N₄/AgPt
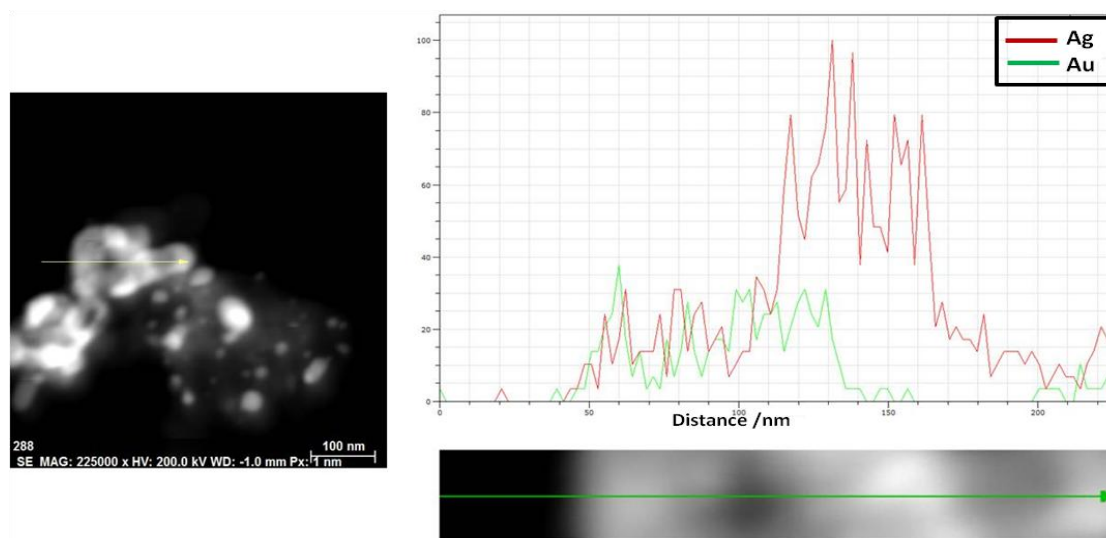
Figure 3.15: Line mapping of C₃N₄/AgAu
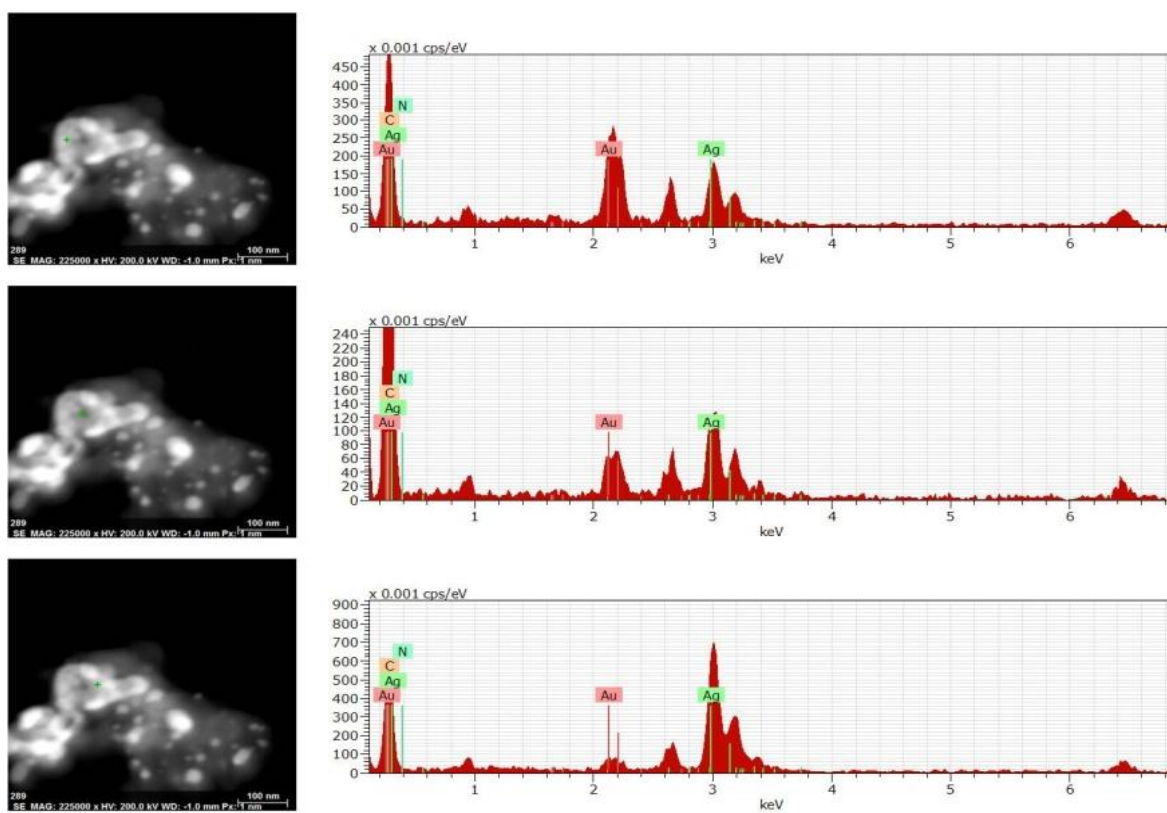
Figure 3.16: EDS point mapping of C3N4/AgAu

71

3.4. Mechanism of formation of bimetallic NPs on C_3N_4 Surface

The mechanism of formation of bimetallic NP on C_3N_4 surface are discussed herewith. Initially, Ag NP formation occurs via simple reduction technique using $NaBH_4$ as a reducing agent. C_3N_4 was sonicated for 0.5 h to get a dispersed solution and then $AgNO_3$ was added to it and reduced with $NaBH_4$. After that C_3N_4/Ag NP was washed thoroughly to remove impurities and dried in air for further use. Ag NP was distributed homogeneously throughout the C_3N_4 surface, which is confirmed from Figure 3.7. The Ag NP formation reaction using reducing agent is shown below (equation 1). 5.0 mg of C_3N_4/Ag was used for galvanic exchange reaction with K_2PdCl_4, K_2PtCl_4, and $HAuCl_4$ precursors to produce AgPd, AgPt, and AgAu bimetallic combinations on C_3N_4 surface. During galvanic exchange reaction 2.0 mL of 10^{-2} M aqueous metal precursor solution was used directly without any further dilution. Immediately, color change was observed from brownish to grayish black, and light blue, which is due to the formation of Pd(0), Pt(0), and Au(0) on already formed Ag(0), respectively. The reduction potential values are, $E^0_{Ag+/Ag} = 0.78$ V, $E^0_{Pd2+/Pd} = 0.83$ V, $E^0_{Pt2+/Pt} = 1.2$ V, and $E^0_{Au3+/Au} = 1.5$ V vs. NHE, which favors the formation of alloy particle with Ag. Galvanic exchange is simply a redox reaction, metals having low reduction potentials are subjected to oxidize and metals having high reduction potential undergoes reduction and subsequent deposition. The galvanically exchanged materials are interested because of change in the number of surface atoms. The change in surface atoms drastically change their optical, electrical, mechanical, and catalytic properties. [40-44] As the reduction potential value of Pd^{2+}/Pd, Pt^{2+}/Pt, and Au^{3+}/Au systems is higher than Ag^+/Ag system, therefore, Ag(0) will oxidize and metal ions (Pd^{2+}, Pt^{2+}, and Au^{3+}) will reduce to zero oxidation state. For the formation of every Pd and Pt atoms two Ag^+ ions were replaced, whereas, for every Au atom three Ag^+ ions were replaced via galvanic exchange. However, due to presence of solid C_3N_4 substrate the galvanic exchange reaction is not stoichiometric and added precursor salts slowly reacted with prepared Ag NP, which results in the formation of bimetallic NP. The presence of Ag(0) confirmed from XRD, XPS, HRTEM, and EDS mapping analysis. Finally, the synthesized C_3N_4/AgPd, C_3N_4/AgPt, and C_3N_4/AgAu materials were washed thoroughly with NH_4OH to remove AgCl. So, in this process no AgCl is present after galvanic exchange reaction on catalyst surface. The absence of AgCl was also confirmed from XPS analysis. Lee and co-workers reported the synthesis of Ag-Pt nanoplates with shape-dependent Pt particle, where, Pt^{2+} ions reacted slowly with synthesized Ag nanoplates results in the formation of Ag-Pt bimetallic

Chapter 3

NP. [24] Bhargava and co-workers also mentioned complete replacement of initial material (here it is Ag) is generally not achieved via galvanic replacement reaction during the synthesis of Ag/Pt bimetallic NP. [25] The formation of AgPd, AgPt, and AgAu on C_3N_4 surface via galvanic exchange reaction is shown below.

$$C_3N_4 + Ag^+ + NaBH_4 \longrightarrow C_3N_4/Ag \tag{1}$$

$$C_3N_4/Ag_{(s)} + PdCl_4^-{}_{(sol)} \longrightarrow C_3N_4/AgPd_{(s)} + Ag^+{}_{(sol)} + 4Cl^- \tag{2}$$

$$C_3N_4/Ag_{(s)} + PtCl_4^-{}_{(sol)} \longrightarrow C_3N_4/AgPt_{(s)} + Ag^+{}_{(sol)} + 4Cl^- \tag{3}$$

$$C_3N_4/Ag_{(s)} + AuCl_4^-{}_{(sol)} \longrightarrow C_3N_4/AgAu_{(s)} + Ag^+{}_{(sol)} + 4Cl^- \tag{4}$$

3.5. Application in hydrogen evolution reactions

Before doing hydrogen evolution reaction the working electrode was prepared, 1.0 mg catalyst (C_3N_4/AgPd, C_3N_4/AgPt, and C_3N_4/AgAu) and 20.0 µL of 5 wt % nafion solution was dispersed in 100.0 µL of isopropyl alcohol via sonication for 30 min to get a homogeneous suspension. After that, 3.0 µL catalyst suspension was drop casted onto a glassy carbon electrode (3 mm in diameter) and dried in air. The amount of catalyst was loaded on GCE surface is ~0.352 mg/cm^2. Pt wire and Ag/AgCl were used as counter electrode and reference electrode, respectively. Prior to use, 0.3 µm and 0.05 µm alumina slurry and polishing cloth were used to polish the GCE followed by sonication in millipore water for 10 min and dried in nitrogen gas flow. Throughout the electrochemical study, 0.5 M H_2SO_4 (pH = 0.301) was used as an electrolyte. Initially, all the potentials were measured against Ag/AgCl and then converted to RHE.

3.5.1. Linear sweep voltammetry (LSV) study of C_3N_4/Ag C_3N_4/AgPd, C_3N_4/AgPt, and 5% Pt/C for hydrogen evolution reactions

The preliminary electrocatalytic activity of C_3N_4/AgPt, C_3N_4/AgPd, C_3N_4/AgAu, and C_3N_4/Ag catalysts was studied towards hydrogen evolution reaction by linear sweep voltamograme (LSV) technique. Aqueous solution of 0.5 M H_2SO_4 and 10 mV/s scan rate were used throughout the electrochemical measurements for hydrogen evolution. Initially, all the potentials are measured using Ag/AgCl reference electrode but finally reported with respect to RHE. Bare GCE and C_3N_4 show negligible response in the observed potential window. Catalytic activity of Ag decorated on C_3N_4 was checked and C_3N_4/Ag exhibits very low activity towards hydrogen evolution reaction.

73

Ag nanoparticle decorated on C_3N_4 requires -508 mV potential to achieve current density of 10 mA/cm^2. Cathodic polarization curves shown in Figure 3.17a exhibits remarkable increase in current densities in case of C_3N_4/AgPt, AgPd, and AgAu with successive anodic shift in the onset potential. Amongst all, C_3N_4/AgPt shows efficient catalytic activity towards HER. It requires only -150 mV to generate 10 mA/cm^2 current density whereas, C_3N_4/AgPd, and C_3N_4/AgAu require -308, and -424 mV potential (Figure 3.17b). To check the extent of efficiency of C_3N_4/AgPt in HER reaction, 5% Pt/C was used. Figure 3.17b shows that for 5%
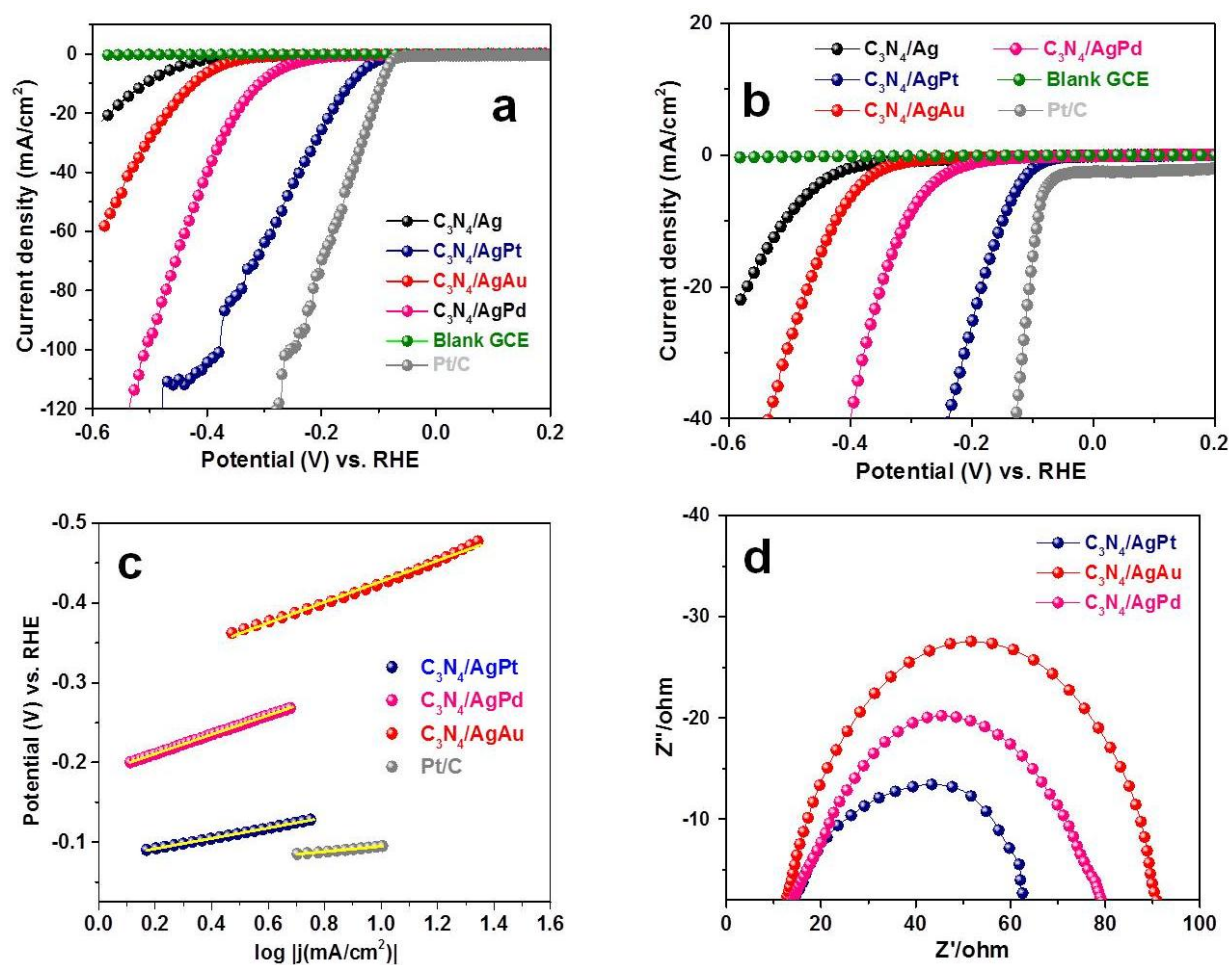
Figure 3.17: Linear sweep voltammogram curve of bare (a) GCE, C_3N_4, C_3N_4/Ag, C_3N_4/AgPd, AgPt, AgAu, and 5% Pt/C in high scale and (b) low-scale for hydrogen evolution reactions. (c)Tafel slope values for C_3N_4/AgPd, AgPt, AgAu, and 5% Pt/C and (d) electrochemical impedance measurement plot for AgPd, AgPt, AgAu catalyst on C_3N_4 surface

74

Pt/C only -94 mV potential is required to achieve 10 mA/cm^2 current density. To prove the higher activity of all the catalyst material mass activity has also been calculated at -0.25 V. It can be seen from Table 3.1 that the mass activity of C$_3$N$_4$/AgPt shows 125.21 A/g, whereas, AgPd and AgAu exhibits 9.57 and 1.44 A/g, respectively. Higher mass activity favours higher catalytic activity of AgPt. Therefore, the following activity order is observed towards hydrogen evolution 5% Pt/C>C$_3$N$_4$/AgPt>C$_3$N$_4$/AgPd>C$_3$N$_4$/AgAu. From TEM analysis it is clearly observed that AgPt, AgPd and AgAu have the hollow structure. In case of hollow C$_3$N$_4$/AgPt, the active sites of the catalyst are more exposed to electrolyte and enhanced the electrocatalytic activity. The presence of Ag in bimetallic NP was confirmed by XRD, XPS, HRTEM, and EDS mapping analysis. The presence of Ag in C$_3$N$_4$/AgPt sample was also confirmed from cyclic voltammetry (CV) analysis performed in 0.5 M H$_2$SO$_4$ (Figure 3.18) following a Ag stripping peak appeared at 0.5 V (vs. Ag/AgCl).

Table 3.1. Loading amount, overpotential, mass activity, and Tafel slope for C$_3$N$_4$/AgPt, AgPd, and AgAu catalyst

Cathode	Loading amount (mg/cm^2)	Overpotential required to generate 10 mA/cm^2	Mass activity (A/g) at -0.25 V	Tafel slope (mV/dec)
C$_3$N$_4$/AgPt	0.352	- 0.1503 V	125.21	65
C$_3$N$_4$/AgPd	0.352	- 0.308 V	9.57	120
C$_3$N$_4$/AgAu	0.352	- 0.424 V	1.44	130
5% Pt/C	0.352	- 0.094 V	285.08	33

Furthermore, it can be seen from Figure 3.18 that, hydrogen adsorption/desorption region also prominent in AgPt sample. Bhargava and co-workers also reported similar Ag stripping peak using CV analysis in case of hollow Pt nanocatalyst synthesized by galvanic exchange. [25] All the electrochemical data, catalyst loading, overpotential at 10 mA/cm^2, mass activity, and Tafel slope values for C$_3$N$_4$/AgPt, C$_3$N$_4$/AgPd, C$_3$N$_4$/AgAu, and 5% Pt/C are shown in Table 3.1. To have a clear
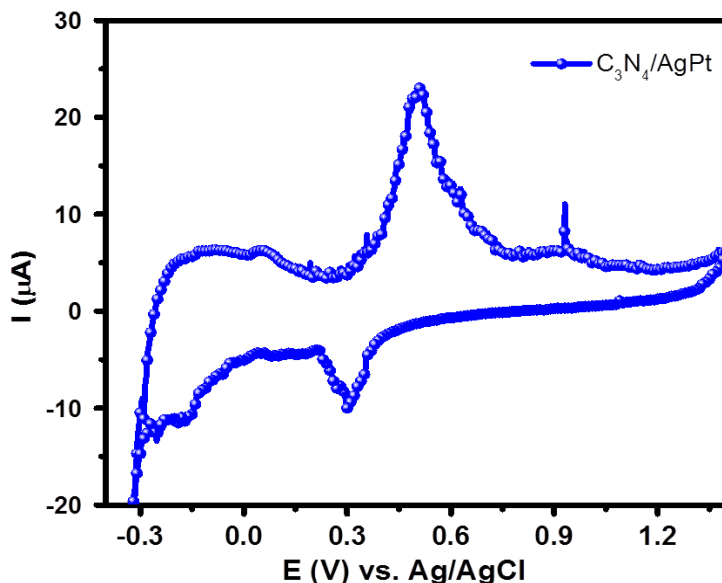
Figure 3.18: CV of C₃N₄/AgPt in 0.5 M H₂SO₄

understanding for the superior catalytic activity of C_3N_4/AgPt synthesized by galvanic exchange method, AgPt bimetallic NPs were also synthesized on C_3N_4 surface via co-reduction technique. Co-reduction technique was followed by mixing of 5.0 mg C_3N_4, 20.0 μL of 1 M AgNO₃, and 2.0 ml of 10^{-2} M K₂PtCl₄ in a reaction vessel. The concentration of Ag and Pt in C_3N_4/AgPt via co-reduction technique are exactly same as C_3N_4/AgPt synthesized via galvanic exchange. Finally, the reaction mixture was treated with 1.0 mL of 1 M NaBH₄ and stirred for complete reduction. The product was washed with water followed by ethanol for electrocatalytic study and confirmed by XRD analysis, shown in Figure 3.19. To confirm the formation of AgPt nanoalloy via co-reduction technique on C_3N_4 surface TEM and EDS analysis were also performed. It can be seen from Figure 3.20 that the particles are spherical in shape and average particle size is 8±2 nm. The presence of (111) plane of both Pt and Ag is confirmed from HRTEM analysis. The composition of Ag and Pt is confirmed from EDS analysis, which shows ~1:1 wt% ratio of Ag:Pt in C_3N_4/AgPt alloy via co-reduction method (Figure 3.21). Remarkable shift in onset potential of C_3N_4/AgPt (galvanic exchange) as compared to C_3N_4/AgPt (co-reduction) was observed (Figure 3.22). C_3N_4/AgPt (galvanic exchange) generates 10 mA/cm² current density upon -150 mV applied potential, while, C_3N_4/AgPt (co-reduction) requires -187 mV. The higher activity
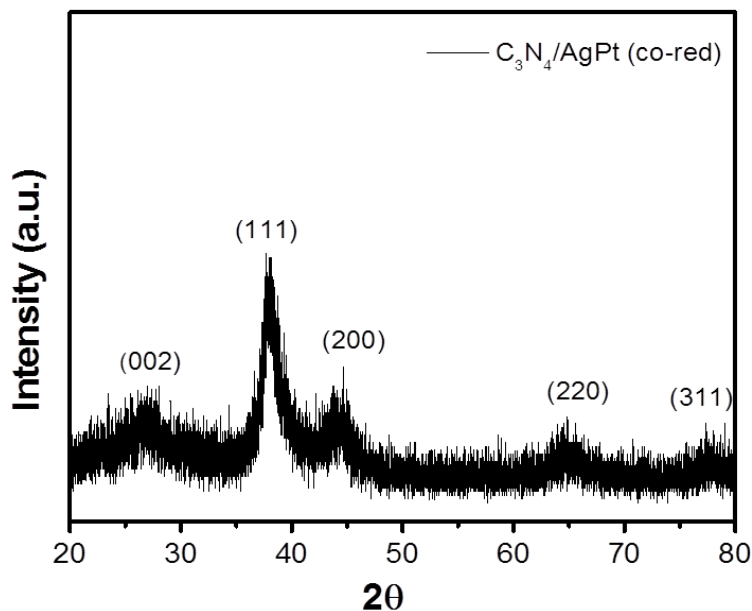
Figure 3.19: PXRD of C₃N₄/AgPt (co-red)
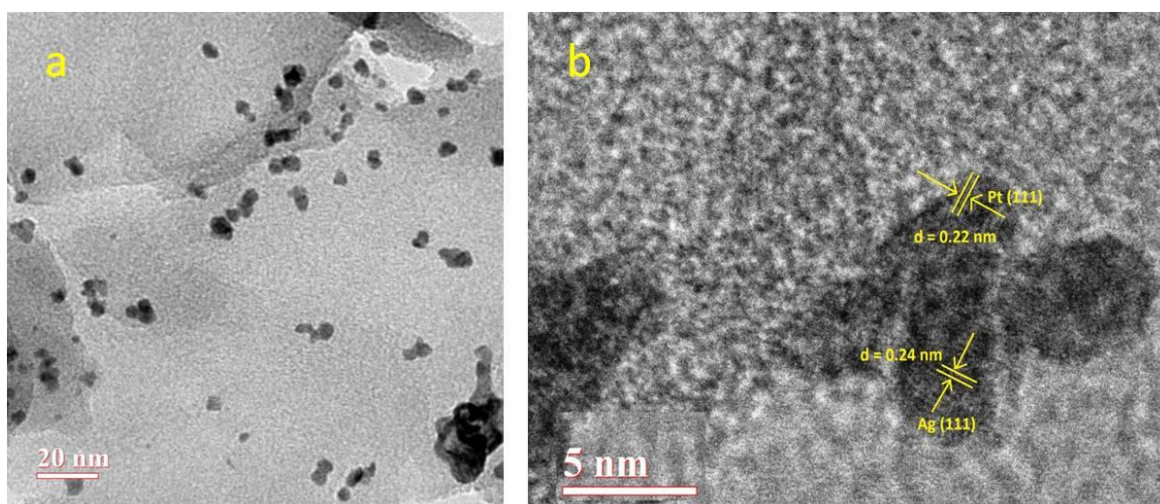
Figure 3.20: Representation of (a)TEM and (b) HRTEM images of C₃N₄/AgPt (co-red)

of C_3N_4/AgPt (galvanic exchange) is presumably due to the hollow structure (Figure 3.9a), which is helpful to penetrate the electrolyte smoothly onto the catalyst surface. Therefore, C_3N_4/AgPt (galvanic exchange) can generate higher current density upon low applied potential. The role of C_3N_4 substrate is very important for enhanced hydrogen evolution activity. There are

El	AN	Series	[wt.%]
Ag	47	L-series	1.72
Pt	78	L-series	1.52
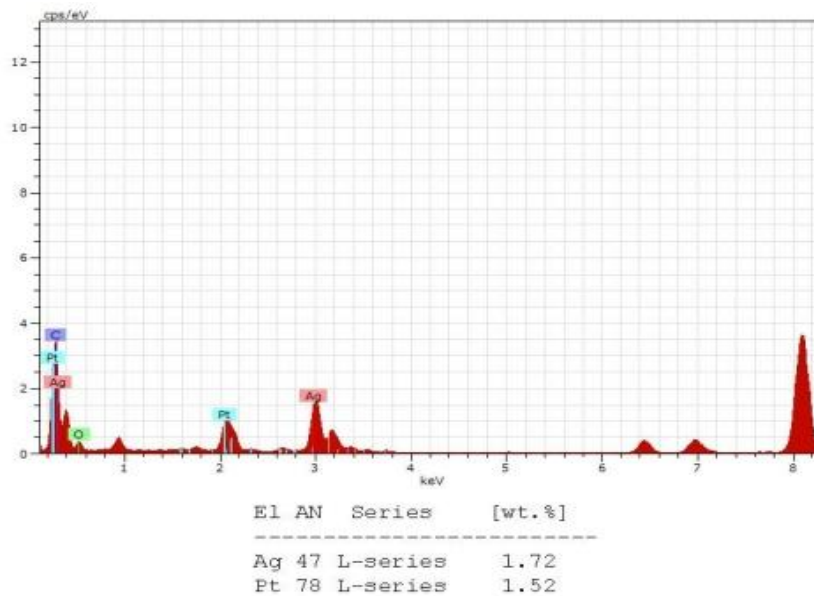
Figure 3.21: EDS spectrum of C$_3$N$_4$/AgPt (co-red)
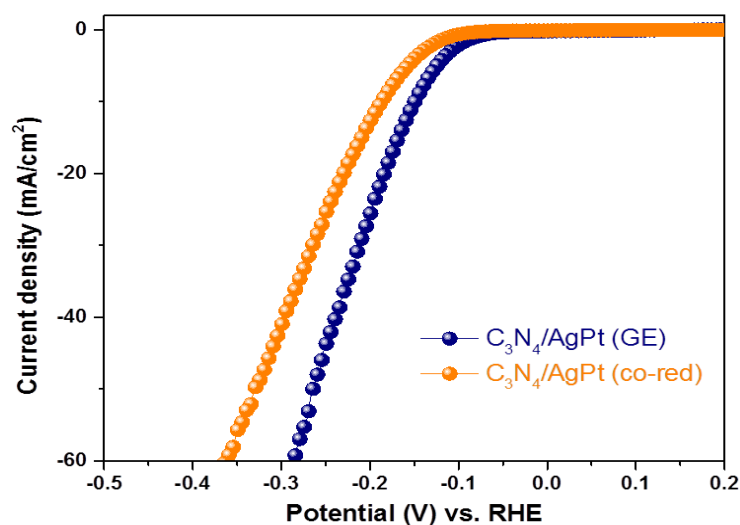
Figure 3.22: LSV Comparative study of C$_3$N$_4$/AgPt (GE) and C$_3$N$_4$/AgPt (co-red) after 1000 cycles

many advantages for C$_3$N$_4$ substrate. First, form the point of morphology, these interconnected sheet like structure of C$_3$N$_4$ are helpful for electronic transportation. Such an enhancement may

be due to the ready penetration of the electrolyte in the porous sheet like structure which get saturated with time. Second, conducting nature of C_3N_4 helps for faster electronic transportation which results in higher electrocatalytic activity of the material. Third, change in Fermi energy level of Pt, Pd, and Au metal NPs may occur. However, the change in energy level presumably due to the electronic movement between NP and support resulting from the difference in chemical potential. Carbon nanotube (multi walled) and carbon nanopowder were also used to synthesize AgPt catalyst and compare the electrocatalytic activity with C_3N_4 substrate. For the synthesis of AgPt catalyst on CNT and carbon nanopowder substrate similar galvanic exchange method was followed. It can be seen from Figure 3.23 that the presence of (200), (111), (220), and (311) planes confirms the formation of AgPt on CNT and carbon surface.
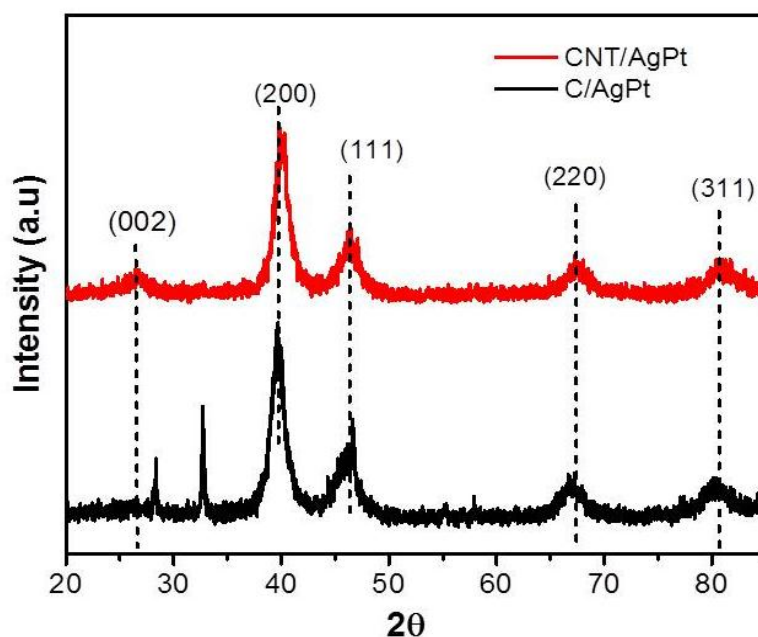
Figure 3.23: PXRD of CNT/AgPt and C/AgPt

The LSV curve for HER activity using CNT/AgPt and C/AgPt is shown in Figure 3.24. Based on our experimental observations the required potential for CNT/AgPt and C/AgPt are 128 mV and 188 mV, respectively, to generate 10 mA/cm^2 current density. However, C_3N_4/AgPt produce 10 mA/cm^2 upon application of 150 mV potential. Therefore, for hydrogen evolution, C_3N_4 obviously a better substrate than carbon nanopowder but slightly less reactive as compared to CNT, which may be due to less electrochemical conductivity of C_3N_4 than multi walled CNT. To

check the stability of $C_3N_4/AgPt$, $C_3N_4/AgPd$, and $C_3N_4/AgAu$ hydrogen evolution reaction was checked up to 1000 cycle in 0.5 M H_2SO_4 solution (Figure 3.25 a, b, and c). There is no significant change in current density and onset potential as well. Therefore, it can be concluded that $C_3N_4/AgPt$, AgPd, and AgAu samples are very stable in acid electrolyte. Morphology of $C_3N_4/AgPt$ NPs was checked using SEM analysis after 1000 run of electrocatalysis, which is shown in Figure 3.26. The morphology of AgPt paprticle is same as it was before electrocatalysis.
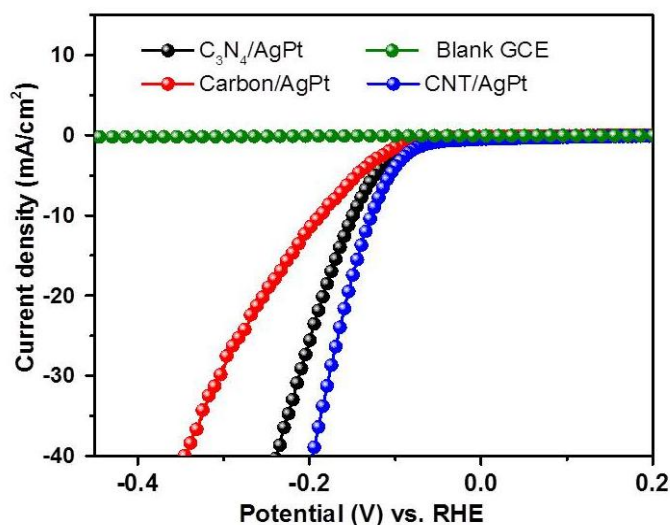
Figure 3.24: Comparative LSV analysis of CNT/AgPt, C/AgPt, C_3N_4/AgPt, and blank GCE
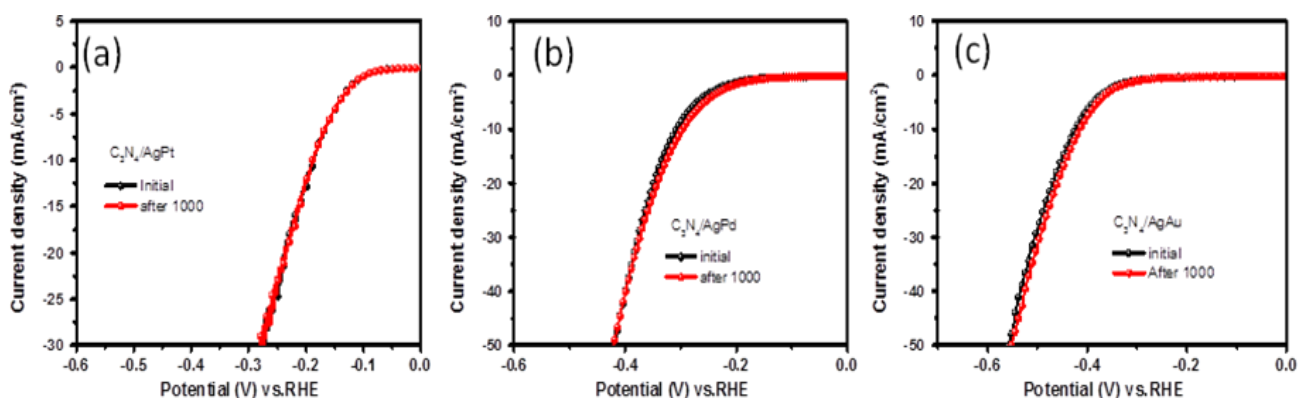
Figure 3.25: LSV of initial and after 1000 cycle of (a) C_3N_4/AgPt (b) C_3N_4/AgPd and (c) C_3N_4/AgAu catalyst

3.5.2. Mechanism of HER

Hydrogen evolution reaction follows two step process. The first step of hydrogen evolution is the Volmer or discharge reaction, where, an electron is coupled to the absorb proton in a vacant site
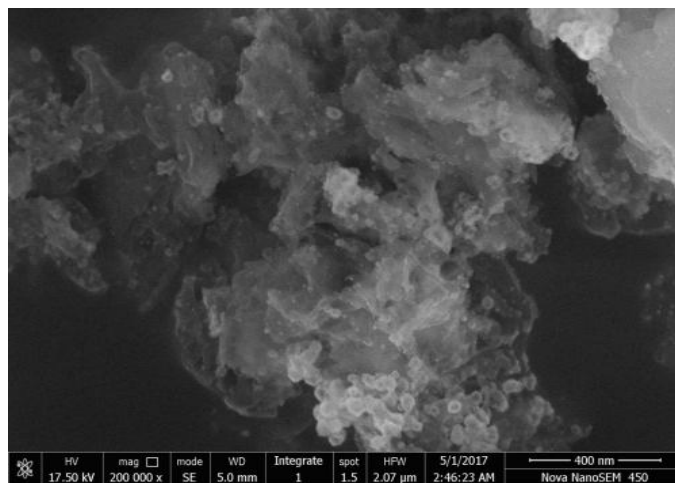
Figure 3.26: FESEM image of C_3N_4/AgPt after electrocatalysis

of the catalyst to yield an absorbed hydrogen atom. The second step of hydrogen evolution is may be either Heyrovsky step (desorption reaction) or Tafel step (combination). The first possibility is transfer of a second electron to the already absorbed hydrogen atom with simultaneously coupling of another proton from the solution to evolve hydrogen gas. The second possibility is already absorbed two hydrogen atoms can combine on the electrode surface to produce hydrogen gas. In the third step of hydrogen evolution the mechanism and rate determining step is studied by the Tafel slope, which is known as Tafel or combination reaction. Tafel slope is also useful to determine the effectiveness of a catalyst. In order to calculate the tafel slope the linear portion of the Tafel plots is to be fitted in the Tafel equation (η = b log (j)+ a, where η = overpotential, b and a = Tafel slope, and j = current density). [45] In this study, Tafel slope value for C_3N_4/AgPt (galvanic exchange) is 65 mV/dec, suggesting that discharge reaction is fast and H_2 is evolved by a rate determining Volmer-Heyrovsky reaction with Heyrovsky as rate determining step, shown in Figure 3.17c. Whereas, the Tafel slope value for C_3N_4/AgPt (co-red) is 112 mV/dec (Figure 3.27), which is less active than C_3N_4/AgPt *via* galvanic exchange. The Tafel slope value of 5% Pt/C is 33 mV/dec, which is well matched with literature reported value. [46,47] However, Tafel slope values for C_3N_4/AgPd and C_3N_4/AgAu

are 120 and 130 mV/dec (Figure 3.17c), respectively, indicating the discharge reaction is slow. In case of C_3N_4/AgPd and AgAu the reaction follows either Volmer-Tafel or Volmer-Heyrovsky mechanism but Volmer step is the rate determining step. All the Tafel slope values are summarized in table 3.1. The overall hydrogen evolution reaction using C_3N_4/AgPt catalyst is shown below.

$$C_3N_4/AgPt + H_3O^+ + e^- = C_3N_4/AgPt\text{-}H_{abs} \tag{1}$$

$$C_3N_4/AgPt\text{-}H_{abs} + e^- + H_3O^+ = C_3N_4/AgPt + H_2 + H_2O \tag{2}$$

$$C_3N_4/AgPt\text{-}H_{abs} + C_3N_4/AgPt\text{-}H_{abs} = H_2 + C_3N_4/AgPt \tag{3}$$
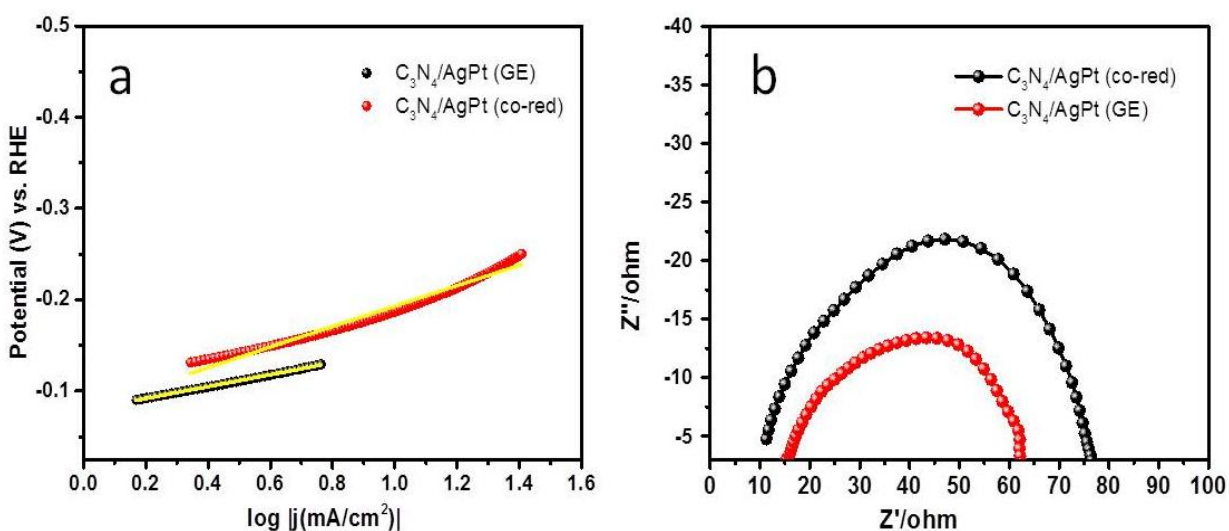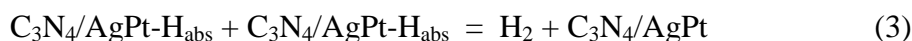
Figure 3.27: Representation of (a) Tafel plot and (b) Impedance of C_3N_4/AgPt (GE) and C_3N_4/AgPt (co-red)

Table 3.2 shows detailed comparative study of potentials required for 10 mA/cm^2 current density, catalyst loading, electrolyte, onset potentials, and Tafel slopes of our catalysts with other mono- and bi-metallic NPs. It can be seen from table 3.2 that the synthesized catalysts (C_3N_4/AgPt, C_3N_4/AgPd, and C_3N_4/AgAu) in this chapter are comparable with literature report.

3.5.3. Electrochemical impedance measurements

To study electrocatalytic activity of all the synthesized catalysts, we have carried out electrochemical impedance measurement. The semicircle represents resistance due to charge

Table 3.2: Comparative study of HER activity of reported references

Catalyst	Medium	Catalyst loading (mg/cm^2)	Onset potential in (mV)	Potential (mV) to generate 10 mAcm^{-2} current density	Tafel Slope (mV/dec)	Reference
AuPd NCs/g-C$_3$N$_4$	0.5 M H$_2$SO$_4$	0.17	- 29	-83 mV at 30 mA/cm^2	47	[35]
Ag-Pd nanoalloy (Ag/Pd = 20:80)	0.1 M H$_2$SO$_4$	-	-270	-	156	[21]
Ag/Pt nanocatalysts	0.5 M H$_2$SO$_4$	10 µL Ag/Pt NP solution	-280 (Ag/AgCl)	-	-	[25]
Ag-Pt$_{triangular}$	1 M H$_2$SO$_4$	8.33×10^{-3} mg	-230	-	-	[24]
Ultrafine Pt/Pd on MWCNTs	0.5 M H$_2$SO$_4$	-	-210	-	38	[23]
Ni-Mo nanopowder	2 M KOH	1.0	-	<100	-	[48]
C$_3$N$_4$/AgPd, AgPt, and AgAu	0.5 M H$_2$SO$_4$	0.353	-186	-308	120	This work
			-80	-150	65	
			-305	-424	130	

transfer. Evaluated data can be fitted using the equivalent circuit composed of constant phase element (CPE), solution resistance (R$_s$), and charge transfer resistance (R$_{ct}$). Nyquist impedance plots are measured for C$_3$N$_4$/AgPt, C$_3$N$_4$/AgPd and C$_3$N$_4$/AgAu at their respective onset potentials. Smaller radius of semi-circle in the Nyquist plots was observed in C$_3$N$_4$/AgPt nanomaterial functionalized electrode. Nyquist plots of C$_3$N$_4$/AgPt is shown in Figure 3.17d, which shows R$_{ct}$ = 45.44 Ω (Table 3.3) and indicates that there is easy electron transfer through C$_3$N$_4$/AgPt. A comparative Nyquist plot of C$_3$N$_4$/AgPt (galvanic exchange, R$_{ct}$ = 45.44 Ω) and C$_3$N$_4$/AgPt (co-red, R$_{ct}$ = 64.61 Ω) is shown in Figure 3.27b, which shows that the electron transfer is easier in AgPt alloy synthesized by galvanic exchange method. Charge transfer resistances of C$_3$N$_4$/AgPd and C$_3$N$_4$/AgAu are 66.27 and 77.21 Ω, respectively. The information from electrochemical impedance spectroscopy revealed that C$_3$N$_4$/AgPt functionalized electrodes

offers the least resistance to the electron transportation followed by C_3N_4/AgPd and C_3N_4/AgAu electrodes.

Table 3.3. R_{CT} values of C_3N_4/AgPd, AgPt, and AgAu NPs

Materials used	R_{CT} value (Ω)
C_3N_4/AgPd	66.27
C_3N_4/AgPt	45.44
C_3N_4/AgAu	77.81

3.6. Conclusion

In conclusion, galvanic exchange synthetic strategy was followed to synthesize bimetallic (AgPd, AgPt, and AgAu) alloy NPs on semiconducting C_3N_4 surface. For galvanic exchange method, initially, silver nanoparticles were synthesized on C_3N_4 surface via chemical reduction and then Ag NPs were galvanically exchanged for the synthesis of alloy NPs. During the formation of AgPd and AgPt alloy NP, Pd and Pt atoms replaced by two Ag^+ ions, whereas, Au atom replaced by three Ag^+ ions in galvanic exchange technique. All the synthesized materials were characterized by using various characterization techniques. C_3N_4/AgPd, AgPt, and AgAu were used for hydrogen evolution and superior activity was observed with C_3N_4/AgPt. pristine Pt (5% Pt/C) was also used to verify the superior activity of C_3N_4/AgPt. Therefore, the activity order is 5% Pt/C>C_3N_4/AgPt>C_3N_4/AgPd>C_3N_4/AgAu towards hydrogen evolution. The higher activity of AgPt was also confirmed from Tafel slope and electrochemical impedance measurement. Tafel slope values for C_3N_4/AgPt, C_3N_4/AgPd, and C_3N_4/AgAu are 65, 120, and 130 mV/dec, suggesting that in C_3N_4/AgPt discharge reaction is fast and Heyrovsky as rate determining step. Finally, nyquist plots of C_3N_4/AgPt indicates easy electron transfer on the catalyst surface. Therefore, this study leaves an avenue for the synthesis of bimetallic NPs on semiconducting surface for better efficiency in hydrogen evolution, which is demanding in present scenario.

3.7. References

[1] J. A. Turner, Science, 305 (2004) 972-974.

[2] C. G. Morales-Guio, L.-A. Stern, X. Hu, Chem. Soc. Rev., 43 (2014) 6555-6569.

[3] M. S. Dresselhaus, I.L. Thomas, Nature, 414 (2001) 332.

[4] J. A. Turner, Science, 285 (1999) 687-689.

[5] M. Shalom, D. Ressnig, X. Yang, G. Clavel, T.P. Fellinger, M. Antonietti, J. Mater. Chem. A, 3 (2015) 8171-8177.

[6] B. You, N. Jiang, M. Sheng, S. Gul, J. Yano, Y. Sun, Chem. Mater., 27 (2015) 7636-7642.

[7] J. Swaminathan, R. Subbiah, V. Singaram, ACS Catal., 6 (2016) 2222-2229.

[8] S. Cobo, J. Heidkamp, P.-A. Jacques, J. Fize, V. Fourmond, L. Guetaz, B. Jousselme, V. Ivanova, H. Dau, S. Palacin, M. Fontecave, V. Artero, Nature Mater., 11 (2012) 802.

[9] M. G. Walter, E. L. Warren, J. R. McKone, S. W. Boettcher, Q. Mi, E. A. Santori, N. S. Lewis, Chem. Rev., 110 (2010) 6446-6473.

[10] Z. Peng, H. Yang, Nano Today, 4 (2009) 143-164.

[11] N. Furuya, S. Motoo, J. Electroanal. Chem., 88 (1978) 151-160.

[12] F. Li, P. Bertoncello, I. Ciani, G. Mantovani, P.R. Unwin, Adv. Funct. Mater., 18 (2008) 1685-1693.

[13] F. Li, I. Ciani, P. Bertoncello, P.R. Unwin, J. Zhao, C.R. Bradbury, D.J. Fermin, J. Phys. Chem. C, 112 (2008) 9686-9694.

[14] D. Wang, Y. Li, Bimetallic Adv. Mater.,23 (2011) 1044-1060.

[15] A. K. Singh, Q. Xu, ChemCatChem, 5 (2013) 652-676.

[16] X. Peng, Q. Pan, G. L. Rempel, Chem. Soc. Rev., 37 (2008) 1619-1628.

[17] R. Ferrando, J. Jellinek, R. L. Johnston, Chem. Rev., 108 (2008) 845-910.

[18] F. A. Al-Odail, A. Anastasopoulos, B. E. Hayden, Top. Catal., 54 (2011) 77-82.

[19] L. A. Kibler, Electrochim. Acta, 53 (2008) 6824-6828.

[20] M. Lukaszewski, T. Kedra, A. Czerwinski, Electrochim. Acta, 55 (2010) 1150-1159.

[21] A. Safavi, S.H. Kazemi, H. Kazemi, Fuel, 118 (2014) 156-162.

[22] G. Darabdhara, M. A. Amin, G. A. M. Mersal, E. M. Ahmed, M. R. Das, M. B. Zakaria, V. Malgras, S. M. Alshehri, Y. Yamauchi, S. Szunerits, R. Boukherroub, J. Mater. Chem. A, 3 (2015) 20254-20266.

[23] M. Xiao, X. Liang, W. Li, Y. Yang, Y. Miao, J. Electrochem. Soc., 162 (2015) H415-H418.

[24] C.-L. Lee, C.-M. Tseng, J. Phys. Chem. C, 112 (2008) 13342-13345.

[25] V. Bansal, A. P. O'Mullane, S.K. Bhargava, Electrochem. Commun., 11 (2009) 1639-1642.

[26] S. Krishnamurthy, P.V. Kamat, J. Phys. Chem. C, 117 (2013) 571-577.

[27] T. Bhowmik, M.K. Kundu, S. Barman, ACS Catal., 6 (2016) 1929-1941.

[28] Y. Zhang, J. Liu, G. Wu, W. Chen, Nanoscale, 4 (2012) 5300-5303.

[29] P. Fageria, R. Nazir, S. Gangopadhyay, H.C. Barshilia, S. Pande, RSC Adv., 5 (2015) 80397-80409.

[30] L. Perini, C. Durante, M. Favaro, V. Perazzolo, S. Agnoli, O. Schneider, G. Granozzi, A. Gennaro, ACS Appl. Mater. Interfaces, 7 (2015) 1170-1179.

[31] V. Di Noto, E. Negro, S. Polizzi, F. Agresti, G.A. Giffin, ChemSusChem, 5 (2012) 2451-2459.

[32] Y. Chen, J. Wang, H. Liu, M. N. Banis, R. Li, X. Sun, T.-K. Sham, S. Ye, S. Knights, J. Phys. Chem. C, 115 (2011) 3769-3776.

[33] J. H. Lee, M.J. Park, S. J. Yoo, J. H. Jang, H.-J. Kim, S. W. Nam, C. W. Yoon, J. Y. Kim, Nanoscale, 7 (2015) 10334-10339.

[34] P. Fageria, S. Uppala, R. Nazir, S. Gangopadhyay, C.-H. Chang, M. Basu, S. Pande, Langmuir, 32 (2016) 10054-10064.

[35] J.-J. Feng, L.-X. Chen, P. Song, X.-l. Wu, A.-J. Wang, J. Yuan, Int. J. Hydrogen Energy, 41 (2016) 8839-8846.

[36] P. Fageria, S. Gangopadhyay, S. Pande, RSC Adv., 4 (2014) 24962-24972.

[37] Y. Sun, B. T. Mayers, Y. Xia, Nano Lett., 2 (2002) 481-485.

[38] Y. Sun, B. Mayers, Y. Xia, Adv. Mater., 15 (2003) 641-646.

[39] J. Chen, B. Wiley, Z.Y. Li, D. Campbell, F. Saeki, H. Cang, L. Au, J. Lee, X. Li, Y. Xia, Adv. Mater, 17 (2005) 2255-2261.

[40] G. Collins, E.K. McCarty, J.D. Holmes, Cryst. Eng. Commum., 17 (2015) 6999-7005.

[41] B. D. Anderson, J. B. Tracy, Nanoscale, 6 (2014) 12195-12216.

[42] X. Xia, Y. Wang, A. Ruditskiy, Y. Xia, Adv. Mater., 25 (2013) 6313-6333.

[43] Y. Yin, R. M. Rioux, C. K. Erdonmez, S. Hughes, G. A. Somorjai, A. P. Alivisatos, Science, 304 (2004) 711-714.

[44] D. H. Son, S.M. Hughes, Y. Yin, A. Paul Alivisatos, Science, 306 (2004) 1009-1012.

[45] M.-R. Gao, J.-X. Liang, Y.-R. Zheng, Y.-F. Xu, J. Jiang, Q. Gao, J. Li, S.-H. Yu, Nat. Commun., 6 (2015) 5982.

[46] P. Xiao, M. A. Sk, L. Thia, X. Ge, R. J. Lim, J.-Y. Wang, K. H. Lim, X. Wang, Energy Environ. Sci., 7 (2014) 2624-2629.

[47] S. Anantharaj, P. E. Karthik, B. Subramanian, S. Kundu, ACS Catal., 6 (2016) 4660-4672.

[48] J. R. McKone, B. F. Sadtler, C. A. Werlang, N. S. Lewis, H. B. Gray, ACS Catal., 3 (2013) 166-169.

Chapter 4

Decoration of gold nanoparticles on copper sulfide surface *via* photoreduction route for enhanced electrochemical hydrogen evolution and photocatalysis

Abstract

An efficient hydrogen evolution catalyst has been developed by decorating Au nanoparticle on the surface of CuS nanostructure following a green and environmental friendly approach. CuS nanostructure is synthesized through a simple wet-chemical route. CuS being a visible light photocatalyst is introduced to function as an efficient reducing agent. Photogenerated electron is used to reduce Au(III) on the surface of CuS to prepare CuS/Au heterostructure. The as-obtained heterostructure shows excellent performance in electrochemical H_2 evolution reaction with promising durability in acidic condition, which could work as an efficient alternative for novel metals. The most efficient CuS-Au heterostructure can generate 10 mA/cm^2 current density upon application of 0.179 V vs. reversible hydrogen electrode. CuS-Au heterostructure can also perform as an efficient photocatalyst for the degradation of organic pollutant. This dual nature of CuS and CuS/Au both in electrocatalysis and photocatalysis has been unveiled in this study. The process of formation of hydrogen gas and degradation of Methylene blue (MB) dye is shown in scheme 4.1
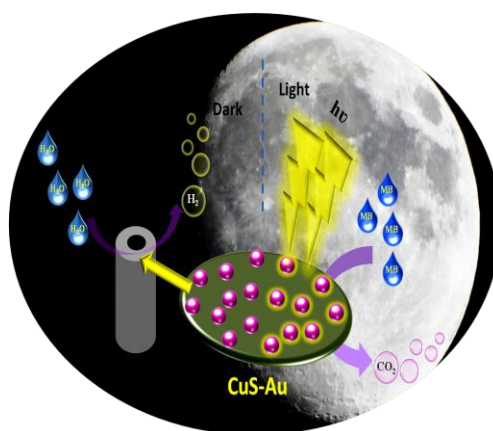
Scheme 4.1: Diagrammatic representation of dual functionality of CuS/Au both in photocatalysis and electrocatalysis

4.1. Introduction

Hydrogen is being considered as the surrogate for the limited fossil fuels hidden in the earth crust to address the global energy demand. [1] Hydrogen can be generated from different sources like water, coal, biomass etc. Generation of hydrogen from water splitting can provide the unique green path way without having any environmental pollution. Plenty of research have already been dedicated to discover efficient catalyst, which can drive the hydrogen evolution reaction (HER) with application of a minimum over potential. [2-7] The most effective and efficient catalyst for HER is Pt and Pt based compounds, which can generate hydrogen almost having onset potential of 0 V. [8] The main drawback is the cost and the availability of Pt, which restricts the industrial application. Therefore, to establish hydrogen as the competitive energy source, it is very important to develop low cost and efficient catalyst, which can generate large scale of hydrogen in very low over potential.

To replace Pt different earth-abundant metal and their corresponding compounds are also studied as catalyst for HER. Transition-metal chalcogenides are possessing similar electronic structure like noble metals, being studied as HER catalyst from last decade and establish themselves as alternative to Pt. [9] Mostly used non-precious-metal as an alternative to Pt are MoS_2, MoC_2, WS_2, WSe_2, CoS_2, $CoSe_2$, NiS_2, FeS_2, Ni_2P etc. [10-18] Different metal alloys like Ni-Mo, Ni-Fe, Ni-Mo-Zn are also successfully used as catalyst for HER reaction. [19-21] Recently, CuS is being studied for its electrocatalytic activity in HER reaction along with its photocatalytic performance. [22] It is already proved both experimentally and theoretically that the sulfur atoms on the exposed surface of transition metal chalcogenides increases the HER activity of a material. [23] At the exposed surface sulfur atoms are much more unsaturated which plays an important role to increase the electrocatalytic activity of MoS_2. [24] CuS posses layered crystal structure having weak van der Waals interactions between two double layers of Cu_2S_2. [25] Sulfur present in the CuS have empty 3p orbitals which further helps to easy capture electrons and promotes electron transportation. Although CuS is chosen very rarely as a suitable electrocatalyst for HER reaction, but the prompt feasibility of electron acceptance and transportation by CuS can establish it as a promising HER catalyst. Recently Xi *et al.*, reported electrocatalytic activity of CuS and $NiCo_2O_4$/CuS heterostructure. [26]

89

Being inspired from the above studies we have synthesized CuS following a simple wet-chemical route. CuS is a widely studied efficient visible light active photocatalyst and also very active under indoor light. In this study we have introduced a photochemical reduction approach to synthesize Au nanoparticle on the surface of CuS. Initially, CuS was excited under visible light to generate electrons and holes and simultaneously $HAuCl_4$ undergoes photoreduction by photo-generated electrons. Following this green technique without using any reducing agent we have synthesized Au nanoparticle on the surface of CuS (CuS-Au-n, with varying Au loading). Finally, the synthesized CuS and CuS-Au-n were studied as catalyst in electrocatalytic HER reaction and also in photocatalysis (Figure 4.1). Best catalytic efficiency is achieved in case of CuS-Au-3 (weight percentage of Au = 19.98) and it can generate 10 mA/cm^2 current density in -0.179 V vs. RHE. CuS-Au-3 also shows the best performance in photocatalysis with rate constant (k) value 3.7×10^{-1} min^{-1} which is 21 times higher compared to bare CuS. Superior electrocatalytic and photocatalytic activity of CuS-Au-3 is explained with the help of impedance spectroscopy and photoluminescence study, respectively.
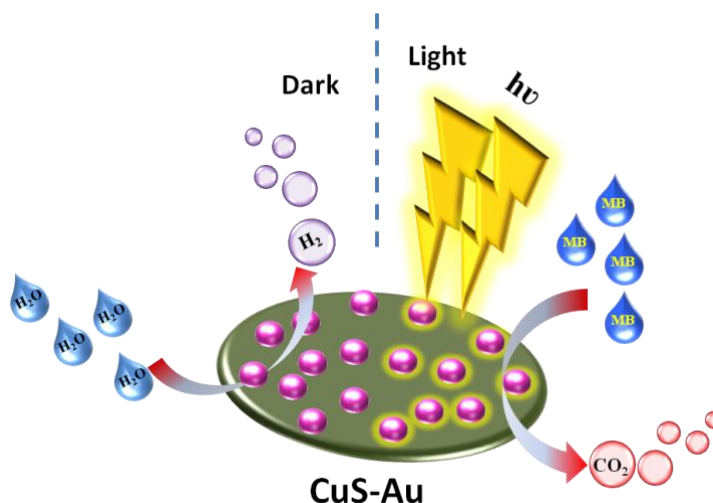
Figure 4.1: Diagrammatic representation of the dual functionality of CuS/Au (photocatalysis under light irradiation and electrocatalytic activity under dark)

4.2. Experimental section

4.2.1. Synthesis of CuS nanostructure

Following a very simple wet-chemical route CuS was synthesized. Cu(II)-sulfate & thioacetamide (TAA) were used as precursor of Cu and S, respectively. 0.3 g of Cu(II)-sulfate was dissolved in 20 mL water and stirred for 5 min and labelled as solution A. On the other hand, 0.07 g of TAA was dissolved in 20 mL water and then 1mL 1 M NaOH was added and sonicated for 10 min and marked as solution B. After that solution A was kept on a water bath at temperature ~80 °C. Then solution B was added drop wise to solution A. Finally, the whole mixture was kept on water bath for 30 min. the bluish-green color compound was collected by several washing with water and followed by ethanol.

4.2.2. Decoration of Au nanoparticles on CuS nanostructure.

The as-synthesized CuS nanostructure was used to synthesize Au nanoparticles where CuS function as reducing agent as well as support for the growth of Au nanoparticle. For this procedure, 30 mg of CuS nanostructure was thoroughly dispersed in 30 mL DI water via ultrasonication for 30 min. After that the dispersed CuS was kept under visible light irradiation in stirring condition. Different amounts of (1, 2, 3 and 4 mL 1.25×10^{-2} M HAuCl$_4$) was added in the CuS dispersion and stirred for 1.5 h. 1.0 mL, 2.0 mL, 3.0 mL, and 4.0 mL aliquots of HAuCl$_4$ were added to CuS and named as CuS-Au-1 (5.92 weight % Au), CuS-Au-2 (12.85 weight % Au) , CuS-Au-3 (19.98 weight % Au), and CuS-Au-4. The diagrammatic representation of the decoration of Au nanoparticles on CuS plates is shown in scheme 4.2.
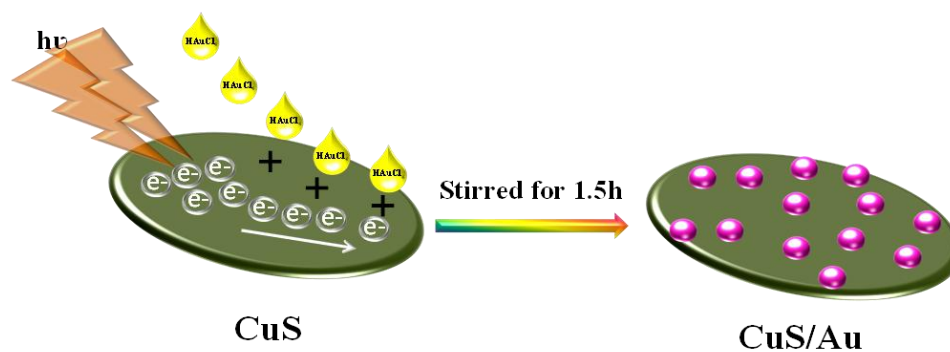
Scheme 4.2: photochemical reduction of Au ions to Au nanoparticles on the surface of CuS plates

4.3. Results and Discussion

4.3.1. X-ray diffraction analysis of CuS and CuS-Au-n (n = 1, 2, and 3)

 With the help of powder X-ray diffraction analysis phase purity and crystallinity of the synthesized CuS and CuS-Au-n (n=1, 2, 3, 4) samples were determined. Figure 4.2 shows the PXRD pattern of bare CuS and CuS-Au-n (n=1, 2, 3) samples. XRD of CuS is well matched with the JCPDS no 00-006-0464. In the present system CuS crystallizes in hexagonal crystal system. Presence of any impurity, intermediate product, starting compound is not detected through XRD analysis. XRD pattern of CuS-Au-n clearly shows three diffraction of (111), (200) & (220) planes which are the characteristic peaks due to Au and well matched with the JCPDS no 04-0784. XRD pattern of Au nanoparticle suggests that Au nanoparticle crystallizes in cubic system. With the increase in concentration of $HAuCl_4$, it was observed that there is successive enhancement in the intensity of the corresponding peak of Au on CuS. Finally, in case of CuS-Au-3 it is very clear that peaks of Au is dominating over the peaks of CuS. From the comparison of the highest intense peaks of CuS and Au it is clear that in case of CuS-Au-1, CuS-Au-2, CuS-Au-3 CuS:Au peak intensity ratio is ~ 2:1, ~3:2, ~1:1, respectively. Therefore, from this observation it can be claimed that surface of CuS in CuS-Au-3 sample mostly covered with Au nanoparticle.
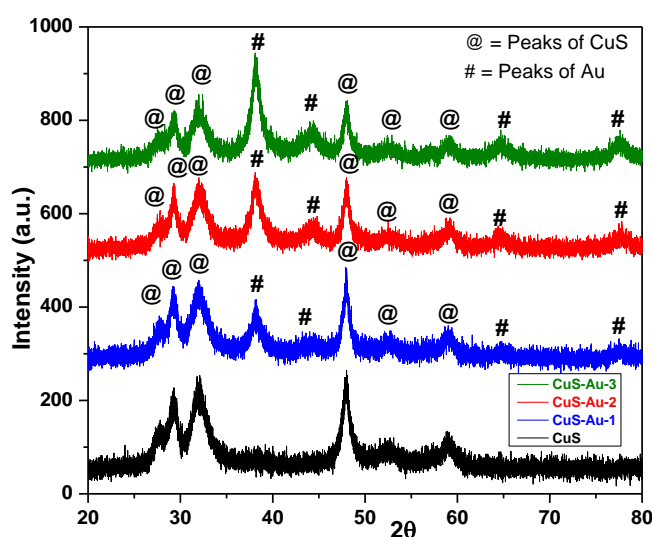
Figure 4.2: PXRD pattern of CuS and CuS-Au-n (n= 1, 2, 3) showing the variation in the intensities of the highest intense peak of CuS and Au

4.3.2. Raman analysis of CuS

Crytallinity of CuS was determined with the help of Raman spectroscopy, which is shown in Figure 4.3a. It exhibits a very strong peak at 468 cm^{-1} which is due to the vibration mode of S-S covalent bonds in CuS. Peak at 468 cm^{-1} is corresponding to the well-known A1g mode of CuS. [27] It is worth mentioning that there is no additional impurity peaks are present for any copper substrate like $Cu(OH)_2$ and also un-reacted precursor compound.

4.3.3. Study of UV-vis spectroscopy of CuS and CuS/Au

UV-vis spectroscopy of CuS and CuS/Au heterostructure was determined by utilizing the ethanolic dispersion, shown in Figure 4.3b. Both the spectra show an enhanced absorption closer to the near IR region. Literature reports that covellite CuS shows two characteristic absorption peaks: one in visible region and another in near IR region. In our present case, CuS exhibits enhanced absorption near 400 nm having the band edge at 550 nm, which again dictates about the band gap about 2.2 eV. Due to having absorption both in visible and in near IR region a valley is visualized in between 500 to 780 nm and this phenomena is supported in literature also. [28] However, after deposition of Au nanoparticle on the surface of CuS, there is a certain increase in the absorption intensity in the visible region, which further wraps the valley of CuS. The absorption localized in the region 500 to 600 nm is probably due to the surface plasmon resonance effect of Au nanoparticles.
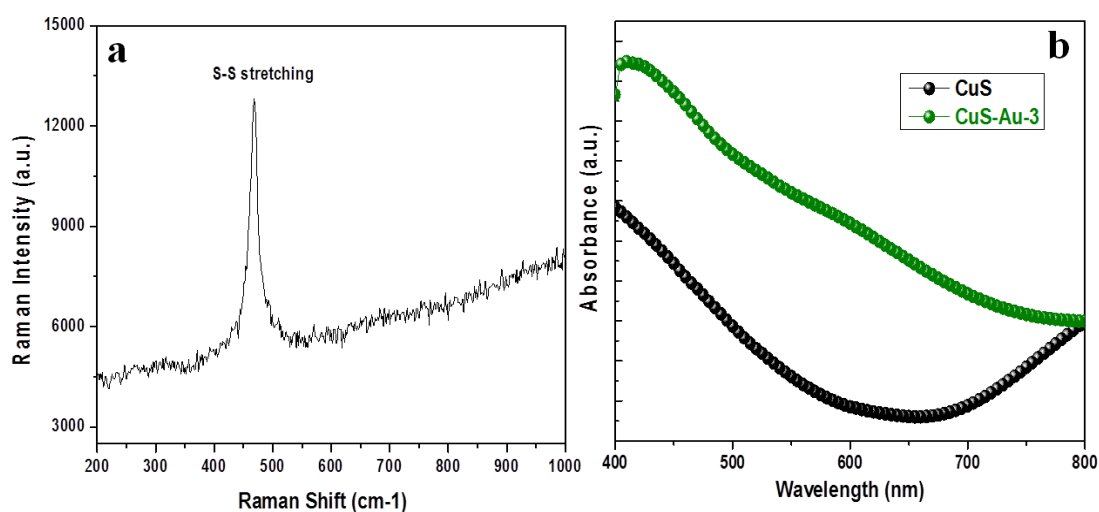
Figure 4.3: (a) Raman spectrum of CuS only and (b) UV-vis absorption spectrum of CuS and CuS-Au-n

4.3.4. XPS study of CuS and CuS/Au

To determine the surface electronic state and the composition of the product XPS analysis was carried out. Wide scan spectra of CuS sample indicates the presence of Cu and S as well as C and O due to the exposure in air, shown in Figure 4.4a. XPS spectrum of CuS reveals that the $Cu2p_{3/2}$ peak has binding energy at 231.8 eV which is the characteristic of CuS and this value is 0.7 eV lower than that of Cu_2S. [29, 30] Binding energies of $Cu2p_{1/2}$ and $Cu2p_{3/2}$ peaks at 951.7 and 931.8 eV are shown in Figure 4.4b. Two satellite peaks centered at 943.1 and 963.5 eV indicates the presence of the paramagnetic chemical state of Cu^{2+}. Binding energy of $Cu2p_{3/2}$ and $Cu2p_{1/2}$ are separated by 20 eV are essentially identical binding energies of Cu2p of Cu(II). [31] The corresponding XPS spectra of S have been shown in Figure 4.4c. The binding energy peaks observed in the S2p spectrum at 161.7 and 162.7 eV, which are attributed to the $S2p_{3/2}$ and $S2p_{1/2}$ states respectively, also confirm the formation of CuS.
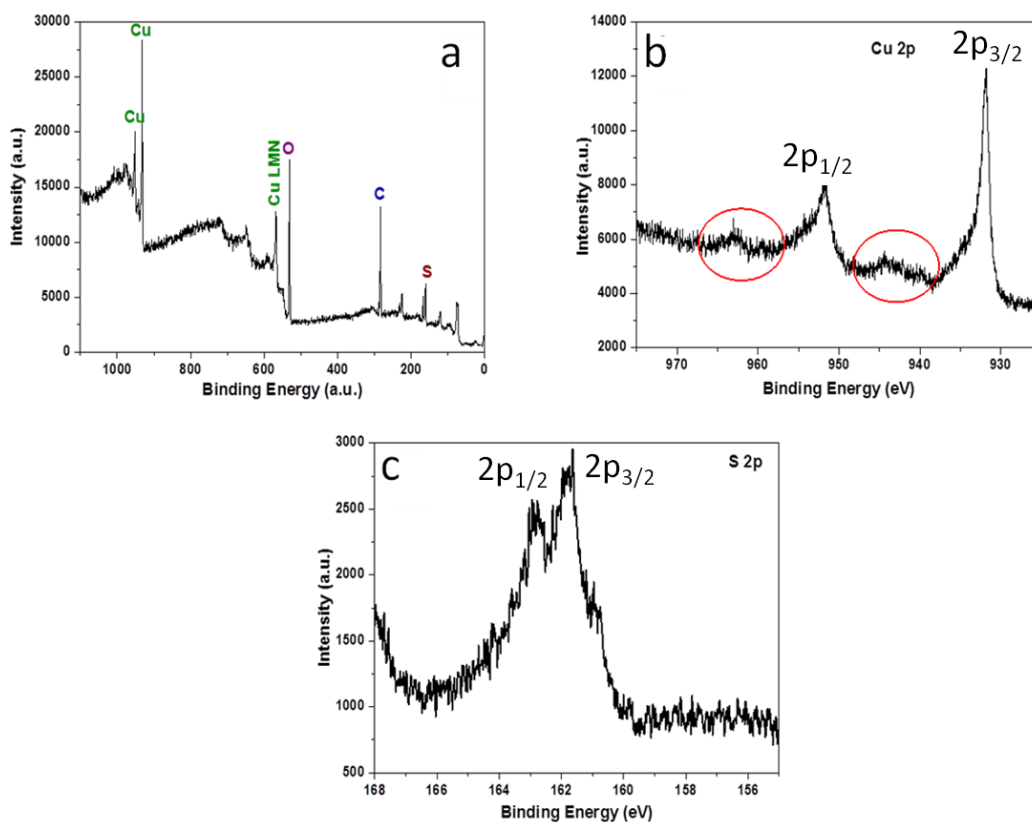
Figure 4.4: XPS spectra (a) wide scan spectra of CuS, (b) binding energy of Cu (2p) and (c) binding energy of S (2p) region

A wide scan spectrum of CuS-Au-3 sample shows the presence of Au, S, Cu, O and C (Figure 4.5a). Binding energy of Cu and S remains unchanged even after deposition of Au on the surface of CuS (Figure 4.5b and 4.5c). The binding energy of Au 4f is found as Au4f$_{7/2}$ and Au4f$_{5/2}$ at 83.7 and 87.4 eV respectively (Figure 4.5d). This binding energy values are consistent with the bulk gold and indicates the formation of Au(0) on the surface of CuS. [32-34]
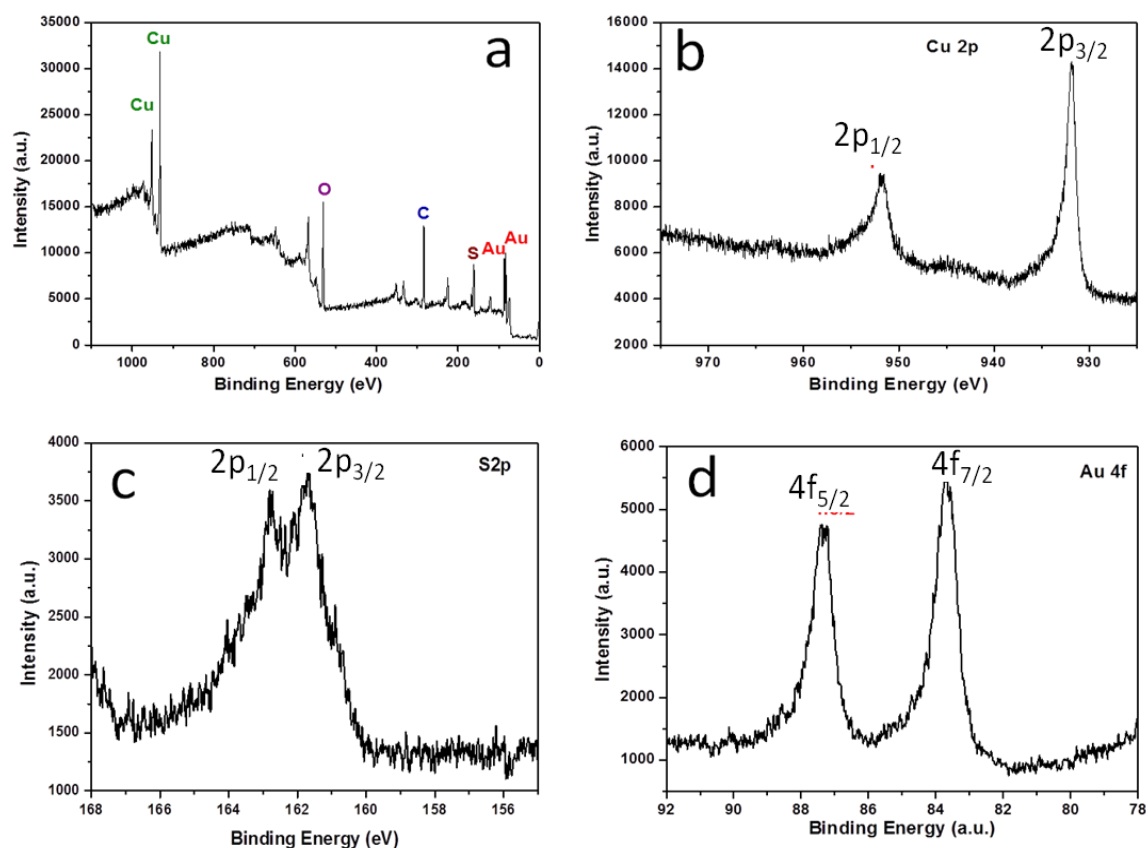
Figure 4.5: XPS spectra (a) wide scan spectra of CuS-Au-3, binding energy of (b) Cu (2p), (c) S(2p), and (d) Au (4f) region

4.3.5. Scanning electron microscope analysis of CuS and CuS/Au

 To observe the possible growth of CuS and successive deposition of Au on the surface of CuS, we did field emission scanning electron microscopy (FESEM) measurement for both CuS and CuS-Au-n (n=3) (Figure 4.6a, b). It can be seen from Figure 4.6a that highly dense and small nanoplates of CuS are present. Nanoplates are having the edge length ~25 nm. After

photochemical deposition of Au on the surface of CuS, small particles of Au were observed through FESEM analysis, highlighted by encircling in Figure 4.6b.
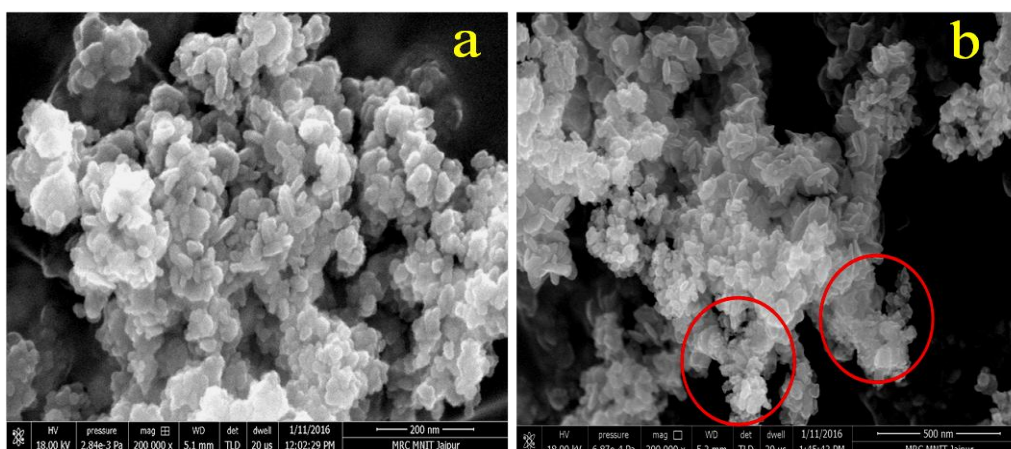
Figure 4.6: FESEM image of (a) CuS stacked plates and (b) CuS-Au-3 on CuS surface. Encircled area shows attachment of small particles on CuS plates

4.3.6. Transmission electron microscope study of CuS and CuS/Au

With the help of transmission electron microscopy analysis morphology of CuS was further verified. Figure 4.7a shows the typical TEM images of CuS. From low magnification TEM image it is clear that highly dense CuS nanoplates, which are not properly aligned, are synthesized following our method. High magnification image shows that there are some light shaded small plates and also some dark strips (inset of Figure 4.7a). Dark strips are corresponding to the CuS plates, which are present as perpendicular to the basal plane. Both the alignment (perpendicular and parallel) are observed from the high magnification image. Edge length of the CuS plates are ~25 nm, which is in agreement with SEM images. To determine the crystallinity of the as-synthesized product HRTEM was carried out. HRTEM image clearly demonstrate the lattice spacing of the crystalline CuS is 0.308 nm, corresponding to the spacing between two crystal plane (102) (Figure 4.8a) which matches well with the literature. [35, 36] Decoration of photochemically deposited Au nanoparticle on the plates of CuS was also verified with the help of TEM analysis. Figure 4.7b shows the arrangement of Au nanoparticle on the surface of CuS plates. High magnification image shown in the inset of Figure 4.7b confirms that the Au nanoparticles deposited on CuS have particle size ~5-10 nm. HRTEM image was taken

on the surface of Au deposited CuS plates which clearly shows the interface between Au nanoparticles and CuS nanoplates. Figure 4.8b shows the 'd' spacing calculated from the lattice spacing of deposited Au nanoparticle is ~0.24 nm which is due to the spacing between two crystal planes (111) of Au and it is well matched with the literature. [34]
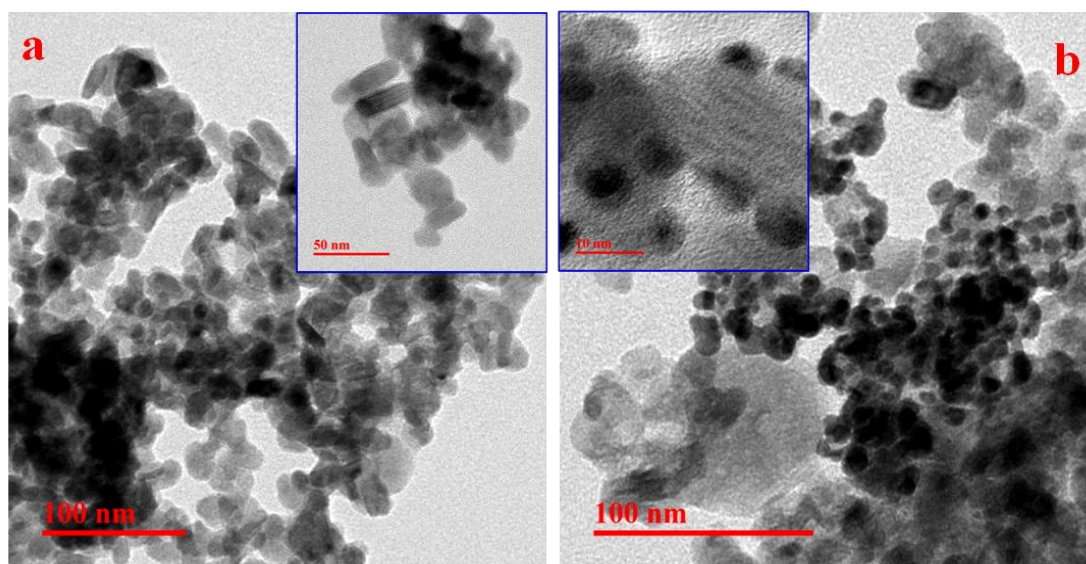
Figure 4.7: Low magnification TEM image of (a) CuS and (b) CuS-Au-3. Inset shows high magnification images of very small plates of CuS and very small particles of Au on CuS surface
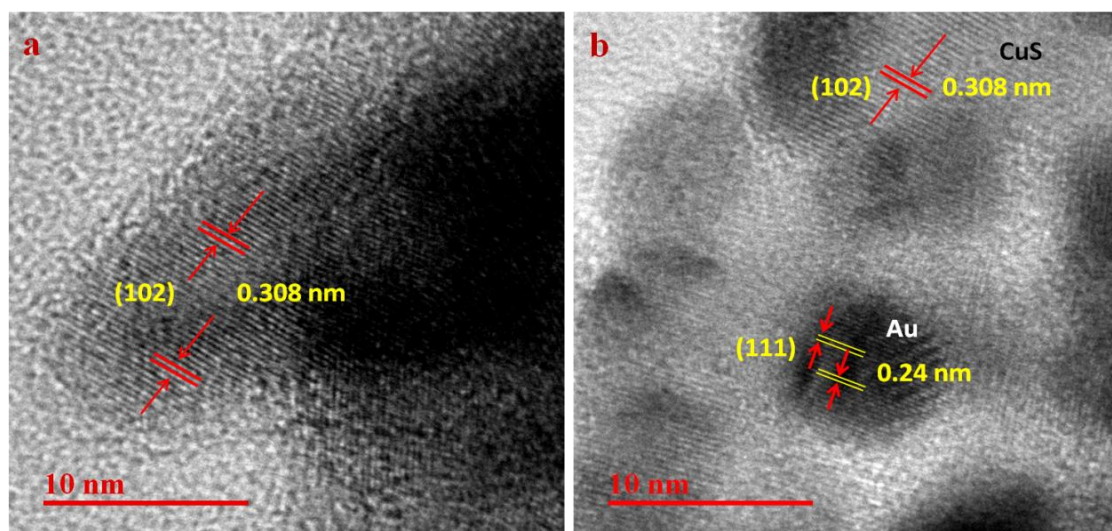
Figure 4.8: HRTEM image of (a) CuS and (b) CuS-Au-3

4.4. Electrocatalytic Activity

Before checking the hydrogen evolution reaction ink was prepared. Ink of CuS and CuS-Au-n were prepared by dispersing 5.0 mg of the sample in 300 µL of isopropanol. Then 30 µL of nafion was added as binder and sonicated for 30 min for uniform dispersion. Finally, 5.0 µL dispersed compound was drop casted carefully on 3 mm diameter GC electrode.

4.4.1. Detailed study of LSV polarization curves of bare GC, CuS, CuS-Au-1, CuS-Au-2 and CuS-Au-3

The electrocatalytic activity of CuS and CuS-Au-n was evaluated by using linear sweep voltammogram (LSV) technique. All the electrochemical measurements for hydrogen evolution were carried out in 0.5 M H_2SO_4 aqueous solution with scan rate of 50 mV/s.
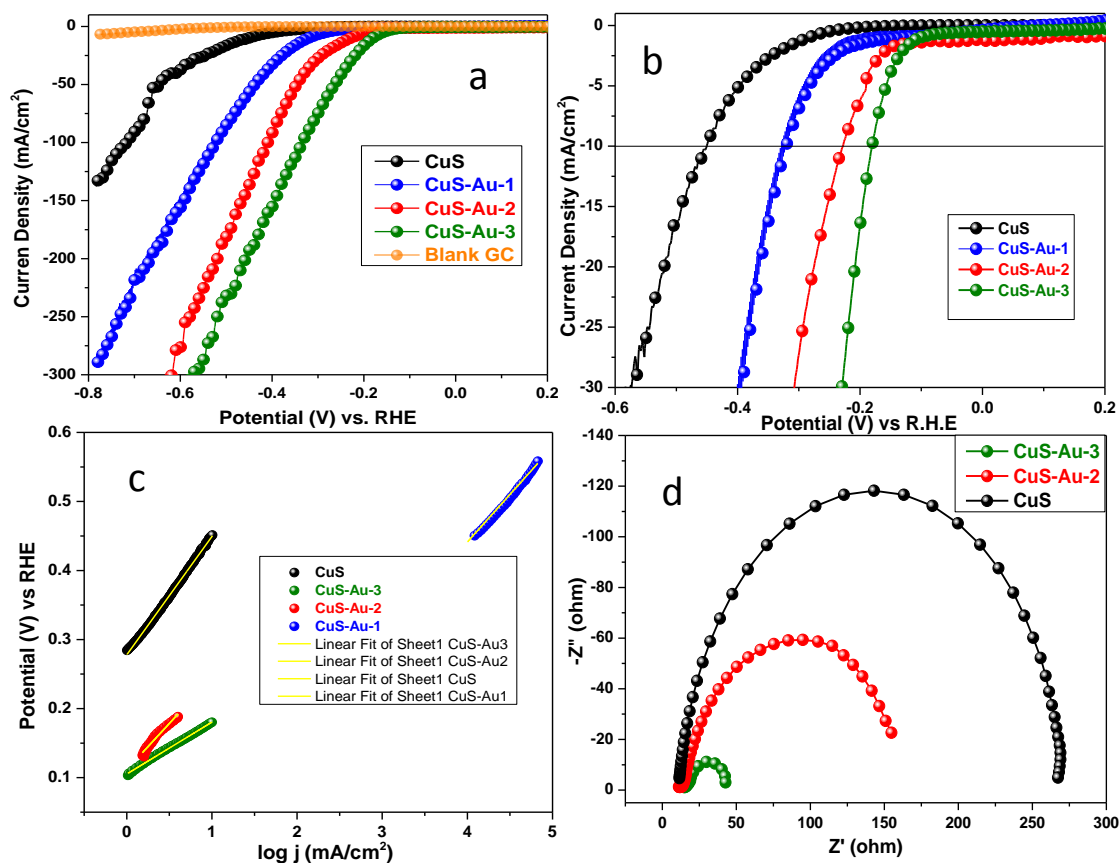
Figure 4.9: Polarization curves for bare GC, CuS, CuS-Au-1, CuS-Au-2 and CuS-Au-3 in 0.5 M H_2SO_4 (a) high scale and (b) low scale (c) Tafel plots of CuS, CuS-Au-1, CuS-Au-2, and CuS-Au-3, (d) Nyquist plot of CuS, CuS-Au-2 and CuS-Au-3

Potentials are recorded with reference to Ag/AgCl and reported with respect to reversible hydrogen electrode and the polarization curves are shown in Figure 4.9a, b. Au nanoparticle decorated CuS shows a remarkably enhanced current density with successive anodic shift in the onset potential compared to bare CuS. With successful increase in the amount of Au on the surface of CuS, there is successive enhancement in the current density and at the same time there is clear anodic shift in the onset potential. CuS nanoplates require -0.449 V potential to generate current density of 10 mA/cm^2. In comparison, to achieve current density of 10 mA/cm^2, CuS-Au-1 needs overpotential -0.324 V. Again, in case of CuS-Au-2 and CuS-Au-3, it needs -0.226 V and -0.179 V, respectively to reach current density of 10 mA/cm^2. CuS-Au-3 shows best catalytic activity but still it is less compared to Pt, as reported in the literature. [37] In all cases, Au nanoparticle modified CuS shows the enhanced catalytic activity compared to the bare CuS. At potential -0.475 V bare CuS can generate only 12.5 mA/cm^2 current density whereas, in case of CuS-Au-1 the value increased up to 70.63 mA/cm^2. Current density further increased for CuS-Au-2 to 159.6 mA/cm^2 and the highest current density was achieved in case of CuS-Au-3, which is 215.5 mA/cm^2. This superior activity of CuS-Au compared to CuS may be attributed to the fact that Au nanoparticle on CuS surface can function as an electron sink and successfully snatch the carrier from the surface of CuS and transport to electrolyte where it reacts with H$^+$ ion to generate H$_2$. For better understanding about the contribution on Au nanoparticle on the surface of CuS, electrocatalytic activity of CuS-Au-4 was also checked.
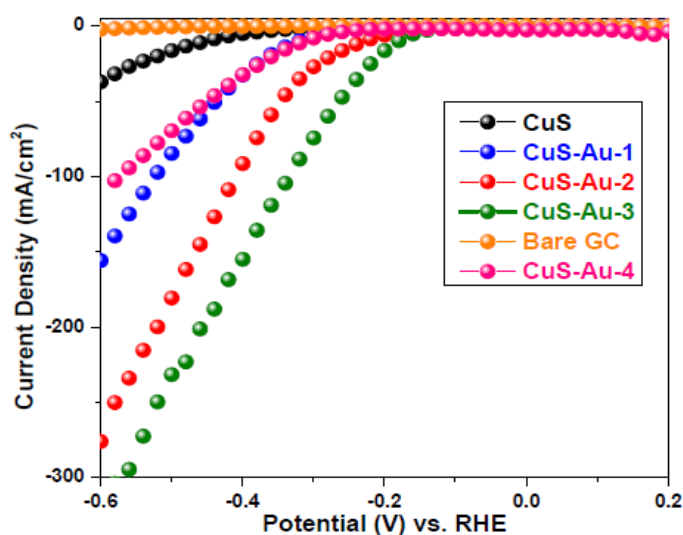
Figure 4.10: Polarization curves for bare GC, CuS, CuS-Au-n (n = 1, 2, 3, & 4) in 0.5 M H$_2$SO$_4$

With further increase in the concentration of Au certainly decrease the electrocatalytic activity of CuS and successive cathodic shift in the onset potential were observed (Figure 4.10). In presence of Au nanoparticle initially a positive shift in the onset potential was observed where Au nanoparticle functions as electron collectors and makes faster electron transportation. But excess amount of Au on CuS further decreases the electrocatalytic activity. The possible reasons for this decrease in the electrocatalytic activity are firstly, high amount of Au loading may cover all the active sites of CuS and further hindering its contact with water molecule. Secondly, more amount of Au may work as aggregates and further large particle size leads to disappearance of surface effects. Electrocataytic activity of pure Au nanoparticle was also checked and shown Figure 4.11. Pure Au nanoparticle needs -0.531 V vs. RHE to generate 10 mA/cm^2 current density. It can achieve only 16.8 mA/cm^2 current density upon application of -0.58 V vs. RHE, which is poor as compared to CuS and CuS-Au-3.
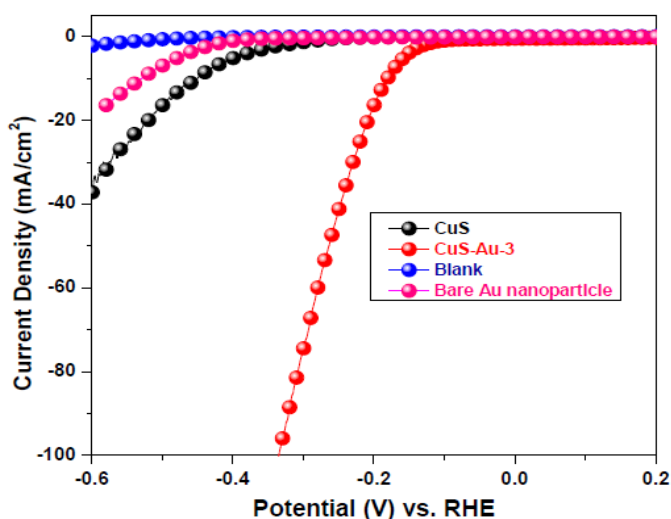
Figure 4.11: Polarization curves for bare GC, pure Au nanoparticle, CuS, and CuS-Au-3 in 0.5M H_2SO_4

4.4.2. Mechanism of HER

Tafel slope is the intrinsic property of a material and focus the rate determining step in HER reaction. Tafel slope is also useful to determine the effectiveness of a catalyst. The linear portion of the Tafel plots were fitted in the Tafel equation (η = b log(j) + a, where b is the Tafel slope). [38, 39] The values of Tafel slope for CuS, CuS-Au-1, CuS-Au-2 and CuS-Au-3 are 171, 138,

133 and 75 mV/decade, respectively (Figure 4.9c). Tafel slope data indicates that with increase in the amount of Au nanoparticle on CuS, there is further enhancement in the electrocatalytic activity of CuS. Tafel slop value also confirms that among all these catalysts, CuS-Au-3 is electrocatalytically much more active than others. Generally HER reaction follows two possible mechanisms in acidic medium: It may be Volmer-tafel or it may be Volmer-Heyrovsky. The First step is the Volmer step also called discharge step: $H_3O^+ + e- \rightarrow H_{ads} + H_2O$. This reaction is either followed by Heyrovsky process or called as desorption step: $H_{ads} + H_3O^+ + e^- \rightarrow H_2 + H_2O$ or Tafel step which is also called recombination step: $H_{ads} + H_{ads} \rightarrow H_2$. It is expected that the Tafel slope should be 120, 40 or 30 mV/decade if the Volmer, Heyrovsky and Tafel is the respective rate determining step. In case of CuS, HER reaction follows Volmer-Heyrovsky mechanism following Volmer as the rate determining step. In case CuS-Au-3 the HER reaction follows same mechanism but the rate determining step is the Heyrovsky reaction. Stability of CuS and CuS-Au-3 were checked upon continuous scan of 1000 cycles. It is very clear from Figure 4.12, there is negligible change in the current density and onset potential as well, which further claims the stability of CuS and CuS-Au-3 in acidic medium. Digital image of H_2 evolution from GC electrode is shown in Figure 4.13.
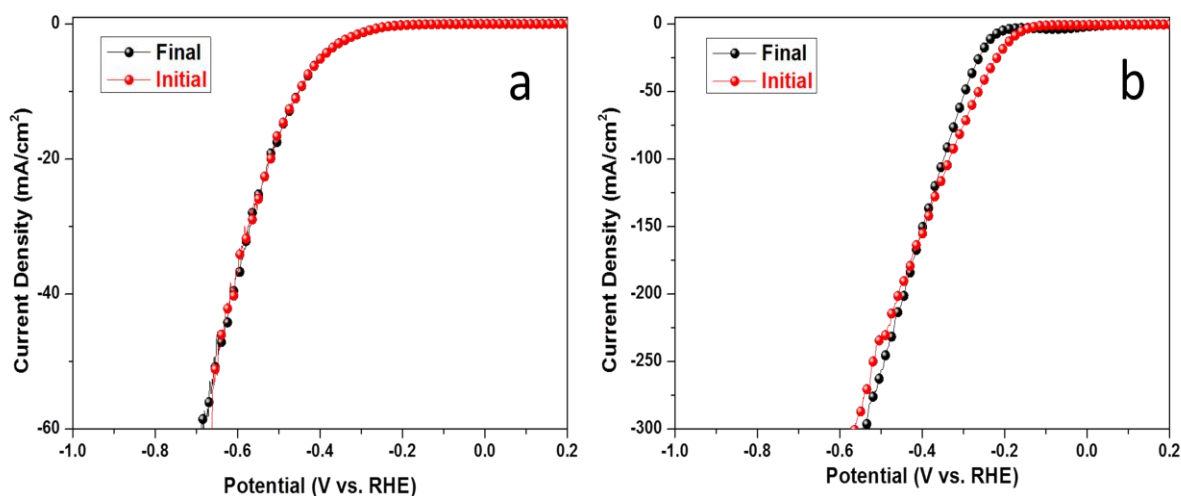
Figure 4.12: Comparative polarization curve of (a) CuS and (b) CuS-Au-3, initial run and after 1000 cycle

4.5. Impedance measurement

To have a clear understanding about the electrocatalytic activity of CuS and CuS-Au-n sample, we have carried out electrochemical impedance measurement. Electrochemical Impedance study clearly gives the idea about the ease of electron transportation on different electrode surface.
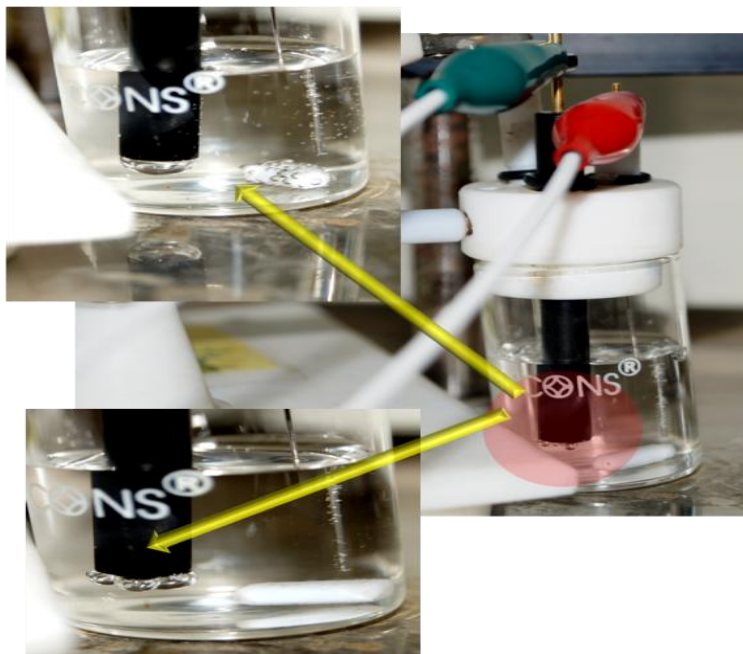
Figure 4.13: Digital image of hydrogen evolution on electrode surface in case of CuS-Au-3

Nyquist impedance plots have been measured for CuS at -0.368 V vs. RHE, which is the onsetpotential for CuS. On the other hand for CuS-Au-2 and CuS-Au-3, it was measured at the onset potentials of the respective compounds. The evaluated data can be fitted with an equivalent circuit composed of a constant phase element (CPE) for CuS and CuS-Au-n and the resistance (R_S), which represent the core resistance of the material and R_{ct} dictates about the charge transfer resistance from the electrode surface to electrolyte. Impedance curve has been fitted and the resistance values are summarized in table 4.1 (Figure 4.9d). R_s resistance of CuS and, CuS-Au-2 and CuS-Au-3 are 10.5, 11.7 and 14.8 Ω, respectively. With the increase in the amount of Au on CuS surface it is very clear that R_{ct} value decreases from CuS to CuS-Au-2 and that to CuS-Au-3. The R_{ct} value decreases very sharply from CuS to CuS-Au-2 to finally CuS-Au-3. All these

data have been noted in table 4.1. The charge transfer resistance from CuS to electrolyte is 255.4 Ω in case of CuS. Whereas, in case of CuS-Au-2 this value decreases to 143.7 Ω and finally for CuS-Au-3 it further decrease to 31.1 Ω. Successive decrease in the charge transfer resistance from CuS surface to electrolyte with the increase in the amount of deposited Au further depicts that Au helps in the faster charge transfer from electrode to electrolyte. Photochemically deposited Au nanoparticle on CuS surface can function as an electron sink [40] or trap which captures the electrons from CuS upon application of external bias. The impedance results are in well agreement with our as-observed electrocatalysis result. Higher loading of Au nanoparticle on CuS surface further decreases the electrocatalytic activity.

Table 4.1: Fitted Charge Transfer values of CuS, CuS-Au-2 and CuS-Au-3 on GC electrode.

Cathode	$R_s(\Omega)$	R_{ct} (Ω)
CuS	10.5	255.4
CuS-Au-2	11.7	143.7
CuS-Au-3	14.8	31.1

4.6. Photoluminescent study

In case of semiconductor nanostructure, PL is an efficient and suitable tool to study the electron transfer, migration and at the same time the fate of the photogenerated electron hole-pair. Mechanism of electron transfer was determined with the help of photoluminescence. PL study was carried out using the ethanolic dispersion of CuS at room temperature with an excitation wavelength of 350 nm (3.54 eV). In case of bare CuS a broad emission band in the visible region was observed centered at 509 nm (2.43 eV) (Figure 4.14). This observation clearly matches with the reported literature. [41] Furthermore to understand the charge transfer process; PL study was also carried out for CuS-Au-3 sample at room temperature. CuS-Au-3 sample almost shows the same emission band with much lower band intensity. Originally, PL emission spectra result from the recombination of the free electrons and holes. Successive decrease in the emission intensity

was observed in case of CuS-Au-3 compared to CuS, which may be attributed due to the electron sink nature of Au attached with CuS. Au decorated on CuS snatches the photogenerated electron from CuS, helps in inhibiting the recombination of charge carrier in CuS, which further results in lowered PL intensity.
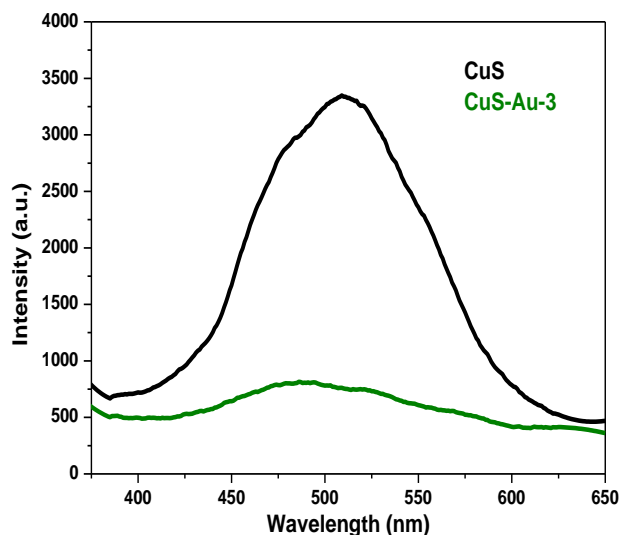
Figure 4.14: Comparative PL spectra of CuS and CuS-Au-3

4.7. Photocatalysis

To determine the photocatalytic activity of CuS and CuS-Au-3, Methylene blue (MB) was applied as a model dye. MB has a sharp optical absorption at 663 nm, which was used to monitor the degradation process and to study the kinetics. 10 mg of the desired catalyst was first immobilized in 30 mL of 2×10^{-5} M aqueous MB solution. After immobilization of catalyst molecule in the MB solution, it was stirred in dark for 30 min to establish the adsorption-desorption equilibrium. A tungsten bulb (100 W), which emits a continuous spectrum of light in between 300-1400 nm was used as visible light source to irradiate the solution after reaching to equilibrium. After agitation, the reaction mixture was kept under tungsten light to initiate the reaction with continuous stirring and the distance between the light source and reaction mixture was fixed at ~20 cm. Photocatalysis was carried out in neutral pH and room temperature. To monitor the photocatalysis process, at a regular interval 3.0 mL of aliquots were taken out from

the reaction mixture and then centrifuged and used to check the optical absorbance. Remaining dye in the solution was quantified from the observed absorbance intensity. % Degradation was calculated from the given equation:

$$X\% = (A_0 - A_t)/A_0 \times 100$$

Where, A_0 = initial peak intensity and A_t = peak intensity at time 't'. A plot of 'A_t/A_0' vs. 't' was used to evaluate the order of the reaction and the corresponding $\ln(A_t/A_0)$ vs. 't' was used to find out the rate constant of the reaction.
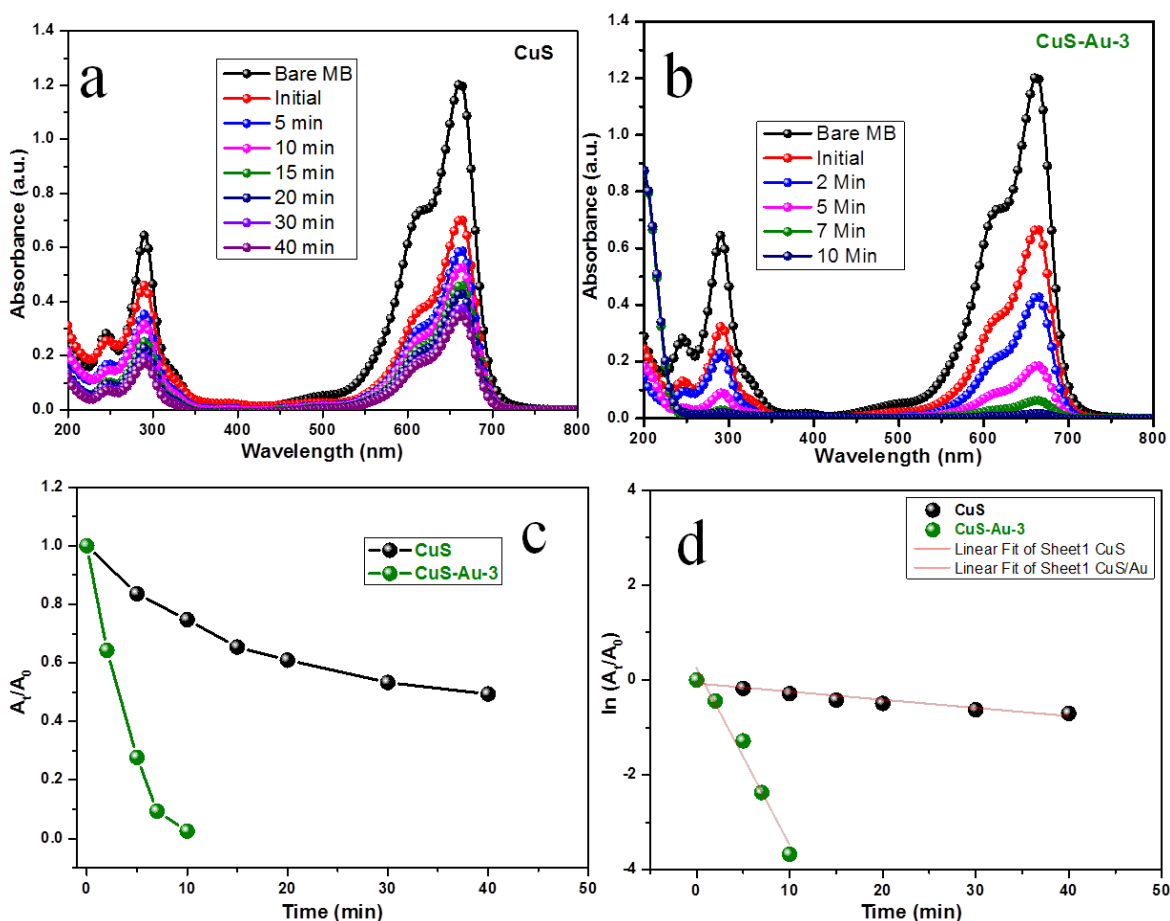
Figure 4.15: Photocatalytic decomposition of MB dye by using (a) CuS (b) CuS-Au-3 catalyst: absorbance vs. wavelength plot, (c) Plot of (A_t/A_0) vs. time for both CuS and CuS-Au-3, and (d) Plot of $\ln(A_t/A_0)$ vs. time for both CuS and CuS-Au-3. Conditions: [MB] = 2×10^{-5} M and catalyst = 10 mg

To study the photocatalytic activity of CuS and CuS-Au-3, MB was chosen as a model cationic dye. MB has optical absorbance maxima at 663 nm. Photocatalytic activity of CuS and CuS-Au-3 was estimated by scrutinizing consecutive decrease in the absorption intensity of MB with time under irradiation of visible light (Figure 4.15a, b). Previously, we have unveiled that CuS hexagonal plates can function as photocatalyst under indoor light. [22] Here, CuS have the negative surface charge as it was synthesized in alkaline condition. So, cationic dye MB is easily adsorbed on the surface of CuS. MB does not degrade under visible light irradiation in absence of any catalyst. Under stirring in dark 41.6% MB was adsorbed on the surface of CuS whereas 44.6% on the surface of CuS-Au-3. CuS shows only 25% dye degradation within 10 min of reaction. On the other hand CuS-Au-3 shows enhanced photocatalytic activity with 97% dye degradation within 10 min (Figure 4.15b). Comparative % dye removal efficiency of CuS and CuS-Au-3 is shown in Figure 4.16. Plot of A_t/A_0 vs. t shows that the photocatalytic degradation follows pseudo-first order reaction in both the cases (Figure 4.15c). From the plot of ln (A_t/A_0) vs. t, rate constant 'k' was determined. In case of bare CuS the value of 'k' is 1.7×10^{-2} min^{-1}, whereas, when CuS-Au-3 was used as photocatalyst the value of 'k' increased 21 times and the value become 3.7×10^{-1} min^{-1} (Figure 4.15d). With the increase of MB concentration, degradation efficiency decreases. Photocatalytic performance of CuS-Au-3 sample was checked introducing MB concentration as 2.5×10^{-5} M.
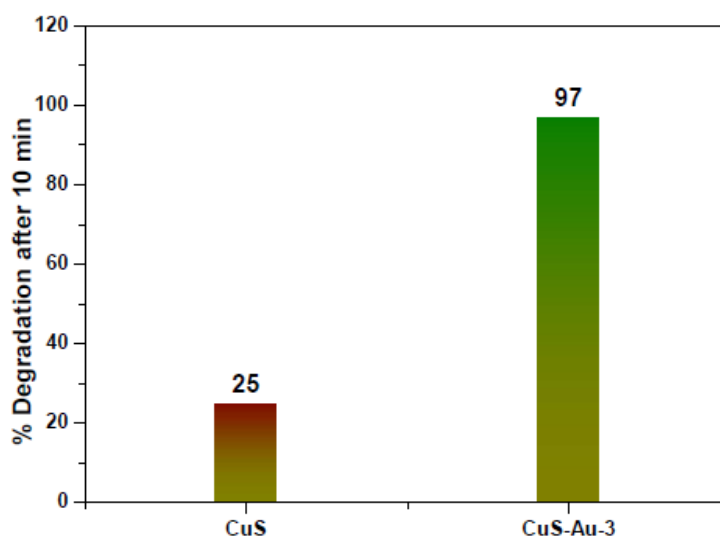
Figure 4.16: Comparative photocatalytic study of CuS and CuS-Au-3 showing the bar diagram of % dye removal efficiency

Keeping all other reaction parameters unaltered when the concentration of MB is increased there is little decrease in the catalytic efficiency still the reaction follows pseudo-first order kinetics as A_t/A_0 vs. t plot shows the exponential decay (Figure 4.17). From the plot of $\ln(A_t/A_0)$ vs. t, 'k' is determined and the value is 1.9×10^{-1} min^{-1} which is ~0.5 times lowered compared to the previous concentration. From UV-vis absorption of CuS-Au it was observed that Au nanoparticles enhance visible light absorbance of CuS nanoplates. PL study also clearly dictates that Au nanoparticle snatches the photogenerated electrons from the surface of CuS and readily transfers to MB which further results in high degradation efficiency with enhanced 'k' value. Au nanoparticle present on the surface of CuS nanoplates executes duel property to enhance the activity of CuS: It enhances the visible light absorption and at the same time it delays the recombination of photogenerated electron hole pair. CuS-Au-3 shows better performance in photocatalysis than CuS, which can be explained by the work function values.
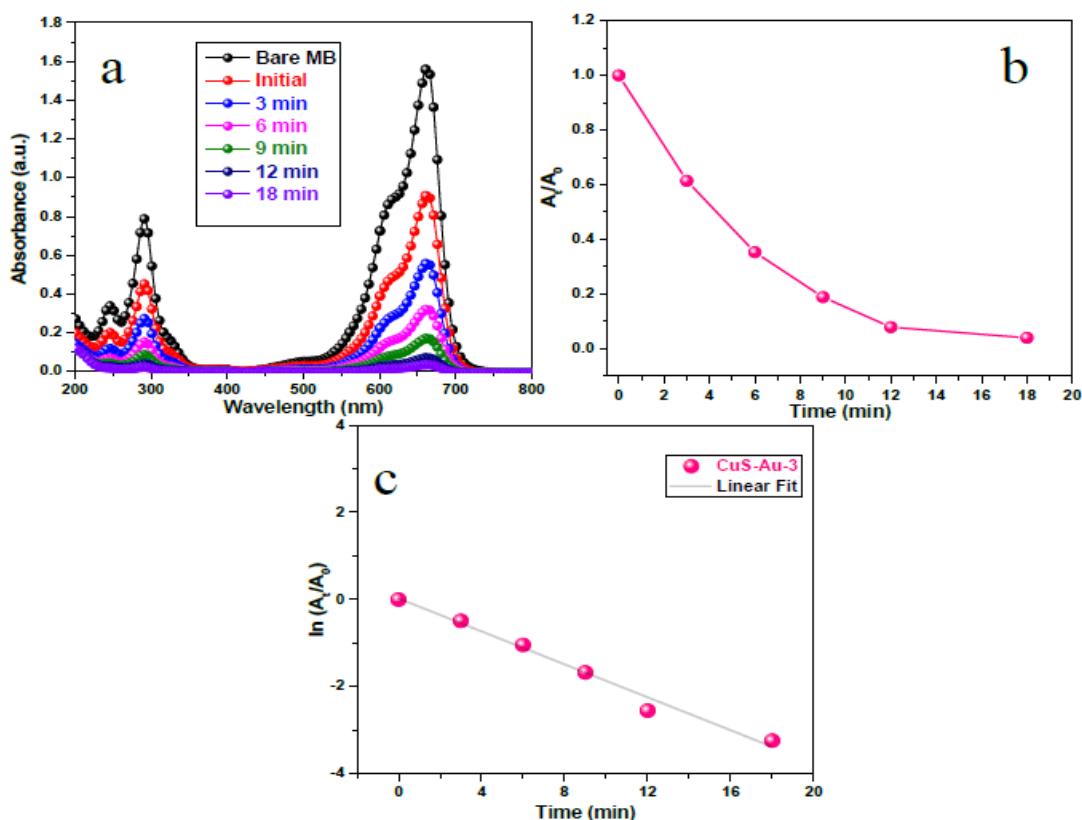

Figure 4.17: Photocatalytic decomposition of MB dye using CuS-Au-3 (a) absorbance vs. wavelength plot, (b) Plot of A_t/A_0 vs. time shows the kinetics and (c) Plot of $\ln(A_t/A_0)$ vs. time. Conditions, [MB] = 2.5 x 10-5 M and catalyst = 10 mg

Reported work function value for Au and CuS is 5.1 eV and 4.95 eV, respectively. [34, 42] So, in CuS-Au-3, a Schottky barrier will form, which helps in electron transfer between lower work function (CuS) material to higher (Au) work function material. [43-46] Upon irradiation with visible light, electrons will be excited to the conduction band leaving behind holes in valence band of CuS. Now, the excited electron can easily be shifted from the CB of CuS to the Au nanoparticle surface due to higher work function. These electrons react with dissolved oxygen and helps in the formation of superoxide radical anion ($O_2^{.-}$), which also react with H_2O to from hydroxyl radicals ($OH^.$). [40] On the other hand holes present in the VB of CuS also reacts with H_2O to generate $OH^.$. These hydroxyl radicals are main active species for MB dye degradation. Au metal nanoparticles on CuS surface behave as an electron sink or trap for photogenerated electrons and can easily adsorb electrons from the CB of CuS and prevent immediate recombination. [40, 42, 43] Hence, CuS-Au-3 exhibit better photocatalytic efficiency shows ~97% dye degradation with in 10 min which is much faster compared to CuS. The overall photocatalysis mechanism is shown in Figure 4.18.
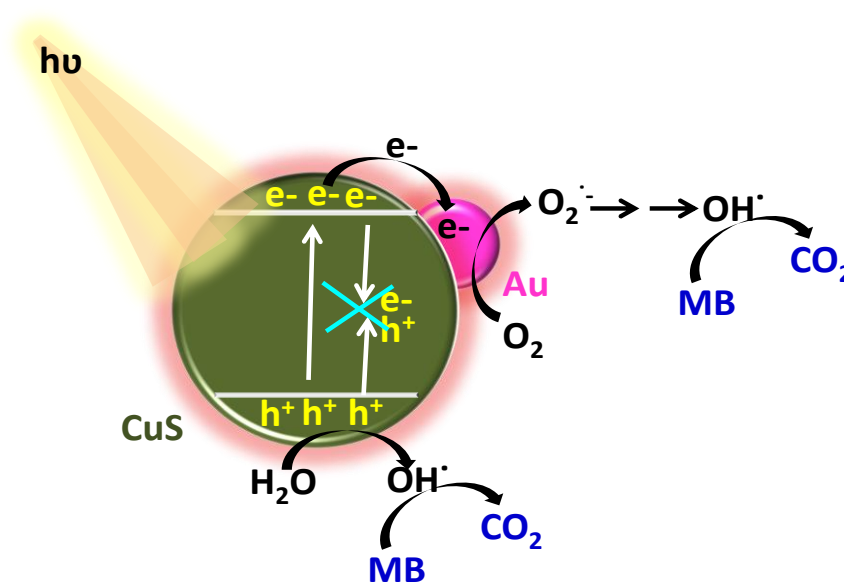
Figure 4.18: Diagrammatic representation of MB degradation under visible light irradiation on CuS decorated with Au nanoparticles

4.8. Conclusion

In summary, the Au nanoparticle decorated CuS nanoplates have been fabricated *via* photochemical reduction of Au(III) ions to Au nanoparticles on the surface of CuS plates. Significant enhancement in photocatalytic activity of CuS was observed after surface modification by Au nanoparticle. CuS-Au-3 shows the best performance in photocatalytic decomposition of MB dye under visible light. On the other hand, Au nanoparticle modified CuS nanostructure function as an efficient electrocatalyst in electrocatalytic Hydrogen evolution reaction. Au nanoparticle present on the surface of CuS functioned as electron sink, which drags photo generated electron from CuS under irradiation of visible light and facilitate the MB degradation process nearly 21 times. Whereas, upon application of external potential Au nanoparticles helps in rapid charge transfer from CuS to electrolyte to enhance the electrocatalytic performance in hydrogen evolution reaction.

4.9. References

[1] A. Fujishima, K. Honda, Nature, 238 (1972) 37-38.

[2] D. Voiry, M. Salehi, R. Silva, T. Fujita, M. Chen, T. Asefa, V.B. Shenoy, G. Eda, M. Chhowalla, Nano Lett., 13 (2013) 6222-6227.

[3] M. G. Walter, E. L. Warren, J. R. McKone, S. W. Boettcher, Q. Mi, E. A. Santori, N. S. Lewis, Chem. Rev., 110 (2010) 6446-6473.

[4] G. Wang, Y. Ling, H. Wang, L. Xihong, Y. Li, Journal of Photochem. Photobio. C: Photochem. Rev., 19 (2014) 35-51.

[5] F. E. Osterloh, Chem. Soc. Rev., 42 (2013) 2294-2320.

[6] H. M. Chen, C. K. Chen, R.-S. Liu, L. Zhang, J. Zhang, D. P. Wilkinson, Chem. Soc. Rev., 41 (2012) 5654-5671.

[7] Z. Li, W. Luo, M. Zhang, J. Feng, Z. Zou, Energy Environ. Sci., 6 (2013) 347-370.

[8] N. Furuya, S. Motoo, J. Electroanal. Chem., 88 (1978) 151-160.

[9] D. H. Youn, S. Han, J. Y. Kim, J. Y. Kim, H. Park, S. H. Choi, J. S. Lee, ACS Nano, 8 (2014) 5164-5173.

[10] Y. Yan, B. Xia, Z. Xu, X. ACS Catal., 4 (2014) 1693-1705.

[11] W. F. Chen, C. H. Wang, K. Sasaki, N. Marinkovic, W. Xu, J. T. Muckerman, Y. Zhu, R. R. Adzic, Energy Environ. Sci., 6 (2013) 943-951.

[12] K. Xu, F. Wang, Z. Wang, X. Zhan, Q. Wang, Z. Cheng, M. Safdar, J. He, ACS Nano, 8 (2014) 8468-8476.

[13] A. Ambrosi, Z. Sofer, M. Pumera, Chem. Commun., 51 (2015) 8450-8453.

[14] M. S. Faber, M. A. Lukowski, Q. Ding, N. S. Kaiser, S. Jin, J. Phys. Chem. C, 118 (2014) 21347-21356.

[15] H. Zhang, B. Yang, X. Wu, Z. Li, L. Lei, X. Zhang, ACS Appl. Mater. Interfaces, 7 (2015) 1772-1779.

[16] X. Long, G. Li, Z. Wang, H. Zhu, T. Zhang, S. Xiao, W. Guo, S. Yang, J. Am. Chem. Soc., 137 (2015) 11900-11903.

[17] D. Jasion, J. M. Barforoush, Q. Qiao, Y. Zhu, S. Ren, K. C. Leonard, ACS Catal., 5 (2015) 6653-6657.

[18] E. J. Popczun, J. R. McKone, C. G. Read, A. J. Biacchi, A. M. Wiltrout, N. S. Lewis, R. E. Schaak, J. Am. Chem. Soc., 135 (2013) 9267-9270.

[19] E. Navarro-Flores, Z. Chong, S. Omanovic, Mol. Catal. A: Chem., 226 (2005) 179-197.

[20] I. A. Raj, K. Vasu, J Appl. Electrochem., 20 (1990) 32-38.

[21] D. G. Nocera, The artificial leaf, Acc. Chem. Res. 45, 45 (2012) 767-776.

[22] M. Basu, A. K. Sinha, M. Pradhan, S. Sarkar, Y. Negishi, Govind, T. Pal, Environ. Sci. Technol., 44 (2010) 6313-6318.

[23] C. Tsai, F. Abild-Pedersen, J. K. Nørskov, Nano lett., 14 (2014) 1381-1387.

[24] K. Chang, Z. Mei, T. Wang, Q. Kang, S. Ouyang, J. Ye, ACS nano, 8 (2014) 7078-7087.

[25] S. Conejeros, I. d. P. Moreira, P. Alemany, E. Canadell, Inorg. Chem., 53 (2014) 12402-12406.

[26] L. An, L. Huang, P. Zhou, J. Yin, H. Liu, P. Xi, Adv. Funct. Mater., 25 (2015) 6814-6822.

[27] P. J. Jin, Z. Q. Yao, M. L. Zhang, Y. H. Li, H. P. Xing, J. Raman Spectrosc., 41 (2010) 222-225.

[28] Y. Du, Z. Yin, J. Zhu, X. Huang, X.-J. Wu, Z. Zeng, Q. Yan, H. Zhang, Nature commun., 3 (2012) 1177.

[29] A. Tang, S. Qu, K. Li, Y. Hou, F. Teng, J. Cao, Y. Wang, Z. Wang, Nanotechnology, 21 (2010) 285602.

[30] M. Sam, M. Bayati, M. Mojtahedi, K. Janghorban, Appl. Surf. Sci., 257 (2010) 1449-1453.

[31] M. Tanveer, C. Cao, Z. Ali, I. Aslam, F. Idrees, W. S. Khan, F. K. But, M. Tahir, N. Mahmood, CrystEngComm, 16 (2014) 5290-5300.

[32] S. Pande, S. K. Ghosh, S. Praharaj, S. Panigrahi, S. Basu, S. Jana, A. Pal, T. Tsukuda, T. Pal, J. Phys. Chem. C, 111 (2007) 10806-10813.

[33] A. Mansour, Surf. Sci. Spectra, 3 (1994) 197-201.

[34] P. Fageria, S. Gangopadhyay, S. Pande, Rsc Adv., 4 (2014) 24962-24972.

[35] Y. Lei, H. Jia, Z. Zheng, Y. Gao, X. Chen, H. Hou, CrystEngComm, 13 (2011) 6212-6217.

[36] Y. Lu, X. Liu, W. Wang, J. Cheng, H. Yan, C. Tang, J.-K. Kim, Y. Luo, Sci. Rep., 5 (2015).

[37] X. Huang, Z. Zeng, S. Bao, M. Wang, X. Qi, Z. Fan, H. Zhang, Nature commun., 4 (2013) 1444.

[38] T. Shinagawa, A. T. Garcia-Esparza, K. Takanabe, Sci. Rep., 5 (2015).

[39] A. Behranginia, M. Asadi, C. Liu, P. Yasaei, B. Kumar, P. Phillips, T. Foroozan, J.C. Waranius, K. Kim, J. Abiade, Chem. Mater., 28 (2016) 549-555.

[40] E. Kowalska, H. Remita, C. Colbeau-Justin, J. Hupka, J. Belloni, J. Phys. Chem. C, 112 (2008) 1124-1131.

[41] X. L. Yu, C. B. Cao, H. S. Zhu, Q. S. Li, C. L. Liu, Q. H. Gong, Adv. Funct. Mater., 17 (2007) 1397-1401.

[42] Z. Song, H. Lei, B. Li, H. Wang, J. Wen, S. Li, G. Fang, Phys. Chem. Chem. Phys., 17 (2015) 11790-11795.

[43] V. Subramanian, E. E. Wolf, P. V. Kamat, J. Phys. Chem. B, 107 (2003) 7479-7485.

[44] S. A. Ansari, M. M. Khan, M. O. Ansari, J. Lee, M. H. Cho, J. Phys. Chem. C, 117 (2013) 27023–27030.

[45] P. Sangpour, F. Hashemi, A. Z. Moshfegh, J. Phys. Chem. C, 114 (2010) 13955-13961.

[46] L. Jing, W. Zhou, G. Tian, H. Fu, Chem. Soc. Rev., 42 (2013) 9509-9549.

Chapter 5

RuO$_2$ nanorod: An efficient and stable electrocatalyst for hydrogen and oxygen evolution reaction

Abstract

RuO_2 nanorod, a dual catalyst for hydrogen and oxygen evolution reaction is developed *via* wet-chemical route. RuO_2 NR has been synthesized using Ru^{3+} salt, urea, and glucose followed by calcination at 500 °C for 10 h. In this study, initially a carbon slurry has been prepared using glucose and urea to get homogeneously distributed Ru^{3+} ion and then *via* calcination RuO_2 NR has been synthesized. The synthesized material has been well characterized using FESEM, TEM, PXRD, and XPS analysis. The average aspect ratio of a single RuO_2 rod is ~ 4.37. The synthesized RuO_2 NR has been used extensively for hydrogen and oxygen evolution reaction. It shows cathodic potential of -130 mV vs. RHE to achieve current density of 10 mA/cm^2 during hydrogen evolution reaction. During oxygen evolution, 1.508 V vs. RHE is required to generate 10 mA/cm^2 current density. Electrochemically active surface area and Tafel slope have been calculated to exhibit better activity of RuO_2 NR as compared to that of commercial RuO_2. The overall electrocatalysis mechanism has also been discussed in detail. The representation of formation of HER and OER is shown in scheme 5.1
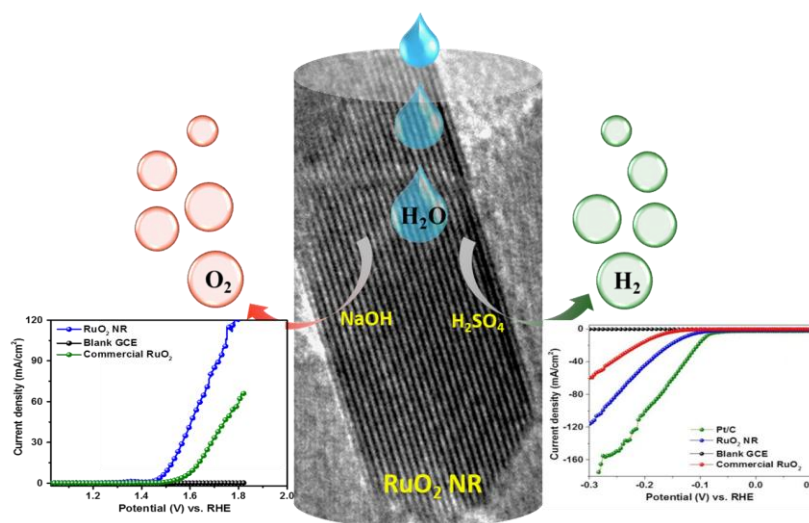
Scheme 5.1: Diagrammatic representation showing production of oxygen and hydrogen gases using RuO$_2$NR as catalyst

5.1. Introduction

Global demands for energy are increasing day by day. To meet the global energy demands and to take care of the depletion of fossil fuel reserves, there is a constant search for alternate source of energy. [1] Hydrogen is one of the cleanest renewable energy. [2] Hydrogen has highest energy density per unit mass and produces only water on combustion. [3] Electrochemical splitting of water into hydrogen and oxygen is a method for producing and storing renewable source of energy [4], which is known for more than 200 years but researchers started working for the development of efficient electrocatalysts only a decade ago. [3] Therefore, the demand for electrocatalyst, which can undergo both hydrogen and oxygen evolution reaction is constantly increasing as few are reported. [4]

Effort and progress have been made for the development of efficient, stable, and durable bifunctional catalyst for HER and OER. An important class of bifunctional catalysts for both HER and OER that have come to light in last few years are perovskite nanostructure, nickel iron sulphides on nickel foam (NiFeS/NF), Co-Mo-B nano-composition, cobalt disulfide/graphite, and NiFeOx nanoparticles. [5-10] There has been consistent efforts to design electrocatalysts, which can improve electrode kinetics and stability in different electrolyte environments. Recently, Qiao and co-workers showed 2.5 times higher hydrogen generation rate of metallic Ru than Pt in alkaline solutions. [11] RuO_2 catalysts have been pretty successful in OER using both acidic and alkaline electrolytes. However, the stability of RuO_2 in both electrolytes under high anodic potential is still a challenge because during OER RuO_2 gets readily oxidised to form soluble RuO_4. [2, 12, 13] Synthesis of RuO_2 and IrO_2 spherical nanoparticles for OER in both alkaline and acidic mediums has been reported by Horn and co-workers. [14] Both the catalysts showed incredible activities towards OER, where RuO_2 exhibits mass activity of 10 A/g at 1.48 V vs. RHE. Kokoh and co-workers synthesized a core-shell IrO_2@RuO_2 electrocatalyst for electrochemical water splitting and showed that the intimate contact of oxides attribute high accessibility of active sites than individual oxides. [15] Barman and co-workers synthesised C_3N_4 supported RuO_2 nanowires and applied for HER and OER at all pH values. They reported C_3N_4 supported RuO_2 nanowires showed improved catalytic efficiency, which is attributed to 1D morphology of RuO_2 and catalyst-support interactions. [2] RuO_2 is already a renowned catalyst for OER but it has been hardly applied for HER. Performance of HER catalysts is limited by reactivity, poor electron transport, low surface area, and instability under operating conditions,

which need to be improved for an electrocatalysts. [3,16] Zhou and co-workers developed a simple and convenient wet-chemical route for the synthesis of metal oxide (TiO_2, Fe_2O_3, Co_3O_4, ZnO, and WO_3) nanosheet via calcination at 500 ^{o}C. [17]

Being interested from the above studies, we have demonstrated a facile wet-chemical route for the synthesis of highly crystalline RuO_2 1D nanostructure without using any support. RuO_2 nanostructure was synthesized using glucose, urea, and Ru^{3+} salt as a carbon source, hydrolyzing agent, and metal precursor salt, respectively, followed by calcinations at 500 °C. The as-synthesised materials were characterised using powder x-ray diffraction, scanning electron microscopy, x-ray photoelectron spectroscopy, and transmission electron microscopy etc. techniques. To probe the catalyst efficiency, both hydrogen and oxygen evolution reaction were carried out using 0.5 M H_2SO_4 and 1.0 M NaOH as an electrolyte. RuO_2 catalyst needs cathodic potential of -130 mV to achieve current density of 10 mA/cm^2 for hydrogen evolution. Whereas, for OER 88 mV overpotential is required to gain 10 mA/cm^2 current density. The advantages of this work are multifold. First, a simple and facile methodology for exclusive formation of RuO_2 nanorod without using any support or stabilizer. Second, 1D morphology of RuO_2 has high surface to volume ratio, which create more active sites for electrocatalysis. Third, dual electrocatalytic behaviour of RuO_2 NR for HER and OER.

5.2. Experimental Section

5.2.1. Synthesis of RuO₂ nanorod

Synthesis of RuO_2 was performed in two steps. First step was pre-calcination step, where, 1.0 g of urea, 5.0 g of glucose and 2.0 mL of 0.02 M $RuCl_3.2H_2O$ were taken in a beaker and heated at 150 ^{o}C for 6 h. Black colour carbon slurry was formed. In the second step, calcinations step, the as-obtained carbon slurry was crushed and transferred in a covered silica crucible for calcination at 550 ^{o}C for 10 h using a muffle furnace. Finally, black coloured RuO_2 product was observed and used without further purification. The overall synthetic procedure of RuO_2 nanomaterial is shown in scheme 5.2.
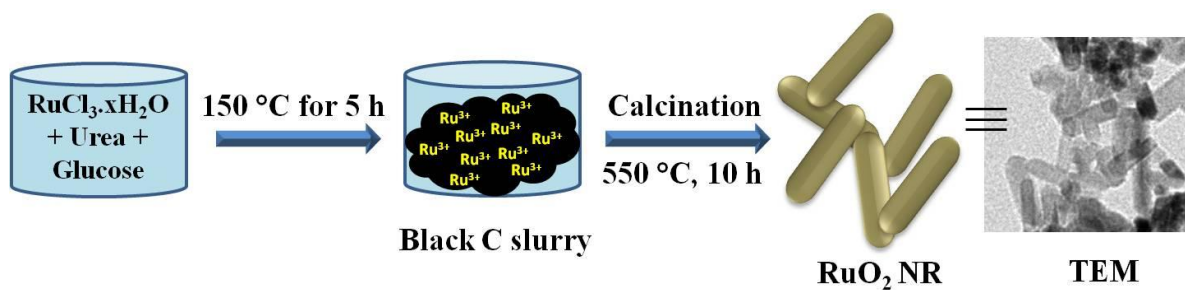
Scheme 5.2: Synthesis of RuO₂ NR *via* wet chemical route

5.3. Results and Discussion

5.3.1. Powder X-ray diffraction of RuO₂ nanorod

To determine the structural identification and phase purity of RuO_2, XRD analysis was performed. It can be seen from Figure 5.1 that the $2\theta = 28.15^o$, 35.11^o, 40.24^o, 54.43^o, 57.98^o, 59.68^o, 65.71^o, 67.29^o, 69.66^o, 74.52^o, 83.59^o and 88.18^o corresponding to (110), (101), (200), (211), (220), (002), (310), (112), (301), (202), (321), and (222) crystal planes of RuO_2, respectively (JCPDS no 88-0322). [18]
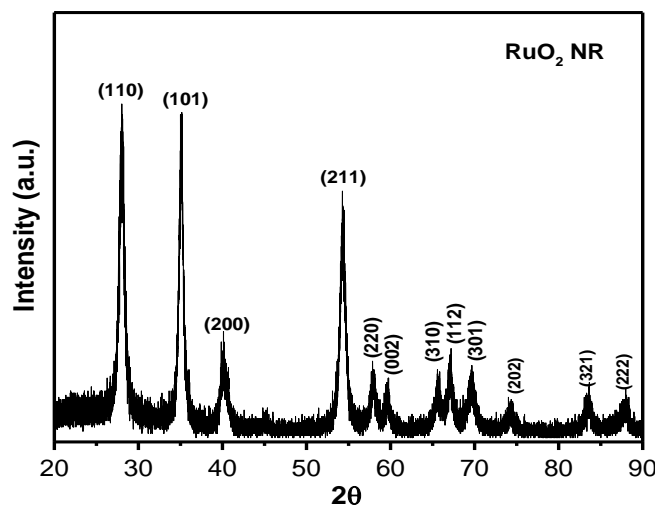
Figure 5.1: Powder X-ray diffraction patterns of RuO₂ NRs

The diffraction pattern reveals that RuO_2 is well crystallized with a rutile tetragonal structure. The synthesized RuO_2 sample is pure and there is no formation of ruthenium and other impurities, which is confirmed from XRD analysis.

5.3.2. FESEM analysis of RuO_2 nanorod

FESEM and TEM analysis were performed to elucidate the size, shape, and morphology of as-synthesized RuO_2. Well developed, uniform, and rod shaped particles are observed from FESEM analysis, shown in Fig. 5.2a and b.
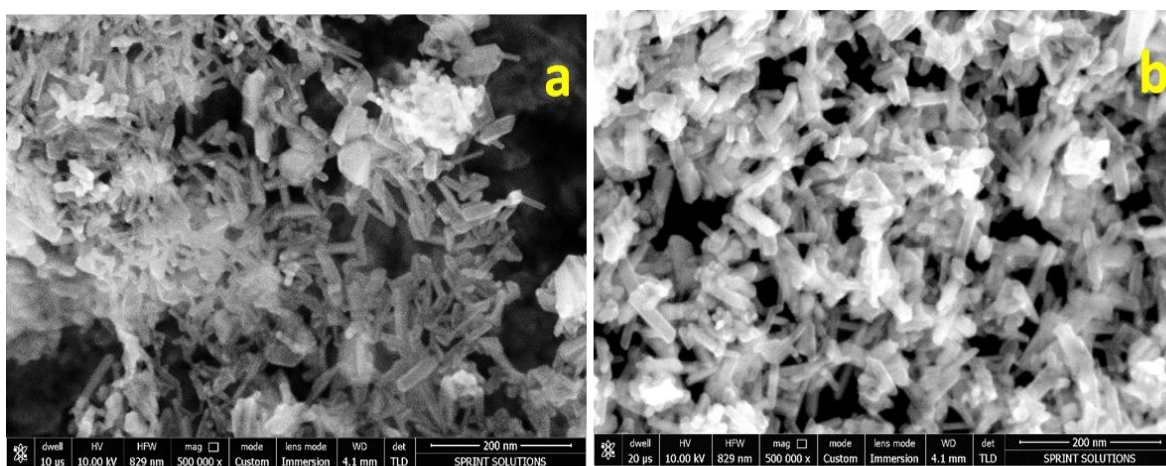
Figure 5.2: FESEM image of RuO_2 NR

Elemental mapping analysis of RuO_2 substantiates the presence of ruthenium and oxygen (Figure 5.3). More specifically, line mapping analysis of RuO_2 (Figure 5.4) also exhibits the existence of ruthenium and oxygen in RuO_2 nanostructures.

5.3.3. TEM analysis of RuO_2 nanostructure

It can be seen from Figure 5.5a that uniform and rod shaped structure of RuO_2 is formed in this synthetic procedure. The average aspect ratio of a single rod is ~ 4.37, which is shown in inset of Figure 5.5a. HRTEM image of RuO_2 NR is shown in Figure 5.5b, which clearly exhibits an interplanar spacing value, d = 0.33 nm for (110) plane of RuO_2. Therefore, the growth of rutile RuO_2 crystal occurs through (110) plane, which is corroborated with XRD analysis.
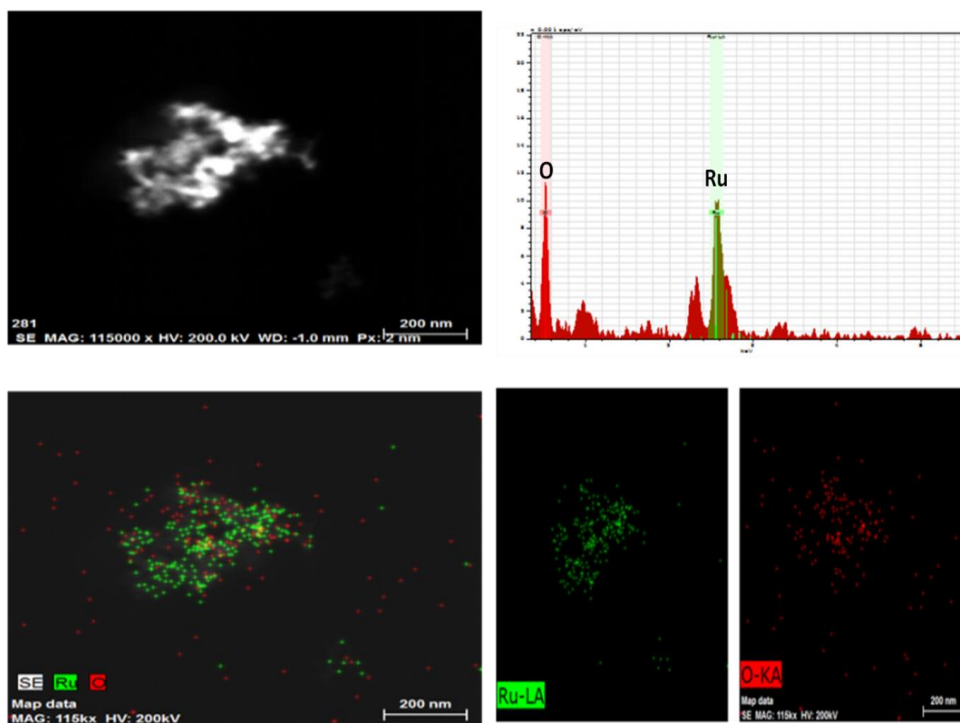
Figure 5.3: Elemental mapping analysis of RuO₂
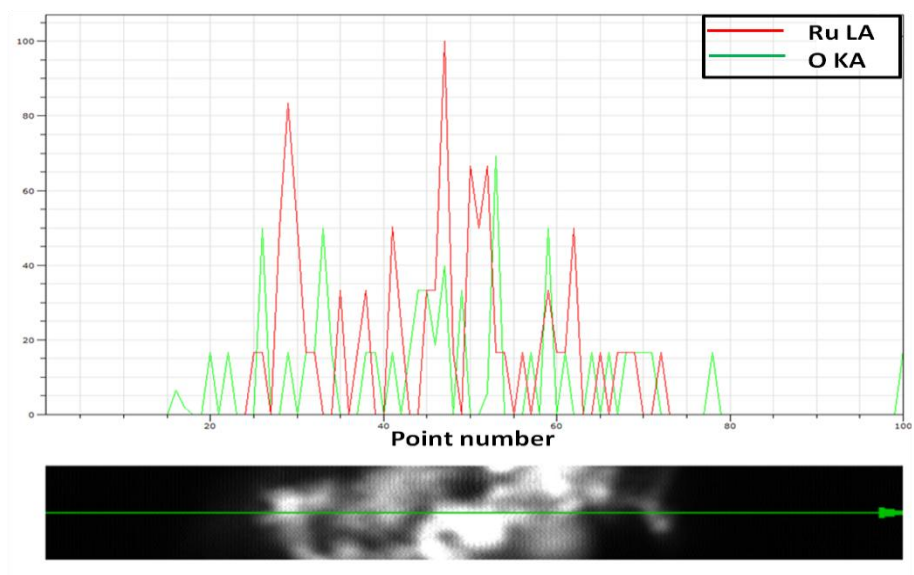
Figure 5.4: line mapping analysis of RuO₂ NR with FESEM image
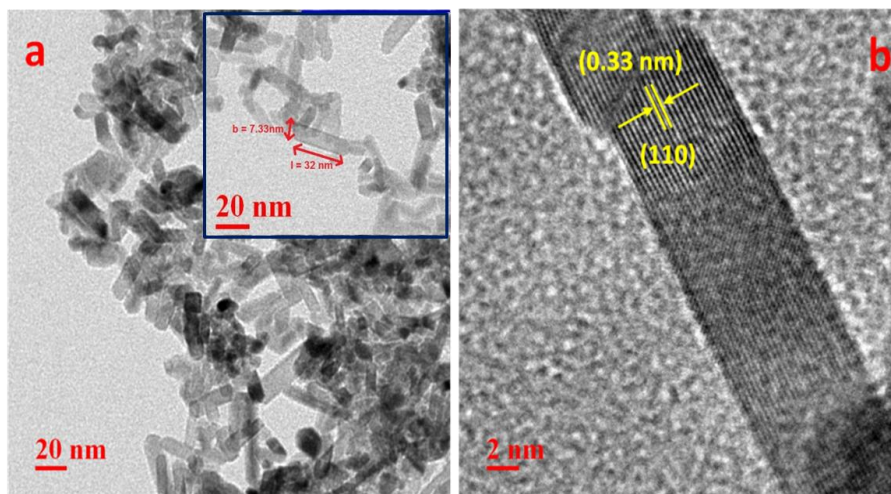
Figure 5.5: Representation of (a) TEM image of RuO₂ NRs and inset shows aspect ratio of RuO₂ NR and (b) HRTEM image of RuO₂ NR

5.3.4. X-ray photoelectron spectroscopy analysis

To understand the oxidation state of Ru in RuO$_2$ sample XPS analysis was performed. The deconvoluted XPS spectra of Ru^{4+} in RuO$_2$ is shown in Figure 5.6. It can be seen from Figure 5.6a that Ru 3d$_{5/2}$ and 3d$_{3/2}$ peaks are present at 280.36 eV and 284.36 eV, which is well matched with literature report. [19-21] The difference between the two 3d peak is 4.0 eV, well acquainted with literature. [19-20] In addition to the main 3d binding energies two satellite peaks at 282.24 eV and 286.69 eV is also present in Figure 5.6a.
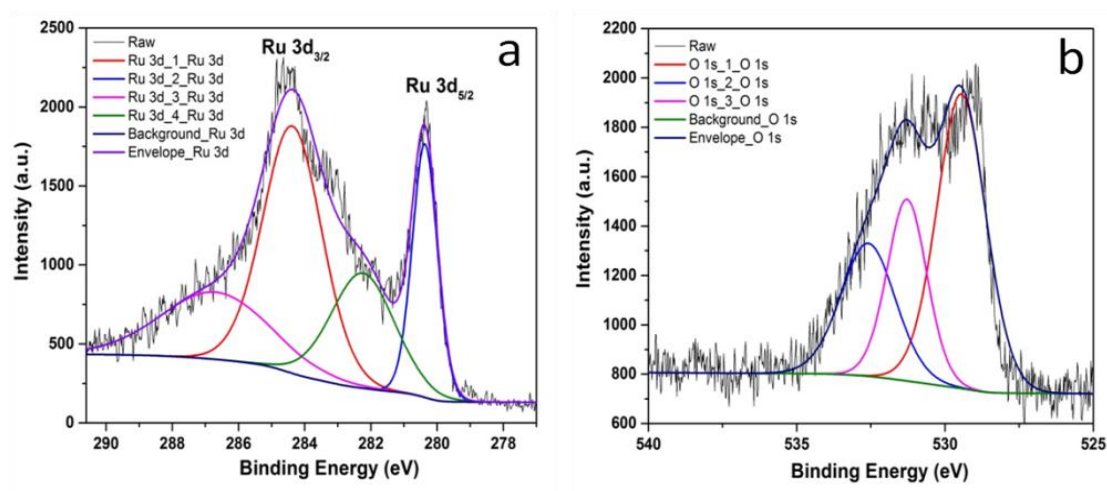
Figure 5.6: Deconvoluted XPS spectra of (a) Ru 3d and (b) Oxygen 1s

119

Similar satellite peaks in RuO_2 sample is also reported by other scientists. [20] The $O1_S$ binding energies are at 529.44 eV and 531.21 eV, (Figure 5.6b) which is due to the presence of O in RuO_2 sample or Ru-O-Ru interactions. The other peak at 532.58 eV is due to physisorbed or chemisorbed oxygen or oxygen in OH or C-O functional groups. Kwak and co-workers reported a peak at 532.4 eV, which is attributed to oxygen in OH and C-O groups. [20] The overall survey spectrum shows the peak for Ru and O, shown in Figure 5.7.
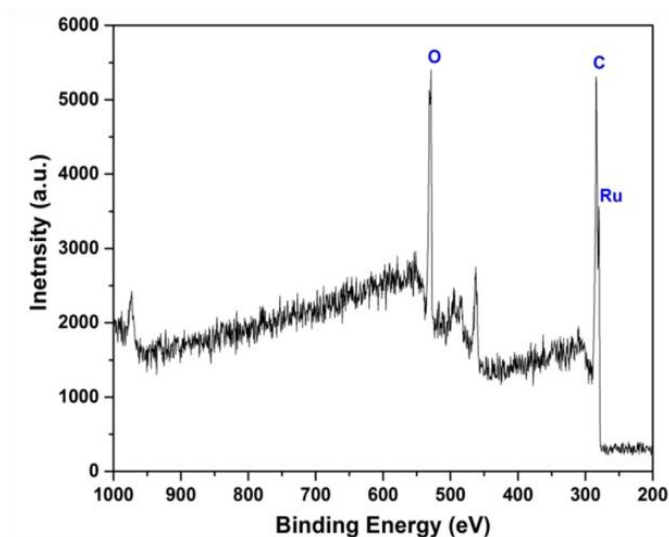
Figure 5.7: survey spectrum of RuO_2 NR

5.4. Mechanism of nanorod formation

Synthesis of RuO_2 NR occurs in two steps. First, precalcination step in which urea, glucose, and ruthenium chloride were mixed properly and the mixture was heated at 150 ^{o}C for 6 h resulting in the formation of a black carbon slurry with uniform distribution of ruthenium salt. Glucose was chosen as a low melting solid (137 ^{o}C) and converted as a molten syrup at 150 ^{o}C. The presence of rich oxygen functional group in glucose helps for the homogeneous distribution of ruthenium metal salts. On the other hand, urea also decomposes at 150 ^{o}C as its melting point is 135 ^{o}C and produced various gases. Furthermore, syrupy form of glucose undergoes polymerization and gases from urea blew the polymer to form a large bubble of carbon slurry. Therefore, during precalcination step a porous carbon slurry was obtained with uniform distribution of Ru^{3+} salt. The exposed gases from urea at 150 ^{o}C play a vital role for the

formation of large carbon slurry. To confirm the role of evolved gases from urea, only glucose and ruthenium chloride were heated at 150 ^{o}C but there was no formation of large bubble of carbon slurry. However, without urea the distribution of Ru^{3+} ions would not be uniform and difficult to follow the calcination step. Therefore, in precalcination step the role of glucose and urea are very important to get a large porous carbon slurry with uniform distribution of Ru^{3+} ions. Zhou and co-workers reported the synthesis of metal oxide nanosheet with large area *via* calcination using glucose, urea, and corresponding metal procurer salts. [17] Second, calcination step, the as-obtained porous carbon slurry has been crushed and poured in a covered silica crucible and kept in a muffle furnace at 550 ^{o}C for 10 h. To check the growth morphology of RuO_2 NR during calcination step, the sample was also collected after 3 h and 6 h. FESEM and PXRD analysis have been performed for 3 h and 6 h samples. It can be seen from PXRD (Figure 5.8) analysis that the formation of RuO_2 occurs even after 3 h but the peak intensity is less and few peaks are not even clear. PXRD of 6 h sample is slightly better in terms of peak intensity than 3 h sample but still less than 10 h sample. From Figure 5.8 it is quite evident that 10 h sample of RuO_2 NR is having prominent peaks with high intensity and crystallinity as compared to 3 h and 6 h sample. Therefore, the formation of RuO_2 nanomaterials occur at 3 h which continues for 6 h and 10 h. To confirm the morphology of RuO_2 at different time intervals FESEM analysis was performed. It can be seen from Figure 5.9 that the seed formation started after 3 h of calcination at 550 ^{o}C.
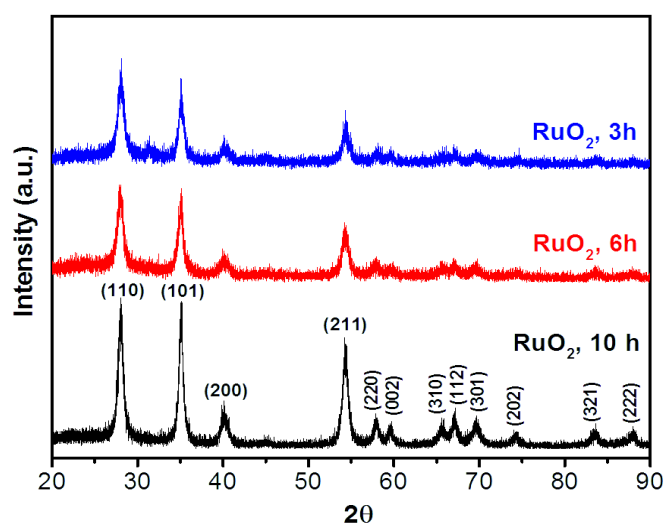
Figure 5.8: PXRD of RuO$_2$ sample after 3 h, 6 h, and 10 h of calcination

After 6 h of heating uniform growth of RuO_2 sample occur, which exhibits the formation of small rod shaped morphology. Further calcination up to 10 h shows the complete growth and formation of rod shaped particle with an aspect ratio of ~ 4.37. It has been observed from HRTEM analysis of RuO_2 NR that the growth is uniform. The overall growth of RuO_2 NR in different calcination time is shown in Figure 5.9.
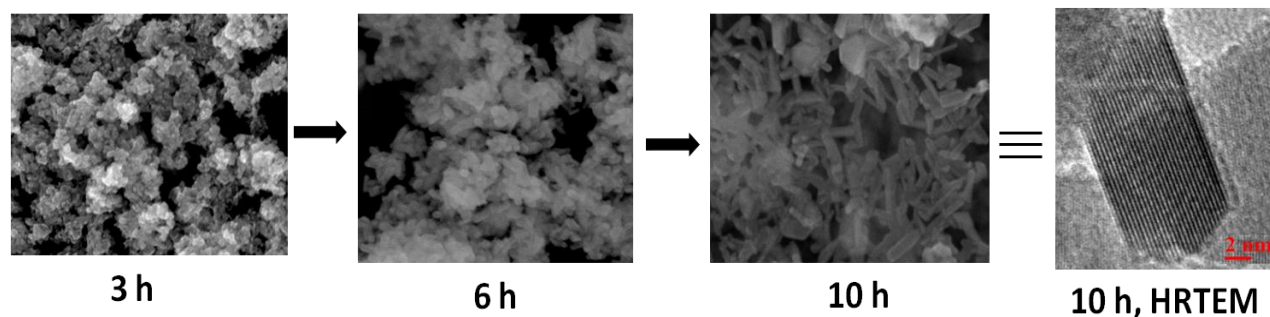
Figure 5.9: FESEM images of RuO_2 after 3 h, 6 h, and 10 h of calcination

5.5. Hydrogen evolution reaction

To functionalize the GCE surface, an ink was prepared with 1.0 mg RuO_2, 100.0 μL of isopropyl alcohol, and 20.0 μL nafion. Using this freshly prepared ink 3.0 μL catalyst suspension was drop casted onto GCE and dried in air. The amount of catalyst loaded on the GCE surface was ~0.357 mg/cm^2. Prior to use GCE was cleaned properly using 1.0 μm, 0.3 μm and 0.05 μm alumina slurry in three different polishing cloth. After cleaning the polished GCE was sonicated in millipore water for 10 min and dried in nitrogen gas flow.

5.5.1. LSV study of bare GC, RuO_2 NR, commercial RuO_2, and Pt/C catalyst for hydrogen evolution reaction

 All the electrochemical measurements for hydrogen evolution reaction were conducted in 0.5 M H_2SO_4 aqueous solution following linear sweep voltamogram (LSV) technique with scan rate of 10 mV/s. Potentials were measured with respect to Ag/AgCl electrode and reported with respect to RHE. RuO_2 NRs require only 130 mV cathodic potential to achieve current density 10 mA/cm^2 (Figure 5.10 a and b).
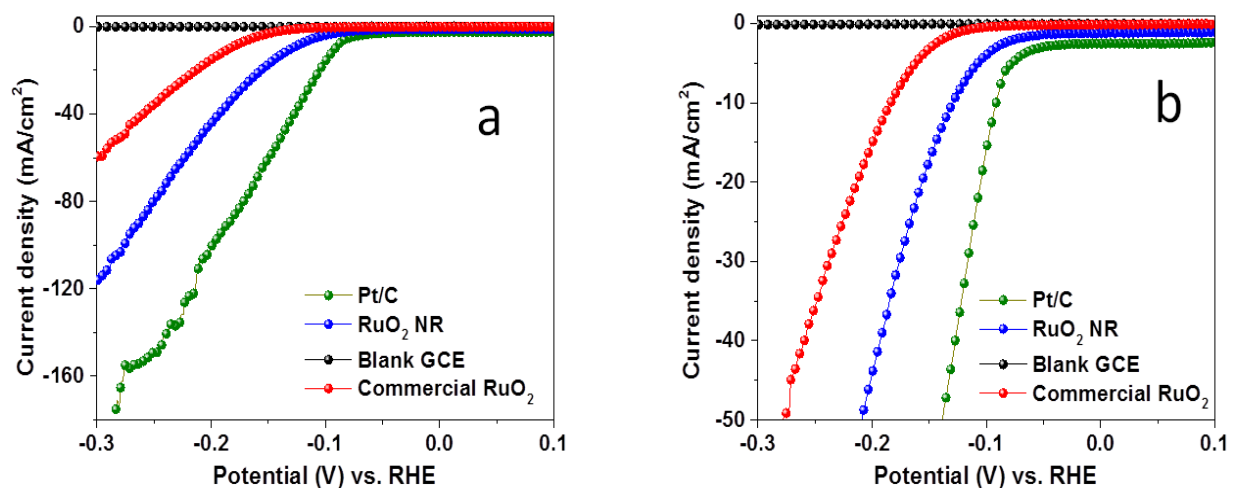
Figure 5.10: Linear sweep voltammogram of bare GCE, commercial RuO_2, RuO_2 NR, and 5% Pt/C in (a) high scale and (b) low scale for HER

Catalytic activity for HER of the as-synthesized RuO_2 NR is compared with the commercial RuO_2. Commercial RuO_2 requires potential of -184 mV to achieve current density of 10 mA/cm². This result significantly suggest that the synthesized RuO_2 NR is catalytically more active compared to the commercially available RuO_2 which needs 54 mV more cathodic potential to generate a current density 10 mA/cm² as compared to RuO_2 NR. Pt is known as the most efficient electrocatalyst for HER. Here catalytic activity of RuO_2 NR is compared with Pt/C (5%) and is shown in Fig. 5.10a and b. Pt/C (5%) can generate 10 mA/cm² current density upon application of -92 mV potential vs. RHE. The comparative study of various kinetic parameters of RuO_2 NR with commercial RuO_2, and Pt/C catalyst is shown in table 5.1. To have an in depth understanding on the superior electrocatalytic activity of RuO_2 NR compared to commercial RuO_2, electrochemically active surface area was determined for both the samples. To determine ECSA, first cyclic voltammogram was carried out for RuO_2 NR (Figure 5.11a) and commercial RuO_2 (Figure. 5.11b) at the potential range of 0.2157 to 0.1157 V vs. RHE. To determine the double layer capacitance (C_{dl}), current at a fixed potential of 0.1657 V vs. RHE was plotted against scan rate (Fig. 5.11c) which gives a straight line and the slope provides the value of C_{dl}. Double layer capacitance value for RuO_2 NR is 0.909 mF, whereas, for commercial RuO_2 the value is 0.277 mF.

Table 5.1 The detailed comparison of the electrocatalytic activity of RuO_2 NR, commercial RuO_2, and Pt/C catalyst.

Catalyst	Mass loading mg/cm^2	Mass Activity (A/g) at - 0.2 V	Potential required to generate 10 mA/cm^2	ECSA (cm^2)	Roughness factor (R_f)	Tafel slope (mV/dec)
Pt/C	0.357	281.33	-92 mV			33
Commercial RuO$_2$	0.357	42.60	-184 mV	4.61	65.02	82
RuO$_2$ NR	0.357	124.61	-130 mV	15.15	213.38	71.5

ECSA is calculated from the C_{dl} and the values are 15.15 cm^2 and 4.61 cm^2 for RuO_2 NR and commercial RuO_2, respectively. Roughness factor (R_f) is also calculated for RuO_2 NR and commercial RuO_2 from ECSA and the values are reported as 213 and 65, respectively. Higher the ECSA and roughness factor indicates the efficient electrocatalytic activity of RuO_2 NR. Therefore, RuO_2 NR has more exposed electrochemically active surface area as compared to commercial RuO_2 during HER activity. To have deeper understanding on the efficient activity of RuO_2 NR, mass activity is calculated at a fixed potential of -0.2 V vs. RHE. Mass activity values for RuO_2 NR, commercial RuO_2, and Pt/C (5%) are 124.61 A/g, 42.60 A/g, and 281.33 A/g, respectively. Therefore, from the mass activity value it is again clear that the efficient electrocatalyst is RuO_2 NR than commercial RuO_2. All the electrochemical values for hydrogen evolution are summarized in (Table 5.1). A detailed HER comparison of our catalyst with other ruthenium based catalysts is shown in table 5.2. Stability and morphology of an electrocatalyst on electrode surface during hydrogen evolution is very important. Here, we have checked the stability of RuO_2 NR by continuous run of LSV technique. The stability of RuO_2 NR was checked up to1000 continuous cycles and the LSV curve of the initial and after 1000 cycles is shown in Figure 5.12. It can be seen from Figure 5.12 that there is no significant difference between the initial and final cycle LSV run, which confirms the robustness of the catalyst on electrode surface in strong acid medium. Furthermore, after electrocatalysis the morphology of RuO_2 NR was checked with the help of TEM analysis, shown in Figure 5.13. There is no change in rod shaped morphology of RuO_2 before and after electrocatalysis.
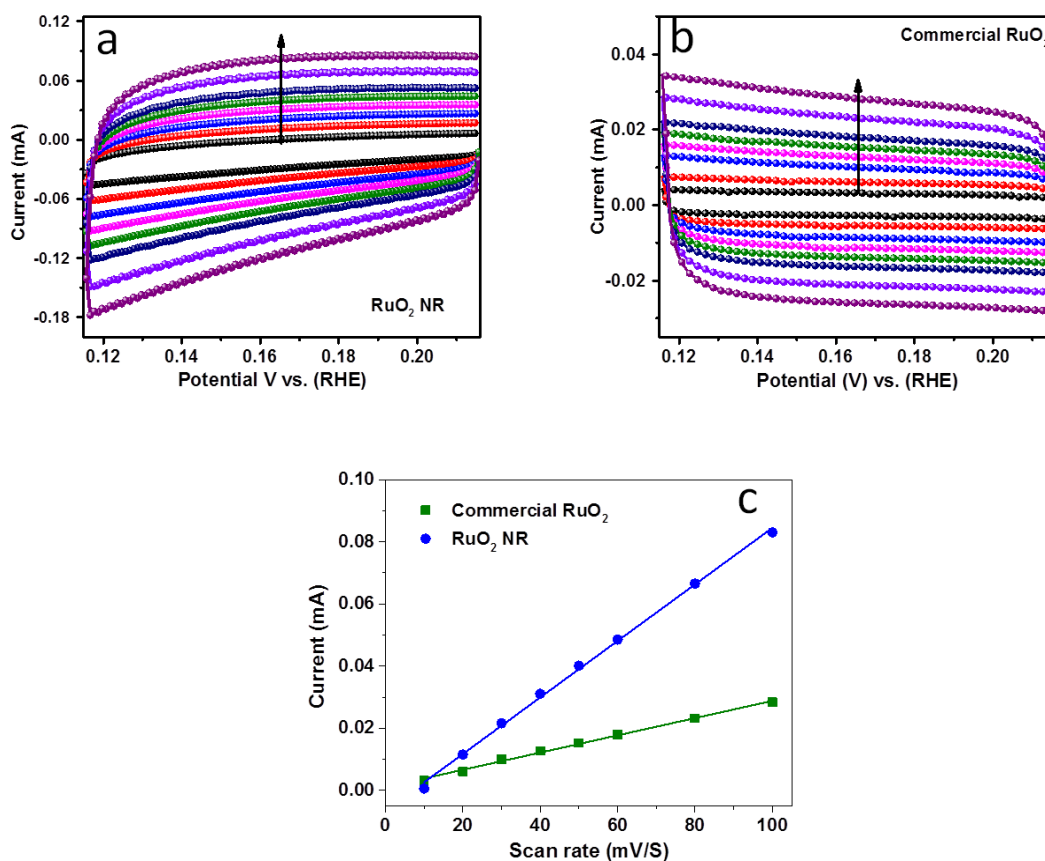
Figure 5.11: **CV measurements of (a) RuO$_2$, (b) commercial RuO$_2$ and (c) Current vs. scan rate plot for RuO$_2$ NR and commercial RuO$_2$**

5.5.2. Detailed mechanism of hydrogen evolution reaction

To validate the overall performance of a catalyst, calculation of Tafel slope is important which helps to determine the mechanism of the electrocatalytic hydrogen evolution reaction. In order to calculate the Tafel slope the linear portion of the Tafel plots is to be fitted in the Tafel equation (η = b log (J) + a, where η = overpotential, b = Tafel slope, and J = current density). [22, 23] The value of Tafel slope is 71.5 mV/dec and 84 mV/dec for RuO$_2$ NR and commercial RuO$_2$, respectively (Figure 5.14). Whereas, Tafel slope value for Pt/C (5%) is 33 mV/dec, which is well matched with literature report. [6, 24-26] Lower the Tafel slope value of Pt/C shows best activity in hydrogen evolution, which is well acquainted in the literature.

Table 5.2: Comparative study of RuO$_2$NR with other Ru based electrocatalysts

Catalyst	Substrates	Medium	Current density (mA cm^{-2}) at any specific over potential	Over potential (mV) at 10 mA cm^{-2}	Tafel slope	Ref.
r-RuO$_2$ NPs (OER)	GCE	0.1 M HClO$_4$	10 A/g oxide @ 1.48 V	-	-	[9]
Ru$_x$Ir$_{1-x}$O$_2$ (OER)	Ti	0.5M H$_2$SO$_4$	1 @ 240 mV	-	39	[32]
IrO$_2$@RuO$_2$ (OER)	Au	0.5M H$_2$SO$_4$	11 @ 270 mV	-	50	[10]
Ru$_{0.2}$Ir$_{0.8}$O$_2$ (OER)	gold disk	0.5M H$_2$SO$_4$	-	1.62 (V)	-	[33]
1D-RuO$_2$-CN$_x$ (OER)	GC	0.5 M KOH	-	260	56	[2]
1D-RuO2-CNx (HER)	GCE	0.5 M KOH	-	-93	70	[2]
Ru/C$_3$N$_4$/C (HER)	GCrotating disk	0.5 M H$_2$SO$_4$	-	79		[6]
RuO$_2$ NR (HER)	GCE	0.5 M H$_2$SO$_4$	-	-130	71	This work
RuO$_2$ NR (OER)	GCE	1M NaOH	-	78.4	92	This work
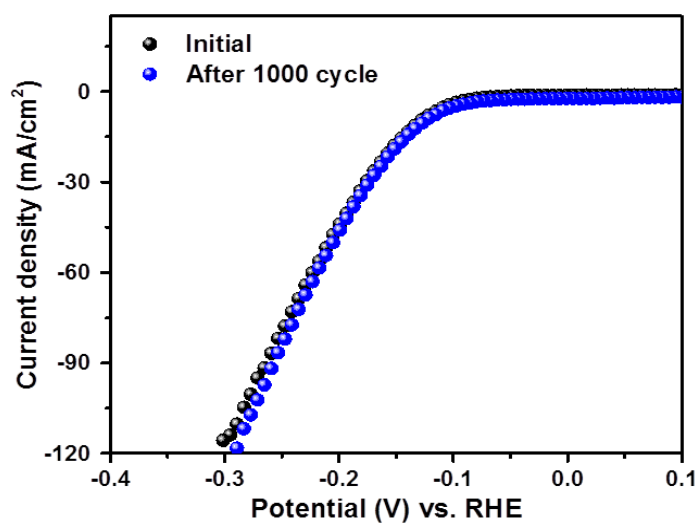
Figure 5.12: LSV curve of the initial and after 1000 cycles in a strong acid
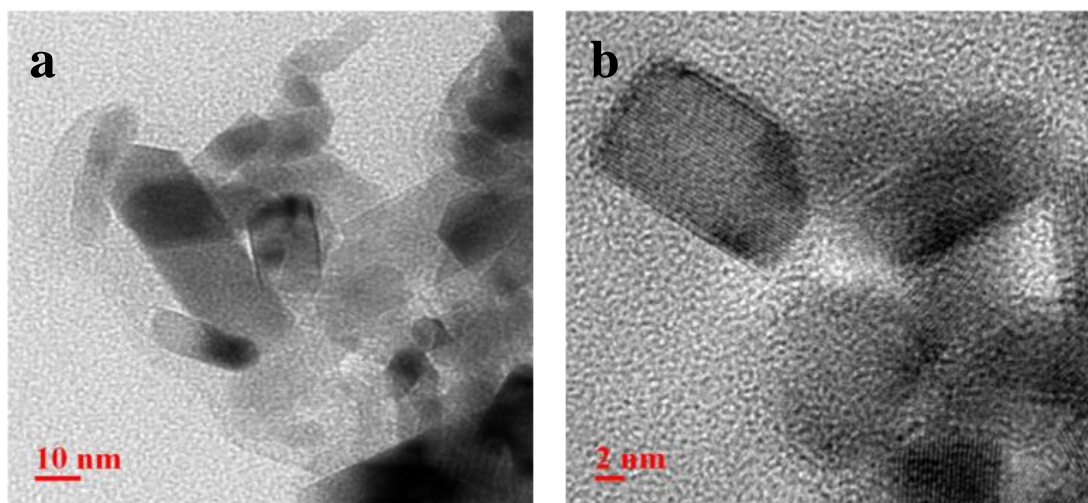
Figure 5.13: TEM analysis after electrocatalysis (a) low resolution and (b) high resolution

In comparison with commercial RuO_2, RuO_2 NR shows lower Tafel slope value that confirms the superior activity towards the hydrogen evolution reaction. All the Tafel slope values are summarized in table 5.1. There are two pathways for evolution of hydrogen gas during HER reaction in an acidic medium. The first step is the discharge step and also known as Volmer reaction, where, an electron is transferred to proton or H_3O^+ and lead to the formation of RuO_2-Hads.
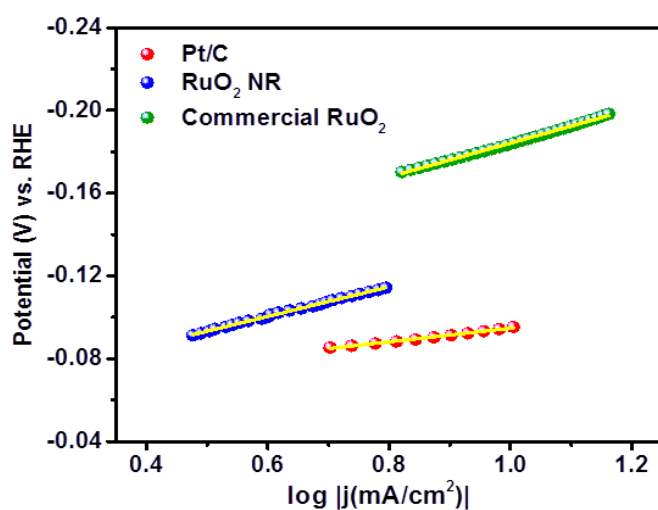
Figure 5.14: Tafel slope values for commercial RuO_2, RuO_2 NR, and 5% Pt/C

The other two steps are the reaction may follow a desorption step also known as Heyrovsky reaction, where, the already absorbed hydrogen atom on the surface of catalyst combine with H_3O^+ to form hydrogen gas. Elsewhere, the reaction may follow recombination step or Tafel reaction, where, the absorbed hydrogen on catalyst surface may combine to form hydrogen gas. The Volmer, Heyrovsky, and Tafel reaction steps are shown below. In both the cases, larger surface area of the catalyst increased the extent of absorption, which leads evolution of more hydrogen gas. If the Tafel slope values are 120 mV/dec, 40 mV/dec, and 30 mV/dec then the rate determining step of the HER reaction is the Volmer step, Heyrovsky step, and Tafel step, respectively. [27] In this study, Tafel slope value of RuO_2 NR (71.5 mV/dec) suggest that HER reaction follows Volmer-Heyrovsky mechanism with Heyrovsky as rate determining step.

$$RuO_2 + H_3O^+ + e^- \longrightarrow RuO_2\text{-}H_{abs} + H_2O \text{ (Volmer reaction)}$$

$$RuO_2\text{-}H_{abs} + H_3O^+ + e^- \longrightarrow RuO_2 + H_2 + H_2O \text{ (Heyrovsky reaction)}$$

$$RuO_2\text{-}H_{abs} + RuO_2\text{-}H_{abs} \longrightarrow RuO_2 + H_2 \text{ (Tafel reaction)}$$

5.5.3. Electrochemical impedance spectroscopy analysis

Electrochemical impedance spectroscopy measurement study was carried out to exhibit the higher activity of RuO_2 NR. The EIS study is helpful to understand the ease of electron transportation from the electrode surface to the electrolyte. The Nyquist impedance measurement for RuO_2 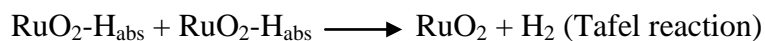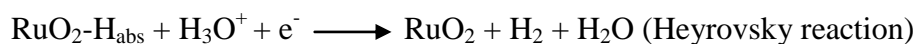NR and commercial RuO_2 samples were carried out at their respective onset potential and in 0.5 M H_2SO_4 medium, shown in Figure 5.15. This semicircle represents resistance due to charge transfer. Evaluated data can be fitted using the equivalent circuit composed of one constant phase element (CPE), solution resistance (R_S), and charge transfer resistance (R_{CT}) between electrode surface to electrolyte. All the resistance values are summarized in table 5.3. Solution resistance for both the materials are almost similar, 9.58 Ω and 10.09 Ω for comm. RuO_2 and RuO_2 NR, respectively. However, it can be seen from table 5.3 that the R_{CT} value for RuO_2 NR is 20.44 Ω, lower than commercial RuO_2 (23.58 Ω). Lowering of R_{CT} value for RuO_2 NR indicates that there is easy, faster charge transfer, and more electrocatalytically active than commercial RuO_2. EIS measurement of RuO_2 NR is well matched with electrocatalytic result.
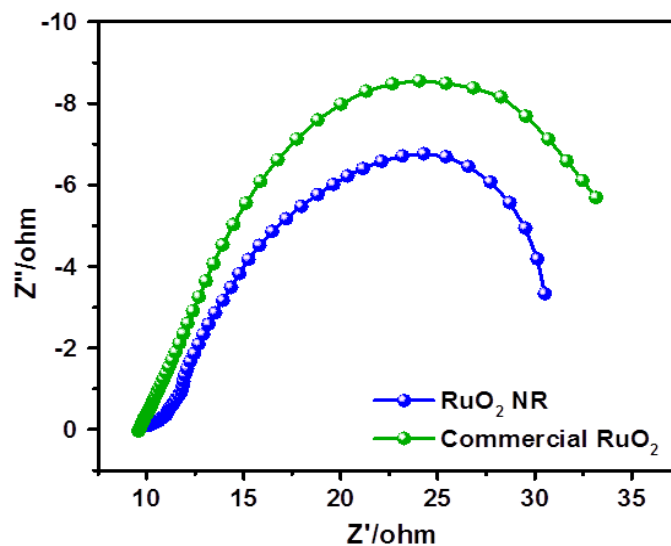
Figure 5.15: Electrochemical impedance measurement plot for RuO$_2$ NR and commercial RuO$_2$

Table 5.3: Charge transfer resistances (R$_{CT}$) values of RuO$_2$ NR and commercial RuO$_2$

Catalyst	R$_s$ (Ω)	R$_{ct}$ (Ω)
RuO$_2$ NR	10.09	20.44
Commercial RuO$_2$	9.58	23.58

5.6. Oxygen evolution reaction

5.6.1. LSV study of bare GC, RuO$_2$ NR, and commercial RuO$_2$ for OER

The activity of RuO$_2$ NR for OER was studied by using linear-sweep voltammetry. All the electrochemical measurements were conducted in 1.0 M NaOH aqueous solution with scan rate of 10 mV/s. Potentials were measured with respect to Ag/AgCl electrode and reported as RHE electrode. The current densities are normalized to the geometric surface area of the electrode. It can be seen from Figure 5.16a and b that RuO$_2$ NR exhibit two anodic oxidation peak. The first peak located at 1.24 V vs. RHE for the oxidation of Ru(IV) to Ru(VI) or Ru(VIII). During anodic potential sweep higher valence state of Ru at metal-electrolyte interface is well matched with literature. [18-30] Kötz and co-workers reported the higher valence state of Ru species

during oxygen evolution reaction in alkaline medium. [31] The second peak centred at 1.41 V vs. RHE is due to the oxidation of water. During electrocatalysis it is noted that the potential of 1.50 V vs. RHE is required to generate 10 mA/cm^2 using RuO_2 NR, whereas, for commercial RuO_2 1.61 V vs. RHE is required. Within this potential window bare GCE does not show any catalytic activity. Successive increase of current density has been observed with further applied potential. Therefore, RuO_2 NR is more catalytically active than commercial RuO_2. To show higher electrocatalytic activity of RuO_2 NR mass activity of both RuO_2 samples has been calculated at a potential of 1.65 V vs. RHE. The mass activity values are 52.49 A/g and 177.56 A/g for commercial RuO_2 and RuO_2 NR, respectively. Therefore, higher value of mass activity represents an efficient electrocatalyst for water oxidation. To exhibit the superior activity of RuO_2 NR Tafel slope value was calculated from the polarization curve. Figure 5.17 shows the Tafel slope value of RuO_2 NR is 92.6 mV/dec, whereas, for commercial RuO_2 Tafel slope is 122 mV/dec. The lower Tafel slope value of RuO_2 NR indicates remarkably high electrocatalytic activity, ease of charge transportation, and suggest electrolyte to penetrate and attach with the surface active site of catalyst. The stability of RuO_2 NR on electrode surface in alkaline medium was checked up to 500 continuous cycles and the result is reported in Figure 5.18. The negligible change in current density and onset potential of initial and final LSV was observed, which dictates the robustness of the catalyst in a highly alkaline condition.
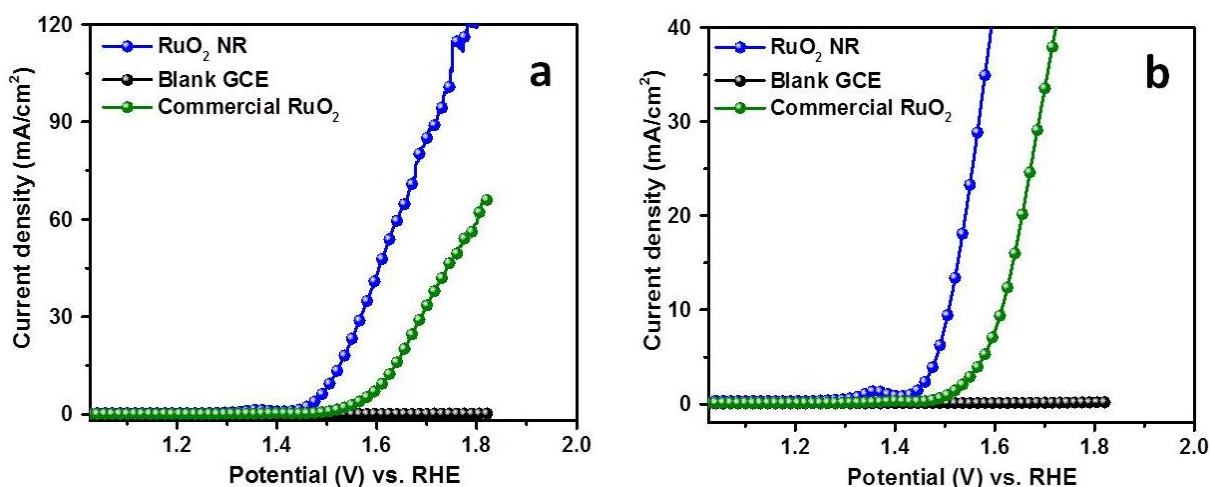
Figure 5.16: Linear sweep voltammogram curve of bare GCE, commercial RuO_2, RuO_2 in (a) high scale (b) low scale for OER
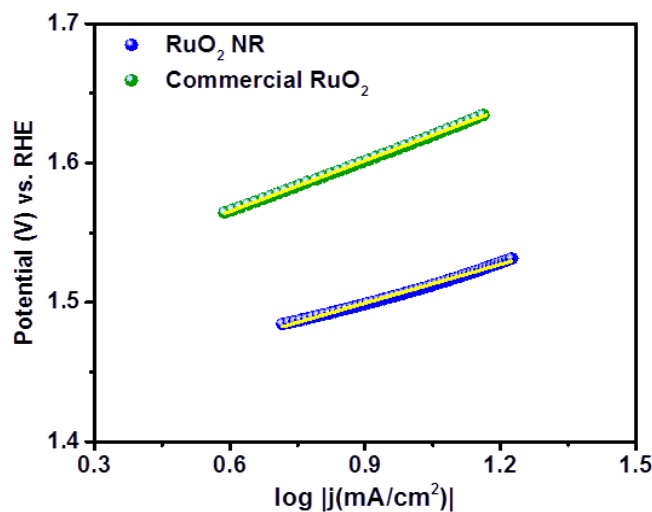
Figure 5.17: Tafel slope values for commercial RuO$_2$ and RuO$_2$ NR

A detailed comparison of all the electrochemical kinetic parameters of our catalysts with ruthenium based metal oxides in both HER and OER are shown in Table 5.2. From the table it is evident that our synthesized RuO$_2$ NR is comparable in OER and HER activity with other RuO$_2$ based morphology.

5.6.2. Electrochemical impedance spectroscopy for OER

To know the charge transportation between electrode and electrolyte EIS analysis was performed at the respective onset potentials in 1.0 M NaOH. Figure 5.19 shows the Nyquist plot
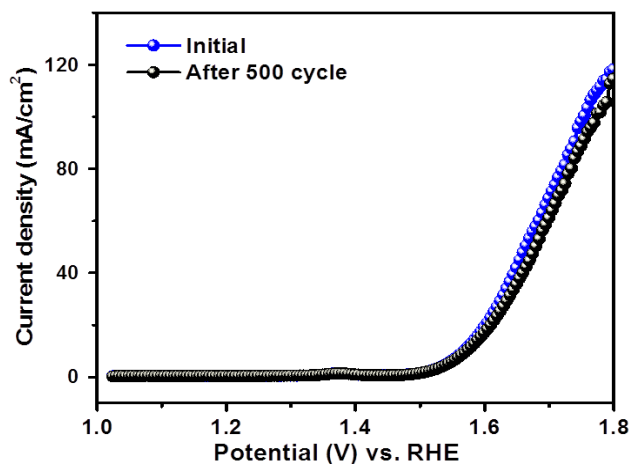
Figure 5.18: LSV curve of the initial and after 1000 cycles in a strong base

of both RuO$_2$ NR and commercial RuO$_2$. From the plot it is clear that in case of RuO$_2$ NR there is a diffusion part along with the charge transfer. Observed charge transfer resistance of RuO$_2$ NR is only 3.8 Ω whereas in case of commercial RuO$_2$ it is 67.82 Ω. Lower the charge transfer resistance value indicates the higher electrocatalytic activity of RuO2 NR compared to commercial RuO$_2$ in OER.
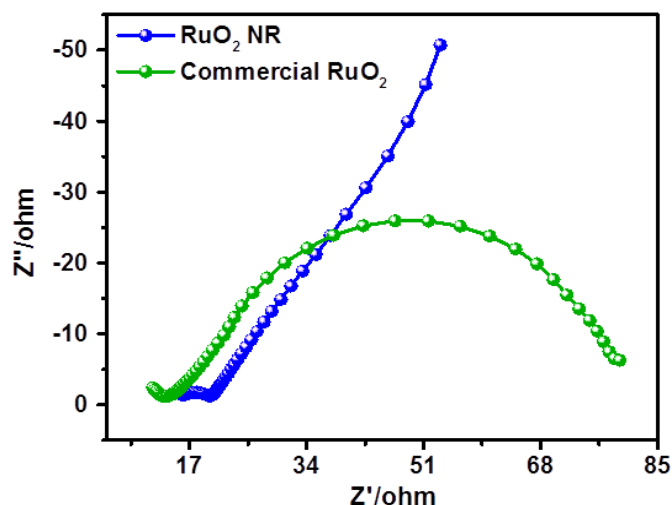
Figure 5.19: Electrochemical impedance measurement plot for commercial RuO$_2$ and RuO$_2$ NR

5.7. Conclusion

In conclusion, a simple and facile thermal methodology for the synthesis of highly crystalline 1D RuO$_2$ NR without using any support. RuO$_2$ nanorod samples have been characterized by XRD, XPS, FESEM, and TEM analysis. The growth mechanism of RuO$_2$ nanorod formation has been confirmed from FESEM analysis. RuO$_2$ NR showed excellent electrocatalytic activity for both hydrogen and oxygen evolution reaction. In HER, lower (71.5 mV/dec) Tafel slope value of RuO$_2$ NR suggest that HER reaction follows Volmer-Heyrovsky mechanism with Volmer is rate determining step. The Tafel slope value of RuO$_2$ NR is 92.6 mV/dec in oxygen evolution reaction. Therefore, this catalyst proved to be a prominent substitute of other oxide and sulphide nanomaterials in HER and OER.

5.8. References

[1] M. S. Dresselhaus and I. L. Thomas, Nature, 414 (2001) 332-337.

[2] T. Bhowmik, M. K. Kundu and S. Barman, ACS Appl. Mater. Interfaces, 8(2016) 28678-28688.

[3] C. G. Morales-Guio, L. A. Stern and X. Hu, Chem. Soc. Rev., 43 (2014) 6555-6569.

[4] L. A. Stern, L. Feng, F. Song and X. Hu, Energy Environ. Sci., 8 (2015) 2347-2351.

[5] H. Wang , H. Lee, Y. Deng, Z. Lu, P. Hsu, Y. Liu, D. Lin and Y. Cui, Nat. Commun., 6 (2015) 7261.

[6] P. Ganesan, A. Sivanantham and S. Shanmugam, J. Mater. Chem. A., 4 (2016) 16394-16402.

[7] Y. Zhu, W. Zhou, Y. Zhong, Y. Bu, X. Chen, Q. Zhong, M. Liu, and Z. Shao, Adv. Energy Mater., 7 (2017) 1602122.

[8] Y. Tong, X. Yu, G. Shi, Phys. Chem. Chem. Phys., 19 (2017) 4821-4826.

[9] S. Gupta, N. Patel, R. Fernandes, S. Hanchate, A. Miotello and D.C. Kothari, Electrochim. Acta. 232 (2017) 64-71.

[10] Y. Jia, L. Zhang, G. Gao, H. Chen, B. Wang, J. Zhou, M. T. Soo, M. Hong, X. Yan, G. Qian, J. Zou, A. Du, and X. Yao, Adv. Mater., 29 (2017) 1700017.

[11] Y. Zheng, Y. Jiao, Y. Zhu, L. Hua Li, Y. Han, Y. Chen, M. Jaroniec, S. Z. Qiao, J. Am. Chem. Soc.,138 (2016) 16174-16181.

[12] R. Frydendal, E. A. Paoli, B. P. Knudsen, B. Wickman, P. Malacrida, I. E. L. Stephens and I. Chorkendorff, ChemElectroChem, 1 (2014) 2075-2081.

[13] N. Hodnik, P. Jovanovic, A. Pavlisic, B. Jozinovic, M. Zorko, M. Bele, V. S. Selih, M. Sala, S. Hocevar and M. Gaberscek, J. Phys. Chem. C, 119 (2015) 10140-10147.

[14] Y. Lee, J. Suntivich, K. J. May, E. E. Perry and Y. S-Horn, J. Phys. Chem. Lett., 3 (2012) 399-404.

[15] T. Audichon, T. W. Napporn, C. Canaff, C. U. Morais, C. M. Comminges and K. B. Kokoh, J. Phys. Chem. C, 120 (2016) 2562-2573.

[16] H. Over, Chem. Rev., 112 (2012) 3356-3426.

[17] Y. Zhou, G. Chen, Y. Yu, C. Yan, J. Sun and F. He, J. Mater. Chem. A, 4 (2016) 781-784.

[18] A. Ananth, M. S. Gandhi and Y. S. Mok, J. Phys. D: Appl. Phys., 46 (2013) 155202.

[19] G. Wang, C.-S. Hsieh, D.-S. Tsai, R.-S. Chen, and Y.-S. Huang, J. Mater Chem. 14 (2004) 3503-3508.

[20] K.-H. Kwak, D. W. Kim, Y. Kang and J. Suk, J. Mater. Chem. A, 4 (2016) 16356-16367.

[21] P. A. Cox, J. B. Goodenough, P. J. Tavener, D. Telles and R. G. Egdell, J. Solid State Chem., 62 (1986) 360-370.

[22] T. Shinagawa, A. T. Garcia-Esparza and K. Takanabe, Sci. Rep., 5 (2015) 13801.

[23] A. Behranginia, M. Asadi, C. Liu, P. Yasaei, B. Kumar, P. Phillips, T. Foroozan, J. C. Waranius, K. Kim, J. Abiade, R. F. Klie, L. A. Curtiss and A. Salehi-Khojin, Chem. Mater., 28, 2016, 549-555.

[24] S. Anantharaj, P. E Karthik, B. Subramanian, and S. Kundu, ACS Catal., 6 (2016) 4660-4672.

[25] M. Basu, R. Nazir, C. Mahala, P. Fageria, S. Chaudhary, S. Gangopadhyay, and S. Pande, Langmuir, 33 (2017) 3178-3186.

[27] R. Nazir, P. Fageria, M. Basu, and S. Pande, J. Phys. Chem. C, 121 (2017) 19548-19558

[28] B. E. Conway, and B. V. Tilak, Electrochim. Acta, 47 (2002) 3571-3594.

[29] L. D. Burke, O. J. Murphy, J. F. O'Neill and S. Venkatesan, J. Chem. Soc., Faraday Trans. 1, 73 (1977) 1659.

[30] A. Damjanovic, A. Dey and J. O. M. Bockris, Electrochim. Acta, 11 (1966) 791. (c) G. Lodi, E. Sivieri, A. Battisti and S. Trasatti, J. Appl. Electrochem., 8 (1978)135-143.

[31] R. Kötz, H. J. Lewerenz and S. Stucki, J. Electrochem. Soc., 130 (1983) 825-829.

[32] F. I. Mattos-Costa, P. de Lima-Neto, S. A. S. Machado, and L. A. Avac, Electrochim. Acta, 144 (1998) 1515-1523.

[33] N. Mamacaa, E. Mayousse, S. Arrii-Clacens, T. W. Napporna, K. Servat, N. Guillet and K.B. Kokoh, Appl. Catal. B: Environ., 111 (2012) 376-380.

Chapter 6

Synthesis and characterization of IrO$_2$ nanosheet for oxygen evolution reaction

Abstract

IrO_2 nanosheet, a catalyst for oxygen evolution reaction is developed via wet-chemical route. IrO_2 NS was synthesized using Ir^{3+} salt, urea, and glucose followed by calcination at 500 ℃ for 10 h. The 2D morphology of IrO_2 was aimed to produce a good OER catalyst with admirable activity as compared to other IrO_2 catalyst with different morphologies. IrO_2 NS needs a potential of 1.6 V vs. RHE to generate 10 mA/cm^2 current density. On comparison with the commercial IrO_2 it has been confirmed that commercial IrO_2 requires the overpotential of 246 mV to achieve current density of 10 mA/cm^2 that indicates 150 mV more overpotential is required to generate a current density of 10 mA/cm^2 as compared to IrO_2 NS. The reason for excellent oxygen evolution activity of IrO_2 NS corresponds to 2D morphology which has high surface area and possibly of more active sites that can make rapid electron flow during electrocatalytic reaction. Formation of oxygen using IrO_2 nanosheet as an electrocatalyst is represented in scheme 6.1.

IrO$_2$ Nanosheet
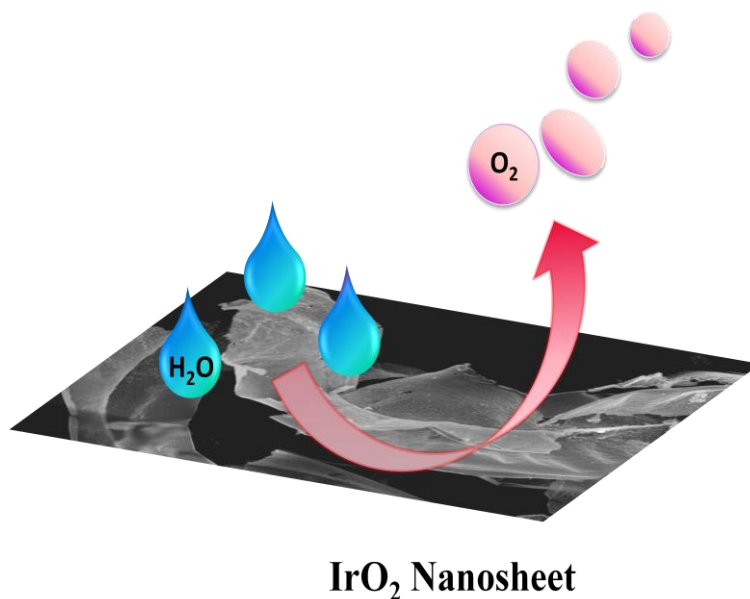
Scheme 6.1: Diagrammatic representation of oxygen evolution using IrO$_2$ NS

6.1. Introduction

One of the most important natural phenomenon that human beings have tried is photosynthesis (natural splitting of water). Artificial splitting of water is the biggest challenge in front of scientific community because it is very difficult to split water into oxygen and hydrogen gas under normal conditions. Strong and effective efforts have been put forward to bring this interesting phenomenon (artificial photosynthesis) to happen. The phenomenon of artificial photosynthesis have achieved considerable attention round the globe, because it is believed that artificial photosynthesis is one of the important technique to store energy and to produce green fuel, H_2 gas. [1, 2]

Production of oxygen gas via electrocatalytic oxidation of water has attained plenty of interest, because water splitting via oxygen evolution is playing a vital role in chemical energy storage. [3] Oxygen evolution reaction (OER) is a basic phenomenon for many important and convenient energy conversion and storage technologies like electrolysis of water and rechargeable metal-air batteries. [3, 4] Need of time demands the invention and discovery of efficient water oxidation electrocatalyts to improve future energy technology. Various metal oxides like Co_3O_4, Mn_2O_3, Rh_2O_3, IrO_2, and RuO_2 have solved this problem to certain extent. [5-9] It has been proclaimed that for OER, metal oxide catalysts formed from 4d/5d metal elements (e.g., RuO_2 and IrO_2) have shown better efficiency than 3d metals. [3] Though 4d/5d metal oxides are more promising in OER but on the other hand they are too expensive. One of the drawback for metal oxide based catalysts for OER is the stability of high metal oxidation state. [10] However, IrO_2 and RuO_2 have shown great success both in terms of stability and efficiency. In comparison between IrO_2 and RuO_2 metal oxide, IrO_2 is considered as a better catalyst because RuO_2 readily gets converted to higher and unstable oxidation state RuO_4. [11, 12]

Different efforts and techniques have been employed for the synthesis of IrO_2 nanomaterial, e.g., vapor deposition, thermal decomposition, and pulsed-laser deposition using iridium salt. [13-15] One of the widely discussed process is calcination of iridium metal precursor to synthesize iridium oxide nanomaterial. Tak and co-workers reported, with the increase in calcination temperature Ir metal precursor is converted into iridium oxide nanoparticles. [16] The study revealed that metal precursors are initially converted into metallic iridium and then oxidized to iridium oxide. The same group also reported the increase in crystallinity during particle growth with increase in calcination temperature. [16] The formation

of thin iridium oxide by calcination was also studied by Johnson and co-workers. [17] Chen and co-workers reported the pyrolysis of iridium metal precursors under high temperature to synthesize colloidal IrO_2 nanoparticles for OER. [18] Zhou and co-workers developed a fascinating chemical pathway for the synthesis of metal oxide nanosheets at 500 °C for energy conversion. [19]

Being inspired from the above studies we hereby elucidated a simple and facile thermal method to synthesize highly crystalline IrO_2 nanosheet (NS) without using any stabilizer. IrO_2 NS was synthesized using a wet-chemical approach. During the synthesis, Ir^{3+} salt was added in glucose and urea and the mixture was heated at 150 °C for 6 h, resulting in the formation of black floppy mass of carbon slurry with homogeneously distributed Ir^{3+} salt. The carbon slurry was calcined for 10 h at 500 °C to get IrO_2 NS. To prove the authenticity of the material IrO_2 NS was characterized using powder X-ray diffraction, field emission scanning electron microscopy, X-ray photoelectron spectroscopy, and transmission electron microscopy techniques. The 2D morphology of IrO_2 NS was aimed to increase surface area, number of active sites, and fast electron transfer during electrocatalytic activity. The activeness of the catalyst was justified by OER results. For OER, 1.62 V potential was required to gain 10 mA/cm^2 current density. The advantages of as-synthesized IrO_2 NS are multifold. First, a simple and convenient approach has been used to synthesize IrO_2 NS without any stabilizer. Second, IrO_2 NS has been explored for oxygen evolution electrocatalysis. 2D morphology of IrO_2 has high surface area and possibly more number of active sites that can make rapid electron flow during OER.

6.2. Experimental Section

6.2.1. Synthesis of IrO_2 nanosheet

A simple and convenient wet-chemical method was developed by Chen and co-workers for the synthesis of TiO_2, Fe_2O_3, Co_3O_4, ZnO and metal oxide nanosheet. [19] Similar method was followed for IrO_2 synthesis. This method consists of pre-calcination and calcination steps. In pre-calcination step, a black color carbon slurry with uniformly distributed Ir^{3+} salt was obtained by giving a heat treatment to 1.0 g urea, 5.0 g glucose, and 2.0 mL of 0.02 M $IrCl_2.3H_2O$ at 150 °C for 6 h. After that the carbon slurry was calcined at 500 °C for 10 h in a muffle furnace. Prior to calcination the carbon slurry was well crushed using mortar pastle and transferred into a covered

crucible. Finally, a black color product was left in the crucibles and was used without any further purification. The formation of IrO_2 is shown in scheme 6.2.
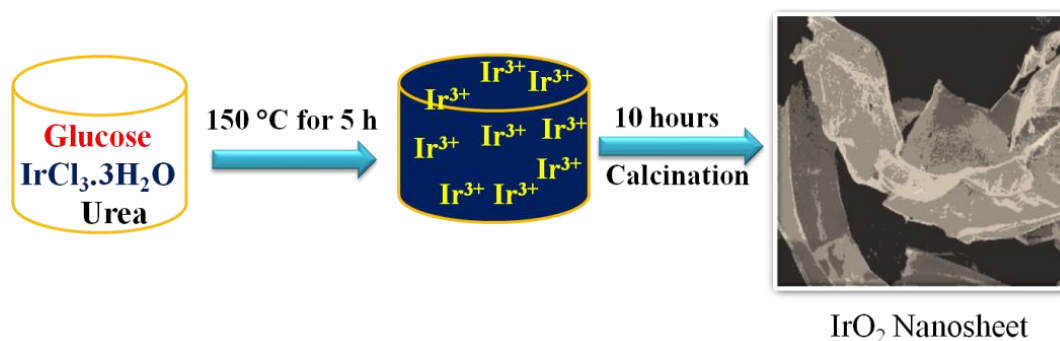
Scheme 6.2: Schematic representation for IrO₂ NS synthesis using wet chemical route

6.3. Results and Discussion

6.3.1. Powder X-ray diffraction pattern of IrO₂ NS

The diffraction pattern and crystal phase was determined by PXRD as shown in Figure 6.1. The diffraction peaks were compared with literature and is well (JCPDS 88-0288) agreement with our result. [20] The diffraction peaks at 2θ = 28.033°, 34.74°, 40.28°, 54.11°, 58.37°, 66.07°, 69.16° and 73.26° corresponding to (110), (101), (200), (211), (220), (310), (301) and (202) planes, which authenticates that IrO_2 is pure with rutile structure. Similar rutile structure of IrO_2 has been reported by Sampath and co-workers. [21]
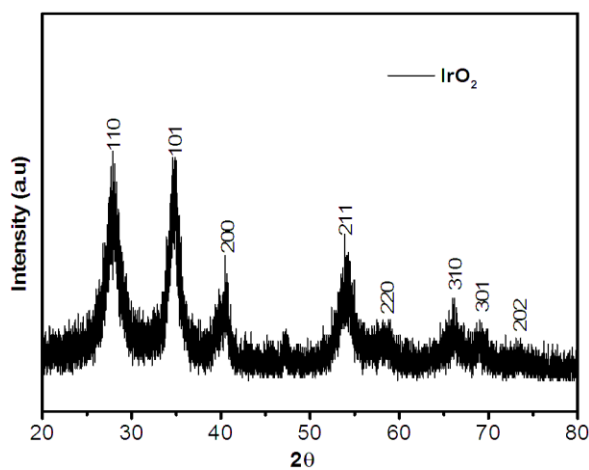
Figure 6.1: Powder X-ray diffraction patterns of IrO₂ NS

6.3.2. FESEM and TEM analysis

To study the nature and morphology of IrO_2 FESEM images were taken as shown in Figure 6.2. The images revealed well developed two dimensional sheet type morphology of IrO_2. The information from TEM analysis also elucidate the sheet morphology of as-synthesized IrO_2, shown in Figure 6.3. It can be seen from the TEM images that there are superimpositions of the planes, this overlapping of planes justify sheet formation (Figure 6.3b). HRTEM image shows interplanar distance equal to 0.258 nm, which infers the growth mainly occurs through (101) plane (Figure 6.3b). The presence of Iridium and Oxygen are confirmed by EDS analysis (Figure 6.4) The authentication of the presence of Iridium and Oxygen elements is also confirmed by EDS line mapping analysis (Figure 6.5).

Figure 6.2: FESEM images of IrO_2 NS

Figure: 6.3 (a) TEM and (b) HRTEM image of IrO_2 NS. HRTEM image shows the d-spacing calculation

Figure 6.4: EDS spectrum of IrO$_2$ NS

Figure 6.5: Line mapping of IrO$_2$ NS

6.3.3. XPS study of IrO_2 NS

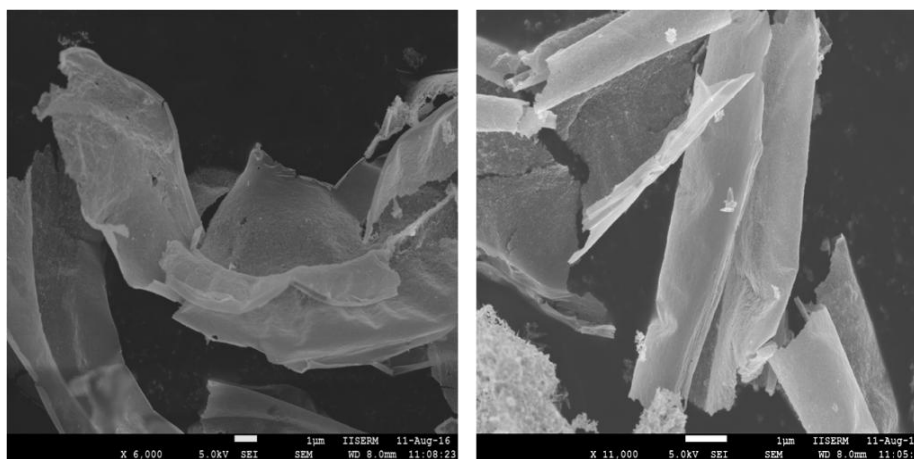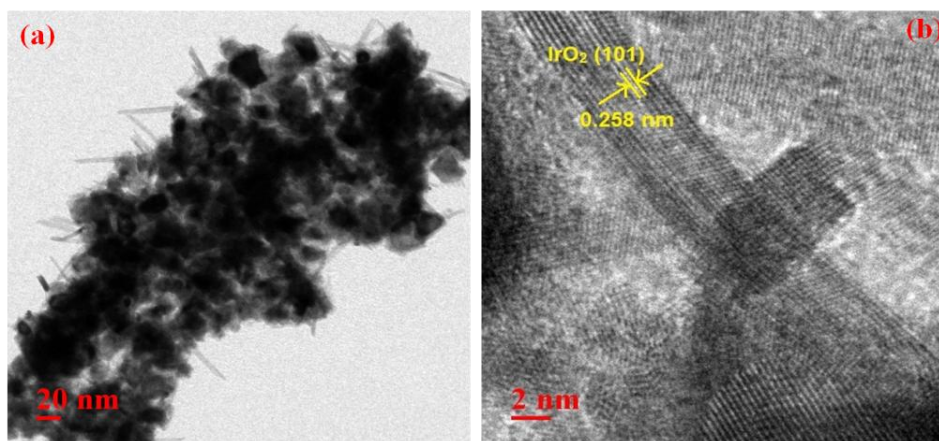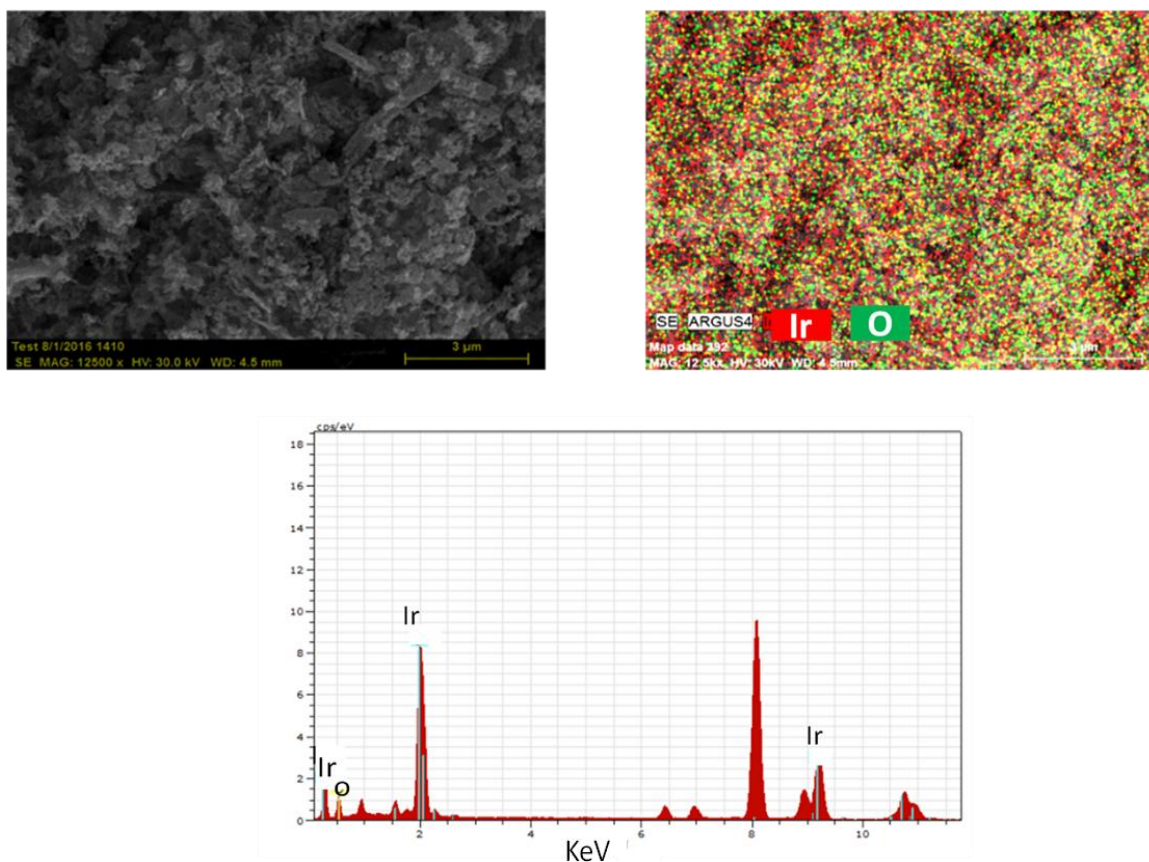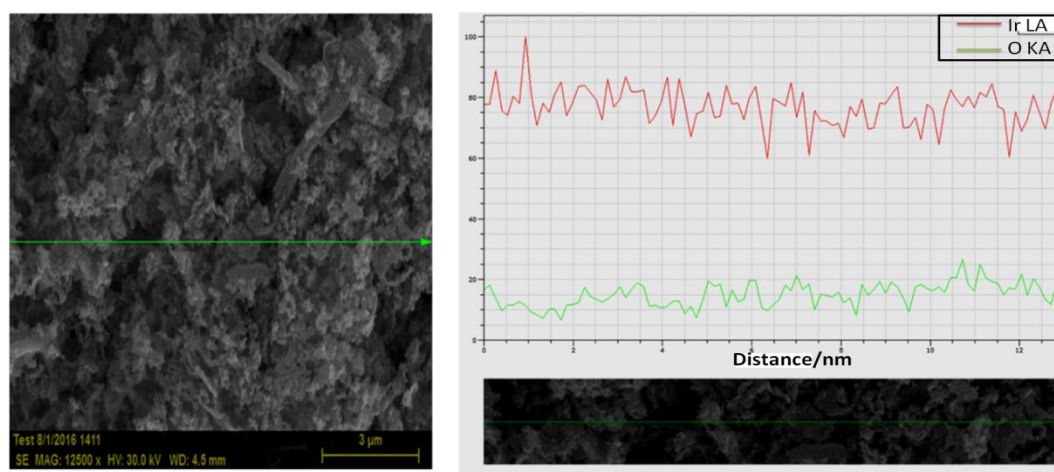The whole XPS analysis of IrO_2 is shown in Figure 6.6. The survey spectrum reveals the presence of Ir 3d (313.5 eV and 297.2 eV) [24, 25], O1s (531.1 eV) [22, 26] and C1s (284 eV). The high resolution XPS spectra of Ir 4f and O 1s is illustrated in Figure 6.6b, and c, which confirms Ir(IV) oxidation state in IrO_2. For Ir 4f two energy states, $4f_{7/2}$ and $4f_{5/2}$ are attributed to the binding energy of 61.2 eV and 64.01 eV, respectively. While for O 1s the binding energy is 531.1 eV. Peuckert and co-workers reported similar binding energy of Ir in electrochemically grown layer of IrO_2. [22]
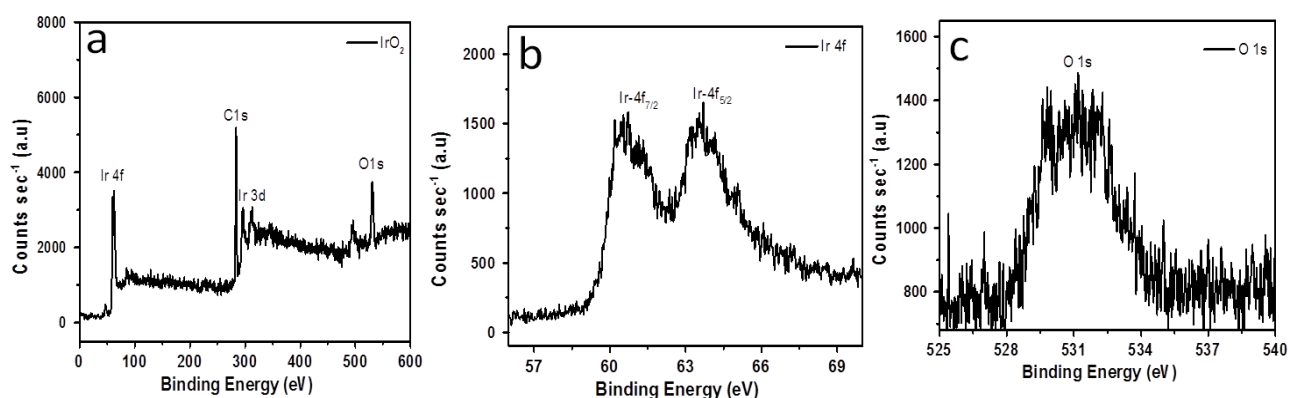
Figure 6.6: XPS analysis of IrO_2 (a) survey spectrum high resolution of (b) Iridium (c) Oxygen

6.4. Formation mechanism of IrO_2 nanosheet

A simple and wet chemical approach has been used to synthesize IrO_2 NS. Urea, glucose and iridium chloride have been used *via* heat treatment of 6 h at 150 °C in a beaker resulting in the formation of fluffy mass of carbon slurry. This has been followed by calcination, in which the as-obtained carbon slurry has been calcined for 10 h at 500 °C in a muffle furnace. Prior to calcination, the carbon slurry has been well crushed in a mortar pastle and kept in a covered crucible. In order to know the mechanism of formation and growth morphology, heat treatment of 3 h and 6 h have been given at 500 °C. As the melting point of glucose and urea is 137 °C and 135 °C, respectively, so, during the precalcination treatment glucose is turned into molten syrup (polymeric form of glucose). During the process gases (CO_2, NO_2 etc.) driven from urea blow

142

the polymeric form of glucose into a large number of bubbles. The metal salts are also associated with these thin walled bubbles. By the time the bubble walls gradually get thinner by the continuous blow of gases from urea and results in the formation of porous carbon foam containing metal salts. This precalcination step is interesting for so many reasons. First, in molten form of glucose metal salts are not thermally decomposed. Second, molten glucose could be easily turned into bubbles by the blowing of gases. Third, most importantly the molten form of glucose is abundant in the oxygen functional groups which helps in uniform and homogeneous distribution of metal salts. FESEM and PXRD analysis have been performed for both 3 h and 6 h samples. PXRD (Figure 6.7) analysis of 3 h sample revealed that along with IrO_2 small amount of metallic Ir is also present. The existing 2θ values at 40.9°, 47.4°, 69.2°, 83.5° and 87.7° with the crystal planes (111), (200), (220), (311) and 222, respectively are attributed to metallic iridium. [16, 20, 21, 27-30] Interestingly, in 6 h sample all the peaks of metallic iridium are almost disappear, while the peak intensity of (110), (101) and (200) at 2θ = 28.03°, 34.74°, and 40.28° increases. This information interprets higher crystallinity and growth of IrO_2 at 6 h as compared to 3 h sample.
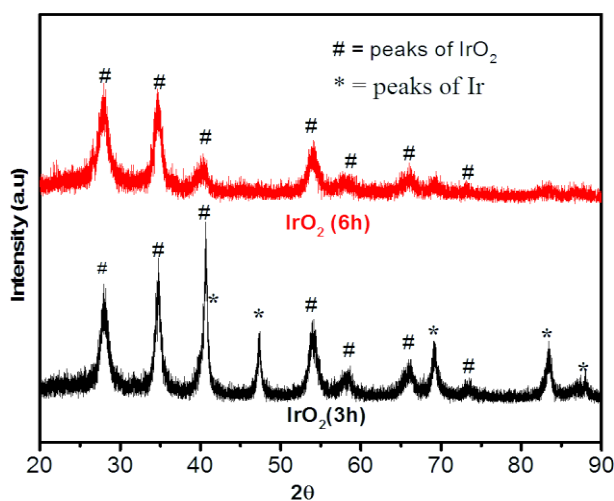
Figure 6.7: PXRD analysis of IrO₂ sample after 3 h and 6 h of calcination

Tak and co-workers also reported with the increase in calcination time and temperature metallic Ir converted into IrO_2 and more crystalline. [16] Degree of crystallinity increases with the increase in calcination temperature has also been reported by Linkov and co-workers. [27] The

results shown by Kraehnert and co-workers are also in line that increase in crystallinity of IrO_2 sample with time. [31] FESEM analysis of 1 h, 3 h, 6 h and 10 h IrO_2 samples have been carried out. From the FESEM study it is quite clear that the sheet formation starts just after 1 h and 3 h calcination treatment, but the sheets are very thick. After 6 h of calcination the sheets become thinner and finally, the sheets are extremely thin after 10 h heat treatment, which is shown in Scheme 6.3.

1h   3h   6h   10h
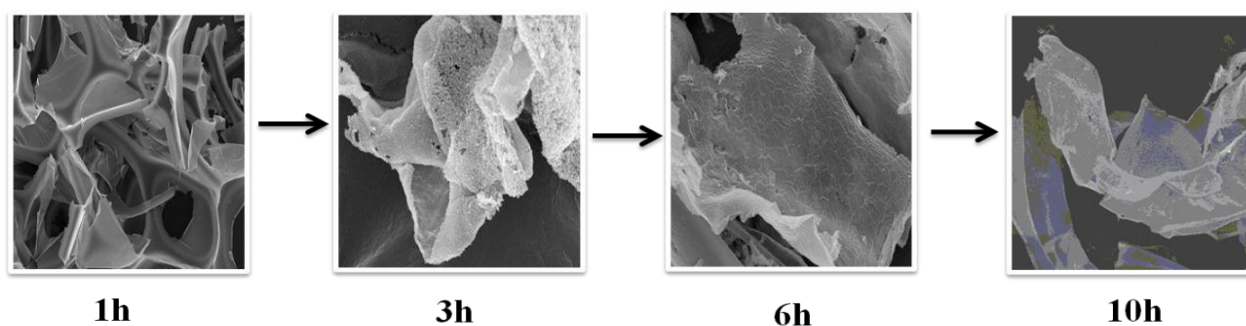
Scheme 6.3: Representation of formation of IrO_2 NS in different time intervals

6.5. Application in oxygen evolution reaction

An ink was prepared by using 1.0 mg IrO_2 sample, 100 μL of isopropyl alcohol, and 20.0 μL nafion. In order to functionalize GCE, 3.0 μL freshly prepared catalyst suspension was drop casted on GCE surface. This results in loading of ~0.357 mg/cm^2 amount of catalyst on the surface of GCE. Before drop casting GCE was cleaned properly by 1.0 μm, 0.3 μm and 0.05 μm alumina slurry in three different polishing cloth. After that well cleaned and polished GCE was sonicated in millipore water for 10 min and dried in nitrogen gas flow prior to use.

6.5.1. LSV comparative study of bare GC, IrO_2 NS, and commercial IrO_2

To check the electrocatalytic OER activity of IrO_2 NS, linear sweep voltammetry (LSV) technique was used. All the experiments were conducted in 0.5 M KOH. The scan rate of 10 mV/s was taken during the measurements of LSV polarization cures. Potentials were measured

with respect to Ag/AgCl electrode and finally converted to RHE electrode. The current densities so obtained were normalized to the geometric surface area of the electrode. From the anodic polarization curves Figure 6.8a & b, IrO_2 NS has onset potential of 1.526 V vs. RHE and overpotential of 96 mV is required to achieve current density of 10 mA/cm^2. To know the electrocatalytic efficiency of as-synthesized catalyst we have compared the activity with commercial IrO_2.
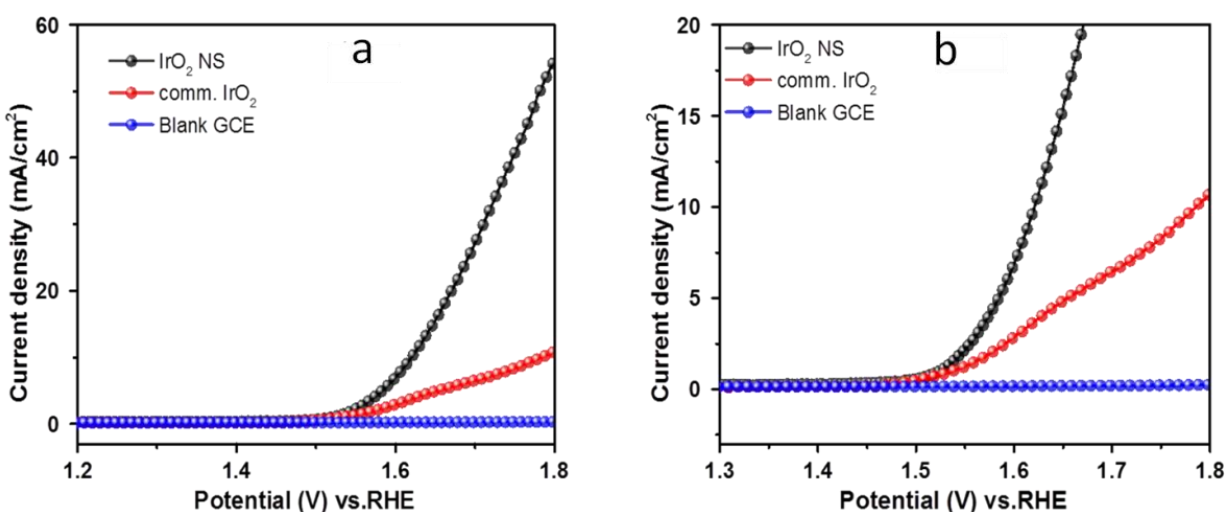
Figure 6.8: LSV curve of bare GCE, IrO$_2$ (10 h), and commercial IrO$_2$ in (a) high scale and (b) low scale

The results illustrated that the onset potential of commercial IrO_2 is 1.541 V and it requires the overpotential of 246 mV to achieve current density of 10 mA/cm^2 that indicates commercial IrO_2 needs 150 mV more overpotential for 10 mA/cm^2 as compared to IrO_2 NS. The reason behind the better efficiency of IrO_2 catalyst can be explained based on electrochemical surface area calculation. ECSA values are obtained by plotting CV curves of IrO_2 NS and commercial IrO_2 in the potential region of 1.00 to 1.10 V (vs. RHE) at different scan rates in 0.5 M H_2SO_4 solution (Figure 6.9a and b). The double layered charging current was then measured from CV curves at a potential of 1.06 V and these values were plotted against different scan rates, which gives linear relationship (Figure 6.9b). The slope is equal to double layer capacitance (C_{dl}) of IrO_2 NS and commercial IrO_2 electrode. The measured double layered capacitance of IrO_2 NS and

commercial IrO_2 catalysts are 0.74 mF and 0.125 mF, respectively. Finally, ECSA values are calculated by taking the ratio of non-Faradaic capacitive current to smooth surface area of IrO_2 oxide where, C_s is the specific capacitance of smooth surface of an IrO_2 oxide and is equal to 60 µF. ECSA value of IrO_2 NS and commercial IrO_2 are 12.34 and 2.08, respectively. The greater ECSA value of IrO_2 NS favors more activity and better efficiency. Detailed comparison of mass activity, ECSA, roughness factor (R_f) (which have been utilized to predict the performance of electrocatalysts) of IrO_2 NS and commercial IrO_2 are summarized in table 6.1.

In order to know the stability of IrO_2 catalyst, 500 continuous cycle has been performed during OER. It has been observed (Figure 6.10) from the LSV curve of initial and after 500 cycle that there is no significant change in current density and onset potential. This indicates the robustness of the catalyst in a strong base. Comparison of OER activity of as-synthesized IrO_2 and literature report with IrO_2 based catalysts under both acidic and basic conditions is shown in table 6.2.

6.6. Mechanism of OER

Formation of oxygen-oxygen double bond requires four electrons, hence a very difficult process to monitor. Removal of four electrons is unfavorable both kinetically as well as thermodynamically. So, OER has sluggish kinetics. The most widely applied technique to study electrocatalytic reactions is steady-state Tafel plot analysis. In the present study the Tafel slope value is 82 mV dec^{-1}, which is shown in Figure 6.11.

Table 6.1: Comparison of different kinetic parameters of IrO_2 NS with commercial IrO_2

Anode	Mass loading mg/cm^2	Mass Activity (A/g) at 1.620 V	Over potential required to generate 10 mA/cm^2	ECSA	Rough-ness factor (R_f)	Tafel slope (mV/dec)
Commer-cial IrO_2	0.357	10.11	246 mV	2.08	29.44	154
IrO_2 NS (10h)	0.357	27.2	96 mV	12.34	173.80	97
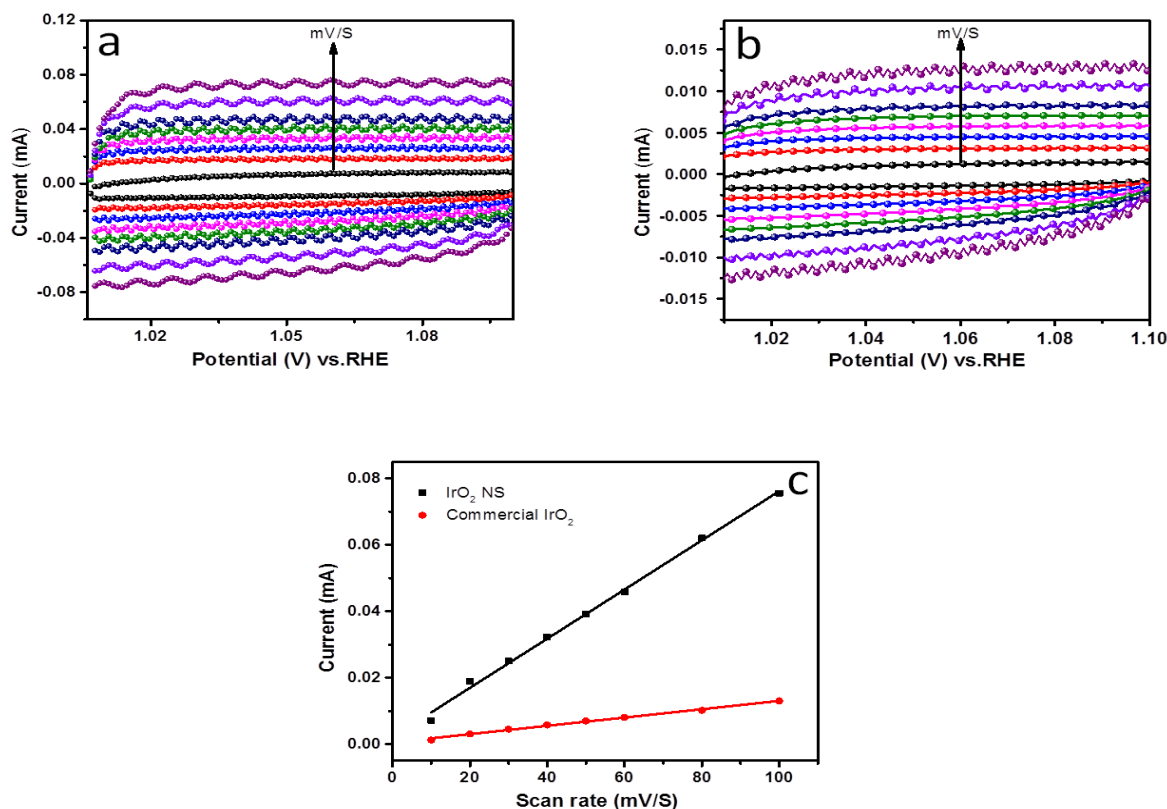
Figure 6.9 Current vs. potential plot of (a) IrO₂ NS, (b) commercial IrO₂, and (c) current vs. scan rate plot

Table 6.2: Comparison of OER activity data for different catalyst in acid and basic medium.

Catalyst	substrates	Medium	Current density (mA cm^{-2}) at any specific overpotential	Overpotential (mV) at 10 mAcm^{-2}	Tafel Slope	Reference
IrO₂-TiO₂	GCE	0.1 M HClO₄	10 Ag^{-1}@ 1.485 V	-	42	[6]
IrOx/Au	Au	0.1M NaOH	-	370		[10]
IrO₂	RDE	0.1 M HClO₄	3.4 A gox^{-1} at E = 1.48 V	-	44	[20]
IrOₓ(OH)ᵧ film	FTO	0.1 M phosphate solution	12.4 mA cm^{-2} at 1.6 V	-	42	[12]
IrO₂	GCE	0.5M H₂SO₄	-	0.24 V at 0.5 mA cm^{-2}	-	[18]
DNA@IrO₂ NPs	GCE	0.1M NaOH	-	312	90	[24]
IrO₂ NS	GCE	0.5M KOH	-	96	97	This work
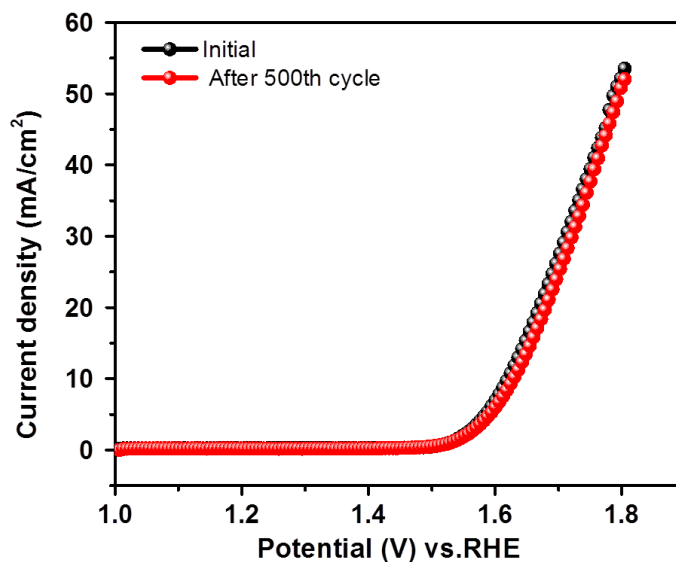
Figure 6.10: LSV curve of the initial and after 500 cycles in a strong base

6.7. Electrochemical impedance spectroscopy

To know the charge transport efficiency, impedance measurements are carried out for IrO_2 catalysts at their respective onset potentials in 0.5 M KOH. The results are obtained through RC (resistor–capacitor) circuit. The semicircle in the Nyquist plot is attributed to single "time constant" and determines the resistance offered because of charge transfer.
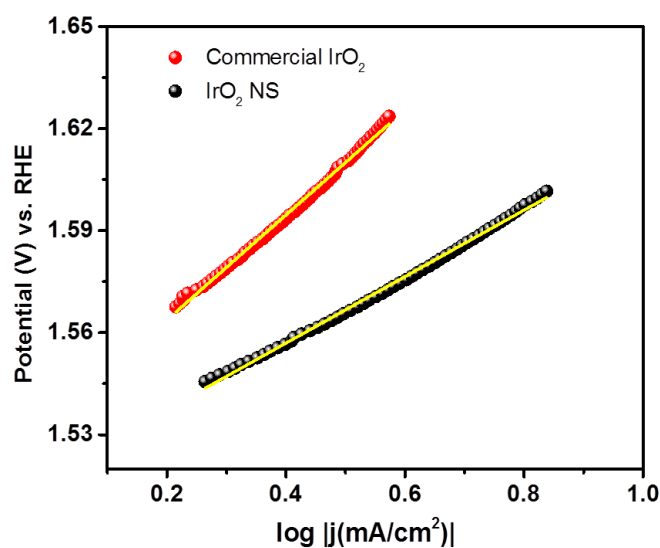
Figure 6.11: Tafel slope for IrO₂ NS and commercial IrO₂
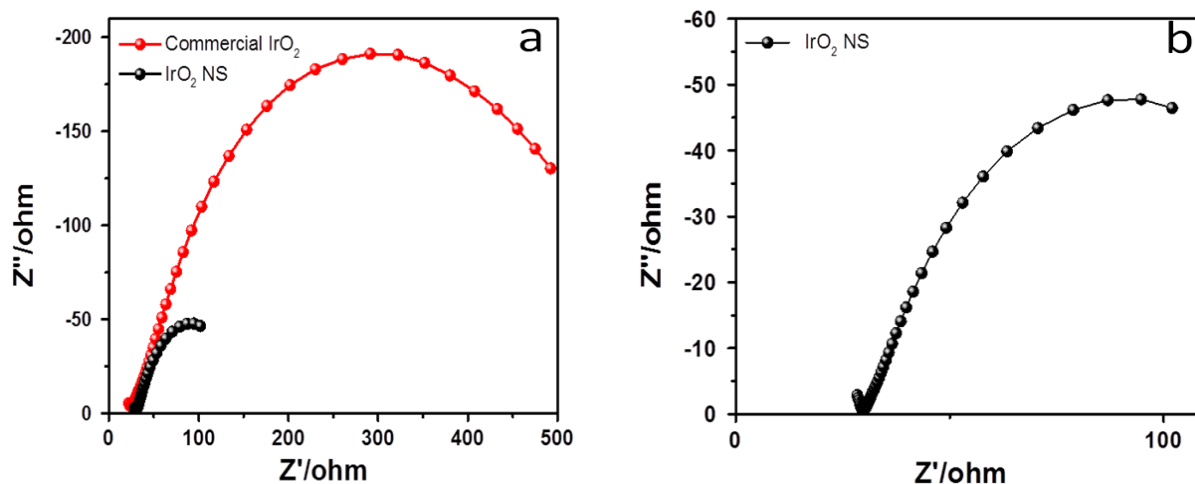
Figure 6.12: Electrochemical impedance measurement plot for (a) IrO$_2$NS and commercial IrO$_2$ (b) magnified version of IrO$_2$ NS

An equivalent circuit that is composed of one constant phase element (CPE), R$_S$ = solution resistance and R$_{CT}$ = charge transfer resistance is used to fit the evaluated data. The Nyquist plot, are presented in (Figure 6.12) The calculated solution resistance (R$_S$) and charge transfer resistance (R$_{CT}$) are shown in Table 6.3. R$_{CT}$ value of IrO$_2$ lies in low frequency region and the value is 81 Ω. The low R$_{CT}$ value infers fast reaction kinetics, which also indicates high charge transport efficiency and excellent electrolyte electrode interface connectivity.

Table 6.3: Charge transfer resistance and solution resistance of IrO$_2$ NS and commercial IrO$_2$

Anode	R$_S$(Ω)	R$_{CT}$(Ω)
IrO$_2$ (10 h)	24	81
Commercial IrO$_2$	19	476

6.8. Characterization after electrocatalysis

After doing the electrocatalysis study we have collected the sample in order to know the morphology of the nanosheet. We have checked the morphology with FESEM analysis and the

presence of metal ions has been confirmed from EDS analysis. The results revealed that the nanosheet has retained the sheet morphology with similar composition (Figure 6.13).
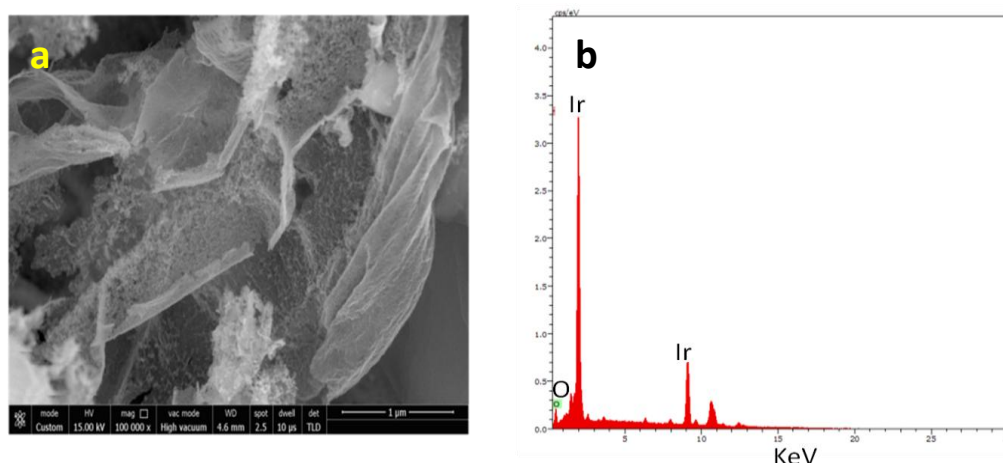
Figure 6.13: FESEM (a) and EDS (b) analysis after electrocatalysis of IrO$_2$ NS

6.9. Conclusion:

In conclusion, we have demonstrated a simple and facile thermal methodology for the synthesis of highly crystalline IrO$_2$ NS without any support. IrO$_2$ NS samples have been characterized by XRD, XPS, FESEM, and TEM analysis. The growth mechanism of IrO$_2$ nanosheet formation has been confirmed from FESEM analysis. IrO$_2$ NS showed excellent electrocatalytic activity for oxygen evolution reaction. IrO$_2$ NS required potential of 1.622 V to gain 10 mA/cm^2 current density with the Tafel slope value of 97 mV/dec in OER. So IrO$_2$ NS proved to be better catalyst than commercial IrO$_2$.

6.10. References

[1] T. R. Cook, D. K. Dogutan, S. Y. Reece, Y. Surendranath, T. S. Teets, D. G. Nocera, Chem. Rev. 110 (2010) 6474-6502.

[2] S. Dahl, I. Chorkendorff, Nat. mater., 11 (2012) 100-101.

[3] H. Ooka, A. Yamaguchi, T. Takashima, K. Hashimoto, R. Nakamura, J. Phys. Chem C, 121 (2017) 17873-17881.

[4] J. Suntivich, K. J. May, H. A. Gasteiger, J. B. Goodenough, Y. Shao-Horn, Science, 334 (2011) 1383-1385.

[5] A. Harriman, I. J. Pickering, J. M. Thomas, P. A. Christensen, J. Chem. Soc., Faraday Trans. 1, 84 (1988) 2795-2806.

[6] E. Oakton, D. Lebedev, M. Povia, D. F. Abbott, E. Fabbri, A. Fedorov, M. Nachtegaal, C. Copéret, T. J. Schmidt, ACS Catal., 7 (2017) 2346-2352.

[7] J. Kiwi, M. Grätzel, Angew. Chem., Int. Ed. Engl., 18 (1979) 624-626.

[8] A. Mills, N. McMurray, J. Chem. Soc., Faraday Trans. 1, 84 (1988) 379-390.

[9] G. Beni, L. Schiavone, J. Shay, W. Dautremont-Smith, B. Schneider, Nature, 282 (1979) 281-283.

[10] P. E. Karthik, K. A. Raja, S. S. Kumar, K. Phani, Y. Liu, S.-X. Guo, J. Zhang, A. M. Bond, RSC Adv., 5 (2015) 3196-3199.

[11] F. Hine, M. Yasuda, T. Noda, T. Yoshida, J. Okuda, J. Electrochem. Soc., 126 (1979) 1439-1445.

[12] D. Chandra, D. Takama, T. Masaki, T. Sato, N. Abe, T. Togashi, M. Kurihara, K. Saito, T. Yui, M. Yagi, ACS Catal., 6 (2016) 3946-3954.

[13] R. S. Chen, Y. S. Chen, Y. S. Huang, Y. L. Chen, Y. Chi, C. S. Liu, K. K. Tiong, A. J. Carty, nanostructures J. Chem. Vap. Deposition 9 (2003) 301-305.

[14] M. El Khakani, M. Chaker, Thin Solid Films, 335 (1998) 6-12.

[15] M. El Khakani, M. Chaker, E. Gat, Appl. Phys. Lett., 69 (1996) 2027-2029.

[16] I. Jang, I. Hwang, Y. Tak, Electrochim. Acta, 90 (2013) 148-156.

[17] B. Johnson, F. Girgsdies, G. Weinberg, D. Rosenthal, A. Knop-Gericke, R. Schlogl, T. Reier, P. Strasser, J. Phys. Chem. C, 117 (2013) 25443-25450.

[18] W. Hu, Y. Wang, X. Hu, Y. Zhou, S. Chen, J Mater. Chem., 22 (2012) 6010-6016.

[19] Y. Zhou, G. Chen, Y. Yu, C. Yan, J. Sun, F. He, J Mater. Chem A, 4 (2016) 781-784.

[20] D. F. Abbott, D. Lebedev, K. Waltar, M. Povia, M. Nachtegaal, E. Fabbri, C. Copéret, T. J. Schmidt, Chem. Mater., 28 (2016) 6591-6604.

[21] K. Chakrapani, S. Sampath, Chem. Commun., 51 (2015) 9690-9693.

[22] M. Peuckert, Surf. Sci., 144 (1984) 451-464.

[23] C. Angelinetta, S. Trasatti, L.D. Atanasoska, Z. Minevski, R. Atanasoski, Mater. Chem. Phys., 22 (1989) 231-247.

[24] S. Anantharaj, P. Karthik, S. Kundu, J Mater Chem A, 3 (2015) 24463-24478.

[25] I. Kodintsev, S. Trasatti, M. Rubel, A. Wieckowski, N. Kaufher, Langmuir, 8 (1992) 283-290.

[26] H. Y. Hall, P. M. Sherwood, J Chem. Soc., Faraday Transactions 1, 80 (1984) 135-152.

[27] C. Felix, T. Maiyalagan, S. Pasupathi, B. Bladergroen, V. Linkov, Micro and nanosystems, 4 (2012) 186-191.

[28] I. Jang, I. Hwang, Y. Tak, Electrochim. Acta, 90 (2013) 148-156.

[29] V. W. Faria, M.F. Brunelli, C. W. Scheeren, RSC Adv., 5 (2015) 84920-84926.

[30] I. Matanovic, H. T. Chung, Y. S. Kim, J. phys. chem. lett., 8 (2017) 4918-4924.

[31] M. Bernicke, E. Ortel, T. Reier, A. Bergmann, J. Ferreira de Araujo, P. Strasser, ChemSusChem, 8 (2015) 1908-1915.

Chapter 7

Conclusion and future scope

7.1. Conclusion

Nanoscience and Nanotechnology is the great invention in the field of science. Recent advancement in the synthesis approach and new innovations in electronic microscopes and other instruments have shown great impact in the synthesis and characterization process of nanomaterials. Materials in nanodimension have shown better efficiency than the bulk materials.

Graphitic-carbon nitride (g-C_3N_4) proved to be one of the important substrates for the synthesis of metal nanoparticles. Monometallic Pd and Pt nanoparticles were decorated on the surface of C_3N_4 results in the formation of C_3N_4/Pd and C_3N_4/Pt composites. These nanocomposites proved efficient catalysts for nitrocompound reduction and hydrogen evolution reactions. In nitro aniline reduction C_3N_4/Pd proved to be the best catalyst while in case of hydrogen evolution reaction C_3N_4/Pt was a better catalyst.

We further explored the semiconducting surface of C_3N_4 and succeed in synthesizing bimetallic alloy nanoparticles of AgPd, AgPt and AgAu via galvanic exchange, where Ag acted as sacrificial atom. As the galvanic exchange took place on the solid surface, so 100% replacement of Ag could not be achieved. In this process initially Ag NPs were synthesized on the surface of C_3N_4 and later sacrificial Ag was replaced by Pd, Pt and Au nanoparticles resulting in the combination of C_3N_4/AgPd, AgPt and AgAu alloys. These bimetallic alloys were applied in hydrogen evolution reactions where C_3N_4/AgPt proved to be a best catalyst.

Au nanoparticle decorated CuS nanoplates were fabricated via photochemical reduction of Au(III) ions to Au nanoparticles on the surface of CuS plates. Au nanoparticle modified CuS nanostructure function as an efficient electrocatalyst in electrocatalytic hydrogen evolution reaction as well as photocatalytic decomposition of MB dye under visible light. Upon application of external potential Au nanoparticles helps in rapid charge transfer from CuS to electrolyte to enhance the electrocatalytic performance in hydrogen evolution reaction. CuS-Au-3 showed best performance in photocatalytic decomposition of MB dye under visible light. Au nanoparticle present on the surface of CuS behave as an electron sink, which drags photo generated electron from CuS under irradiation of visible light and facilitate the MB degradation process nearly 21 times.

We also developed a simple and facile thermal methodology for the synthesis of highly crystalline 1D RuO_2 NR without using any support. The growth mechanism of RuO_2 nanorod formation was confirmed from XRD and FESEM analysis. RuO_2 NR

showed excellent electrocatalytic activity for both hydrogen and oxygen evolution reaction. Therefore, this catalyst proved to be a prominent substitute of other oxide and sulphide nanomaterials in HER and OER.

Similar wet chemical route like RuO_2 NR was also used to synthesize IrO_2 2D nanosheet. Mechanism of formation of IrO_2 NS was studied in detail by giving different calcinations treatment to the carbon slurry obtained in pre-calcination step. IrO_2 NS proved an excellent OER catalyst and electrocatalytic activity of IrO_2 NS was better than commercial IrO_2.

7.2. Future Scope

- **Synthesis of g-C_3N_4/IrO_2, g-C_3N_4/IrO_2/Pd and Pt:** Combination of C_3N_4/IrO_2 is possible by synthesizing IrO_2 on the surface of C_3N_4. The as synthesized combination of C_3N_4/IrO_2 nanocomposites can be decorated with Pd or Pt nanoparticles for photocatalysis as well as electrocatalysis.

- **Synthesis of bimetallic alloy of Pd and Pt in different ratios on the surface of carbon nitride for HER:** Alloy of PdPt can be decorated on C_3N_4 in different proportions and can be used to check HER activity as well as nitro aromatic reduction.

- **Synthesis of IrO_2/Pd or RuO_2/Au composition as bifunctional electrocatalyst (HER and OER):** Simple and facile thermal methodology for the synthesis of highly crystalline 1D RuO_2 NR and 2D IrO_2 NS without using any support can be further modified by decorating Au and Pd nanoparticles on RuO_2 and IrO_2 surface for OER and HER.

Appendices

List of Publications

[#][1] **Roshan Nazir**, Pragati Fageria, Mrinmoyee Basu, Subhashis Gangopadhyay and Surojit Pande, Decoration of Pd and Pt nanoparticles on a carbon nitride (C_3N_4) surface for nitro-compounds reduction and hydrogen evolution reaction, *New J. Chem.*, 2017, **41**, 9658-9667.

[#][2] **Roshan Nazir**, Pragati Fageria, Mrinmoyee Basu , and Surojit Pande, Decoration of Carbon Nitride Surface with Bimetallic Nanoparticles (Ag/Pt, Ag/Pd, and Ag/Au) via Galvanic Exchange for Hydrogen Evolution Reaction, *J. Phys. Chem. C*, 2017, 121 (36), 19548-19558.

[#][3] Mrinmoyee Basu, **Roshan Nazir**, Pragati Fageria & Surojit Pande, Construction of CuS/Au Heterostructure through a Simple Photoreduction Route for Enhanced Electrochemical Hydrogen Evolution and Photocatalysis, *Sci. Rep.*, 2016, 6, 34738.

[4] Mrinmoyee Basu, **Roshan Nazir**, Chavi Mahala, Pragati Fageria, Sumita Chaudhary, Subhashis Gangopadhyay, and Surojit Pande, Ag_2S/Ag Heterostructure: A Promising Electrocatalyst for the Hydrogen Evolution Reaction, *Langmuir*, 2017, 33 (13), 3178-3186.

[5] Pragati Fageria, Shravan Uppala, **Roshan Nazir**, Subhashis Gangopadhyay, Chien-Hsiang Chang, Mrinmoyee Basu, and Surojit Pande, Synthesis of Monometallic (Au and Pd) and Bimetallic (AuPd) Nanoparticles Using Carbon Nitride (C_3N_4) Quantum Dots via the Photochemical Route for Nitrophenol Reduction, *Langmuir*, 2016, 32 (39), 10054-10064.

[6] Pragati Fageria, Sudharshan K.Y., **Roshan Nazir**, Mrinmoyee Basu and Surojit Pande, Decoration of MoS_2 on g-C_3N_4 surface for efficient hydrogen evolution reaction, *Electrochim. Acta*, 2017, 258, 1273-1283.

[7] Sonam Sharma, **Roshan Nazir**, Surojit Pande and Bibhas R. Sarkar, Microwave-Assisted Efficient Suzuki-Miyaura Cross-Coupling Reactions in Water Catalyzed by Nano-Pd/gC_3N_4 Composite, *Chemistry Select*, 2017, 2, 8745-8750.

[8] Pragati Fageria, **Roshan Nazir**, Subhashis Gangopadhyay, Harish C. Barshilia and Surojit Pande, *RSC Adv.*, 2015, 5, 80397-80409.

[#][9] **Roshan Nazir**, Uttaran Basak and Surojit Pande, RuO_2 Nanorod: An Efficient and Stable Electrocatalyst for Hydrogen and Oxygen Evolution Reaction (Manuscript submitted).

[#][10] **Roshan Nazir** and Surojit Pande, IrO_2 Nanosheet: A catalyst for OER (Manuscript under preparation)

(# incorporated in the thesis)

❖ <u>R. Nazir</u> and S. Pande, Decoration of Mono- (Pd and Pt) and Bimetallic (Pd-Pt) Nanoparticles on Graphitic-Carbon Nitride (g-C_3N_4) Surface and their Application in Electrocatalysis and Nitro Compound Reduction, International Conference on Nascent Developments In Chemical Sciences: Opportunities for Academia-Industry Collaboration (NDCS 2015), Organized by BITS Pilani-Pilani Campus, Rajasthan, India during 16-18 October, 2015.

❖ <u>R. Nazir</u>, S. Gangopadhyay, and S Pande, Decoration of mono- (Pd and Pt) and bimetallic (Pd-Pt) nanoparticles on graphitic-carbon nitride (g-C_3N_4) surface for reduction of Nitro arenes and Hydrogen evolution reactions, International Conference on Nanoscience and Technology (ICONSAT 2016), Organized by IISER-Pune, India during February 29 to March 2, 2016.

❖ <u>R. Nazir</u>, M. Basu[*], and S. Pande, CUS and CUS/Au Nanomaterials: Efficient electrocatalyst for H_2 evolution reaction and a promising photocatalyst, International Conference on Advances in Nanomaterials and Nanotechnology (ICANN-2016), Organized by Centre for Nanoscience and Nanotechnology, Jamia millia Islamia, New Delhi, India during 4-5 November, 2016.

❖ <u>R. Nazir</u>, and S. Pande Decoration of Carbon Nitride Surface with Bimetallic Nanoparticles(Ag/Pt, Ag/Pd, and Ag/Au) via Galvanic Exchange for Hydrogen Evolution Reaction, National Conference on New Frontiers in Chemistry From Fundamental to Applications (NFCFA 2017), BITS-Pilani, K. K. Birla Goa Campus, 28-29 December, 2017.

❖ <u>R. Nazir</u>, U. Basak, and S. Pande Decoration of mono- (Pd and Pt) and bimetallic (Pd-Pt) nanoparticles on graphitic-carbon nitride (g-C_3N_4) surface for reduction of Nitro arenes and Hydrogen evolution reactions. International Conference on Nano and Functional Materials (NFM-2017), Organized by Department of Chemistry, BITS Pilani-Pilani Campus, Rajasthan, India 16-18 November 2017.

Dr. SUROJIT PANDE
Assistant Professor, Department of Chemistry, BITS Pilani, Pilani campus, Rajasthan, 333031

Dr. Pande did his M.Sc. in Inorganic Chemistry, Kayani University, Kalyani, West Bengal and Ph. D. from Indian Institute of Technology, Kharagpur. During Ph. D., he worked on metal and metal oxide nanoparticles and their application in catalysis and surface enhanced Raman spectroscopy. He worked on application of metal and metal oxide nanoparticles in catalysis, analytical and environmental chemistry, and surface enhance Raman scattering (SERS) studies using DOPAMINE, 1,10 Phenanthroline, and various dyes as a SERS probe. Before joining BITS on March 2012, Dr. Pande was a postdoctoral fellow in the Richard M. Crooks research group at The University of Texas at Austin, Texas, USA with research interests in homogeneous catalysis using dendrimer-encapsulated nanoparticles. He was experienced on spectroscopic study of sixth and fourth generation of hydroxy-terminated poly(amidoamine) (PAMAM) dendrimer. Synthesis of mono- (Au, Pd, and Pt) and bimetallic (Au@Pd and Pd@Au) dendrimer-encapsulated nanoparticles of definite cluster size and atoms (magic no cluster) and their application in electrocatalyst.

Name: Roshan Nazir.

Born at Ratnipora, Pulwama, Jammu & Kashmir, India.

Graduation (B. Sc.,) from Shri Pratap Singh College Srinagar (2009).

Post-Graduation (M. Sc., Inorganic Chemistry) in 20012, from Jamia Millia Islamia, New Delhi.

Permanent Address:
Village and post: RATNIPORA
District: PULWAMA
State: JAMMU AND KASHMIR
Pin Code: 192121

E-mail: roshanandrabi@gmail.com